Investigating the build-up of brightest cluster galaxies over half of cosmic time

DN Groenewald

20569513

Thesis submitted for the degree *Philosophiae Doctor* in Space Physics at the Potchefstroom Campus of the North-West University

Promoter:	Dr SI Loubser
Co-promoter:	Dr DG Gilbank
Assistant Promoter:	Dr RE Skelton

October 2016

"Peace I leave with you.

My peace I give you.

I do not give to you as the world gives.

Do not let your heart be troubled

and do not be afraid."

John 14:27

Abstract

Central galaxies in galaxy clusters are special. These galaxies referred to in the literature as brightest cluster galaxies (BCGs), are the most luminous (or massive) galaxies in their host clusters and are located at the bottom of the clusters' gravitational potential wells. The stellar mass growth of these massive galaxies is a hotly debated topic. The general picture emerging from simulations suggests that star formation dominates the early stellar mass assembly of the BCGs (at $z \geq 2$), while dry mergers are the dominant mechanism through which these massive galaxies increase their stellar masses at later times ($z \leq 1$). The simulations however predict a much higher mass growth for the BCGs than is observed. Observational studies on the other hand report conflicting results regarding the stellar mass growth of BCGs since $z \leq 1$. Some studies find that the BCGs have not experienced any mass growth since $z \sim 1$, while others measure significant growth over the same redshift range. In this thesis we investigate the importance of major mergers in the stellar mass build-up of BCGs between $0.08 \leq z \leq 0.50$. We do this using two independent methods where we respectively measure the: (i) total and (ii) merger-inferred stellar mass growth of the BCGs. In the first method we simply investigate how the average stellar masses of the BCGs change as a function of redshift. In this analysis we account for the relation between the BCG's stellar mass and the host cluster's halo mass in selecting the BCG sample. In the second method we use close pair statistics as a diagnostic of mergers. Thereafter the close pair fraction is used as a proxy for the BCG merger fraction in order to estimate how much stellar mass growth the BCGs will experience due to mergers. We find that major mergers will contribute $24 \pm 14\%$ on average towards the stellar mass growth of a present day BCG since $z = 0.32$. With regards to the total stellar mass growth of the BCGs, we find that it is $0^{+15\%}_{-3\%}$ between $0.08 \leq z \leq 0.35$. The upper limit on this result depends sensitively on the correction applied for the SDSS photometry of the brightest, largest (lowest

redshift) galaxies. The total mass growth is lower than the merger-inferred growth, although they are consistent within the uncertainties. We find that it is important to take the growth of the clusters' halo masses into account, otherwise one runs the risk of obtaining the non-physical result that BCGs are somehow losing stellar mass towards the present day (i.e. shrinking). We further find that the stellar mass growth of BCGs appears to be independent of the range of parent halo masses probed (providing these clusters are descendants/progenitors of each other). We also find that major mergers are the dominant contributor to the intracluster light stellar mass build-up at low redshifts. Together the total and merger-inferred stellar mass growth results imply that mergers are the dominant mechanism through which a BCG's stellar mass can grow at low redshift.

Keywords: brightest cluster galaxies, galaxy clusters, stellar mass growth, mergers, galaxy formation, galaxy evolution, intracluster light.

Opsomming

Die sentrale galaksies in galaksieswerms is baie spesiaal en in die literatuur staan hierdie galaksies as helderste swerm galaksies (HSGs) bekend. HSGs is die helderste (en massiefste) galaksies in hul gasheerswerms en is aan die onderkant van die swerms se gravitasiepotentiale geleë. Die stermassagroei van die HSGs is 'n onderwerp wat steeds hewig in die literatuur gedebateer word. Modelle voorspel dat die vroeë fases ($z \geq 2$) van die HSGs se stermassagroei gedomineer word deur stervorming, terwyl gas-arm, galaktiese samesmeltings die groei domineer in die latere fases ($z \leq 1$). Waarnemings van die groei is egter baie laer as dit wat deur die modelle aangedui word, hoewel daar teenstrydige bevindinge is wat vanuit waarnemings verkry word vir die stermassagroei van HSGs sedert $z \leq 1$. Sommige waarnemings vind dat hierdie massiewe galaksies geen groei ondergaan het sedert $z \leq 1$ nie, alhoewel ander waarnemings op merkbare groei oor dieselfde rooiverskuiwing dui. In hierdie proefskrif ondersoek ons die rol van groot galaktiese samesmeltings in die stermassagroei van HSGs tussen $0.08 \leq z \leq 0.50$. Vir hierdie doeleinde gebruik ons twee onafhanklike metodes waarmee ons onderskeidelik die (i) totale groei en (ii) die groei a.g.v. galaktiese samesmeltings meet. Met die eerste metode ondersoek ons hoe die HSGs se gemiddelde stermassa varieer as 'n funksie van rooiverskuiwing en hier neem ons die korrelasie tussen die HSG se stermassa en die gasheerswerm se halomassa in ag wanneer die HSG steekproef gekies word. In die tweede metode word die breuk van nabygeleë galaksiepare gebruik as 'n aanduiding van galaktiese samesmeltings. Daarna word die paarbreuk gebruik as 'n aanduiding van die HSGs se samesmeltingsbreuk, ten einde te bepaal hoeveel die stermassas van HSGs toegeneem het a.g.v. groot galaktiese samesmeltings. Ons vind dat hierdie samesmeltings $24 \pm 14\%$ (gemiddeld) sal bydra tot die stermassagroei van 'n huidige HSG sedert $z = 0.32$. M.b.t. die totale stermassagroei is dit gevind om $0^{+15\%}_{-3\%}$ te wees tussen $0.08 \leq z \leq 0.35$. Die boonste limiet is sensitief vir die korreksie wat toegepas word vir

die SDSS fotometrie van die helderste, grootste (laagste rooiverskuiwing) galaksies. Alhoewel die totale stermassagroei laer is as die groei verkry deur samesmeltings, vind ons dat hulle ooreenstem as die foute in ag geneem word. Ons vind dit belangrik om die galaksieswerm se halomassagroei in ag te neem, anders verkry ons die nie-fisiese resultaat dat die HSGs op een of ander manier hul stermassa verloor na die huidige dag (d.w.s. krimp). Verder vind ons ook dat die HSGs se stermassagroei onafhanklik is van hul gasheerswerms se halomassa (gegee dat hierdie galaksieswerms afstammelinggalaksies/voorvadergalaksies van mekaar is). Ons vind ook dat groot galaktiese samesmeltings die dominante meganisme is waardeur die stermassa van die interswerm lig toeneem by laer rooiverskuiwings. Tesame impliseer die totale groei en die groei a.g.v. samesmeltings dat galaktiese samesmeltings die dominante meganisme is waardeur die stermassa van 'n HSG groei by laer rooiverskuiwings.

Sleutelwoorde: helderste swerm galaksies, galaksieswerms, stermassagroei, galaktiese samesmeltings, galaktiese vorming, galaktiese evolusie, interswerm lig.

Acknowledgements

First and foremost I want to thank my supervisors, Dr. David Gilbank, Dr. Rosalind Skelton and Dr. Ilani Loubser for their endless patience and guidance throughout the years. Your comments and suggestions have been greatly appreciated. I own you all a big thank you.

To my wonderful husband, Coenie, you will never know how much your love and support has meant to me these last few years. Thank you for coming on this journey with me, without you I would not have made it. Thank you my love.

To all my friends, new and old, thank you for the words of encouragement and support you gave in times of need. A PhD is not a journey one can attempt alone. A special thanks to Marissa and Enrico Kotze for the words of advice, I will always guard them close to my heart.

To my wonderful parents, Barbara and Pierre, a simple 'thank you' can never express my gratitude towards you both. *Dankie mamma and pappa vir alles, ek het julle ontsettend lief.* I also want to thank my wonderful in-laws, Susan and Coenie, for their support and love. *Dankie ma San en pa Coen, julle ondersteuning beteken so baie.*

Above all, I thank the Lord for the privilege to study towards a PhD degree. You blessed me with so many opportunities to make my dreams come true and also to experience the world. My soul stands in awe of Your power and love.

The work presented in this thesis is based in part on observations taken with the Southern African Large Telescope (proposals 2013-2-RSA-008 and 2014-1-RSA_OTH-009). I thank the South African Astronomical Observatory for allocating me the time.

Lastly, I want to acknowledge the help of Mrs. Petro Sieberhagen, Mrs. Elanie van Rooyen and Mrs. Lee-Ann van Wyk for their administrative assistance. I gratefully acknowledge the support of the National Research Foundation (NRF) towards this research (funded under the Professional Development Programme). Opinions expressed and conclusions arrived at, are those of the author and are not necessarily to be attributed to the NRF.

Contents

List of Figures

List of Tables

Chapter 1

Introduction

> "Spirit lead me where my trust is without borders. Let me walk upon the waters wherever You would call me. Take me deeper than my feet could ever wander and my faith will be made stronger in the presence of my Savior."
>
> *Taken from* Oceans
>
> Performed by Hillsong

This thesis is concerned with the observational study of the stellar mass evolution of brightest cluster galaxies over the last 5 Gyr. In this chapter we set the stage by describing the basic ideas of galaxy formation and evolution, whereafter we narrow the focus to take a look at brightest cluster galaxies, i.e. their formation, properties and environments. We end the chapter with a summary of the open questions this thesis attempts to answer.

1.1 Galaxy Formation

The Universe we call home is ever so slowly revealing its mysteries to mankind. One of the most tantalizing discoveries made in the last century is the fact that the Universe is dominated by a form of matter which governs structure formation in the Universe.

The currently favoured cosmological model, used to describe the formation of large-scale structures in the Universe, is the Lambda Cold Dark Matter (ΛCDM) model. Within this model the Universe is flat and expanding with time. The Universe is dominated by dark energy which accounts for 68.3% of the energy density of the Universe, while dark matter accounts for 26.8% (Planck Collaboration et al. 2014a). The remaining 4.9% is contributed by ordinary baryonic matter[1].

1.1.1 Galaxy formation within a cosmological framework

Within the ΛCDM cosmological model it is assumed that the matter in the Universe is uniform and isotropically distributed. Small density perturbations in the early Universe must have been present in order for large-scale structure formation (e.g. groups of galaxies and galaxy clusters) to take place (e.g. Novikov 1964). The origin of these perturbations cannot be explained by standard cosmology, however cosmic inflation (Guth 1981) has been proposed as a possible explanation (e.g. Hawking 1982; Guth & Pi 1982). The perturbations in dark matter grow with time, causing over-dense regions to pull matter towards them and become more dense. These overdense regions eventually collapse under their own gravity. Gravitational instability is therefore responsible for the growth in the density perturbations.

Shortly after the Big Bang (BB) the Universe was very hot and dense. At this stage radiation dominated and the temperature was still hot enough to prevent protons and neutrons from combining, thus preventing any baryonic matter (helium and hydrogen nuclei) from forming. As the Universe expanded it cooled down and ~ 0.4 Myr after the BB the Universe was cool enough for neutral gas to form. This is referred to as the epoch of recombination (e.g. Keel 2007; Longair 2008).

Within the cosmological model it is assumed that each initial perturbation contains baryons and dark matter roughly equal to their universal proportions (e.g. Mo, van den Bosch, & White 2010). Each component of matter reacts differently to the gravitational collapse of the overdense regions. Dark matter is the dominant component of matter (e.g. Bradley et al. 2003; Lee et al. 2012) and is collisionless. Dark matter is therefore only influenced by gravity and since no opposing force (such as radiation pressure) is present to counteract gravity, the dark matter collapses to form dark

[1]The matter out of which the visible Universe, for example stars and galaxies, are made.

matter halos. The baryons (or gas) on the other hand are not collisionless. The temperature of the gas is increased to the virial temperature ($T_{\rm vir}$) of the dark matter halo by the shocks produced during the gravitational collapse. $T_{\rm vir}$ of a dark matter halo is an indication of the binding energy of the halo and only gas or baryons with temperatures $\lesssim T_{\rm vir}$ will be gravitationally bound to the halo. $T_{\rm vir}$ is determined from the virial theorem, which describes a relation between the kinetic energy (KE) and gravitational potential energy (PE) of the objects in a gravitationally bound system. Specifically it states that

$$\langle \mathrm{KE} \rangle = -\frac{1}{2}\langle \mathrm{PE} \rangle \tag{1.1}$$

where $\langle \mathrm{KE} \rangle$ and $\langle \mathrm{PE} \rangle$ denote the average kinetic and potential energy. This theorem can be applied to any gravitationally bound system, for example stars, galaxies, globular clusters and galaxy clusters.

In order for star formation (SF) to take place, the gas has to cool down and this directly depends on the temperature and density of the gas. In the case where the gas cloud is dense enough for the cooling time ($T_{\rm cool}$) of the gas to be short, the gas flows to the centre of the dark matter halo. For gas clouds in hydrostatic equilibrium, the inner regions will eventually collapse due to the loss of radiation pressure, causing the gas to flow towards the centre of the dark matter halos (Rees & Ostriker 1977). The gas at the centre of the dark matter halos will collapse under their own gravity. This in turn, reduces $T_{\rm cool}$ of the gas more rapidly with respect to the collapse time and enables stars to be formed. During the collapse the gas cloud may also be split up into smaller, high density regions in which stars may eventually form and these in turn form the building blocks of a galaxy.

Until now we have only described what happens to an isolated system consisting of dark matter and baryons. In the real Universe however, neither galaxies nor dark matter halos develop in isolation, as illustrated in Fig 1.1. Within the ΛCDM cosmology, dark matter halos (and the galaxies within them) grow through a process known as the hierarchical formation scenario (also referred to as the 'bottom-up' scenario; White & Rees 1978; Frenk et al. 1988; White & Frenk 1991). This scenario predicts that smaller structures form first and large-scale structures are formed later through mergers of smaller structures.

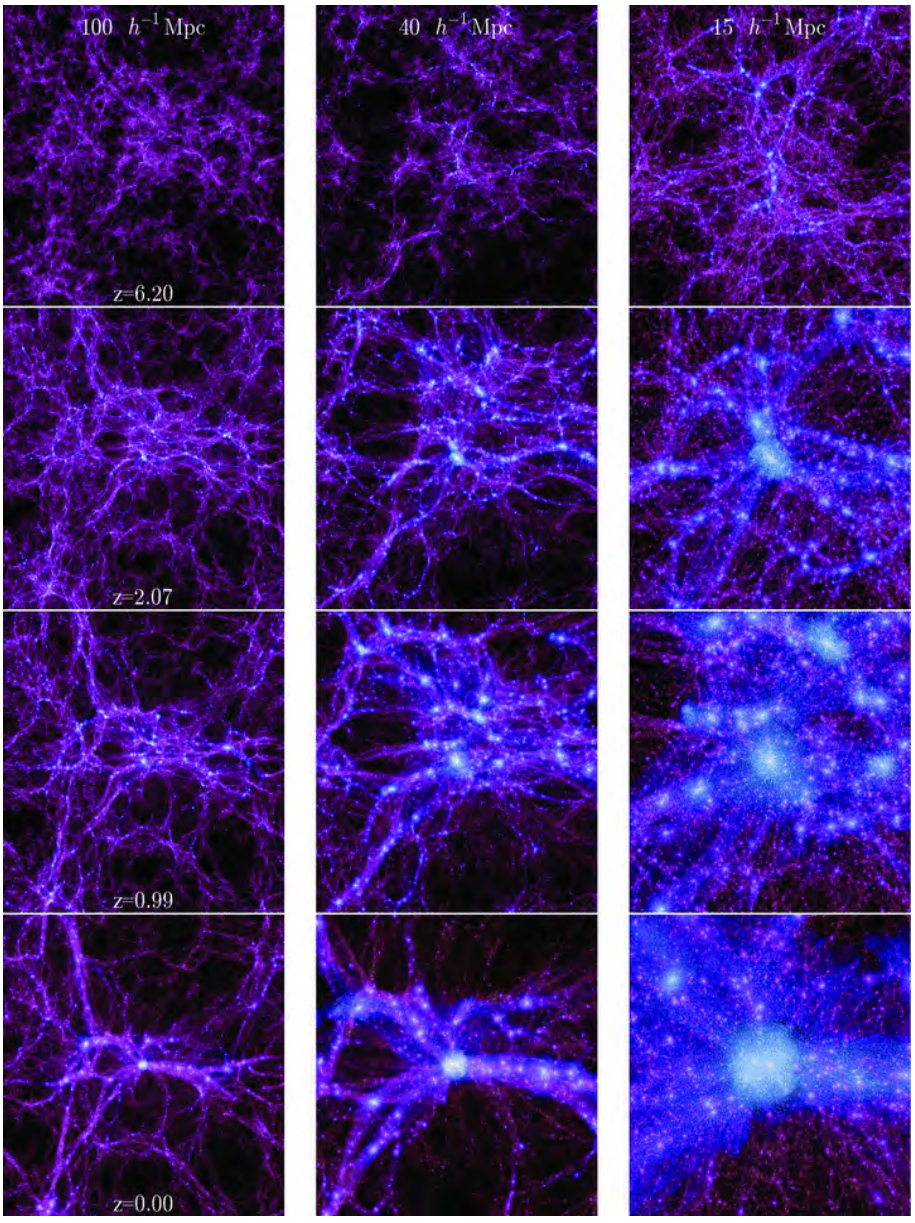

FIGURE 1.1: Figure taken from Boylan-Kolchin et al. (2009). N-body simulations, such as the Millennium II simulation, suggest that matter in the Universe is distributed in a cosmic web of filaments. The image shows large-scale structure formation as a function of time (from top to bottom) for three different cosmological scales, ranging from large (left) to smaller scales (right).

The process of *dynamical friction* is of key importance to ideas used in this thesis, and so we make a small digression here to describe it. Consider a point source (e.g. a galaxy) that is moving with a velocity v through a dark matter halo. Dark matter particles uniformly distributed throughout the halo are attracted to the point source as it moves through the halo. This causes an overdensity of dark matter particles to form behind the point source, which exerts a drag force ($F_{\rm drag}$) on the point source. $F_{\rm drag}$ causes the point source to slow down a little as it loses energy and angular

momentum. This will eventually cause the point source to spiral inward towards the centre of the dark matter halo. This process is known as dynamical friction (Chandrasekhar 1943a;b;c) and is illustrated in Fig 1.2. Dynamical friction ultimately enables the so-called 'satellite galaxies' in a dark matter halo to merge with the 'central galaxy' in the halo. Here the central galaxy is defined as the galaxy with the lowest specific PE, while satellites galaxies refer to the galaxies in orbit around the central (see e.g. van den Bosch et al. 2008; Weinmann et al. 2009; Pasquali et al. 2010).

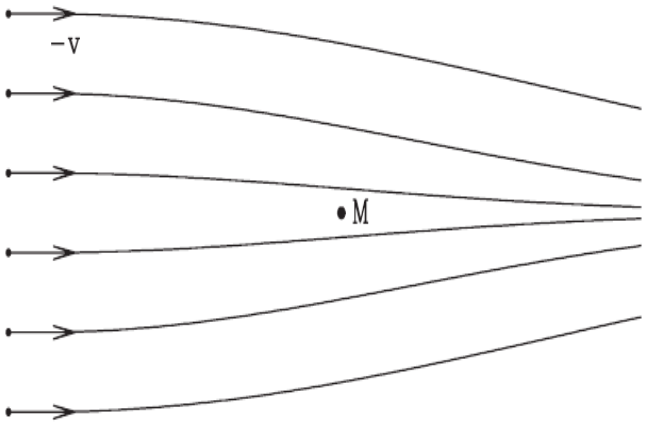

FIGURE 1.2: Figure taken from Mo et al. (2010). A point source (with mass M) is moving with velocity v through a 'sea' of dark matter particles that are uniformly distributed throughout the dark matter halo. As the point source moves through the halo, it attracts the particles and causes an overdensity of dark matter particles to form behind the point source. This in turn exerts a drag force (dynamical friction) on the point source, which will eventually cause the point source to slowly spiral inward towards the centre of the dark matter halo.

1.1.2 Using simulations to study galaxy formation

With technological developments it became possible to study the formation and evolution of galaxies with simulations, more specifically N-body, hydrodynamical simulations and semi-analytical models (SAMs). Both N-body and hydrodynamical simulations make use of a large number of particles to study structure formation and evolution. N-body simulations are used to solve the numerical equations of motion for particles that are gravitationally interacting with each another (e.g. Boylan-Kolchin et al. 2009). Hydrodynamical simulations are primarily used to solve the gravitational, radiative cooling and transfer equations for these particles (e.g. Katz et al. 1992; Evrard et al. 1994; Navarro & Steinmetz 1997). SAMs on the other hand are used to describe the evolution of baryonic matter in galaxies through a number of simplified prescriptions of the physical processes

involved in galaxy formation (such as gas cooling, heating, SF and feedback; Cole et al. 1994; Kauffmann et al. 1994). SAMs can also be 'pasted' onto dark matter simulations (e.g. Bower et al. 2006; De Lucia & Blaizot 2007), in order to populate dark matter halos with galaxies (Kauffmann, Nusser, & Steinmetz 1997).

Confronting models with observations

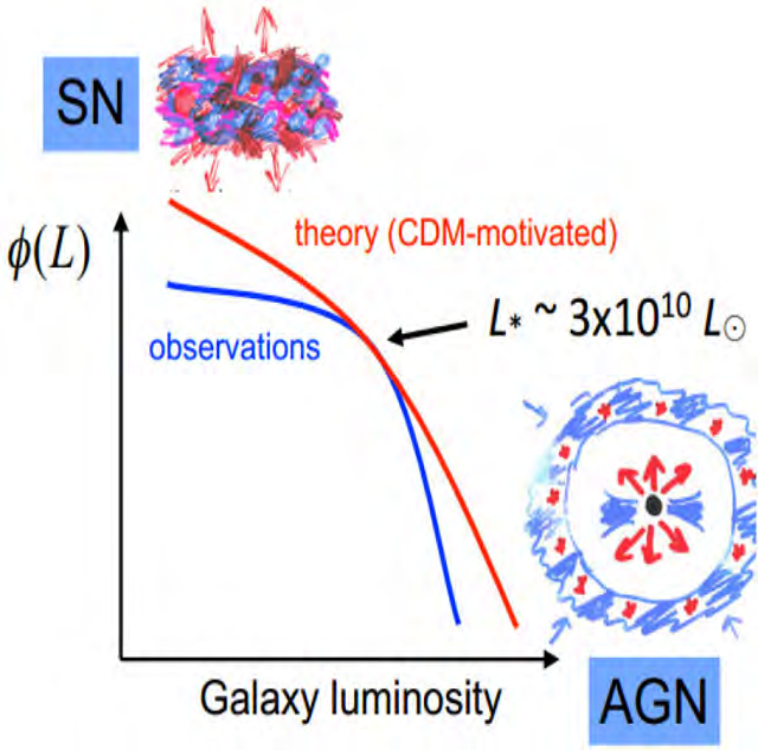

FIGURE 1.3: Figure taken from Silk & Mamon (2012). The galaxy luminosity function in the local Universe that is observed (blue) and predicted by theory (red). Feedback mechanisms have been proposed to solve the discrepancies between the observations and theory. Supernova feedback is sufficient to quench star formation at the low mass end while a stronger source, e.g. active galactic nucleus feedback is needed to quench star formation in massive galaxies.

One of the most fundamental measurements which can be made in astronomy is the luminosity function (LF) - simply counting the number of objects, in this case galaxies, as a function of their brightness. The observed galaxy LF can be described as having a cut-off at the bright end, with a slow increase at the faint end (i.e. many more faint galaxies than bright galaxies; see Fig 1.3). Theory initially assumed that stellar mass follows halo mass (red curve in Fig 1.3), however this predicts too many faint and bright galaxies in the local Universe compared to observations (e.g. Benson et al. 2003).

One of the important contributions made by SAMs is the ability for models to now reproduce the observed LF through the inclusion of feedback mechanisms that suppress SF in galaxies, bringing the theoretical and observational LF into agreement at the bright and faint ends. *Supernova* feedback has been proposed to suppress SF in *low* mass halos (e.g. Larson 1974; Dekel & Silk 1986; Cole et al. 2000; Benson et al. 2003). When a massive star[2] goes supernova it releases an enormous amount of energy into the surrounding gas. This energy is sufficient for the gas in a low mass galaxy to overcome the shallow gravitational potential well of its associated dark matter halo. This ultimately causes the gas to be expelled from the galaxy via galactic winds. A *massive* halo requires a more powerful feedback mechanism to suppress SF and *active galactic nuclei* (AGN; Tabor & Binney 1993; Ciotti & Ostriker 1997; Silk & Rees 1998; Bower et al. 2006; Croton et al. 2006; Peng et al. 2010) have been proposed. This is the active accretion phase of a super massive black hole that is located at the centre of a massive galaxy. As the gas cools, it flows towards the centre of the galaxy. The angular momentum of the gas is conserved during the infall, resulting in the formation of an accretion disk around the black hole in the centre of the galaxy. Friction between the adjoining layers of the accretion disk causes the gas to spiral inward as energy is released in the form of heat. This process continues until the gas reaches the event horizon of the black hole where the temperatures can reach millions of degrees. This high temperature causes an enormous amount of energy to be released which in turn heats up the surrounding gas and expels material via jets and winds.

Through the inclusion of feedback mechanisms into simulations, we are now able to predict the observed properties of galaxies (such as colours, as well as the LF mentioned above) more successfully. In the next section we discuss what information the colours of galaxies can reveal.

1.2 Galaxy Bimodality

One of the most important discoveries made in astronomy over the last 20 years, is the fact that galaxies in the local Universe have a bimodal colour-distribution with two distinct peaks (one peak towards the red part of the distribution and one towards the bluer side; e.g. Strateva et al. 2001;

[2]Stars with stellar masses $\geqslant 8M_{\odot}$ (e.g. Hillebrandt et al. 1984).

Blanton et al. 2003; Kauffmann et al. 2003; Baldry et al. 2004). The colour bimodality of galaxies has been observed out to $z \sim 1$ (e.g. Bell et al. 2004; Faber et al. 2007) and even higher redshifts (e.g. Brammer et al. 2009; Whitaker et al. 2011). It is remarkable that galaxies can be classified into one of two colour bins[3] and this tells us something fundamental about the star formation histories of these galaxies (i.e. whether they are star forming or not). The two peaks in the galaxies' bimodal colour-distribution may indicate that the processes responsible for shutting down star formation in galaxies take place very rapidly.

We illustrate the colour bimodality of galaxies in Fig 1.4. Galaxies on the 'blue cloud' have blue photometric colours and this is attributed to the fact that these galaxies are actively forming stars. The stellar populations of these galaxies are dominated by hot, massive O and B-type stars which typically have lifetimes of $\lesssim 10^8$ Gyr. These massive stars emit most of their energy in the ultraviolet (UV) and the UV-continuum of a galaxy can therefore be used as a tracer of star formation. The UV-diagnostic is however very sensitive to dust extinction. Star forming regions are generally quite dusty and a large fraction of the UV-photons, radiated by the hot young stars, heat the surrounding dust grains to temperatures of $\sim 30 - 50$ K (e.g. Mathis et al. 1983; Leisawitz & Hauser 1988; Rawle et al. 2012), which emit the blackbody peak (radiation) in the far-infrared (FIR), assuming that dust grains act like blackbodies. Because the absorption efficiency of dust is strongly peaked in the UV (Gordon et al. 2003), the FIR-emission of a galaxy can be used as another SF tracer, specifically to trace star formation that is obscured by dust (e.g. Rieke et al. 1980; Teague et al. 1990). Galaxies on the blue cloud typically have disk-like morphologies (i.e. are late-type galaxies).

Red galaxies on the other hand lie on a tight relation between colour and magnitude (or mass) known as the red-sequence and typically have elliptical morphologies (i.e. early-type galaxies, hereafter ETGs; see Fig 1.4). The stellar populations of these galaxies are dominated by old, long-lived stars which primarily emit their energy in the near-IR, causing these galaxies to have red photometric colours. These galaxies are considered to be 'quenched' or are no longer forming new stars because they are gas-poor. Furthermore, there are also some studies which find that red-sequence galaxies are forming stars (less than 10%; see Catinella et al. 2013).

[3]Although, at fixed mass, there is a range of colours among the galaxies in each bin (see e.g. the discussion in Taylor et al. 2015).

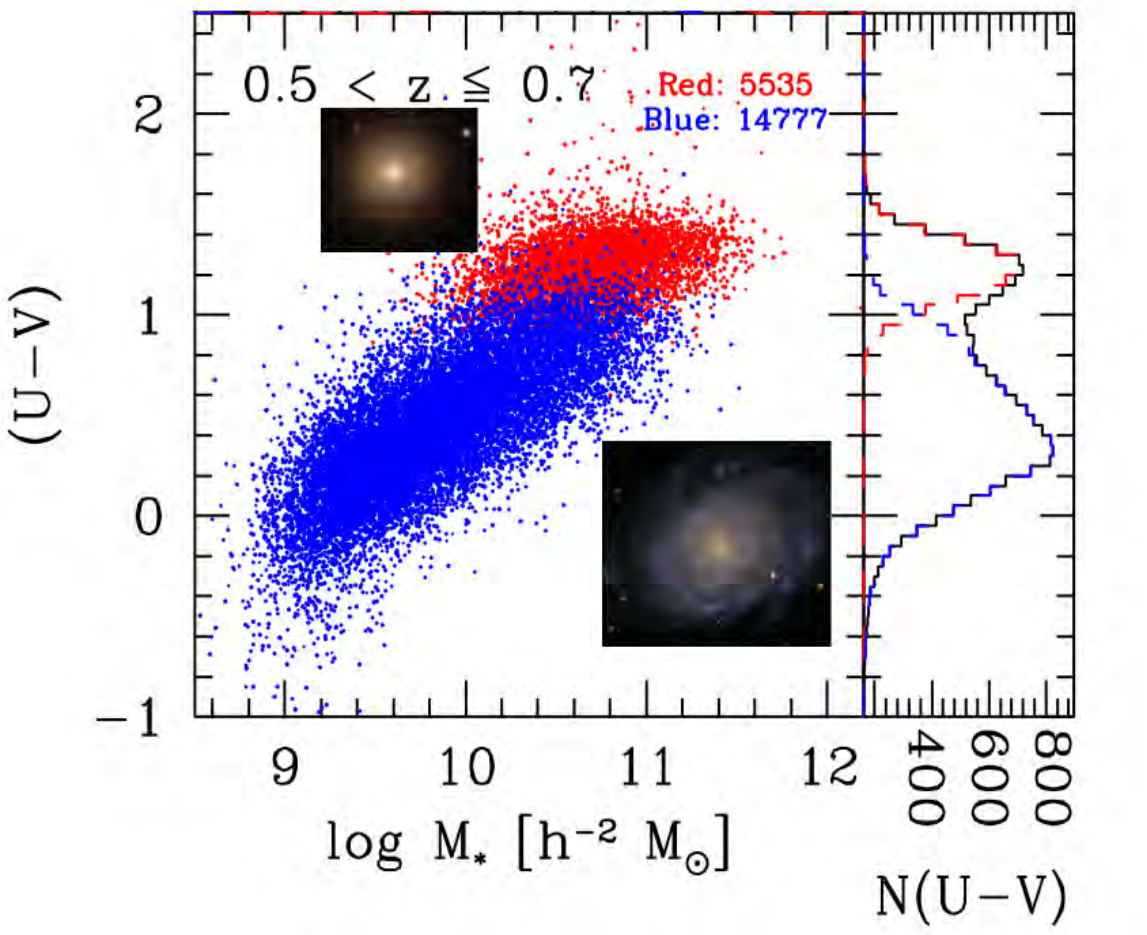

FIGURE 1.4: Figure has been adapted from Fritz et al. (2014). Here the relation between the colour and stellar masses of galaxies is shown. The histogram in the panel to the right shows the number of galaxies in each peak of the bimodal colour-distribution. It is immediately apparent that the red galaxies lie on a tight relation in colour-mass space. These galaxies typically have elliptical morphologies. The galaxies in the blue cloud have a large scatter in colour-mass space and typically have disk-like morphologies.

Separating the two galaxy populations is an important and subtle point which will be used throughout this thesis, so we take a moment here to describe some of the ways this is done. Baldry et al. (2004) found that the colour-distribution of galaxies at a particular magnitude could be approximated by a double Gaussian function (see also Balogh et al. 2004a;b; Baldry et al. 2006; Li et al. 2006; Yang et al. 2007; Wilman et al. 2010). In this approach a single Gaussian function is used to represent each peak in the bimodal distribution. The two Gaussian functions however overlap with

one another. In this overlapping region it is not straightforward to determine whether individual galaxies belong to the red-sequence or blue cloud.

Another method commonly used to separate red galaxies from their blue counterparts is a fixed colour cut (see e.g. Butcher & Oemler 1984; Strateva et al. 2001; Liu et al. 2009; Cucciati et al. 2012; Lin et al. 2013). There is in no easy way to 'cleanly' separate red and blue galaxies. A galaxy above the colour separation line is red by definition, unless it is actually intrinsically blue (i.e. a faint galaxy) and the error bars on its photometry is large enough for it to be scattered into the red region of the colour-magnitude diagram. However, if red and blue galaxies are defined to be members of the two Gaussians in the colour space, then the red peak will always be contaminated by a fraction of blue galaxies (the same is true for the blue peak). The compromise is to find a colour cut that minimizes the contamination from blue galaxies while simultaneously maximizing the number of red galaxies in the red peak. Butcher & Oemler (1984), for example, studied the colour evolution of the galaxies in 33 clusters over $0.04 \leq z \leq 0.5$. They classified galaxies in a particular cluster as blue if their rest-frame $(B - V)$ colours were ≥ 0.2 magnitudes bluer than a cut based on galaxy spectral type. Other studies have made different cuts in colour, choosing for example a distance that depends on the measured width of the red-sequence.

The fact that red galaxies follow a tight relation between colour and luminosity (or stellar mass) - the red-sequence (see Fig 1.4; e.g. Bower, Lucey, & Ellis 1992) - has been used by a number of studies to identify galaxy clusters (see e.g. Gladders et al. 1998; Gladders & Yee 2000; Lubin et al. 2000; Lu et al. 2009; Rykoff et al. 2014). This method relies on the fact that all rich clusters have a population of seemingly passively evolving ETGs that are no longer forming new stars, at least from $z \lesssim 1.3$ (see e.g. the discussions in Gladders & Yee 2000; Lu et al. 2009). Clusters can therefore be identified by searching for an overdensity of red galaxies. A single Gaussian function can be used to approximate the colour-distribution of the red-sequence, whereafter the width can be determined. If the width of the red-sequence is determined in such a way that the number of red galaxies is maximized, while simultaneously minimizing contamination from blue galaxies, then this width can be used as a colour cut with which red and blue galaxies can be separated.

In the previous two sections we described the theoretical framework for galaxy formation and the observed colour bimodality of galaxies. In this thesis we are interested in a particular class of

galaxies found in special environments - large collections of galaxies known as galaxy clusters. We now turn our attention to these structures.

1.3 Galaxy clusters

The highest density perturbations in the early Universe gave way to form the most massive gravitationally bound systems that are known today, namely galaxy clusters. A significant fraction of galaxies in the present Universe are found in structures where the number density of galaxies is higher than the average. For galaxy clusters this ranges between a few tens to hundreds/thousands of galaxies. We show an example of a rich galaxy cluster, Abell 2218, in Fig 1.5. As described above and seen in this image, clusters can be easily identified as overdensities of red galaxies.

FIGURE 1.5: Image of the Abell 2218 cluster as observed with Hubble Space Telescope. The arcs around the cluster centre are produced by background galaxies that are distorted due to gravitational lensing. Image credit: NASA, ESA, Richard Ellis (Caltech) and Jean-Paul Kneib (Observatoire Midi-Pyrenees, France).

1.3.1 Description of cluster galaxies and the intracluster light

In the early 1930s, astronomers realized that the morphological mix of galaxies depends on their local environment (Hubble & Humason 1931). This led to the discovery of the morphology-density relation (Dressler 1980). By studying the morphologies of galaxies in 55 clusters, Dressler found that the fraction of late-type galaxies ($\sim$ 60%) in the field decreased to $\sim$ 10% in rich galaxy clusters. The opposite trend was observed for ETGs, increasing from $\sim$ 10% in the field to $\gtrsim$ 80% in clusters.

With the introduction of large galaxy redshift surveys, for example SSDS[4] (York et al. 2000) and 2dFGRS[5] (Colless et al. 2001), astronomers were able to perform more detailed studies regarding the environmental dependencies of galaxy properties. These studies revealed that, in addition to having a large fraction of ETGs, clusters contain galaxies that are (on average) more massive, redder, more gas-poor and have lower star formation rates (e.g. Lewis et al. 2002; Gómez et al. 2003; Kauffmann et al. 2004; Baldry et al. 2006; Weinmann et al. 2006) than galaxies in less-dense regions.

The brightest and most massive galaxies in clusters are known as brightest cluster galaxies (BCGs, more detail will be given in Section 1.4). BCGs are located at or near the cluster centres (e.g. Jones & Forman 1984; 1999; Beers & Tonry 1986; Rhee & Latour 1991). Although BCGs typically have elliptical morphologies, their properties (e.g. surface brightness profiles and scaling relations) are however very different from that of other ETGs within the same mass range (e.g. Bernardi et al. 2007; von der Linden et al. 2007). BCGs, for example, are at least one magnitude brighter (Sandage 1976; Hoessel, Gunn, & Thuan 1980), have extended light profiles (Matthews et al. 1964; Tonry 1987; Schombert 1988; Gonzalez et al. 2000; 2003), have higher velocity dispersions (see e.g. von der Linden et al. 2007) and are larger than other ETGs (see Bernardi et al. 2007; von der Linden et al. 2007, and references therein). For clusters, the term 'central galaxy' is now synonymously used in the literature to describe BCGs (Weinmann et al. 2006).

BCGs are sometimes surrounded by diffuse, extended light envelopes and are then referred to as cD galaxies, a term first introduced by Morgan (1958) to denote supergiant diffuse galaxies. Today,

[4]Sloan Digital Sky Survey; http://www.sdss.org/
[5]Two-degree-Field Galaxy Redshift Survey; http://www.2dfgrs.net/

however, this term synonymously refers to the centrally dominant galaxy in a cluster (e.g. Matthews et al. 1964; Oemler 1973; 1976; Tonry 1987; Schombert 1986; 1987; 1988; Gonzalez et al. 2000; 2003). The origin of the cD envelope is still uncertain, although it is thought to originate from a population of intracluster stars that has been produced by tidal stripping and galaxy mergers. This intracluster light (ICL) consists of stars that are gravitationally bound to the cluster potential, rather than a single galaxy. Simulations predict these stars to be very old and dynamically different from the stars in BCGs (Murante et al. 2004; Sommer-Larsen et al. 2005) and that the production of these intracluster stars is an ongoing process (Willman et al. 2004). In nearby clusters, the ICL is spread out between the majority of the galaxies in the clusters, although the ICL is often found to be more concentrated around the central galaxies (Mihos et al. 2005; Rudick et al. 2011). This in turn implies that the formation and evolution of the BCGs and ICL are connected to one another.

1.3.2 Mass estimates

In the hierarchical model, structures grow in mass. Indeed, all semi-analytic models of galaxy formation tie the various prescriptions for the relevant physical processes back to the mass of an object's parent halo, to some level. The cluster's mass is therefore a key parameter to measure. The dark matter halo masses of clusters however are not directly observable. Observables (or mass tracers) that correlate with mass are used to derive estimates for the halo masses of the clusters. Examples of observables that correlate with halo mass are: velocity dispersion of the cluster member galaxies, X-ray temperature, the Sunyaev-Zelodvich (SZ; Zeldovich & Sunyaev 1969; Sunyaev & Zeldovich 1970) effect and optical richness.

Galaxy velocity dispersions, X-ray temperature and the SZ-effect are all related to the KE of the cluster. The cluster's kinetic energy is related to the gravitational potential energy of the cluster (via the virial theorem) and this in turn is related to halo mass of the cluster.

Optical richness on the other hand is a measure of the number of galaxies that are associated with a cluster (see e.g. Zwicky et al. 1961). Intuitively, one would expect a massive cluster to have a higher number of galaxies than a lower mass cluster. Studies have quantified this to derive a relation between optical richness and halo masses of clusters (see Section 3.2.1).

Just as halo mass is of fundamental importance in galaxy formation models, it has recently been empirically discovered that the stellar mass of a galaxy appears to be one of the two key parameters governing its evolution (Baldry et al. 2006; Peng et al. 2010). The other key parameter is the environment in which it lives (Baldry et al. 2004; 2006; Peng et al. 2010). We now continue to discuss the physical processes in the cluster environment which transform galaxies.

1.3.3 Environmental processes in clusters

1.3.3.1 Ram-pressure stripping and strangulation

Ram-pressure stripping is the process responsible for the removal of cold galactic gas, located in the galactic disk, through pressure exerted by the intracluster medium (ICM) as the galaxy moves through it (Gunn & Gott 1972; Fujita 1998; 2001; Abadi et al. 1999; Fujita & Nagashima 1999; Toniazzo & Schindler 2001). Ram-pressure stripping also acts on the hot gas which resides in the dark matter halos (as described in Section 1.1.1) surrounding the galaxies. However, this 'gas reservoir' is less strongly bound to the galaxy and is more easily stripped as the galaxy moves through the ICM. Star formation is rapidly quenched in a galaxy where the cold gas is removed, while quenching is slower for galaxies with their hot halo gas removed since this prevents the cold gas supply of the galaxy from being replenished (Larson et al. 1980; Balogh et al. 2000; Drake et al. 2000; Diaferio et al. 2001). The latter is referred to as strangulation because the cold gas supply is slow being cut off as the galaxy falls into a larger dark matter halo.

Ram-pressure stripping may also be responsible for morphological transformations in spiral galaxies since they look like lenticular galaxies once their gas components are removed.

1.3.3.2 Galaxy harassment and tidal stripping

The typical velocities of cluster galaxies are roughly the same as the velocity dispersion of their host clusters ($\sim 1000\ \mathrm{km\,s^{-1}}$; Struble & Rood 1991). Any encounter between two cluster galaxies can therefore only be described as high-speed. During such an encounter, the internal energy of the colliding galaxy is increased and as a result it becomes less gravitationally bound. This increases

the galaxy's chances of being disrupted by future high-speed encounters. The effect of multiple high-speed encounters is known as galaxy harassment (Moore et al. 1996; 1998; 1999; Lake et al. 1998). Tidal stripping on the other hand is the process through which material is stripped from the outer regions of a galaxy (Merritt 1983; 1984; Ghigna et al. 1998).

Both these processes contribute towards the ICL growth and changes the morphologies of galaxies. The influence that tidal stripping has on galaxy morphologies is straightforward from the description given above. Galaxy harassment, on the other hand, has a particularly large effect on the morphologies of disk galaxies. In clusters, high-speed encounters occur so often that a disk galaxy does not have time to return to its previous dynamical state. This results in a large fraction of disk galaxies being completely destroyed in less than the Hubble time (Farouki & Shapiro 1981). Subsequently, this results in a growing population of stars that is not gravitationally bound to any galaxy, but rather associated with the cluster itself (i.e. the ICL).

1.3.3.3 Galaxy cannibalism and mergers

In Fig 1.6 we show an example of a merging pair of galaxies that are known as the Antennae galaxies. These galaxies get their name from the long, sweeping 'antennae-like' arms that are extending out of their centres[6]. The orange bulge components in the lower-left and upper-right corners of the figure represent the old stars at the centres of the two galaxies. The most striking feature in this image is the blue, SF regions that are surrounded by hydrogen gas (which appears pink here) and indicate that these galaxies are gas-rich. The resulting merger between these two, gas-rich galaxies is classified as a 'wet' merger. The resulting galaxy may be actively forming stars and will therefore have a blue photometric colour (in the absence of strong dust extinction). On the other hand, the merger would have been classified as a 'dry' merger in the case where the two galaxies were gas-poor. The resulting galaxy would then have a red photometric colour and be quenched.

Galaxies in clusters are less likely to undergo mergers because of their high relative velocities. Two galaxies will only be able to merge if their velocities are small enough for them to become gravitationally bound to each other. Dynamical friction is the solution to this problem, since it causes

[6]These arms were formed approximately $0.2 - 0.3$ Gyr ago during the initial encounter of these galaxies.

FIGURE 1.6: A true colour optical image of the Antennae galaxies as observed with Hubble Space Telescope and is an example of galactic cannibalism. This image shows a pair of interacting galaxies, NGC 4038 (left) and NGC 4039 (right), that are in the process of merging. Image credit: NASA, ESA, and the Hubble Heritage Team (STScI/AURA)-ESA/Hubble Collaboration.

galaxies to slow down due to the loss of energy and angular momentum. As a result, a galaxy will spiral towards the centre of the cluster and will merge with the central (i.e. the BCG) if the galaxy's dynamical friction timescale ($T_{\rm dyn}$) is short enough (less than the lookback time). The central galaxy is therefore accreting galaxies through a process known as galactic cannibalism (Ostriker & Tremaine 1975; Ostriker & Hausman 1977).

Galactic cannibalism has two important effects: (i) it causes stellar mass growth in the central galaxy (via mergers) and (ii) the depletion of massive satellite galaxies. The $T_{\rm dyn}$ of massive satellite galaxies are shorter than those of lower mass satellites, causing them to merge with the central galaxy on shorter timescales. This results in a magnitude gap between the brightest galaxy (i.e. central galaxy) and the second brightest cluster galaxy (e.g. Tremaine & Richstone 1977; Loh & Strauss

2006; Lin et al. 2010; Tavasoli et al. 2011). Galactic cannibalism is also believed to be responsible for the formation of the ICL and the light envelopes that surround cD galaxies. The ICL and the light envelopes are made up of material that is tidally stripped from 'cannibalized' galaxies as they sink towards the bottom of the cluster's potential well (Gallagher & Ostriker 1972).

How do we know if two objects are going to merge? Consider a scenario where a satellite galaxy is moving with velocity v in a circular orbit (with radius r) around a central galaxy (see Fig 1.7). These two galaxies will only potentially merge if the satellite's velocity is smaller or equal to the escape velocity ($v_{\rm esc}$) of the central galaxy, which is given by

$$v_{\rm esc} = \left(\frac{2GM}{r}\right)^2 \tag{1.2}$$

with M the mass of the central galaxy. In reality however is not straightforward to determine whether two galaxies are going to merge with one another. This is simply because we are unable to measure the three dimensional velocities of galaxies as well as the separation distance between them. We are only able to measure the velocity of a galaxy along the line-of-sight, while the separation distance can be measured in two directions (plane of the sky; see Fig 1.7). Given these limitations the most secure method to identify galaxies that are possibly merging is to obtain velocity estimates for galaxies in close pairs. This approach allows one to identify close galaxy pairs (separated by some distance) that are likely to be gravitationally bound to each other. We will use this idea in Chapter 4.

Due to their location in the centres of clusters, BCGs may have experienced multiple mergers during their lifetimes. This makes BCGs are ideal probes to study galaxy formation with since mergers play such an important role in the hierarchical picture of galaxy formation. In the next section we take a more in-depth look at the properties and formation theories of these massive galaxies.

1.4 Brightest Cluster Galaxies

The central galaxies of galaxy clusters continue to pique the interest of astronomers since they appear to be very special in comparison to other cluster galaxies. In many cases it is visually

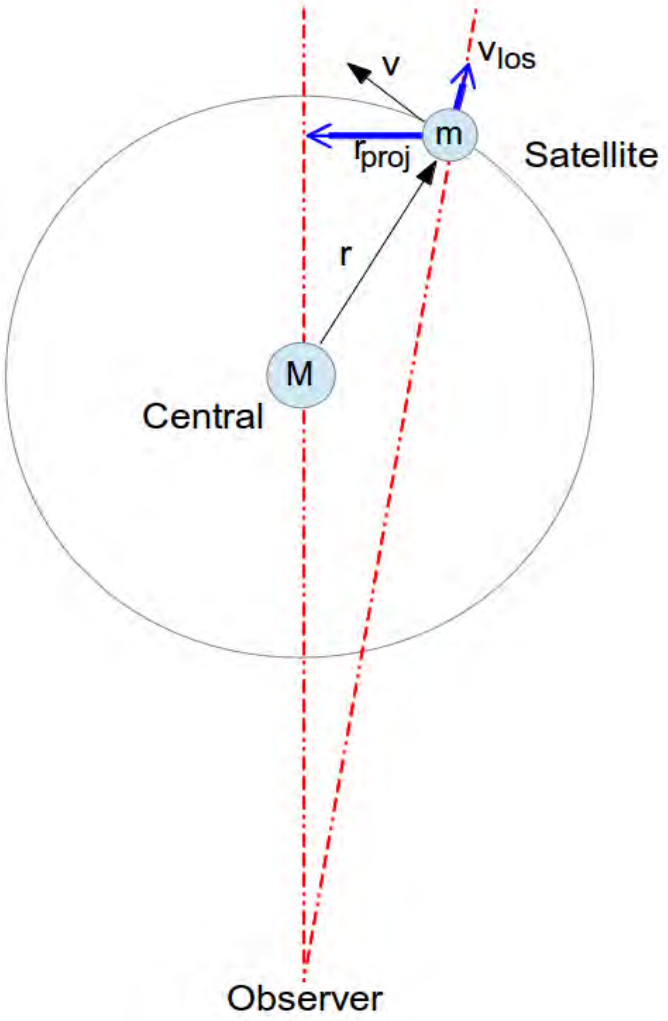

FIGURE 1.7: Schematic of the method used to identify possible mergers. Generally, a satellite galaxy is bound to the central if $v_{\rm sat} \leq v_{\rm esc\,(cen)}$. In reality however we are only able to measure the satellite's velocity along the line-of-sight, while the separation distance can only be measured in two directions (plane of sky). Due to these limitations possible merger candidates are identified using a combination of projected separation distance and relative velocity difference.

possible to discern the centrals from the other cluster members since they are usually the brightest (or most massive) galaxies in their host clusters. This is not the only reason why central galaxies are special. Observational studies have shown that the properties of central galaxies are correlated with those of their satellite galaxies (a phenomenon known as *galactic conformity*; Weinmann et al. 2006). The stellar masses of central galaxies are also known to correlate with the halo masses of their host clusters (the more massive the halo, the more massive the central galaxy; e.g. Edge 1991; Burke et al. 2000; Brough et al. 2008; Whiley et al. 2008; Collins et al. 2009; Lidman et al. 2012; Stott et al. 2012), also seen in lower mass galaxies.

1.4.1 The observational properties of BCGs

1.4.1.1 The spatial position of BCGs

Earlier works that studied the X-ray morphologies of galaxy clusters (e.g. Jones & Forman 1984; 1999; Beers & Tonry 1986; Rhee & Latour 1991) and their velocity structures (Quintana & Lawrie 1982) indicated that BCGs are generally located at or very close to the cluster centres. This was also independently confirmed with gravitational lensing observations of galaxy clusters (e.g. Smith et al. 2005). Subsequently, however, there are also studies which report an offset between the BCGs and the centres of their host clusters (e.g. Beers & Geller 1983; Jones & Forman 1984; 1999; Zabludoff et al. 1993; Malumuth 1992; Oegerle & Hill 2001; Lin & Mohr 2004; Hashimoto et al. 2014). Observational studies (Katayama et al. 2003; Patel et al. 2006; von der Linden et al. 2007; Oliva-Altamirano et al. 2014) and simulations (e.g. Skibba & Macciò 2011) have confirmed that there is a correlation between the presence of these offsets and the disturbed dynamical state of the galaxy clusters (due to mergers).

1.4.1.2 The luminosities and stellar masses of BCGs

At the present epoch, BCGs are among the most massive ($M_\star \sim 10^{12}\,\mathrm{M}_\odot$) and luminous galaxies in the Universe. These galaxies typically have luminosities of $\sim 10L_\star$, where $L_\star = 1.9 \times 10^{10}\,\mathrm{L}_\odot$ (Sandage & Hardy 1973; Hoessel, Gunn, & Thuan 1980; Schombert 1986).

BCGs exhibit low scatter in their absolute magnitudes ($\sim 0.3-0.4$ mag; e.g. Sandage 1972; Sandage & Hardy 1973; Gunn & Oke 1975; Kristian et al. 1978; Hoessel et al. 1980; Sandage 1988; Whiley et al. 2008). This property, along with the extreme luminosities of BCGs have been exploited in earlier works by using BCGs as cosmological standard candles to determine the value of the deceleration parameter q_0 and to study the variation of H_0 with redshift (e.g. Sandage 1972; Sandage & Hardy 1973; Gunn & Oke 1975; Lauer & Postman 1992). Several studies however found that the observed colours and luminosities of ETGs (BCGs included) evolved significantly between $0 < z < 1$ (e.g. Gunn et al. 1986; Aragon-Salamanca et al. 1993; Rakos & Schombert 1995; Lubin 1996), rendering them unusable as a standard of known luminosity.

The light profiles of BCGs (along with other ETGs) are well approximated with the de Vaucouleurs surface brightness law, $\mu(r) \propto r^{1/4}$ over a large range of radii (de Vaucouleurs 1974). cD galaxies on the other hand emit more light at large radii, and deviates from a $r^{1/4}$ profile fitted to the inner regions of these galaxies (the excess of light is known as the 'cD envelope' Matthews et al. 1964; Richstone 1976; Kormendy 1989; López-Cruz et al. 1997). Schombert (1988) argued that these extended light envelopes are very different in profile from those of BCGs and concluded that a two component model best described the surface brightness profiles (out to $r \sim 200 - 1500$ kpc) of BCGs with extended light envelopes (also see Gonzalez et al. 2005). Within this picture, cD envelopes are thought to originate from a population of intracluster stars that has been produced by tidal stripping and galaxy mergers.

1.4.1.3 The stellar populations of BCGs

Recent numerical simulations and SAMs suggest that a large part of the stars ($\sim 80\%$) in BCGs are formed at $z \geq 2$, whereafter dissipationless (or dry) mergers of pre-existing progenitors play an important role in the stellar mass assembly of the BCGs ($z < 1$; e.g. Gao et al. 2004b; De Lucia & Blaizot 2007; Naab et al. 2009; Laporte et al. 2013).

BCGs in the local Universe have red photometric colours and are dominated by red and very old stars. These massive galaxies are considered to be quiescent, passively evolving systems (often described as 'red and dead' galaxies) and are therefore not expected to have experienced any recent SF. However, this is not the case for all BCGs since recent observational studies of BCGs' UV luminosities and IR emission have indicated that a small fraction of these massive galaxies experience ongoing SF (see e.g. Allen 1995; Cardiel et al. 1998; Crawford et al. 1999; Edge 2001; Hicks & Mushotzky 2005; Egami et al. 2006; McNamara et al. 2006; Wilman et al. 2006; Edwards et al. 2007; O'Dea et al. 2008; 2010; Pipino et al. 2009; Liu et al. 2012). Blue cores in some BCGs are also interpreted as evidence that these galaxies recently experienced SF (McNamara & O'Connell 1989; Hicks & Mushotzky 2005; Bildfell et al. 2008; Rafferty et al. 2008; Pipino et al. 2009; Donahue et al. 2010; Hicks et al. 2010; Wang et al. 2010). Observational studies, such as Pipino et al. (2009); Liu et al. (2012); Fraser-McKelvie et al. (2014), found that less than 1% of BCGs in the local Universe have recently experienced additional epochs of star formation. These starbursts however

only increased the stellar masses of the BCGs by a small fraction ($\sim 1-3\%$, see e.g. Sarazin & O'Connell 1983; Cardiel et al. 1995; Pipino et al. 2009; Loubser et al. 2016). Oliva-Altamirano et al. (2014) and Groenewald & Loubser (2014) on the other hand found a higher fraction ($\sim 16\%$ and $\sim 21\%$ respectively) of their BCGs to be star forming, although their star formation rates were too low ($\leq 1\,\mathrm{M}_\odot\,\mathrm{yr}^{-1}$) for SF to make a significant contribution to the mass growth of these massive galaxies.

The above discussion show there are some BCGs with evolutionary histories that are in contrast with the general expectation that these massive galaxies are all quiescent, passively evolving systems with old stellar populations. Supporting evidence is also provided by the independent studies of Groenewald & Loubser (2014) and Oliva-Altamirano et al. (2015), whose findings suggest that their BCGs consists of stellar populations with a wide age range. This implies that a small fraction of these massive galaxies have a more complex star formation history than first assumed.

At earlier epochs ($z > 1$) it is common to find clusters with star forming central galaxies (see e.g. Brodwin et al. 2013). Towards intermediate redshifts ($z \sim 0.5-0.6$) examples of star forming BCGs become less common although they can still be found, i.e. the BCG in the Phoenix cluster ($z = 0.59$) which has a star formation rate of $740 \pm 140\ \mathrm{M}_\odot\,\mathrm{yr}^{-1}$ (McDonald et al. 2012). Even if the starburst only lasted a Gyr, it would still contribute significantly to the stellar mass of the BCG. Towards the present day it becomes increasingly rare to find BCGs that are actively forming stars.

1.4.2 Formation theories of BCGs

Although BCGs typically have elliptical morphologies, their properties are very different from that of other ETGs (see Section 1.3.1). We therefore first take a look at the formation theories of ETGs and then turn our attention to those of BCGs.

Two galaxy formation models have been proposed to explain the formation of elliptical galaxies, specifically the most massive ETGs. The simplest of these models is monolithic collapse (e.g. Larson 1974; Arimoto & Yoshii 1987; Matteucci & Tornambe 1987; Bressan et al. 1994; Merlin & Chiosi 2006), where an ETG is thought to be formed by the collapse of a homogeneous gas cloud. The

collapse is followed by a rapid starburst event during which almost all of the available gas is converted into stars. The stellar populations of the ETGs observed today are composed of these stars. This model predicts that the stars in the majority of the today's ETGs have been in place since $z \sim 3$ after which these galaxies evolved passively down to $z = 0$. ETGs formed through monolithic collapse will be red and dead.

Detailed observational studies of ETGs on the other hand have shown that the formation of these galaxies is much more complex than suggested by the monolithic collapse theory. Taylor et al. (2009), for example, found that only 20% of local ETGs (with stellar masses $> 10^{11}\,\mathrm{M}_{\odot}$) are in place at $z \sim 2$. van der Wel et al. (2008) found that massive ETGs increased their sizes by a factor of two from $z \sim 1$ down to the present day (also see Daddi et al. 2005; Trujillo et al. 2006; 2007; Toft et al. 2007; Cimatti et al. 2008; Franx et al. 2008; van Dokkum et al. 2008; 2009; 2010; Bernardi 2009; Ascaso et al. 2011). Other studies however find no size growth (e.g. Maier et al. 2009; Mancini et al. 2010; Saracco et al. 2010; Valentinuzzi et al. 2010). Kaviraj et al. (2007; 2008) used rest-frame UV observations to study the SFHs of ETGs. Despite the fact that the majority of the stars in these galaxies were very old, they also found that the galaxies continued to form stars over their lifetimes, albeit at a very slow rate. More specifically, Kaviraj et al. (2007) found that $\sim 30\%$ of massive ETGs at $0 < z < 0.11$ experienced recent SF epochs (typically within the last Gyr). These starbursts however contributed very little to the final stellar masses of these galaxies.

The hierarchical formation scenario is the most widely accepted galaxy formation model. In this scenario large systems are formed through the repeated mergers of lower mass systems, which in turn formed earlier on in the history of the Universe (e.g. White & Rees 1978; Schneider & Gunn 1982; Duncan et al. 1983; Frenk et al. 1988; White & Frenk 1991). Studying the formation of ETGs, De Lucia et al. (2006) have shown that the bulk of the stars in these galaxies formed rapidly at high redshifts and are distributed throughout a number of different progenitors. Later on these progenitors assemble into the massive ETGs that are found at present day. Observational studies, conducted in the local Universe and at higher redshifts, have shown that massive galaxies indeed experience gas poor (or 'dry') mergers (see e.g. van Dokkum 2005; Bell et al. 2006a;b; Lotz et al. 2006; Kitzbichler & White 2008; Lin et al. 2008; McIntosh et al. 2008; Liu et al. 2009; Tal et al. 2009; Robaina et al. 2010; Williams et al. 2011; Edwards & Patton 2012).

BCGs are a special subclass of the ETGs as described in Section 1.3.1. The formation mechanisms of BCGs are still heavily debated in the literature. Currently, there are three formation theories that have been proposed to explain the unique properties of BCGs. These theories are not mutually exclusive, and BCGs probably form by a combination of mechanisms.

- Theory 1: BCGs form *in situ* due to SF that is caused by cooling flows (CFs) in clusters (e.g. Cowie & Binney 1977; Fabian et al. 1982; Sarazin 1986; Fabian 1994).
- Theory 2: Primordial collapse - BCGs form from rapid galaxy mergers that take place during the early formation history of the cluster (e.g. Merritt 1983; 1984; 1985; Dubinski 1998).
- Theory 3: Galactic cannibalism - BCGs grow through the accretion of less massive galaxies (e.g. Ostriker & Tremaine 1975; Richstone 1976; Ostriker & Hausman 1977; Schneider & Gunn 1982; Duncan, Farouki, & Shapiro 1983).

1.4.2.1 Theory 1: Cooling flows in cool-core clusters

Within this scenario, the density of gas in the cluster centres is high enough to condense and form stars at the bottom of the gravitational potential well (e.g. Silk 1976; Fabian & Nulsen 1977; Fabian et al. 1982; Sarazin 1986; Fabian 1994). This theory predicts that the stellar populations of BCGs should be young. Observational evidence suggests that the central regions ($\sim$ 100 kpc; e.g. Prestwich & Joy 1991) of some clusters cool to lower temperatures than the outer regions (about a factor of 3, hereafter cool-core clusters; e.g. Best et al. 2007). Further observational evidence in support of the CF theory is examples of BCGs in cool-core clusters that showed signs of recent SF activity, i.e. blue cores and UV-excess (e.g. Crawford et al. 1999; McNamara et al. 2006), along with the presence of young stellar populations (e.g. Groenewald & Loubser 2014; Loubser et al. 2016).

The actual mass deposition rates of CFs are still debated. The mass deposition rates, derived from the X-ray luminosities of the cool-core clusters, are estimated to be several hundred to > 1000 $M_\odot\,yr^{-1}$ (e.g. Allen et al. 1996). These rates imply that $10^{11}M_\odot$ of cool gas will be deposited into the cluster centre in timescales of less than one Gyr. Observationally however this is not seen since

the inferred star formation rates of BCGs are only $\lesssim 10-100\ \mathrm{M_\odot\,yr^{-1}}$ (e.g. Crawford et al. 1999; Liu et al. 2012), which is a factor of $1-2$ lower than expected from the mass deposition rates. It is now well known that AGN feedback is favoured to solve this discrepancy because this feedback mechanism prevents gas from accumulating in the central regions of clusters (e.g. Ciotti & Ostriker 1997; Best et al. 2007; von der Linden et al. 2007).

1.4.2.2 Theory 2: Primordial collapse - rapid galactic mergers during cluster collapse

First proposed by Merritt (1983), this theory suggests that BCGs originated early on in the history of the Universe through rapid galaxy mergers that took place during the cluster collapse (Merritt 1984; 1985; Tremaine 1990; Dubinski 1998). Thereafter the frequency of galaxy mergers in the clusters decreased because of the high relative velocities of cluster galaxies to each other.

Within this theory, stars are removed/stripped from the halos of the galaxies through the mean cluster tidal field during the initial collapse of the cluster. The BCG is not affected since it is situated at the bottom of the cluster's gravitational potential well. The residual stripped material (stars and gas) is then deposited into the centre of the potential well where it forms a diffuse envelope of light around the BCG. Consequently, this theory assumes that tidal stripping is not responsible for the formation of cD halos since tidal events took place before the collapse of the cluster (Schombert 1988). Observational studies, for example Gebhardt & Beers (1991) ague against this formation theory since they found examples of cD galaxies that were not at rest with respect to the centres of their host clusters (offsets of the order of $250-400\ \mathrm{km\,s^{-1}}$; also see Sharples et al. 1988; Teague et al. 1990; Zabludoff et al. 1990).

1.4.2.3 Theory 3: Galactic cannibalism

Currently, the most widely *accepted* formation theory for BCGs is known as galactic cannibalism, first proposed by Ostriker & Tremaine (1975) and later developed by Ostriker & Hausman (1977). This theory predicts that BCGs form through mergers or the capturing of less massive galaxies. Dynamical friction causes galaxies to lose energy and angular momentum, causing them

to spiral towards the centre of the cluster's potential well where they will merge with the central galaxy.

Apart from galactic cannibalism, BCG-formation is also thought to be influenced by tidal stripping (first proposed by Gallagher & Ostriker 1972; Richstone 1976). Within this picture, material is stripped from cannibalized galaxies as they spiral towards the cluster centre, whereafter the tidally stripped material sinks to the centre of the potential well. Together these two theories (galactic cannibalism and tidal stripping) are used to explain the large stellar masses of BCGs as well as the diffuse light envelopes that surround cD galaxies. This is supported by observational studies which find that central galaxies appear to have multiple nuclei (e.g. Schneider & Gunn 1982; Schneider, Gunn, & Hoessel 1983; Hoessel & Schneider 1985; Lauer 1988; Merrifield & Kent 1991; Blakeslee & Tonry 1992; Postman & Lauer 1995).

Although the origin of the ICL is not know, it is thought that tidal stripping of satellite galaxies and merger events (involving BCGs) contribute towards the stellar mass growth of the ICL. Furthermore, the N-body simulations of Conroy et al. (2007b); Murante et al. (2007); Puchwein et al. (2010); Laporte et al. (2013); Contini et al. (2014) predict that $30 - 80\%$ of the BCGs' merging mass should be distributed into the ICL in order to reproduce the distribution observed in nearby clusters. If we are to believe that the majority of the merging mass ends up in the ICL, then this presents us with a scenario that the ICL is being built-up through galaxies that are interacting with the BCGs. That said we would expect to observe a mild evolution in the stellar mass assembly of these massive galaxies (see e.g. Conroy et al. 2007b; Whiley et al. 2008; Collins et al. 2009; Stott et al. 2010; Oliva-Altamirano et al. 2014), while there is a significant increase in the stellar mass of the ICL over the same redshift range. This has indeed been observed in recent studies which find the ICL to form late (mostly after $z \leq 1$; e.g. Conroy et al. 2007b; Contini et al. 2014) and their findings also suggest that the stellar mass of the ICL has increased by a factor of $4 - 5$ from $z = 1 - 0$ (e.g. Krick & Bernstein 2007; Murante et al. 2007; Rudick et al. 2011; Burke et al. 2012; 2015). Consequently, it is clear that the growth and stellar mass build-up of BCGs and the ICL are linked, however it is not clear to what extent merger events contribute towards this. It is therefore important to take this connection into account in order to make any meaningful comparison between the observed and predicted BCG evolution.

1.5 This Thesis

In this thesis we attempt to address three open questions that are specifically related to the formation and evolution of BCGs.

1. There is currently no consensus in the literature regarding the stellar mass growth of BCGs between $0 \leq z \leq 1$. Several observational studies find that BCGs do not experience any stellar mass growth (e.g. Aragon-Salamanca et al. 1998; Whiley et al. 2008; Collins et al. 2009; Stott et al. 2008; 2010; Oliva-Altamirano et al. 2014), while other studies find the opposite (e.g. Lidman et al. 2012; Burke & Collins 2013; Lin et al. 2013; Bai et al. 2014; Burke et al. 2015; Inagaki et al. 2015; Zhang et al. 2016). Theoretical models on the other hand predict a much higher mass growth for these massive galaxies than is observed (see e.g. De Lucia & Blaizot 2007; Tonini et al. 2012). In this thesis we attempt to measure the stellar mass build-up of BCGs between $0.08 \leq z \leq 0.50$. We do this by studying the total stellar mass growth of the BCGs (as a function of redshift) and investigate the role of mergers therein.

2. Both star formation and mergers have contributed towards the total stellar mass build-up of BCGs. Predictions from numerical simulations and SAMs suggests that BCGs formed in two 'phases'. At $z \geq 2$ star formation is found to dominate the BCG's mass growth and at later times ($z \leq 1$) the mass growth is dominated by multiple dry mergers of smaller galaxies (e.g. Gao et al. 2004a; De Lucia & Blaizot 2007; Naab et al. 2009; Laporte et al. 2013). Between $0 \leq z \leq 1$ it is rare to find BCGs that are actively forming stars (e.g. Liu et al. 2012; Fraser-McKelvie et al. 2014) and these starburst epochs are expected to contribute very little to the stellar mass growth of these massive galaxies (Sarazin & O'Connell 1983; Cardiel et al. 1995; Pipino et al. 2009; Liu et al. 2012; Loubser et al. 2016). There is, however, ample observational evidence that indicates that BCGs are undergoing mergers (e.g. Bernardi et al. 2007; Lauer et al. 2007; von der Linden et al. 2007; McIntosh et al. 2008; Liu et al. 2009; 2015). However, observational studies are yet to reach a consensus regarding the amount of mass mergers contribute towards the stellar mass assembly of BCGs since $z = 1$. In this thesis we quantify what fraction of BCGs are undergoing mergers and how much they contribute to the stellar mass growth of these massive galaxies.

3. Although the exact origin of the ICL is still not known, merger events involving BCGs are thought to play a role. Theoretical models predict that the majority of a companion galaxy's stellar mass will be distributed into the ICL during a merger with the BCG (Conroy et al. 2007b; Murante et al. 2007; Puchwein et al. 2010; Laporte et al. 2013). This in turn suggests that the growth and stellar mass build-up of BCGs and the ICL are linked, however, it is not clear to what extent merger events contribute towards this.

The thesis is structured as follows. We describe the BCG sample that is used throughout this thesis along with the parent cluster catalogue from which the BCGs were obtained in Chapter 2. In Chapter 3 we investigate the total stellar mass growth of the BCGs. In Chapter 4 we use close pair statistics to investigate the importance of mergers in the mass growth of BCGs. We describe how the close pairs are selected and measure the pair fraction as a function of redshift. The close pair fraction is used as a proxy for the merger fraction to estimate how much mass growth the BCGs will experience due to mergers. In Chapter 5 we extend our analysis out to moderately high redshifts ($0.4 \leq z \leq 0.5$) by using spectroscopic observations from the Southern Africa Large Telescope (SALT; Buckley et al. 2006; O'Donoghue et al. 2006). We summarise the main science results from this thesis in Chapter 6 and attempt to combine the results from the two independent methods to form a coherent picture regarding the formation and evolution of BCGs. We end by drawing conclusions. Throughout this thesis we assume a flat ΛCDM cosmology with $\Omega_M = 1 - \Omega_\Lambda = 0.3$ and $H_0 = 70\ \mathrm{km\,s^{-1}\,Mpc^{-1}}$. Magnitudes are given in the AB system and the Chabrier (2003) initial mass function is used.

Chapter 2

The BCG sample and redMaPPer cluster catalogue

> "Who spoke the Earth and sky to form? Who sets the sun and calls the dawn? Who breathed me out of dust to life? God of wonder and God of grace. My King forever, Jesus Christ."
>
> *Taken from* Stay And Wait
>
> Performed by Hillsong

For the purpose of investigating the stellar mass build-up of BCGs with redshift, we use version 5.2 of the red-sequence Matched-filter Probabilistic Percolation (redMaPPer[1]) cluster catalogue (Rykoff et al. 2014, hereafter R14). This catalogue has been constructed by using photometry from the eighth data release (DR8[2]; Aihara et al. 2011) of SDSS.

The outline for the chapter is as follows: In Section 2.1 we describe properties of SDSS that are important for our analysis. We continue to describe the construction and properties of the redMaPPer catalogue in Section 2.2 along with the BCG identification. Throughout this thesis we use the

[1] http://risa.stanford.edu/redmapper/
[2] http://www.sdss3.org/dr8/

magnitudes of the galaxies to derive their stellar masses. It is therefore very important to ensure that the photometric measurements of the galaxies are accurate. In Section 2.3 we investigate the SDSS photometry of the redMaPPer BCGs by remeasuring their magnitudes *ourselves* and also discuss the problems we encounter (and the effect thereof on the magnitudes).

2.1 The Sloan Digital Sky Survey

The SDSS is both an imaging and spectroscopic survey that has been used to observe roughly one quarter of the sky. The observations were made on a 2.5 m telescope that is located at the Apache Point Observatory in Southern New Mexico. This telescope is equipped with a mosaic charge-coupled device (CCD) camera which images the sky in five broad optical bands (filters), and a pair of multi-object spectrographs, which covers the whole optical wavelength range. Upon completion in July 2014, the SDSS survey had observed roughly 14 500 $\deg^2$ of the night sky. It contains the spectra of $> 10^6$ galaxies and $\sim 10^5$ quasars, which were all selected from the imaging data (York et al. 2000; Stoughton et al. 2002; Abazajian et al. 2009).

The imaging data from SDSS is stored in Flexible Image Transport System (FITS) files. Each FITS file consists of 2048 columns and 1489 rows[3]. SDSS frames are corrected for pixel-defects. Flat-fielding, cosmic-ray rejection and bias subtraction are also performed. Each of the pixels in the SDSS imaging frames spans $0.396''$ on the sky.

A detailed discussion of the full data reduction pipeline of SDSS will not be given here (see Stoughton et al. 2002, for more detail). We will, however, discuss the methods implemented by SDSS to (i) detect objects, (ii) perform the sky subtraction and (iii) measure the magnitudes of objects. These concepts will be used throughout this thesis.

2.1.1 Object detection

Objects in the imaging frames are detected by the SDSS algorithm as follows. First, pixels with values well above the average sky background ($> 200\sigma$) are detected and flagged as BRIGHT in the

[3]The raw SDSS image contains 1361 rows, however the corrected frame has the first 128 rows of the next corrected frame appended to it.

database. This roughly corresponds to 17.5 mag in the r-band. The 'local' sky level is then estimated by median-smoothing the imaging frame on a scale of $\sim 100''$. This sky estimate is subtracted from the frame. The sky-subtracted frames are smoothed using a Gaussian fit to the point spread function after which the algorithm detects 5σ peaks above the smoothed sky level. Objects are then defined as a connecting set of pixels that are detected in at least one band. The pipeline measures the properties (e.g. position, flux, etc.) of all the detected objects during the last step of object detection. Thereafter the pipeline determines whether a detection consists of more than one object. The pipeline deblends the 'parent' object into its corresponding 'child' objects (for more details on how this is done, see Section 2.3.1.2) and proceeds to measure the properties of each child. The original detected object is flagged as BLENDED in the database, while the corresponding 'child' objects in turn are flagged as CHILD.

It is unavoidable (and indeed desirable) for some of the SDSS fields in the survey area to overlap as the sky is surveyed. This in turn causes duplicate detections to be found in these overlapping fields. Each of the overlapping fields is assigned a value by the SDSS pipeline that depends on whether or not the photometric reductions were successfully completed. All objects that are detected in the field with the highest assigned value are flagged as PRIMARY in the SDSS database. Duplicate detections of these PRIMARY objects in subsequent lower value fields are flagged as SECONDARY.

2.1.2 Sky subtraction

The SDSS pipeline performs two types of sky subtraction:

- **Global:** The initial sky estimate is made using a median clipped method – the median value of every fourth pixel (clipped at 2.33σ) in the image is determined. This is the sky value that is used by the SDSS pipeline during the object detection to find all BRIGHT objects (pixels $> 200\sigma$), e.g. saturated stars. The scattering wings of these bright objects are subtracted from the imaging frame by the pipeline.

- **Local:** After the bright objects are detected and subtracted, a grid of (256×256) pixel boxes (centred on every 128th pixel) is used to estimate the local sky value in the imaging frames. In

each of these boxes the pipeline proceeds to find the same clipped median as in the global sky estimate. These median clipped values are spaced 128 pixels apart and bilinear interpolated to subtract the sky from the imaging frame.

The reduction pipeline of DR7 (and earlier releases) used these methods to perform the sky subtraction in the imaging frames. The local sky value however included light from the extended regions around bright galaxies (Aihara et al. 2011). The sky subtraction algorithm for DR8 and later releases of SDSS has been revised. In the revised sky subtraction algorithm the extended galaxies ($> 51\sigma$) are found, modeled and subtracted before the final sky value is determined. After deblending, the profile of each object is fitted against a model that is a linear combination of an exponential and de Vaucouleur profile (see Section 2.1.3). The pipeline then attempts to remove the extended wings of these bright galaxies by subtracting the composite model from the image frame and then determines the local sky estimate as before.

Numerous studies, e.g. Blanton et al. (2005); Lauer et al. (2007) and Bernardi et al. (2007) have found that the luminosities of large, nearby galaxies are systematically underestimated in DR7 and earlier releases of SDSS because the sky subtraction algorithm over-subtracts the sky in the outer regions of large galaxies.

The sky subtraction algorithm used in DR8 has been improved, however the above-mentioned problem is still prevalent as shown by Aihara et al. (2011). They simulated 1300 galaxies with a range of different inclinations and Sérsic indices, biased toward larger and brighter galaxies since this is where the sky subtraction problem is most pronounced. These model galaxies were then positioned at random into the SDSS sky images, whereafter the images were reduced with both the DR7 and DR8 pipelines. They found that the sky subtraction algorithm of DR8 slightly improved the magnitudes of large galaxies ($r_{50} \gtrsim \log_{10}(1.5\,''$), where r_{50} is the Petrosian half-light radius[4]). The DR7 pipeline measured a magnitude offset of ~ 1 for these large galaxies while DR8 measured an offset of ~ 0.7 magnitudes (see Fig 2.1). Their findings also suggest that the sky subtraction problem is not problematic for smaller galaxies ($r_{50} \lesssim \log_{10}(1.0\,''$)) since both the DR7 and DR8 pipelines measure a magnitude offset close to zero. All the BCGs in our sample have

[4]The radius that contains 50% of the Petrosian flux.

half-light Petrosian radii[5] of $\leq \log_{10}(1.0'')$ in the r-band, and are therefore located in region of the figure where it was found that the background had little to no influence on the magnitudes of the galaxies. This suggests that sky subtraction is unlikely to be problematic for our analysis. However, when remeasuring the SDSS photometry of the BCGs, we found that the magnitudes of the BCGs are underestimated in some cases. This may be redshift dependent since it depends on angular size of the galaxy. We return to this issue in Section 2.3.1.4.

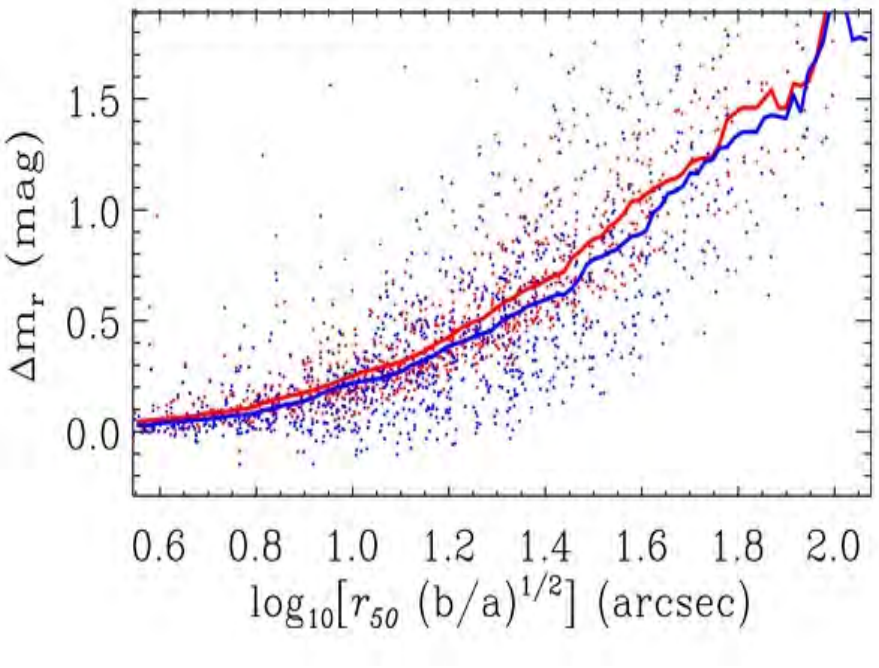

FIGURE 2.1: Figure taken from Aihara et al. (2011). The difference between the measured and true r-band magnitudes of a sample of 1300 simulated galaxies is shown here. These galaxies have a range of different inclinations and Sérsic indices, however the sample is biased toward larger and brighter galaxies. The magnitudes of these galaxies are measured with the DR7 (red line) and DR8 (blue line) pipelines. Even with the improved sky subtraction algorithm of DR8, the true magnitudes of large galaxies ($r_{50} \gtrsim \log_{10}(1.5'')$) are still underestimated by ~ 0.7 magnitudes. This shows that the sky subtraction problem, although slightly improved from DR7, is still problematic for large galaxies in DR8.

2.1.3 Magnitudes

The magnitudes of the detected objects in SDSS are determined using several different methods, e.g. measuring the magnitude within some fixed aperture and model fitting. We will however only discuss the magnitudes that are relevant to our project, e.g.:

[5]Taken from the `petroR50` entry in the SDSS DR8 database.

- Model magnitudes (`Model_Mag`) and;
- Composite model magnitudes (`cModel_Mag`)

In this work we use `Model_Mag` for the colours of the galaxies and to estimate the stellar masses of our galaxies through SED-fitting (e.g. Strateva et al. 2001). We use `cModel_Mag` for the total magnitudes of the galaxies, as advocated by e.g. Abazajian et al. (2009).

2.1.3.1 Model magnitudes

The photometric pipeline determines the flux of an individual galaxy by fitting the two-dimensional image of the galaxy against two models:

1. A de Vaucouleurs profile (de Vaucouleurs 1974):

$$I(r) = I_0 \exp\{-7.67[(r/r_{\rm eff})^{1/4}]\} \tag{2.1}$$

2. An exponential profile:

$$I(r) = I_0 \exp\{-1.68(r/r_{\rm eff})\} \tag{2.2}$$

where $r_{\rm eff}$ is the effective radius.

The `Model_Mag` magnitude of each galaxy is derived from the best-fitting model (either de Vaucouleur or exponential) in the r-band, whereafter the model is used to derive the flux of the galaxy in the remaining bands. This in turn ensures that the same size aperture is used across the different bands to measure the colours of the galaxies. It would be preferable to fit more complex models (e.g. models with a bulge and disk component) to large galaxies. This is computationally expensive and for the majority of the detected objects in SDSS this type of fit is not practical. It is worth mentioning however that some studies, e.g. Simard et al. (2011) and Mendel et al. (2014), have remeasured the photometry of subsamples of galaxies in SDSS by using models that fit both the bulge and disk components of galaxies.

2.1.3.2 Composite model magnitudes:

The `cModel_Mag` magnitude in each band is derived from the best-fitting linear combination of the de Vaucouleur and exponential profiles that describe the two-dimensional image of a galaxy.

For each galaxy the composite flux is given by:

$$F_{\text{composite}} = fracDev \times F_{\text{deV}} + (1 - fracDev)F_{\text{exp}} \tag{2.3}$$

where $fracDev$ is the coefficient of the de Vaucouleur term. The de Vaucouleur and exponential fluxes of the object are respectively given by F_{deV} and F_{exp}. One can then derive `cModel_Mag` from Eq 2.3 by converting $F_{\text{composite}}$ to a magnitude.

Strauss et al. (2002) compared the total magnitudes of elliptical galaxies as given by the `cModel_Mag` and Petrosian (`petro_Mag`; Petrosian 1976) magnitudes. In comparison to the `cModel_Mag` magnitudes, they found that the total magnitudes of these bright galaxies are underestimated by $5 - 10\%$ with the `petro_Mag` magnitudes. This is caused by the fact that the outer regions of these bright galaxies are not enclosed by the Petrosian apertures. They also found that the amount by which the total magnitudes of these galaxies are underestimated, is dependent on (i) the photometric band in which the flux is measured and (ii) the type of galaxy (profile), since models are used to measure the `cModel_Mag` magnitudes.

2.2 The redMaPPer cluster catalogue

The redMaPPer cluster catalogue has been constructed using a new red-sequence photometric cluster finding algorithm that is designed to handle any photometric galaxy catalogue with any arbitrary photometric bands ($\geq$ 3 bands). It uses the idea that all galaxy clusters comprise of an overdensity of galaxies of very similar colours (the red-sequence), and that this colour can be used as a relatively precise indicator of photometric redshift. Version 5.2 of the redMaPPer catalogue roughly covers 10 000 deg^2 of the sky and consists of more than 25 000 clusters that have been optically selected using photometry from SDSS DR8.

The total magnitudes of the galaxies are given by `cModel_Mag` in the i-band (m_i), while `modelMag` in the *u, g, r, i* and z-bands have been used to determine the colours of the galaxies. All magnitudes have been corrected for Galactic extinction using the dust maps of Schlegel, Finkbeiner, & Davis (1998).

2.2.1 The redMaPPer algorithm

The redMaPPer algorithm can be divided into two different stages: (i) calibration of the red-sequence galaxy properties as a function of redshift, and (ii) identification of galaxy clusters and determination of the cluster richness.

2.2.1.1 The red-sequence calibration stage

At the start of the algorithm, a set of 'training clusters' are selected, i.e. clusters with potential red central galaxies (CGs) that have spectroscopic redshifts (hereafter referred to as 'seed' galaxies). The algorithm then searches for overdensities of galaxies with the same colour as these seed galaxies. All galaxies that are selected through this method are referred to as the photometric members of the training clusters.

Galaxies with luminosities $\geq 0.2L^{\star}$ have high probabilities of being cluster members of the training clusters. A full linear red-sequence model is then fitted against these high-probability galaxies to obtain the tilt, scatter and zero point of the red-sequence to calibrate the red-sequence model. SDSS is a magnitude limited spectroscopic survey and the algorithm tries to compensate for this by assigning the spectroscopic redshift of the seed galaxy to the high-probability cluster members. This is done to achieve a better fit of the red-sequence in clusters across all redshifts.

2.2.1.2 The cluster-finding stage

Once the red-sequence model has been calibrated, the algorithm attempts to 'grow' galaxy clusters. All of the photometric galaxies identified in the step above are considered as potential cluster centres. The red-sequence model is then used to determine photometric redshifts for the galaxies

and evaluate the goodness of fit to the galaxy template used in the red-sequence model. It suffices to say that galaxies with no reasonable fit to the template at any redshift will not be considered possible CGs for the purpose of cluster ranking.

Using the redshift of the candidate CG as an initial guess for the cluster redshift, the cluster's richness is determined. All clusters with ≥ 3 red-sequence galaxies within a 500 h^{-1} kpc aperture are selected. The algorithm iteratively determines a photometric redshift for each cluster based on the calibrated red-sequence model, as measured from the photometrically identified candidate cluster members. The process is repeated until convergence is achieved between the member selection and the photometric redshift of the cluster. All the resulting possible cluster centres are then ranked according to probability. The richness and membership probabilities of the highest ranking cluster is then determined, after which the same is done for the second highest ranking cluster and so forth.

2.2.2 Properties of the redMaPPer cluster catalogue

The redMaPPer cluster catalogue has a photometric redshift range of $0.08 \leq z \leq 0.55$ and contains 25 235 clusters. We show the sky coverage (top panel) and the photometric redshift distribution (bottom panel) of the redMaPPer clusters in Fig 2.2. Example SDSS cutouts of clusters from the lowest to the highest redshift in our sample are shown in Fig 2.3.

2.2.2.1 Cluster richnesses

The redMaPPer cluster catalogue contains clusters with a richness threshold of $\lambda \geq 20\, S(z)$, roughly corresponding to 20 red-sequence galaxies, with $S(z)$[6] a scale factor used to correct the cluster richness for the survey depth. This adopted richness threshold of 20 red-sequence galaxies was chosen to provide the most robust cluster catalogue possible with clusters that have halo masses of $M_h \gtrsim 10^{14}\,\mathrm{M}_\odot$ at $z \lesssim 0.35$ (see Rykoff et al. 2012, for more detail). At $z \lesssim 0.35$, the catalogue is volume limited and the survey depth is brighter than the fiducial luminosity cut of $0.2\,L^\star$ – hence $S(z) \sim 1$ (see left panel of Fig 2.4). Above this redshift, the magnitude limit of the survey becomes problematic and only the most massive clusters are detected. This causes the richness

[6] Given by equation 23 of R14.

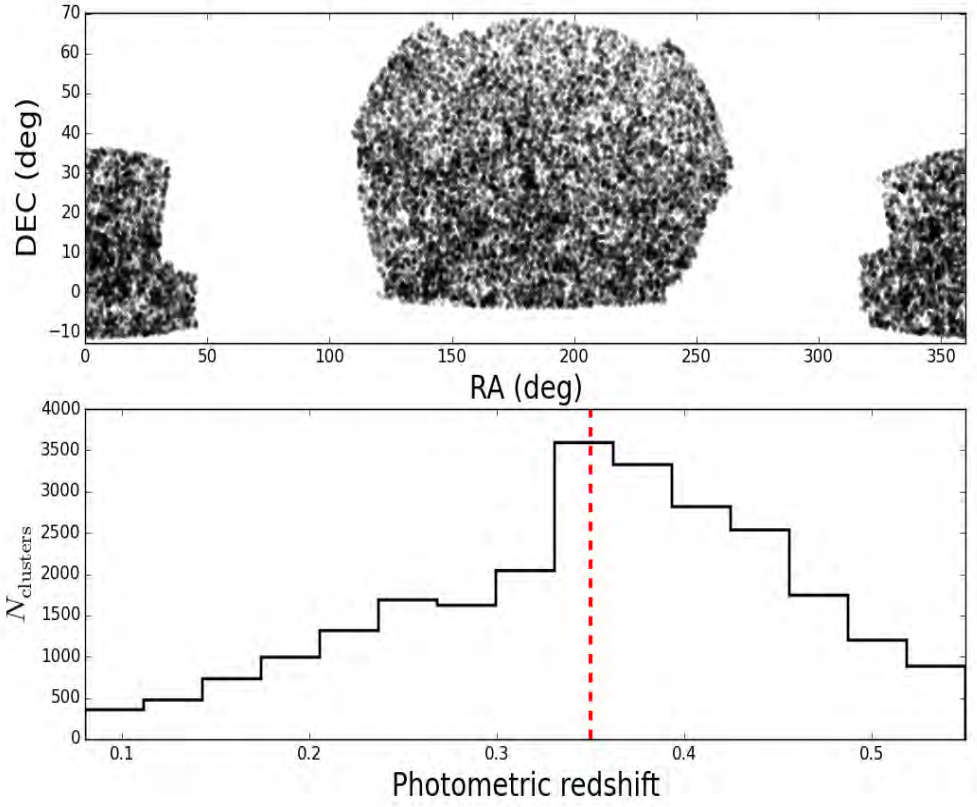

FIGURE 2.2: The sky coverage of the clusters in the redMaPPer catalogue is shown in the top panel. The bottom panel shows the photometric redshift distribution of the clusters. Most of the clusters are located around $z \sim 0.35$ (red dashed line).

threshold to rapidly increase with redshift, resulting in fewer lower richness clusters (see right panel of Fig 2.4). Example SDSS cutouts of low and high richness redMaPPer clusters are shown in Fig 2.5. For the remainder of this thesis, we cut the redMaPPer catalogue to the volume limited sample, i.e. we only consider the 11 230 clusters at $z \leq 0.35$.

2.2.2.2 Probability of being a cluster member

Each cluster in the redMaPPer catalogue has cluster members assigned based on a membership probability ($P_{\rm MEM}$). $P_{\rm MEM}$ indicates the probability of a galaxy being a red-sequence galaxy that belongs to a specific cluster. This follows directly from the method used by the redMaPPer algorithm to identify clusters, e.g. searching for the red-sequence feature in clusters. In order to avoid

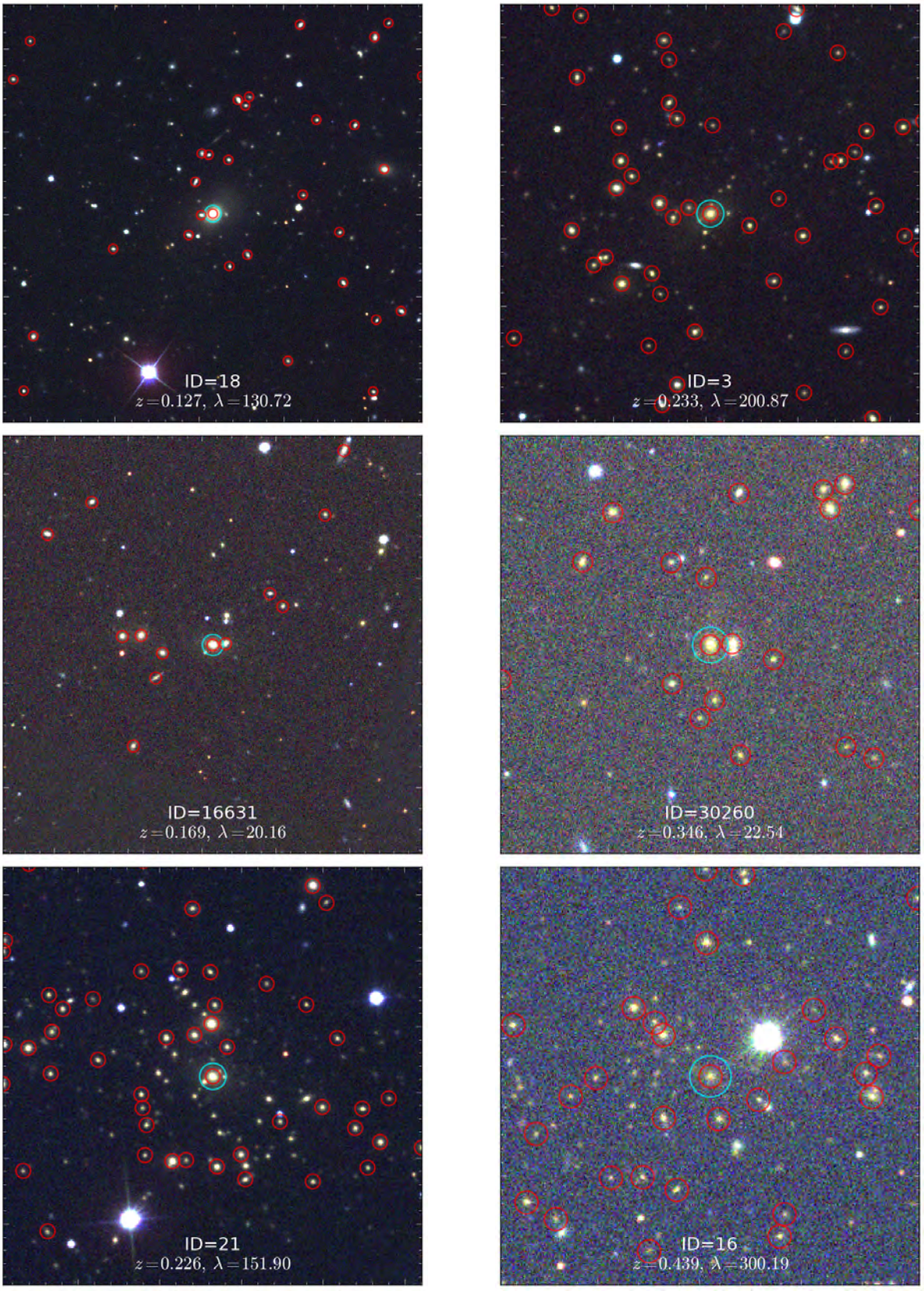

FIGURE 2.3: In the first column we show examples of low redshift redMaPPer clusters, while the remaining column contains examples of high redshift redMaPPer clusters. Each cutout has a physical size of 0.7×0.7 Mpc (at the cluster's photometric redshift) and is centred on the BCG (circled in cyan). The galaxies circled in red are redMaPPer cluster members (with $P_{\rm RSM} > 0$) that are brighter than the $0.2L^{\star}$ magnitude limit.

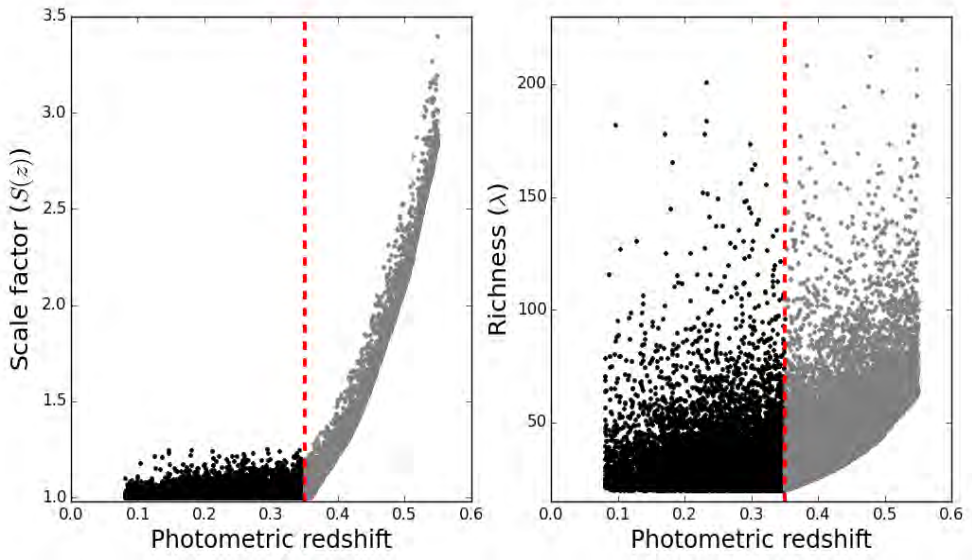

FIGURE 2.4: The scale factor ($S(z)$, left panel) and the richness (λ, right panel) of the redMaPPer clusters are shown as function of the photometric redshifts. The red dashed line indicates $z \lesssim 0.35$ where the catalogue is volume limited. See text for detail.

confusion, hereafter we will refer to $P_{\rm MEM}$ as the probability of a galaxy being a *red-sequence cluster member*, denoted as $P_{\rm RSM}$.

In Fig 2.6 we show the colour-magnitude diagrams ($g-r$ vs. m_i) of the redMaPPer clusters out to $z = 0.35$. Cluster members with $P_{\rm RSM} > 0.0$ and 0.9 are indicated in black and green respectively. In each panel it is apparent that members with large $P_{\rm RSM}$ values form a tighter sequence since these galaxies are more likely to be red-sequence galaxies than those with smaller $P_{\rm RSM}$ values. The solid and dashed lines in the colour-magnitude diagram respectively indicate the location of the red-sequence and the 1σ width. Only high probability cluster members (e.g. $P_{\rm RSM} > 0.9$) have been used to find the red-sequence, since these galaxies are more likely to belong to the red-sequence.

For each cluster in the redMaPPer catalogue, the algorithm assigns five galaxies probabilities of being the CG of the cluster ($P_{\rm CEN}$)[7]. These galaxies are ranked according to probability and are hereafter referred to as the CG candidates. The central probabilities are defined by using three filters: a luminosity filter, photometric redshift filter and a local galaxy density filter. The product of these three filters produces the overall centering filter that is used to determine the central

[7]In the redMaPPer catalogue it is assumed that the centre of the cluster is located at a galaxy position, i.e. the galaxy with highest $P_{\rm CEN}$ (R14).

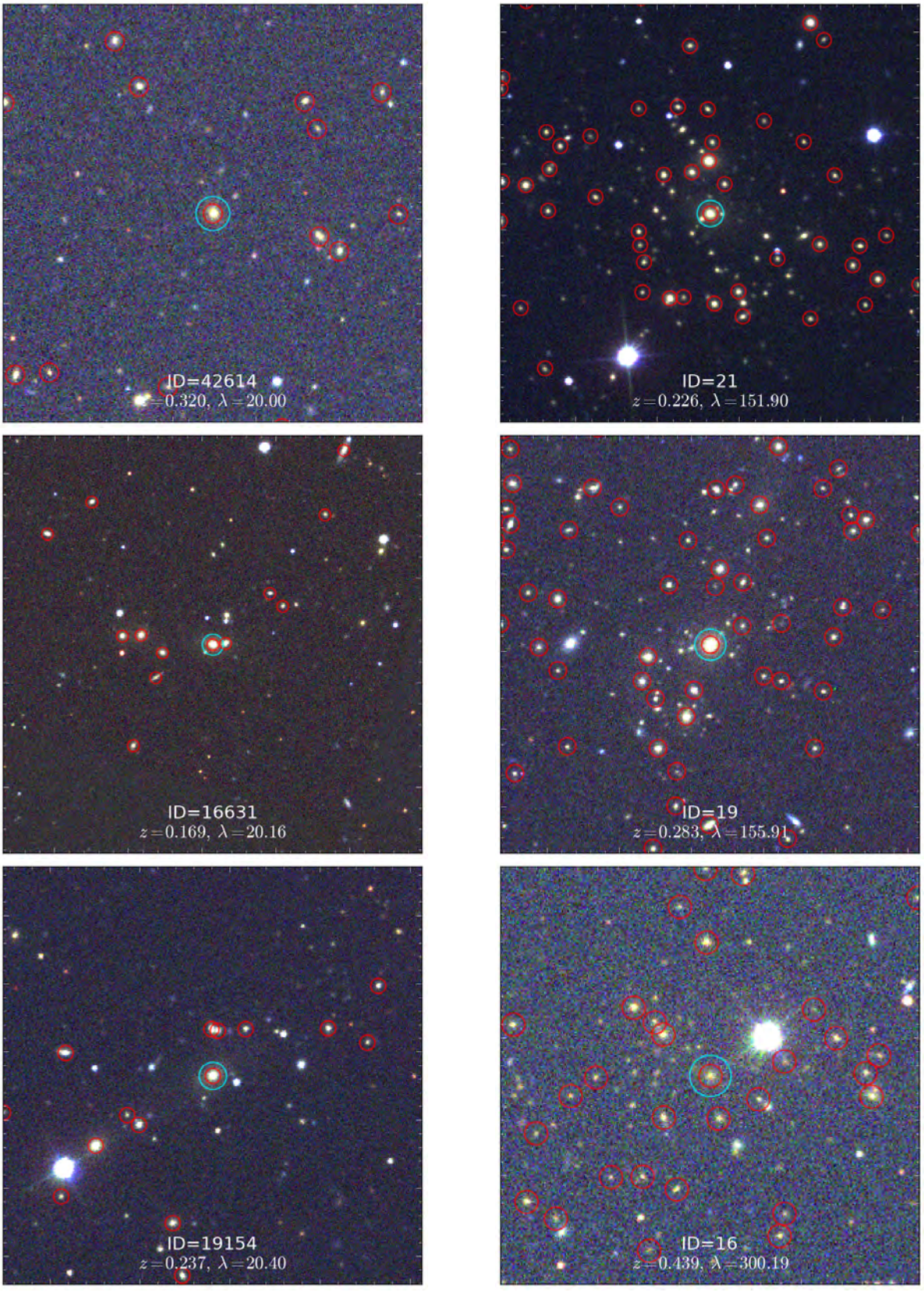

FIGURE 2.5: In the first column we show examples of low richness clusters, while the remaining column contains examples of high richness clusters. Each cutout has a physical size of 0.7×0.7 Mpc (at the cluster's photometric redshift) and is centred on the BCG (circled in cyan). The galaxies circled in red are redMaPPer cluster members (with $P_{\mathrm{RSM}} > 0$) that are brighter than the $0.2L^{\star}$ magnitude limit.

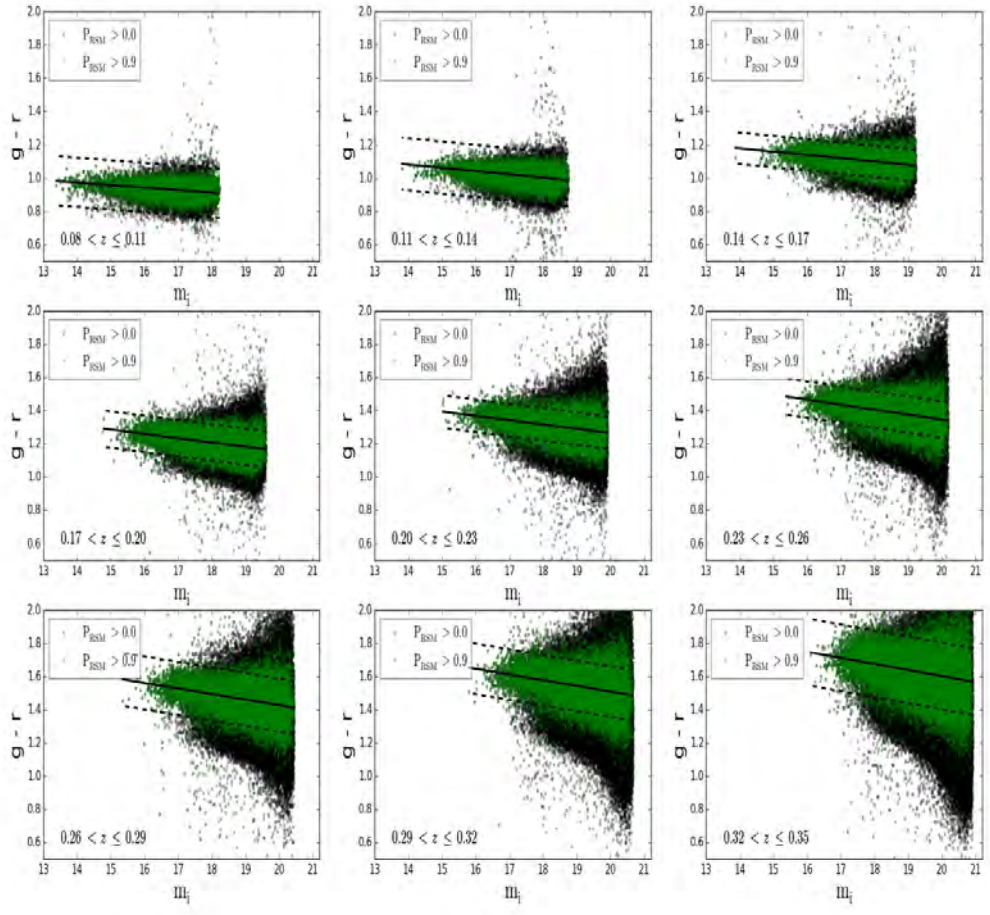

FIGURE 2.6: The colour-magnitude diagram of the redMaPPer clusters in various redshift bins. The cluster members with $P_{\rm RSM} > 0.0$ and 0.9 are shown in black and green respectively. The red-sequence forms a tighter sequence as $P_{\rm RSM}$ increases and becomes redder with redshift. Only galaxies with $P_{\rm RSM} > 0.9$ are considered when the location of the red-sequence is determined as these galaxies have the highest probability of being red-sequence galaxies.

probabilities (see equation 67 of R14). The redshift filter that is used in this equation is slightly broader than the cluster red-sequence filter in order to allow galaxies with slight colour offsets from the red-sequence to be considered as CG candidates. That said, it is possible for the central galaxies to have experienced residual amounts of star formation and therefore have bluer photometric colours. The galaxy with the highest $P_{\rm CEN}$ is not necessarily the brightest galaxy. This is because, apart from the luminosity, the spatial position of (local galaxy density around) the CG candidate is also considered. Central galaxies are expected to be found in the highest density central regions of clusters. Consequently, the redMaPPer algorithm gives higher preference to galaxies in the denser

regions of the clusters to be CGs than those in less dense regions. A less luminous galaxy located in a denser environment than the most luminous galaxy may therefore have a higher $P_{\rm CEN}$.

2.2.2.3 The BCG identification

In our work we select the first CG candidate (galaxy with highest $P_{\rm CEN}$) in each cluster as the BCG. The apparent and absolute i-band magnitude distributions of the BCGs are shown in Fig 2.7. BCGs typically exhibit low scatter in their magnitudes ($\sim 0.3-0.4$ mag; e.g. Sandage 1972; Sandage & Hardy 1973; Gunn & Oke 1975; Kristian et al. 1978; Hoessel et al. 1980; Sandage 1988; Whiley et al. 2008). We measure a scatter of ~ 0.2 in the i-band magnitudes of the BCGs in the redMaPPer catalogue, indicating that the BCGs form a tight sequence. This is not surprising due to the way clusters are identified by the redMaPPer algorithm – the presence of a cluster is indicated by an overdensity of red galaxies. BCGs are therefore selected to be red-sequence galaxies.

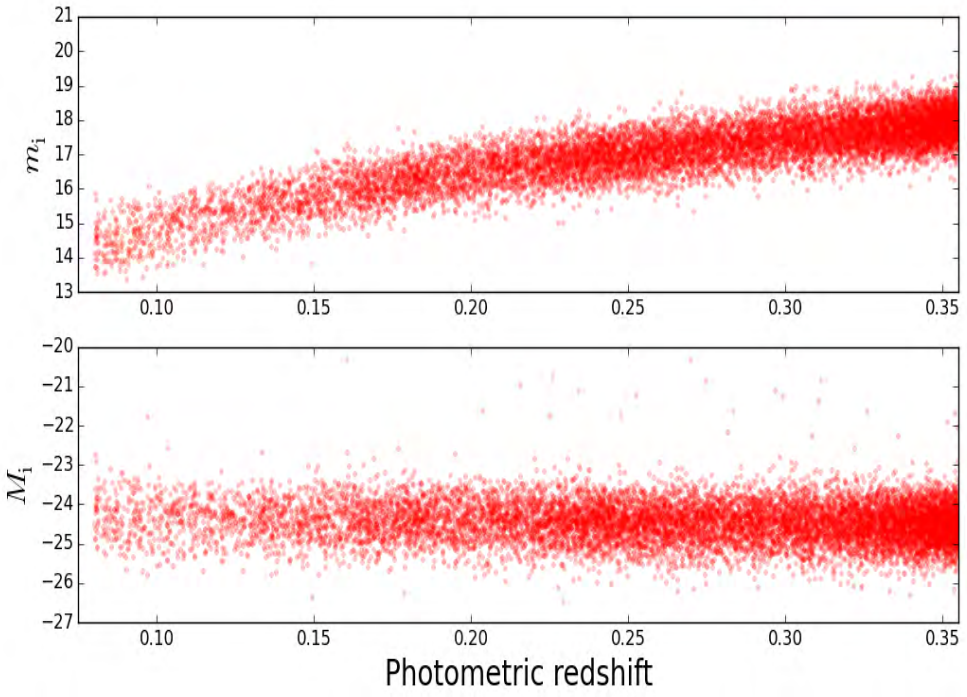

FIGURE 2.7: The apparent (top panel) and absolute (bottom panel) i-band `cModel_Mag` magnitudes of the BCGs as a function of the clusters' photometric redshifts. Due to the manner in which the redMaPPer algorithm identifies clusters, these BCGs are selected to be red-sequence galaxies and subsequently form a tight sequence as seen here.

Not all observed BCGs are red galaxies. The A2035 cluster, for example, has a BCG with a blue photometric colour, indicating that the BCG recently experienced star formation (see e.g. McNamara et al. 2006). In cases like these, where the colour of the true BCGs are $> 2\sigma$ from that of the red-sequence, the redMaPPer algorithm will choose one of the bright satellites as the 'CG candidate'. It is estimated that roughly 2% or less of the clusters in the redMaPPer catalogue will suffer from this, i.e. the true BCGs of the clusters are too blue to be identified as the CG candidates by the redMaPPer algorithm (R14).

2.3 Verifying the SDSS photometry of the BCGs in the redMaPPer catalogue

The main aim of this thesis is to investigate the stellar mass build-up of BCGs as a function of redshift. The stellar masses are derived from the magnitudes as described in Section 3.2.5. It is therefore important to ensure that the photometric measurements are accurate. In this section we explore possible reasons for inaccuracies in the SDSS photometry of BCGs and verify how well SDSS measures their fluxes. For the interested reader we show examples of the SDSS cutouts for a subsample of 200 redMaPPer clusters in Appendix A. The purpose of these cutouts is to give the reader a general impression of the cluster sample, e.g. to indicate how the optical richness of the clusters and the angular sizes of galaxies change as a function of redshift.

Apart from the background, another reason why the magnitudes of bright, nearby galaxies may be underestimated is related to the manner in which the deblending algorithm of SDSS assigns the light in the outer parts of these galaxies to neighbouring objects (stars and galaxies). An example is cluster 305 where the candidate BCG is located near a bright galaxy (see left panel of Fig 2.8). Light from this galaxy may contaminate the light of the BCG, causing SDSS to overestimate its magnitude. In this case a galaxy that looks much fainter than other cluster members has been assigned as the central galaxy, due to contaminating light from its neighbour. We discovered a related issue when looking through the SDSS cutouts of the BCGs (like those shown in Appendix A): we found cases where SDSS missed obvious, bright objects around the BCGs (see right panel of Fig 2.8). The

SDSS pipeline may have incorporated the light of these undetected objects into the BCG, causing this galaxy to be measured brighter than it should be.

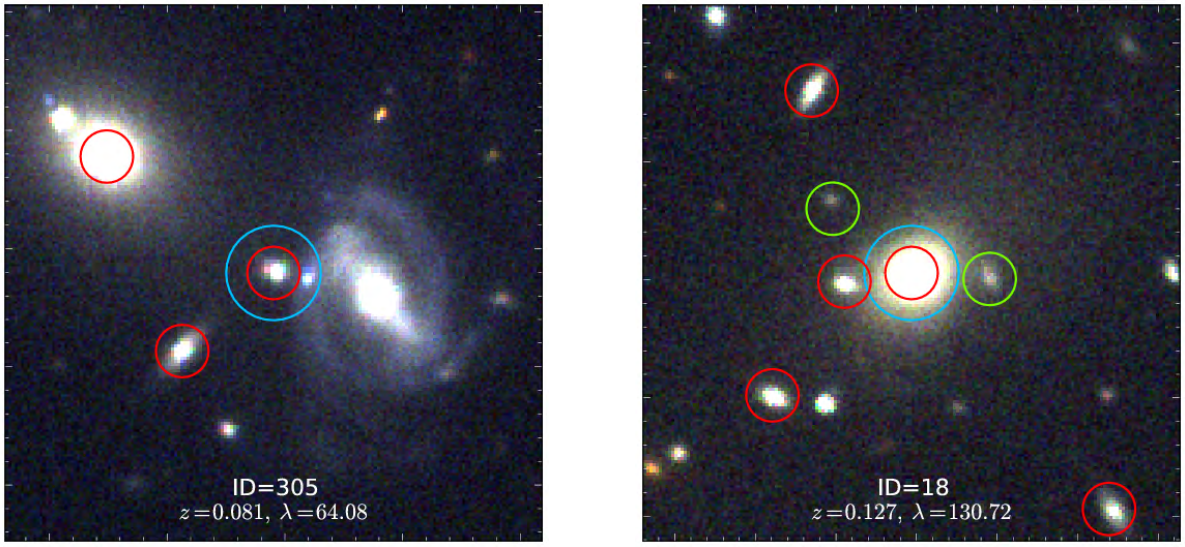

FIGURE 2.8: Example of reasons why the magnitudes of bright, nearby galaxies may be underestimated. Each cutout is centred on the BCG (circled in blue) and is 68″ on a side, which roughly corresponds to 100 kpc at $z = 0.08$. The objects circled in red are the candidate cluster members identified by redMaPPer. Left panel: the BCG candidate is located near another bright galaxy. Here the SDSS magnitude of the 'BCG candidate' is overestimated, causing it to be classified as the BCG even though it is clearly significantly fainter than the other cluster members. Right panel: an example where SDSS did not detect obvious, bright objects (circled in green) around the BCG. SDSS may have incorporated the light of these undetected objects into the BCG, causing the galaxy to be brighter than it should be.

It therefore makes sense to investigate the SDSS photometry of the BCGs for the following two cases:

1. First we consider the simplest case where the BCG is relatively isolated and we do not have to worry about contamination from a neighbouring galaxy's light.

2. In reality BCGs may have nearby galaxies. Searching for close companions to the BCGs (possible merger candidates) is one of the main aims of this thesis. It is therefore imperative that we reliably separate out the photometry of the neighbouring objects from that of the BCGs.

We use two methods to measure the total magnitudes of the BCGs in the above-mentioned cases, i.e. large aperture photometry and using an automated software package. These methods will be

described in the sections hereafter. In order to investigate the SDSS photometry for the BCGs we downloaded a (900 × 900) pixel[8] cutout. This size stamp covers a significant part of the clusters at all redshifts, ensuring (1) we have enough area around the BCG to measure its total magnitude; (2) we will detect all neighbouring objects within 50 kpc (correspond to ≈ 85 pixels at $z = 0.08$). of each redMaPPer cluster from the SDSS database. These cutouts were created using the i-band FITS images and have been centred on the BCGs. Along with the cutouts, we also downloaded the corresponding field calibration and statistics file (tsField) of each cluster since these files are needed to calibrate the magnitudes of the objects.

2.3.1 Case 1 – Isolated BCGs

2.3.1.1 Large aperture photometry with IRAF

Simply put, in large aperture photometry the magnitude of an object is measured by enclosing the object in a circular aperture with radius r and adding up all the light within that aperture (see Fig 2.9). The light that is contributed by the sky in the same region of the object is then estimated by using a slightly larger aperture (called the sky annulus). When the light of the sky is subtracted from that of the object, one is left with the brightness of the object.

The instrumental flux of the object ($F_{\rm inst}$) can be determined as follows:

$$F_{\rm inst} = \sum_{i=1}^{N_{\rm pix,\,ap}} c_{i,\rm ap} - \langle c_{\rm sky\,ann} \rangle \times N_{\rm pix,\,ap} \tag{2.4}$$

where $c_{i,\rm ap}$ is the counts per pixel (including the sky) in the aperture with radius r, $N_{\rm pix,\,ap}$ is the total number of pixels in the aperture and $\langle c_{\rm sky\,ann} \rangle$ is the average sky count per pixel in the sky annulus. $F_{\rm inst}$ is therefore given by the total number of counts in the aperture excluding the counts contributed by the sky.

In general, the magnitude (m) of the galaxy can then be determined from the counts (Eq 2.4) as follows:

$$m = m_{\rm zpt} - m_{\rm inst} \tag{2.5}$$

[8]Each cutout is 356″ on a side and this roughly corresponds to 523 (1710) kpc at $z = 0.08\,(0.35)$.

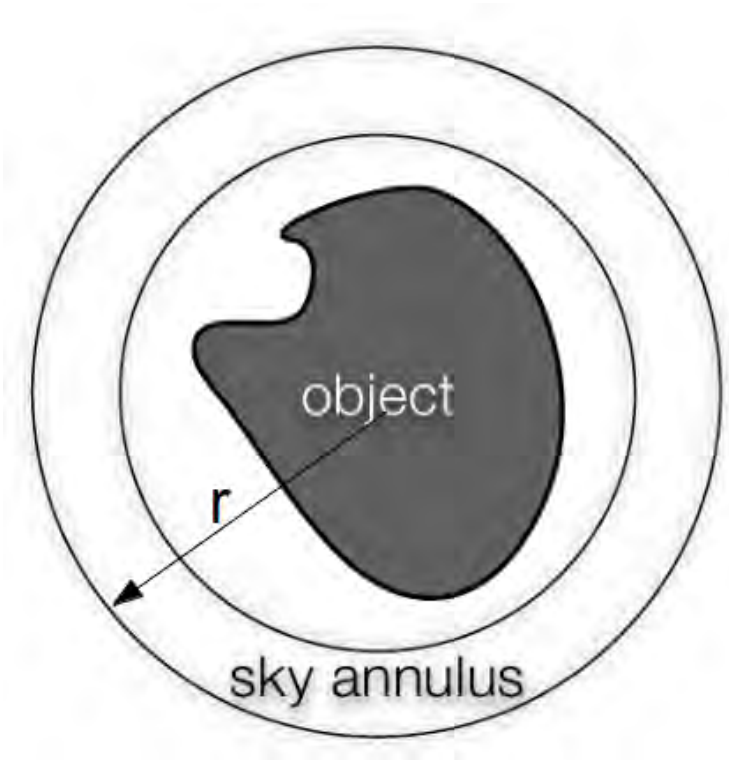

FIGURE 2.9: Illustration of the large aperture photometry technique. The object is enclosed in a circular aperture of radius r while the light from the sky is determined in the sky annulus. The flux of the object is determined by subtracting the background level measured in the sky annulus from the counts in the circular aperture.

with $m_{\rm zpt}$ the zero point of the magnitude scale and $m_{\rm inst}$ the instrumental magnitude, which is given by $2.5\log_{10}(F_{\rm inst})$.

The disadvantage to using large aperture photometry is that this particular method cannot be used to determine the magnitude of objects (e.g. galaxies) in crowded fields, i.e. the galaxy of interest is surrounded by other nearby objects. The light of the galaxy (and/or the sky annulus) may be contaminated by the light of the other neighbouring objects, making it hard to determine the true magnitude of the galaxy.

qhot

The `qhot`[9] routine of the Image Reduction and Analysis Facility (`IRAF`[10]) software is capable of measuring the magnitudes of objects via large aperture photometry. This routine returns a

[9]Can be found in `noao.digiphot.apphot` of `IRAF`.
[10]http://iraf.noao.edu/

few measured properties of the objects (including their associated uncertainties), e.g. the local background value, flux of the object in the aperture, etc. The magnitudes that are given as output by this routine are instrumental magnitudes and therefore have to be calibrated ($m_{\rm cal}$) using:

$$m_{\rm cal} = m_{\rm zpt} - m_{\rm inst} \tag{2.6}$$

where $m_{\rm zpt} = (aa) + (kk \times airmass) - 2.5\ \log_{10}(t_{\rm exp})$, with aa is the photometric calibration zero point, kk is the atmospheric extinction coefficient and $t_{\rm exp}$ is the exposure time (for SDSS images this is 53.9 seconds). For objects in SDSS, the $airmass, aa$ and kk values can be retrieved from the tsField files.

However before `qhot` attempts to measure the magnitude of an object via large aperture photometry, the user is required to specify the radius of the circular aperture (in pixels) in which the flux of the object is to be measured in. The user must also define the width and inner radius of the sky annulus in order for the background contribution to be estimated.

BCGs at lower redshifts appear larger on the sky than those at higher redshifts. This is something that has to be taken into consideration when one decides on the aperture size. When using too small an aperture, one runs the risk of underestimating the flux of the BCG since the BCG could be larger than the aperture. It therefore makes sense to use the lowest redshift ($z \sim 0.08$) BCGs in the redMaPPer catalogue to determine the size of the aperture with which the total magnitudes of the galaxies are to be measured in, at all redshifts.

So the question now becomes, what aperture size should be used to determine the total magnitudes of the BCGs in the redMaPPer catalogue? The aperture size is determined through a curve of growth (COG) analysis, in which a range of apertures are used to determine the magnitude of a galaxy. To explain the COG analysis, we use the BCG in cluster 4931 ($z \sim 0.08$) which has purposefully been chosen to be isolated as an example. The magnitude of the BCG is measured within nine circular apertures, starting with a radius of 10 pixels and increased by 5 pixels for each measurement. The radius of the inner sky annulus is set to 50 pixels while the width is set to 5 pixels. This is shown in Fig 2.10(a) where the nine circular apertures are shown in green and the sky annulus is indicated in red. The COG of the BCG is shown in Fig 2.10(b). For apertures

with radii of $\geq 45 - 50$ pixels the magnitude of the BCG stayed constant, indicating that these apertures contained all of the BCG's light. We find that a circular aperture with a radius of 50 pixels ($\sim 20''$)[11]. is sufficient enough to contain all of the light of the BCGs, regardless of their redshifts. We consider BCGs with no companions within a radius of 55 pixels ($\sim 22''$) to be isolated.

Now that we have established a benchmark against which to test photometry (at least for the simplest case of isolated BCGs), we can proceed to test more sophisticated packages with the aim to being able to accurately measure photometry in the general case. With this in mind, we turn next to the `Source-Extractor` or `SExtractor`[12] package.

2.3.1.2 The `SExtractor` software

`SExtractor` is a very efficient tool used to find sources and measure magnitudes in large astronomical imaging frames. This software is designed to separate blended sources and classify objects into stars/galaxies. A short description of the software will follow (for more details see Bertin & Arnouts 1996).

Objects are detected in `SExtractor` as part of the segmentation process where the objects are separated from the background. This is however a somewhat over simplified definition that is complicated by the fact that objects, for example galaxies, have no clear boundaries and may even overlap with other objects. An 'object' in `SExtractor` is therefore defined as a group of pixels that belong to an object for which the flux contribution is believed to dominant over that of other objects (where objects overlap). A detection threshold limit is used to identify pixels that belong to an astronomical object rather than the sky. A group of connecting pixels above this limit is deemed a detection. Segmentation maps in which objects with different properties (e.g. brightness) are identified and separated are produced by the software. As an example we show the SDSS sky image of redMaPPer cluster 4391 in the top panel of Fig 2.11. The resulting segmentation map, produced during the object detection of `SExtractor`, is shown in the bottom panel.

[11] This is equivalent to $\sim 14\,(4)$ kpc at $z = 0.08\,(0.35)$.
[12] http://www.astromatic.net/software/sextractor

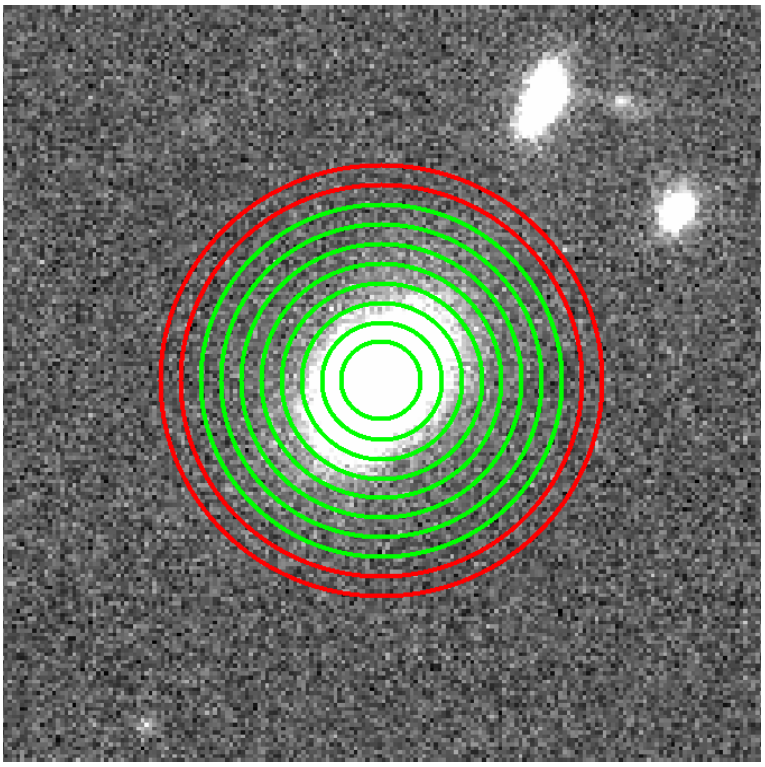

(a) The total magnitude of the BCG is measured within circular apertures with radii ranging from $10 - 50$ pixels (green circles), while the sky annulus (red circles) has a inner radius of 50 pixels and a width of 5 pixels.

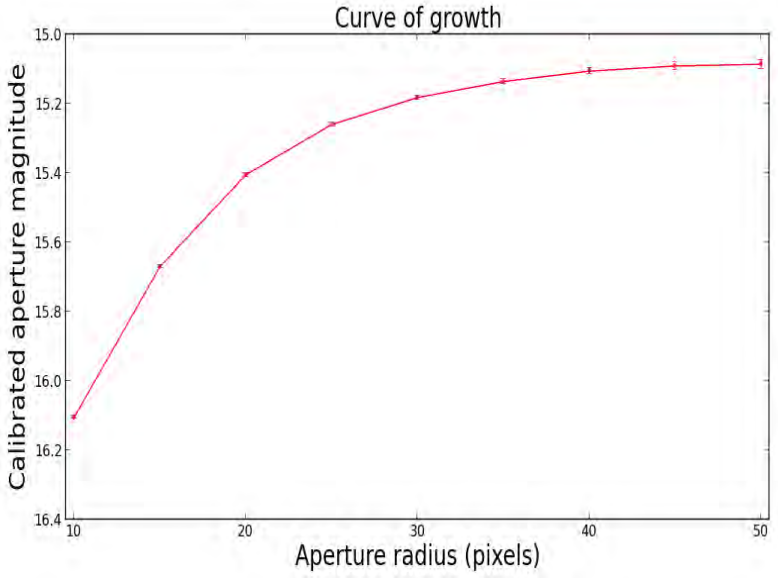

(b) The resulting curve of growth as constructed from the calibrated magnitudes of the BCG as measured in the circular apertures. At $r = 45-50$ pixels the magnitude start to asymptote, indicating that apertures with these radii will contain all of the BCG's light.

FIGURE 2.10: Measuring the magnitude of the BCG in cluster 4391 with large aperture photometry.

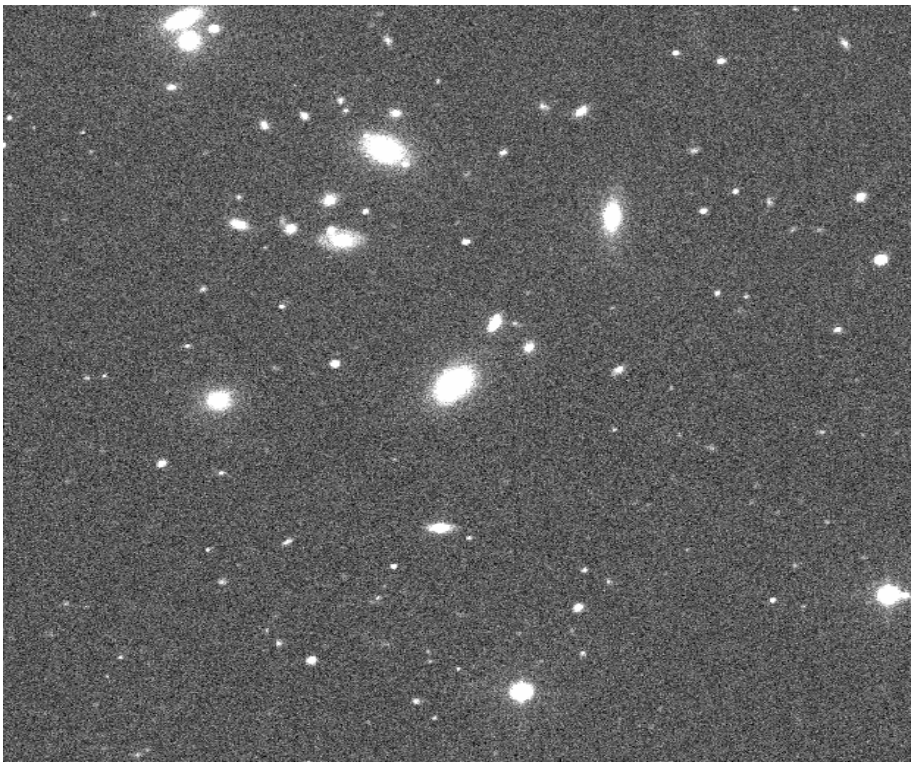

(a) SDSS sky image of cluster 4391, centred on the BCG.

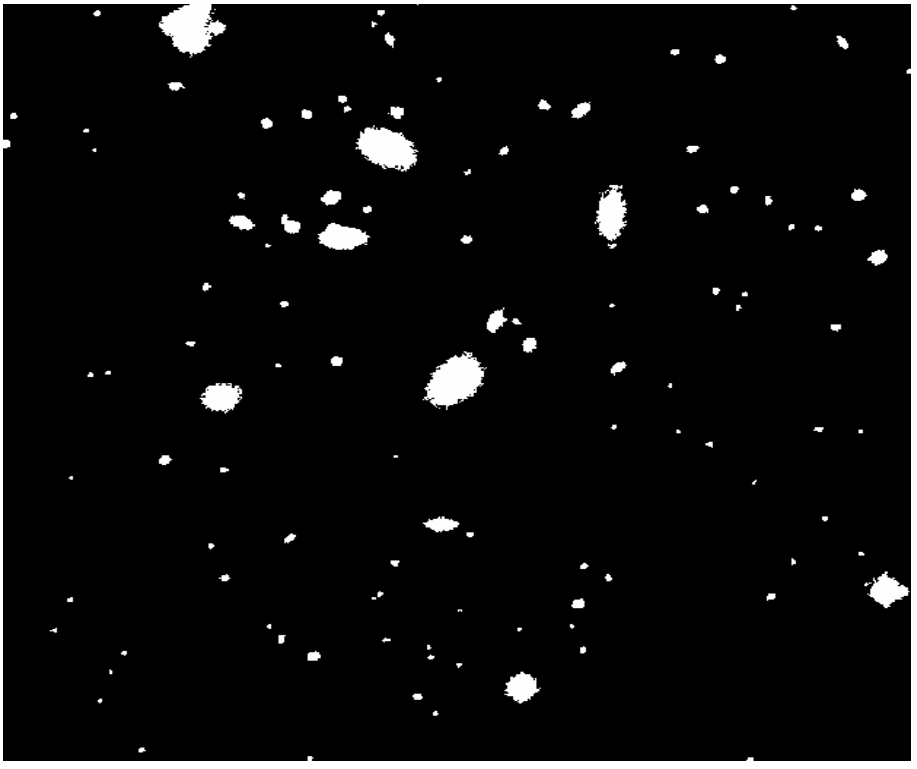

(b) The segmentation map produced during the object detection of `SExtractor`.

FIGURE 2.11

In order to obtain correct flux measurements of objects, it is important to derive a reliable measurement of the background at any region in an astronomical image. In `SExtractor` a 'background map' is constructed by placing a grid mesh over the whole image, after which the local background is determined in each mesh cell. Bertin & Arnouts (1996) used simulations in which various mesh-sizes and object crowding were used, to find that a combination of $\kappa\sigma$ clipping and mode estimation gave a good estimate of the local background in `SExtractor`. In this approach the local background histogram is clipped iteratively until it converges at $\pm 3\sigma$ around its median. During this process, if σ changes by less than 20% the field is considered to be uncrowded. In this case the mean of the clipped histogram is taken as an estimate of the background. However, if the field is crowded (σ changes more than 20%), the background value is taken as the mode of the clipped histogram:

$$\text{mode} = 2.5 \times \text{median} - 1.5 \times \text{mean} \tag{2.7}$$

Once the mesh grid is in place, the software applies a median filter to suppress any background overestimates that might occur due to the presence of bright galaxies. The background map is then produced through bilinear interpolation of the meshes in the grid. The `SExtractor` manual[13] states that a mesh with a width of 32 to 128 pixels works well for most images.

Once the initial object detection is done, it may be necessary to deblend a single object into separate objects. This is done by employing a multiple isophotal analysis technique. The method is illustrated in Fig 2.12. Briefly, each group of connected pixels (defined as a object) is split up into 32 threshold levels that are exponentially spaced between the primary extraction threshold (set by the user) and the peak value of the object. From this, the light distribution within the object can be seen (smooth curve) which is approximated by a tree-like diagram (thick lines). The algorithm starts at the top of the 'branches' and works it way down the 'trunk' of the tree diagram. At each junction, the algorithm determines whether two or more objects will be extracted or whether it should continue down the trunk. Hence, at any junction threshold t_i, any 'branch' will be considered as a separate object if:

[13]Can be found at http://astroa.physics.metu.edu.tr/MANUALS/sextractor/

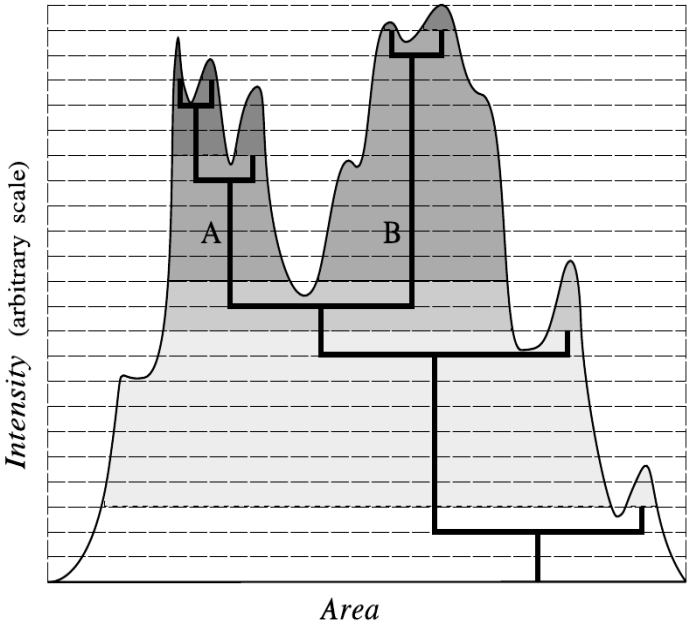

FIGURE 2.12: Figure taken from Bertin & Arnouts (1996). This figure illustrates the method used in `SExtractor` to deblend a composite object. The light profile of the object (smooth curve) can be described by using a tree-like diagram (thick lines). A 'branch' is considered a separate object based on the its relative integrated intensity (shaded area). In this example, the composite object is deblended into two separate objects A and B.

- above t_i, the integrated pixel intensity of the 'branch' is $> \delta_c$, where δ_c is a certain fraction of the composite object's total intensity set by the user, and
- the above condition is confirmed for at least one more 'branch' at the same level as i.

After the objects have been deblended, the algorithm proceeds to measure the photometry and geometric parameters of the objects. We now focus on photometry because it is important to ensure that the photometric measurements of the galaxies are accurate in order for reliable stellar mass estimates to be obtained.

2.3.1.3 `SExtractor` photometry

The `SExtractor` algorithm measures the magnitudes of objects in different ways, e.g. using fixed circular apertures or flexible elliptical apertures that vary depending on the object. Only the magnitudes that are used in the rest of the photometry analysis will be discussed, specifically `MAG_APER` and `MAG_AUTO`.

Similar to large aperture photometry, the MAG_APER magnitude is estimated from the flux above the background within in a circular aperture with some fixed radius that is defined by the user. The MAG_AUTO magnitude is a Kron-like magnitude (Kron 1980) measured within an elliptical aperture. For a given object, the elongation and orientation of the aperture are determined by second-order moments of the light distribution. These magnitudes are preferred when the magnitudes of objects with close neighbours (e.g. galaxies in clusters) are determined as they exclude light from the close neighbours.

In this thesis we use version 2.5 of SExtractor to measure the magnitudes of the BCGs in the redMaPPer catalogue. We experiment with MAG_APER and MAG_AUTO magnitudes and also investigate the influence on the derived magnitudes when a global and local background estimate is used. In order for SExtractor to be run on the SDSS sky images of the BCGs, the user is required to supply some input values for the parameters in the configuration file. Some of these parameters will have the same values as used for qphot, e.g. the aperture size, sky annulus width and magnitude zero point. The parameters in the configuration file are kept as their default values except for the following, which we attempt to optimise via experimentation, as described below. The descriptions are taken from the SExtractor manual.

- DETECT_MINAREA = 14. This sets the minimum number of adjacent pixels with flux values above the local background. If an object does not have more pixels than this value, then SExtractor will not consider it an object. Practical values range between 3 and 20.
- PHOT_APERTURES = 100. Sets the diameter (in pixels) of the circular aperture that will be used to determine MAG_APER.
- BACKPHOTO_THICK = 5. Sets the width (in pixels) of the sky annulus (only set if LOCAL background is used).
- BACKPHOTO_TYPE = LOCAL or GLOBAL. Sets the background to be used to compute magnitudes. If GLOBAL, value will be taken directly from the background map. If LOCAL, value determined in sky annulus.
- MASK_TYPE = CORRECT. In the case where a galaxy's light might be contaminated due to the presence of close neighbours, this parameter will replace the pixels in the contaminated

region with those located directly opposite it. Only used if GLOBAL background setting is used.

- `MAG_ZEROPOINT` = 25. The magnitude zero point.
- `PIXEL_SCALE` = 0.396. Sets the size (in arcsec) of an individual pixel in SDSS.

The retrieved `MAG_APER` and `MAG_AUTO` magnitudes are calibrated using Eq 2.6. The question now becomes, which magnitude (`MAG_APER`/`MAG_AUTO`) and background setting (GLOBAL/LOCAL) should be used when the BCG magnitudes are remeasured with `SExtractor`?

In order to test for the appropriate parameter settings, we compare carefully measured aperture photometry from `IRAF's qphot` routine to the results obtained from `SExtractor`. For this test we choose a subsample of 30 isolated BCGs (see Section 2.3.1.1). It is not unreasonable to expect that large aperture photometry (as measured by `qphot`) gives the most reliable estimates of the isolated BCGs' total magnitudes. With this in mind we find that the GLOBAL background setting and `MAG_AUTO` in `SExtractor` matches the `qphot` background and magnitude values the closest. Subsequently, when `SExtractor` is used to remeasure the BCG magnitudes, we will set `BACKPHOTO_TYPE` = GLOBAL and `MAG_AUTO` will be used as an estimate of a BCG's total magnitude.

2.3.1.4 Comparing `qphot`, `SExtractor` and SDSS magnitudes for isolated BCGs

As already stated we expect that `qphot` (large aperture photometry) will give the most reliable estimate of the total magnitudes of **isolated** BCGs. We use this idea to determine whether the SDSS magnitudes of isolated BCGs are reliable by comparing them to the large aperture photometry (using `qphot`) magnitudes.

From the object catalogues that are obtained with `SExtractor` for each redMaPPer cluster, we construct a subsample of isolated BCGs. A BCG is considered to be isolated if there are no objects located within a radius of 55 pixels from the BCGs. We use a radius of 55 pixels to measure the total magnitudes of the isolated BCGs (see Section 2.3.1.1). Using this criterium we find $\sim$ 200 isolated BCGs in the redMaPPer catalogue. Following the method outlined in Section 2.3.1.1, we measure the magnitudes of these isolated BCGs by using `qphot`.

In Fig 2.13 the total magnitudes of the isolated BCGs are shown as a function of the clusters photometric redshifts. Here the SDSS magnitudes of the isolated BCGs are compared against those measured by `qphot` and `SExtractor`. As previously mentioned (see Section 2.2.2.3), the BCGs will form a tight sequence with redshift as these galaxies have been chosen to be red-sequence galaxies by construction. This is due to the way the redMaPPer algorithm has identified clusters by searching for overdensities of red galaxies. Outliers are present in both the `qphot` and `SExtractor` magnitudes and these may indicate that there are problems with the SDSS photometry of these BCGs. A galaxy is considered an outlier if its magnitude (as measured in either `qphot` or `SExtractor`) is fainter or brighter than $\langle m_i \rangle \pm 2\sigma$, where $\langle m_i \rangle$ is the median `qphot` or `SExtractor` magnitude at some z_{phot} and σ is the standard deviation in the magnitudes. For `qphot`, `SExtractor` and SDSS $\sigma = 0.05$, 0.04 and 0.03 respectively. Using this criteria we find respectively that only ~ 1.5 and 1.0% of the `qphot` and `SExtractor` magnitudes are outliers. Since these percentages are so small we consider the effect these outliers may have on the magnitude comparison negligible.

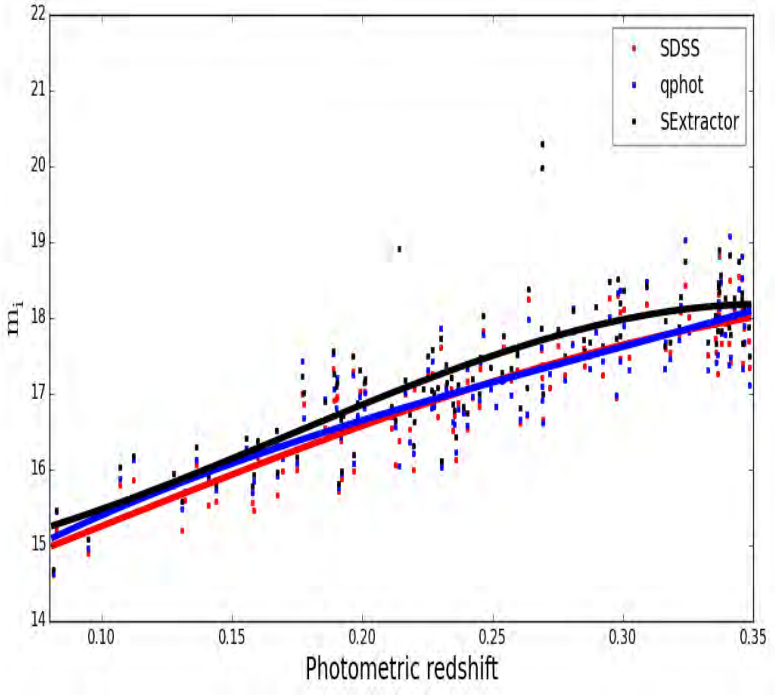

FIGURE 2.13: The magnitudes of the isolated BCGs as remeasured with `qphot` (blue) and `SExtractor` (black). The corresponding SDSS DR8 magnitudes are indicated in red. The solid lines indicate the median magnitudes of each sample, obtained through least-square fitting of a cubic function.

When the magnitudes of the isolated BCGs are compared, one would expect these magnitudes to be similar regardless of the method used to derive the magnitudes. However Fig 2.13 shows that the derived median magnitude is different. Differences may be due to the sky subtraction problem mentioned earlier in Section 2.3. We test this by determining in what region of the magnitude-size relation shown in Fig 2.1, the sizes of our isolated BCG subsample will fall. We find that all the isolated BCGs have half-light Petrosian radii of $\leq \log_{10}(1.0'')$ in the r-band, and are therefore located in region of the figure where it was found that the background had the least influence on the magnitudes of the galaxies, but the magnitudes may still be underestimated by up to 0.20 mag. This may be redshift dependent since it depends on the angular size of the galaxies. We continue to test this idea in the remainder of this section.

We compare the SDSS magnitudes of the isolated BCGs to their corresponding `qphot` and `SExtractor` magnitudes in Fig 2.14. In each panel the black solid line indicates the zero magnitude offset while the black dashed line represents the median magnitude offset of the sample under consideration as measured in $15 \leq m_{\rm i} \leq 18$ mag. Panel (a) shows the comparison between SDSS and `qphot`. We also indicate the median magnitude offset as measured in four redshift bins (indicated by the points), where the uncertainty is given by the error on the mean. The results are summarised in Table 2.1. We find that the median magnitude offsets in the four redshift bins are consistent within the uncertainties. Although SDSS underestimated the total magnitudes of the BCGs in all the redshift bins, the BCGs in the lowest redshift bin is the only place where this offset is significantly different from zero (SDSS magnitudes underestimated by 0.15 mag). The median magnitude offsets for the BCGs in the remaining redshift bins are nearly constant and consistent with zero. We are therefore mainly interested in the magnitude offset of the BCGs in the lowest redshift bin. This median magnitude offset will affect the total stellar mass growth of the BCGs and we will therefore need to consider this systematic uncertainty in the lowest redshift bin when the total stellar mass growth of the BCGs is measured in Chapter 3. Recent works, for example D'Souza et al. (2015); Bernardi et al. (2016), find corrections ranging from $0.02 - 0.31$ magnitudes are needed to account for the fact that SDSS is underestimating the total magnitudes of galaxies. We make a small digression here to perform an independent check of the reliability of the BCGs' total magnitudes in the SDSS (given by `cModel_Mag`) by comparing them against the total magnitudes obtained using the independent method of surface brightness profile (SBP) fitting. For this purpose we use the Galaxy And Mass

Assembly (GAMA[14]; Driver et al. 2011) survey which contains re-analysed SDSS imaging (in the u, g, r, i, z-bands; see Hill et al. 2011; Kelvin et al. 2012, for more details). SIGMA[15] GAMA (Kelvin et al. 2010) was used to calculate a total magnitude for each galaxy via its best-fitting Sérsic profile (see Kelvin et al. 2012, for more details). For this test we use all of the BCGs in our sample (whether they are isolated or not) and cross-match them to galaxies in the GAMA survey. This results in matches for $\sim 2\%$ (210/11 230) of our BCGs. In the lowest redshift bin we find a magnitude offset close to zero (i.e. -0.01 ± 0.12, with the uncertainty given by the error on the mean), which is in agreement with the offsets measured by the above mentioned studies. It has to be mentioned that the magnitudes we measured via large aperture photometry may still be *underestimated*, although it is beyond the scope of this thesis to quantify this further.

TABLE 2.1: Summary of the amount by which SDSS underestimates the total magnitudes of BCGs in various redshift bins, as measured using `qphot` and `SExtractor`.

z	$\Delta m_{\rm i} = m_{\texttt{qphot}} - m_{\rm SDSS}$ **(mag)**	$\Delta m_{\rm i} = m_{\texttt{qphot}} - m_{\texttt{SExt}}$ **(mag)**
$0.08 - 0.15$	-0.15 ± 0.11	-0.11 ± 0.06
$0.15 - 0.21$	-0.06 ± 0.18	-0.14 ± 0.16
$0.21 - 0.28$	-0.03 ± 0.13	-0.19 ± 0.12
$0.28 - 0.35$	-0.01 ± 0.18	-0.26 ± 0.19
$0.08 - 0.35$	-0.04 ± 0.17	-0.10 ± 0.17

In panel (b) the comparison between `qphot` and `SExtractor` is shown. The median magnitude offset is $\sim (-0.10 \pm 0.09)$. This offset can be explained by the fact that `MAG_AUTO` is known to miss some fraction of a galaxy's total flux, however this is dependent on the galaxy's light profile (Graham & Driver 2005). For our isolated BCGs we estimate that `SExtractor` underestimates the total

[14] http://www.gama-survey.org/

[15] Structural Investigation of Galaxies via Model Analysis. This is a specially designed pipeline that is based upon `GALFIT 3` (Peng et al. 2007).

magnitudes by 0.10 ± 0.09 mag, when compared to `qphot` magnitudes. When this correction for missing flux is applied to all the isolated BCGs, we find that the `qphot` and `SExtractor` magnitudes of these BCGs are comparable. Note that if we apply the same correction for missing flux to all the galaxies in our sample, we are very likely to overestimate the magnitudes for some of these galaxies. In the worst case, Graham & Driver (2005) find that `SExtractor` misses 10% of the total light/flux of galaxies with Sérsic indices of 4 (such as BCGs). For galaxies with indices of 1, they find that `SExtractor` only misses 4% of the total flux. If we therefore apply a 10% correction for missing flux to all galaxies, regardless of their Sérsic indices, we will overestimate the total flux of galaxies with small Sérsic indices by 6%.

In summary: We have used large aperture photometry to measure the magnitudes for ~ 200 isolated BCGs in the redMaPPer catalogue. When comparing these magnitudes to their SDSS magnitudes, we measured a small median offset of ~ 0.04 mag, which indicates that the magnitudes are reasonable if we consider the `qphot` large aperture magnitudes to be the best estimate of the total magnitudes. The magnitudes of the isolated BCGs have also been measured with the `SExtractor` software and when compared against the `qphot` magnitudes, we measured a median offset of ~ 0.1 magnitudes. This is approximately the amount by which `MAG_AUTO` is known to underestimate the total magnitude of galaxies. The findings from the test performed in this section have shown that the SDSS magnitudes of the isolated BCGs are *reliable*. Throughout the remainder of this thesis we use the SDSS magnitudes of the BCGs during our analysis of their stellar mass evolution.

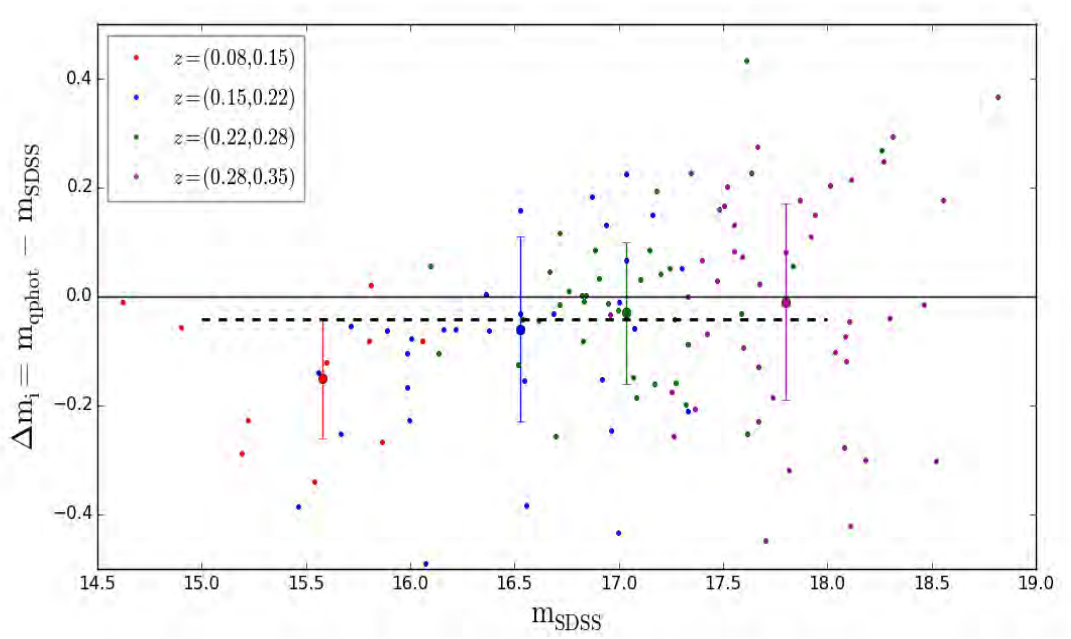

(a) Comparison between `qphot` and SDSS. Notice that the median magnitude offsets in the four redshift bins are consistent within the uncertainties, however only in the lowest redshift bin is this offset significantly different from zero (SDSS magnitudes underestimated by 0.15 mag).

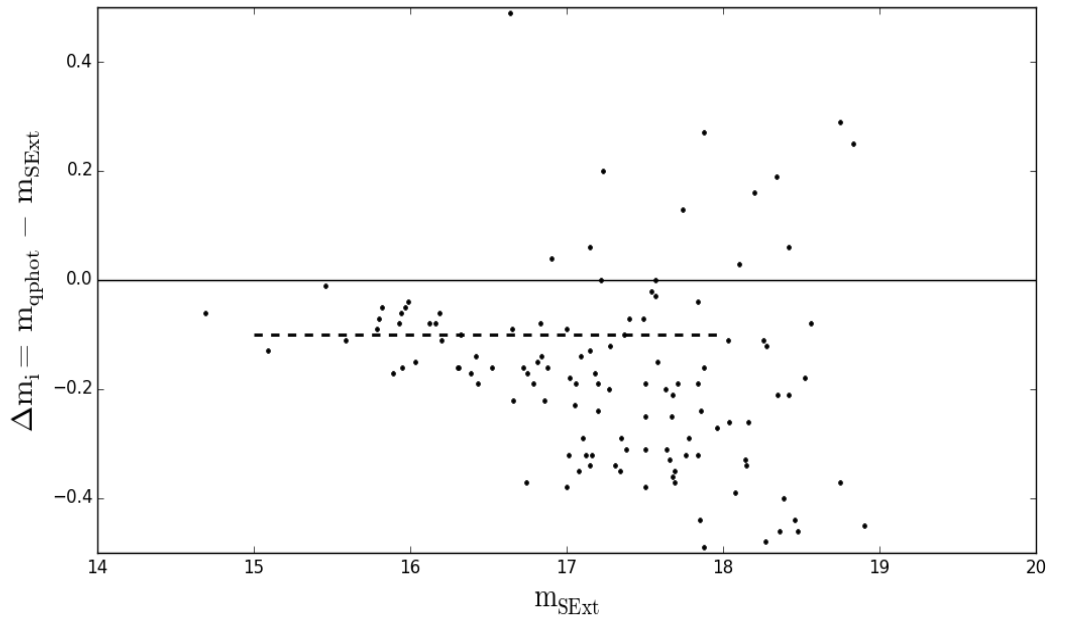

(b) Comparison between `qphot` and `SExtractor`.

FIGURE 2.14: Comparison of the magnitudes of the isolated BCGs as measured with `qphot`, `SExtractor` and SDSS. In panel (a) the magnitudes of SDSS and `qphot` are compared while the the magnitudes of `qphot` and `SExtractor` are compared in panel (b). The black lines represent the zero offset while the black dashed lines show the median magnitude offset in each comparison as measured in $15 \leq m_i \leq 18$ mag. In panel (a) the median offset is ~ 0.04 and in panel (b) it is ~ -0.1. We also indicate the median magnitude offset (uncertainty is given by the error on the mean) in four redshift bins with the large points and error bars. See text for more details.

2.3.2 Case 2 – BCGs in crowded fields

As already mentioned, we derive the stellar masses of the BCGs from their magnitudes and it is therefore very important to get the magnitudes of these BCGs correct. One aspect that could be a problem is the case where a BCG has been identified as a single galaxy in SDSS, although it actually consists of several galaxies. Consequently, for the photometry of the BCGs to be correct, the object detection needs to be correct.

Earlier in our analysis we created SDSS cutouts of the BCGs in the redMaPPer catalogue and found examples where the SDSS pipeline did not detect obvious, bright objects around the BCGs. The reduction pipeline of SDSS is a compromise that is designed to work over a wide range of different environments and on different objects. It cannot simultaneously hope to be the most efficient method in environments such as crowded fields next to large, bright objects, whilst at the same time being optimised for finding the very smallest, faintest objects in relatively empty fields. The pipeline has difficulty detecting objects around and close to the BCGs. A possible reason for this may be that the local detection threshold for objects around the BCG is too high so that when the object detection is performed, these objects are not detected as separate objects by SDSS.

The fact that SDSS has difficulty detecting obvious, bright objects close to the BCGs is problematic for our analysis! These bright objects may have a significant influence on the magnitudes of the BCGs. We therefore attempt to test and improve the detection of bright objects around BCGs using the `SExtractor` software package.

2.3.2.1 Modeling the effect of a nearby galaxy on the BCG magnitudes

Before we move on to investigate the photometry of BCGs in crowded fields, it is helpful to investigate how biased the magnitudes of a BCG can become due to neighbouring objects. Intuitively, the brighter a companion, or the nearer it lies to a BCG, the more influence it will have. Furthermore, the fainter the magnitude of the BCG, the more influence the companion will have. Thus, we need to explore contamination as a function of companion magnitude and distance to the BCG. We investigate this by simulating crowded fields. In our sample we find the magnitudes of the faintest and brightest BCGs ($m_{\rm i} = 19.28$ and 13.28 respectively), along with the magnitudes of the faintest and

brightest companions ($m_{\rm i} = 20.04$ and 14.79 respectively). The worst case of the BCG magnitude contamination will occur when the faintest BCG is paired with the brightest companion. The least contamination (best case) will occur when the brightest BCG is paired with the faintest companion.

We use the worst case to describe the approach we use to study the BCG magnitude contamination. We simulate this by selecting the faintest BCG in our sample. From the same region of sky (in order to keep the noise properties the same) we select another isolated galaxy to act as the companion to the BCG, with a magnitude corresponding to that of the brightest companion. We vary the distance of the companion to the BCG and measure the magnitudes at each distance. The same approach is followed for the remaining cases.

We show the difference in the BCG magnitudes between the simulated contaminated and isolated cases in Fig 2.16. These tests indicate that the companion galaxy will start to affect the BCG magnitude around a distance of $8''$. At a distance of $5''$ we find that the faintest companion only biases the BCG magnitude by 0.04 mag (best case, solid red line). For much larger/more typical distances the effect of the companion decreases to ~ 0.01 mag. The brighter companion on the other hand can bias the BCG magnitude by 0.08 mag at a distance of $1''$ (worst case, solid blue line). The effect of the companion gradually decreases as the distance increases, e.g. to 0.04 mag at $8''$. We investigated a range of other galaxy sizes and magnitudes, finding that the results in Fig 2.16 do bracket the two extremes.

2.3.2.2 `SExtractor` object detection

We randomly selected a subsample of 100 BCGs from the redMaPPer catalogue with $z \leq 0.35$. We identified nine cases where the BCGs had bright, obvious objects around them that were not detected in SDSS (four examples are shown in Fig 2.17). We considered these nine cases in order to optimize `SExtractor` for the detection of bright objects around the BCGs.

Optimizing `SExtractor` for the detection of bright, obvious objects around BCGs

The two parameters in `SExtractor`'s configuration that will have the largest influence on the object detection and deblending are described below. The values of these parameters may have to

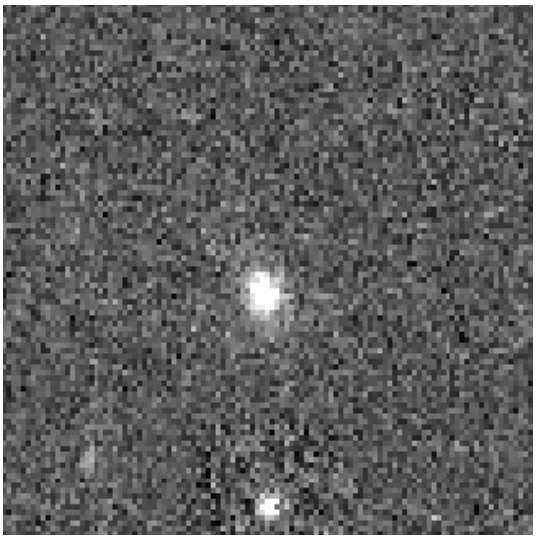

(a) Crowded field 1. Companion (placed at 20″) is ~ 3 magnitudes fainter than BCG.

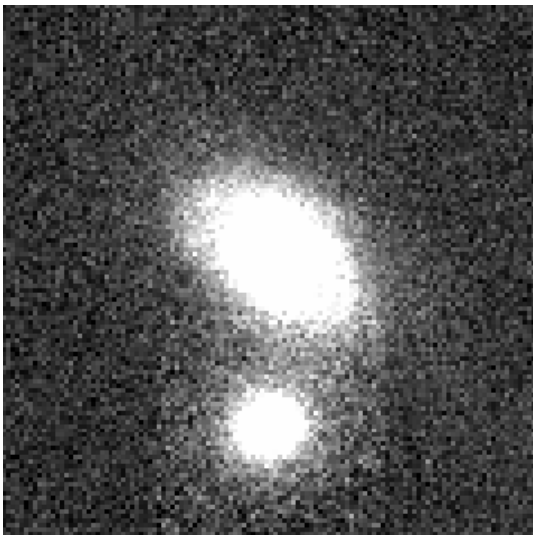

(b) Crowded field 2. Companion (placed at 20″) is ~ 2 magnitudes fainter than BCG.

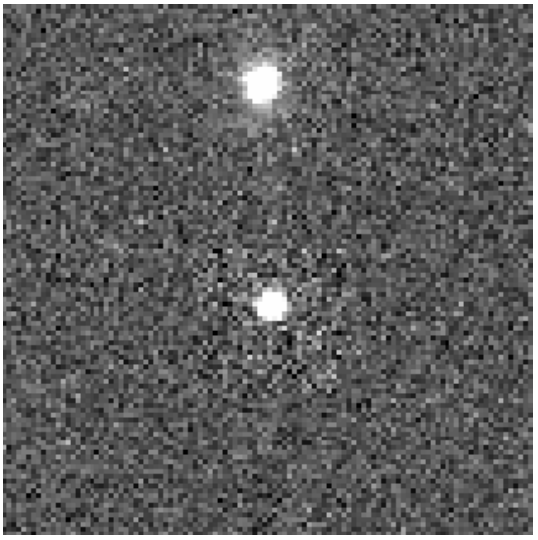

(c) Crowded field 3. Companion (placed at 20″) is ~ 1 magnitudes fainter than BCG.

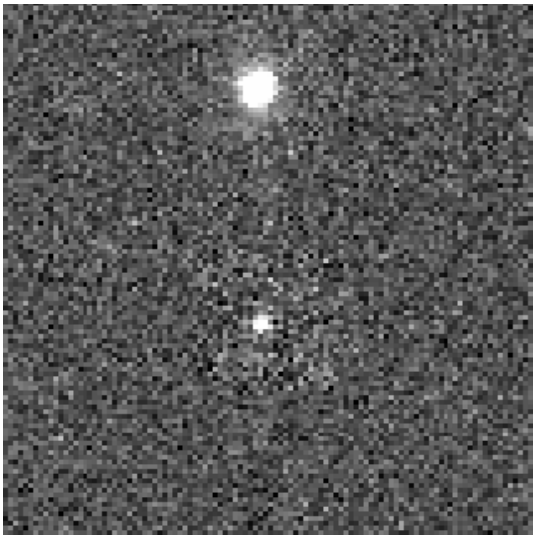

(d) Crowded field 4. Companion (placed at 20″) is ~ 4 magnitudes fainter than BCG.

FIGURE 2.15: Four examples of the modeled crowded fields we used in our analysis. Isolated BCGs, with a range of magnitudes have been selected from the redMaPPer catalogue. From the same region of sky as the BCG, we select a galaxy to act as the BCG's close companion by placing it at different distances from the BCG. Thereafter the magnitudes of both galaxies are measured with `SExtractor`. See text for details.

be adjusted to improve the detection of bright objects close to BCGs.

- `DEBLEND_NTHRESH`. This parameter sets the number of thresholds used when objects are deblended. The default value is 32.

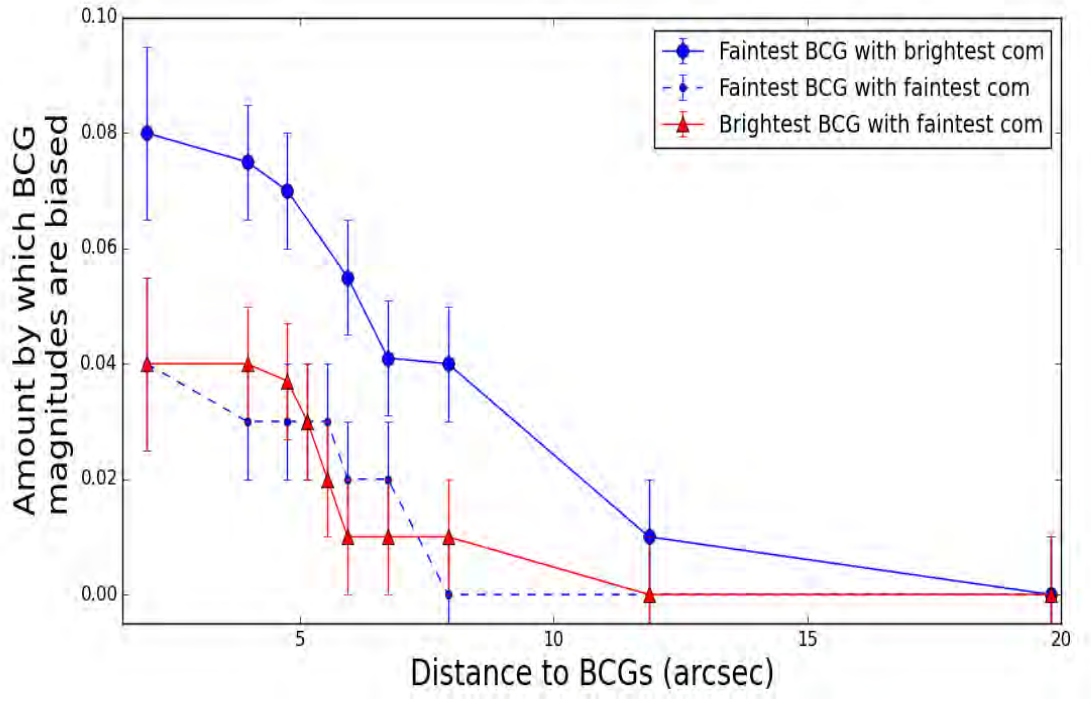

FIGURE 2.16: The expected amounts by which the BCG magnitudes can be biased due to the presence of neighbouring objects (with various magnitudes and distances). The expected contamination in the best (worst) case is indicated with the red (blue) solid line. The blue dashed line show the influence of the faintest companion on the magnitude of the faintest BCG. See text for details.

- `DEBLEND_MINCONT`. For the deblending of objects, this parameter sets the minimum flux ratio that a potential object in an 'island' of connected pixels should have in order for it to be detected as a separate object in `SExtractor` (see Section 2.3.1.2). The default value is 0.005.

We first performed the object detection around the BCGs with the two parameters at their default values. The objects detected by `SExtractor` are circled in magenta in Fig 2.18. Some companions are clearly also missed by `SExtractor` (e.g. cluster 20 in first panel) when the default settings are used.

In order to improve the detection of the obvious, bright objects around the BCGs, we have changed the default values of these two parameters. Fig 2.19 shows the influence that each of these value changes had on the object detection performed by `SExtractor` by taking cluster 18 in Fig 2.17 as an example. We find that if the default value of the `DEBLEND_NTHRESH` parameter is decreased (e.g. to 20 levels), then fewer objects are detected than in the default value case of `SExtractor`

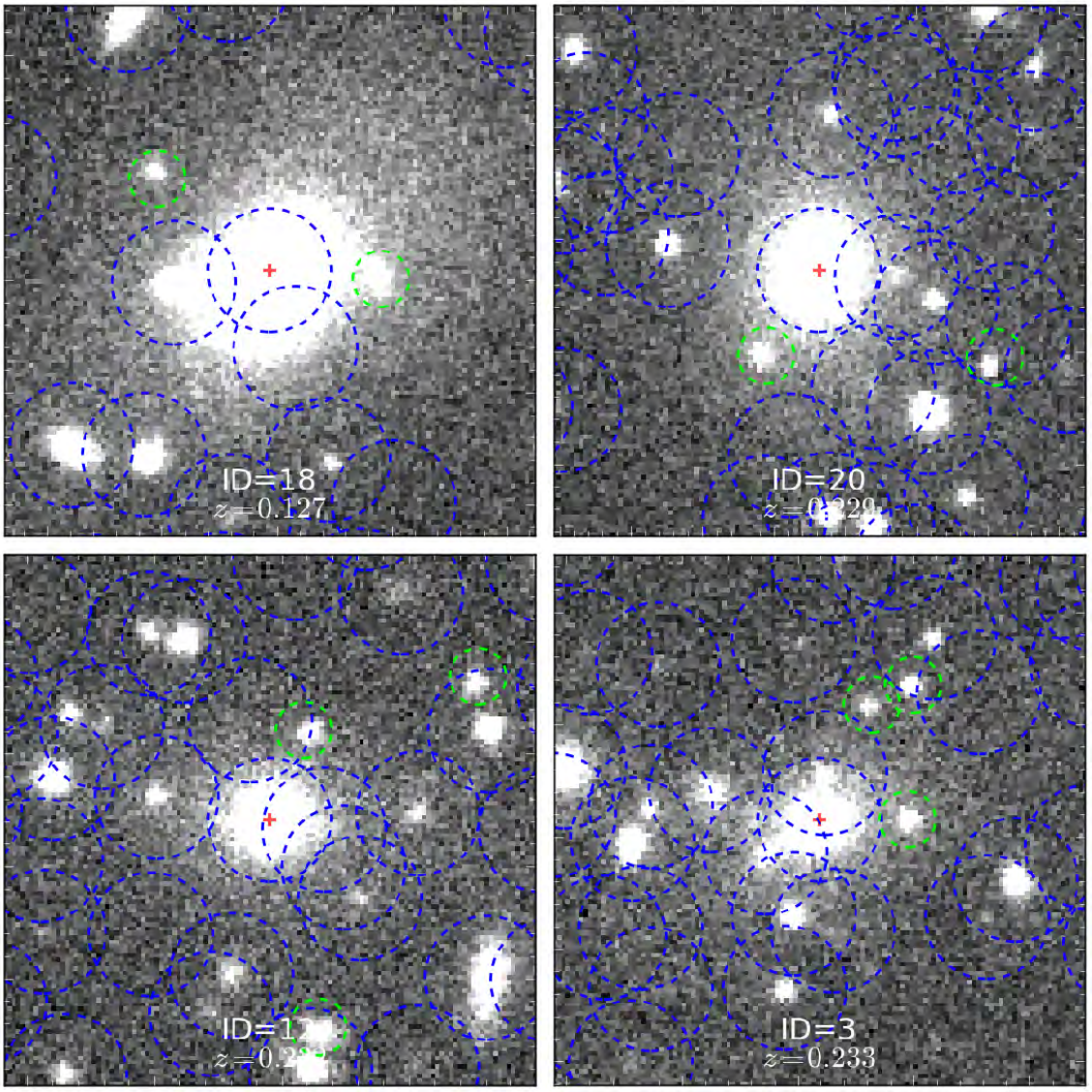

FIGURE 2.17: Four examples of the BCG cutouts where SDSS did not detect obvious bright objects around the BCGs. The BCGs are indicated by the red plus signs. The objects circled in blue are those that have been detected by SDSS while those that have not been found are circled in green. Each image is 48″ on a side, which roughly corresponds to 70 kpc at $z = 0.08$.

(compare panels a and b). The `SExtractor` manual warns the user that it is useless to increase the value of the parameter beyond its default value. We tested this by increasing the parameter value to 60 and found that the same number of objects was detected as in the default value case (result not shown). When we decreased the default value of the `DEBLEND_MINCONT` parameter (e.g. to 0.0001) we found that all the obvious, bright objects, missed by SDSS, around the BCG were detected by `SExtractor` (see panel c). Decreasing the value of this parameter has the overall effect that more objects are detected than in the default value case. Increasing the parameter's value (e.g. to 0.5)

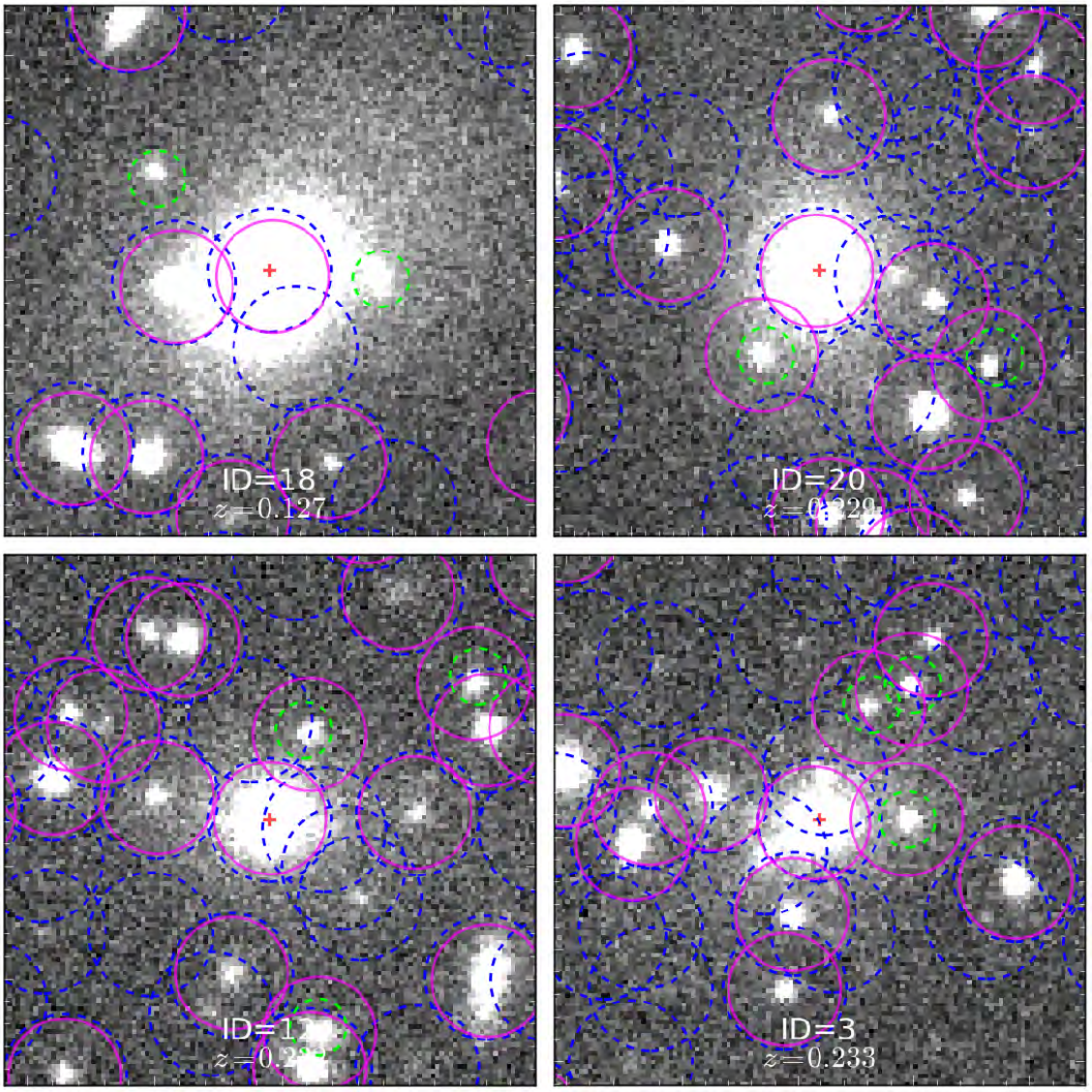

FIGURE 2.18: For the BCGs shown in Fig 2.17, we performed the object detection with `SExtractor`. For this purpose all the parameters in the configuration file have been kept as their default values. Objects detected by `SExtractor` are circled in magenta. Blue and green circles are SDSS detections and non-detections, as in the previous figure. The default settings do not allow all the obvious bright objects (circled in green) to be detected by `SExtractor`.

has the opposite effect, i.e. fewer objects are detected (see panel d).

In the end we optimized `SExtractor` to detect the obvious, bright objects around the BCGs by setting `DEBLEND_NTHRESH` = 32 and `DEBLEND_MINCONT` = 0.0005 in the configuration file. We repeated the object detection for the 11230 clusters in the redMaPPer catalogue at $z \leq 0.35$ using this optimized `SExtractor` configuration. For the BCGs in Fig 2.17, we show the objects detected by `SExtractor`, using the optimized values, in Fig 2.20. With the optimized settings `SExtractor` was

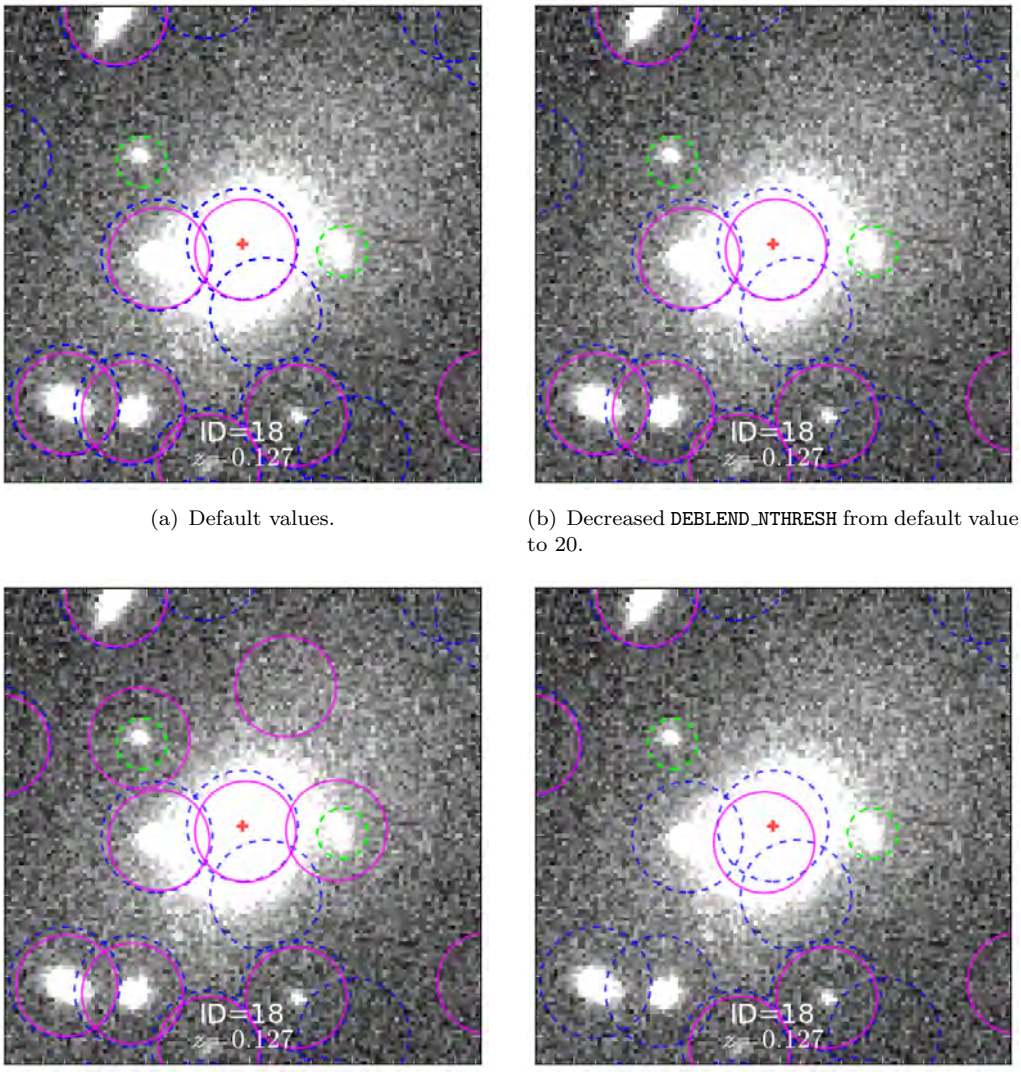

(a) Default values.

(b) Decreased `DEBLEND_NTHRESH` from default value to 20.

(c) Decreased `DEBLEND_MINCONT` from default value to 0.0001.

(d) Increased `DEBLEND_MINCONT` from default value to 0.5.

FIGURE 2.19: Optimizing the detection of obvious, bright objects around BCGs with `SExtractor` by changing the default values of the `DEBLEND_NTHRESH` and `DEBLEND_MINCONT` parameters. Taking cluster 18 as an example, we show the influence each of these value changes has on the object detection. The symbols have the same meaning as in Fig 2.18. See text for detail.

able to detect all the obvious, bright objects around the BCGs, however the software was not able to detect some of the fainter objects that were detected by SDSS. At this stage we are not worried about these faint objects since they are not expected to significantly contaminate the magnitudes of the BCGs.

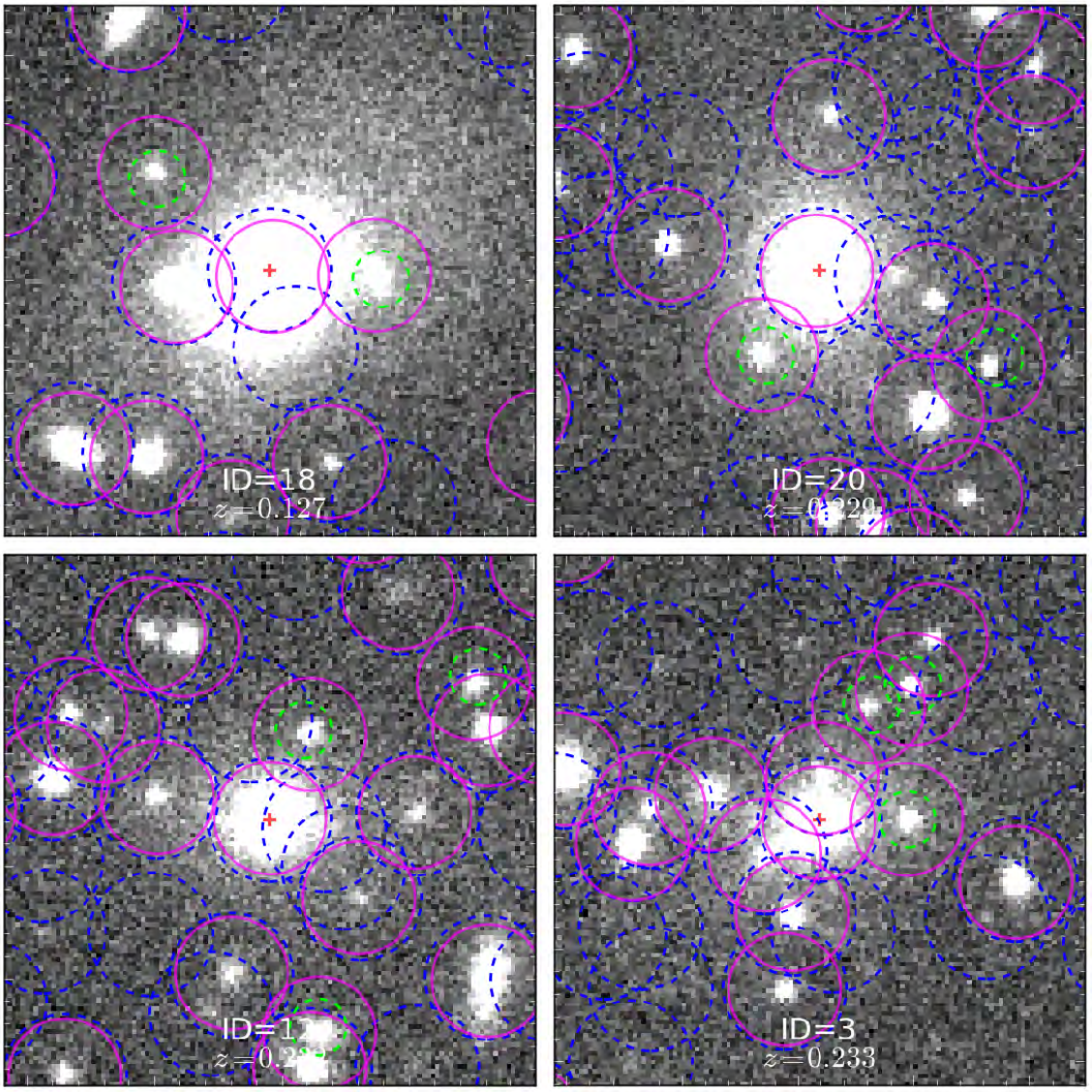

FIGURE 2.20: Same as Fig 2.17, however the optimized parameter values of `SExtractor` have been used to ensure that all the obvious, bright objects around the BCGs are detected. On the other hand the software had some difficulty detecting the fainter objects, which in turn have been detected by SDSS. The meaning of the symbols are the same as in Fig 2.18.

Investigating the effect of bright neighbour contamination on the BCG magnitudes

The fact that SDSS does not detect obvious, bright objects around some of the BCGs, has large repercussions for our project since we are interested in the stellar mass build-up of BCGs. We investigate the mass growth of the BCGs in two different, but complementary parts. In the first part we consider the BCGs themselves and determine how their stellar masses change with redshift (see Chapter 3). The fact that SDSS has missed some bright objects around the BCGs may suggest

that the light of these objects have been incorporated into that of the BCGs, making the BCGs brighter than they should be. This would cause us to overestimate the mass growth of the BCGs since their magnitudes are used to calculate the stellar masses. In the second part we will search for possible close companions around the BCGs (see Chapter 4). The number of potential mergers that the BCGs may experience will be underestimated in the cases where SDSS does not detected the companion objects around the BCGs. We will investigate the influence of these relatively bright objects on the BCG pair fraction in Chapter 4.

It is therefore important to determine how many of the BCGs in our sample suffer from the above-mentioned problem. In Section 2.3.2.1 we used modeled crowded fields to investigated how much close objects, with certain magnitudes and distances, bias the magnitudes of the BCGs. These models suggest that companion galaxies that are (i) within 1.5 magnitudes and (ii) located less than $8''$ from the BCGs will significantly (0.08 mag) bias the magnitudes of the BCGs. Using these criteria we find that $\sim 1\%$ of the BCGs (112/11230) have a nearby companion that is not detected in SDSS. Visual inspection of the SDSS cutouts of these BCGs shows that the bright objects, as detected with `SExtractor`, are indeed real objects. For 88% (99/112) of the cases we find that the bright objects are real detections (four examples are shown in Fig 2.21), constituting an improvement over SDSS. In $\sim 2\%$ (2/112) however we see that there is an additional object, located close to the bright object, that is not detected as a separate object by `SExtractor` (see Fig 2.22(a)). We also find that in 10% of the cases the companions as detected by `SExtractor` are not centered on any visually perceivable objects (see examples in Fig 2.22(b)), despite having a magnitude measured within 1.5 mag of the BCGs. If we are to throw these detections out of our sample, then the fraction of BCGs that suffer from contamination will decrease from $\sim 1\%$ to $\sim 0.8\%$ (99/11230). These spurious detections are likely to have a negligible effect on the average magnitudes (and hence stellar masses) of the full sample.

Consider the 1% of BCGs where `SExtractor` did detect (SDSS-missed) bright objects around them. These bright objects have magnitudes between $15.52 - 20.04$ in the i-band and are $\sim 2 - 8''$ from the BCGs. The companion galaxies used in the modeled crowded fields of Section 2.3.2.1 span this magnitude range and we can therefore use Fig 2.16 to determine the amount with which these companions may bias the BCG magnitudes. In the case where the contamination of the

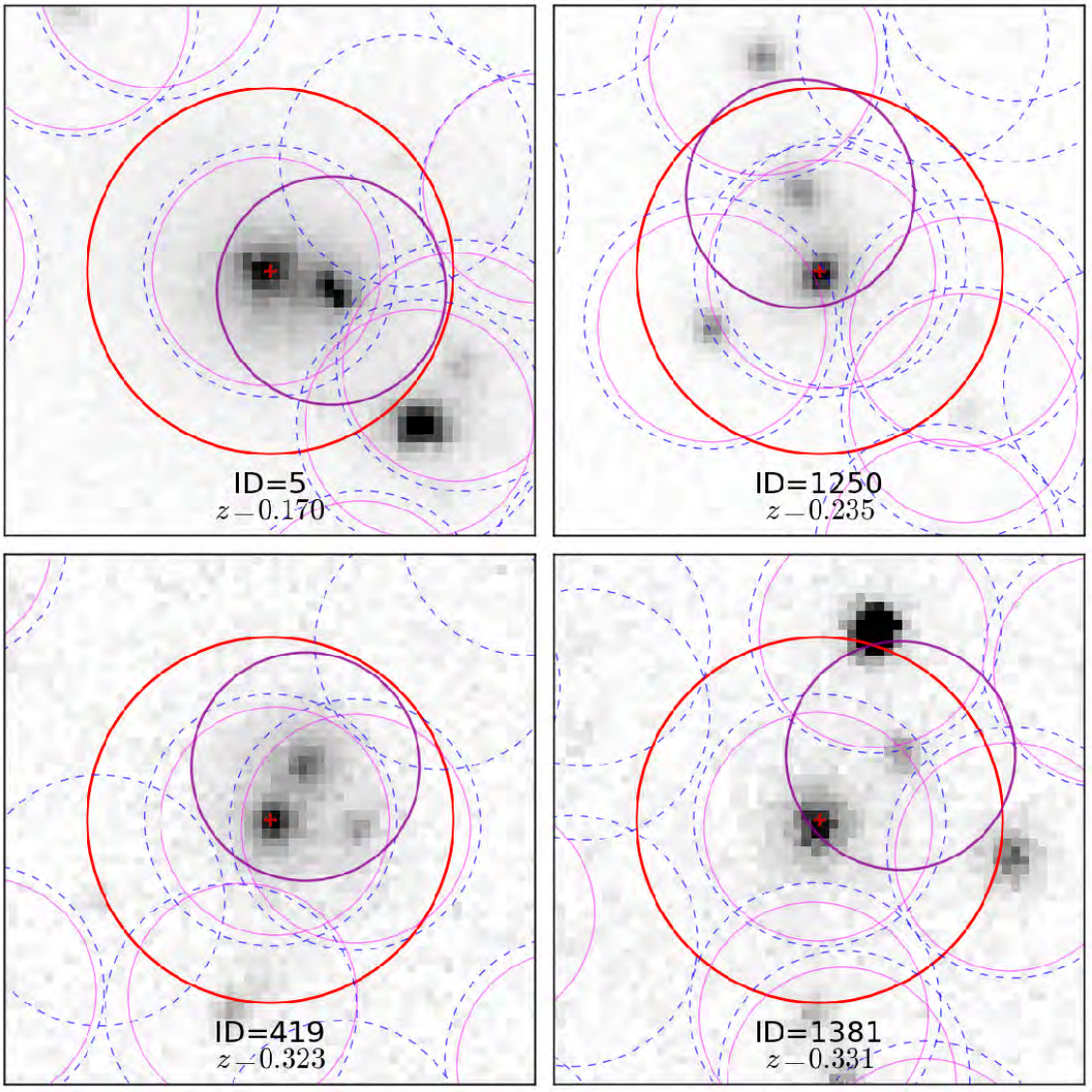

FIGURE 2.21: Four examples of the 112 cases where `SExtractor` detected obvious bright objects around the BCGs. These objects are indicated with the dark purple circles. The red circle shows the radius of 8″ that has been used to search for bright companions (within 1.5 magnitudes of the BCGs) which will affect the BCG magnitudes. As before, blue dashed circles indicate SDSS detections. We circle objects detected by `SExtractor` in pink, highlighting those missed by SDSS in purple.

BCG magnitude is expected to be the worst, i.e. the brightest and closest object, we find that the magnitude of the BCG is only biased by 0.08 mag. The faintest object in turn is expected to bias the BCG magnitudes by 0.04 mag (red line; best case scenario).

Only a very small fraction (1%) of BCGs suffer from contamination. Even if the magnitudes of these BCGs were to be biased by 0.08 mag due to the presence of bright, undetected objects this

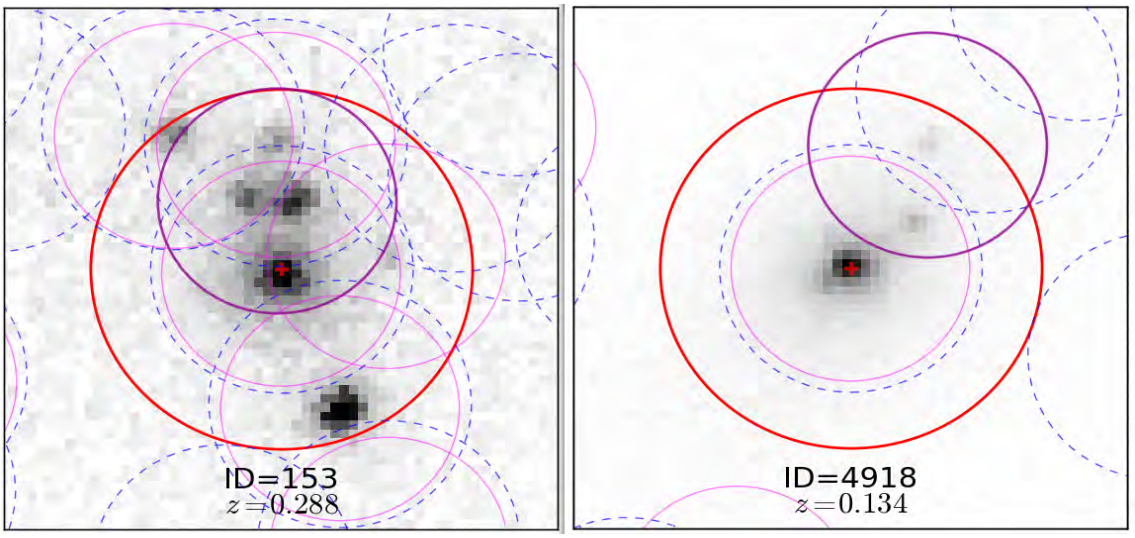

(a) Addition objects, located close to the bright objects, that has not been detected as a separate objects.

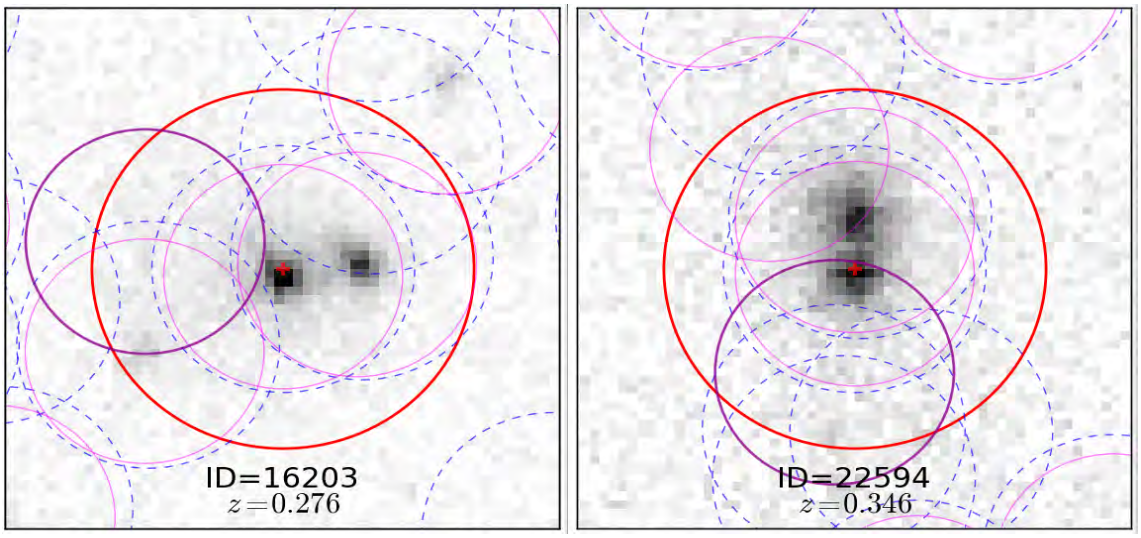

(b) Examples of cases where the bright objects are thought to be spurious detections.

FIGURE 2.22: In the top panel we show the 2% of the cases where additional bright objects have been found close to the bright objects, however they have not been detected separately by `SExtractor`. In the bottom panel we show examples for the cases where the bright objects detected by `SExtractor` seem to be spurious detections. Symbols have the same meaning as in Fig 2.21.

would have a very small effect on the measured average magnitudes (and hence stellar masses) of the sample. Thus, this effect is likely negligible. We will confirm this result in Chapter 3.

Chapter 3

Tracing the total stellar mass build-up of BCGs between $0.08 \leq z \leq 0.35$

> "Lift your eyes up on high and see who has created these stars, the One who leads forth their host by number, He calls them all by name, because of the greatness of His might and the strength of His power, not one of them is missing."
>
> Isaiah 40:26

3.1 Introduction

The stellar mass evolution of BCGs since $z \sim 1$ is currently still debated in the literature. Observational studies have found that these massive galaxies changed their mass by factors that range between 1 (equivalent to no growth; e.g. Aragon-Salamanca et al. 1998; Whiley et al. 2008; Collins et al. 2009; Stott et al. 2010) and 1.4 ± 0.2 (Lin et al. 2013) or 1.8 ± 0.3 (Lidman et al. 2012) since $z \lesssim 1$. Semi-analytical models on the other hand predict that BCGs will change their stellar masses by a factor of $2 - 3$ (e.g. De Lucia & Blaizot 2007; Tonini et al. 2012; Laporte et al. 2013) over a similar redshift range.

One of the main limitations of the samples used to study the mass growth of galaxies, is that these samples are constructed by applying a fixed stellar mass cut across redshift. This approach introduces a bias into the sample selection that we refer to as 'progenitor bias' (although not exactly the same situation, examples are shown by van Dokkum & Franx 1996; 2001; van Dokkum et al. 2000). New galaxies are introduced into the samples at later times (low redshifts) because they increase their stellar masses with time via star formation or mergers. The progenitors of these galaxies will fall out of the samples at high redshift because they are less massive than the fixed stellar mass cut used to construct the samples. On the other hand, the high redshift samples may also include high mass galaxies that have no descendants in the low redshift samples, simply because they are already too massive and the volume probed at low redshift is too small to include these rare objects. Simply stated, this bias will introduce the trend into the data that all the galaxies, regardless of their redshifts, extend down to the 'same' stellar masses. Consequently, if progenitor bias is not corrected for it will cause the stellar mass growth of the BCGs to be underestimated.

With respect to BCG evolution studies however it is important to add that the high-redshift BCGs will be biased towards high stellar masses, not because of a stellar mass limit (as in the case of field galaxies), but rather due to the fact that progenitor bias causes the high-redshift clusters to be biased to high M_h because of the X-ray flux limit. This is because BCG evolution studies, for example Collins et al. (2009); Stott et al. (2010); Lidman et al. (2012), use X-ray selected cluster surveys at high redshift. Because there is a correlation between the stellar masses of BCGs and the halo masses of their host clusters, the BCGs at high redshift will be biased to high stellar masses.

Recent studies (e.g. van Dokkum et al. 2010; Behroozi et al. 2013; Marchesini et al. 2014) have attempted to overcome progenitor bias by tracking galaxies across redshift at a constant comoving number density. This approach assumes that the comoving number density of the most massive galaxies stays constant, allowing one to identify the progenitors of the most massive galaxies in the local Universe at high redshifts. There are, however, limitations to this approach, since the influence of mergers on the measured galaxy properties is ignored. The reason for this is that, by using constant number density, it is implicitly assumed that the rank order of the galaxies (according to their stellar mass) are conserved with redshift, which in turn implies that mergers do not have a strong effect on the rank ordering of the stellar masses of the galaxies (see e.g. Ownsworth et al.

2014). BCGs are thought to increase their mass primarily through mergers (at $z \leq 1$; e.g. De Lucia & Blaizot 2007), so this approach may not be entirely appropriate.

Some observational studies have recently started using simulations to attempt to correct for progenitor bias when the stellar mass evolution of BCGs is studied (see e.g. Lidman et al. 2012; Lin et al. 2013; Oliva-Altamirano et al. 2014). This is done as follows. BCGs are located in clusters and these clusters grow as the Universe ages. The host clusters of the BCGs in an observational sample are selected at high redshift. Within a simulation, dark matter halos (at the same redshift) are selected to have similar halo masses (M_h) as the clusters in the observed sample. The growth of these dark matter halos is then determined down to $z = 0$ by using the simulation. Present day clusters with similar M_h are then identified in the observational sample. Through this approach the progenitors of present day clusters can be identified at high redshift in an observational sample. The average stellar mass growth of the BCGs in this observational sample can then be determined by assuming that the BCGs in these clusters are also progenitors/descendants of one another. We use an approach similar to this in our analysis to account for progenitor bias.

3.2 Method – Deriving the mass growth of the BCGs in the redMaPPer catalogue

For the remainder of this chapter we investigate the stellar mass evolution of BCGs since $z = 0.35$ by using the redMaPPer catalogue. We describe how the stellar masses of the redMaPPer BCGs are determined in Section 3.2.5. The halo masses of the host clusters are determined by using the corrected richnesses of the clusters as a proxy for M_h (see Section 3.2.1). We account for progenitor bias in our analysis by using a method similar to that of Lidman et al. (2012). The results from N-body simulations are used to determine how the M_h of the clusters in the redMaPPer catalogue evolve with redshift (see Section 3.2.3 for more detail). This allows us to construct a sample of clusters that form an evolutionary sequence, since we are able to identify the progenitors/descendants of the clusters at different redshifts (described in Section 3.2.4). We use the assumption that the BCGs in these clusters are progenitors/descendants of one another in order to study the stellar mass build-up of BCGs and determine the impact of progenitor bias.

We proceed to divide the BCGs into various redshift bins whereafter the average stellar mass, denoted $\langle M_\star \rangle$, of the BCGs in each bin is determined (see Section 3.2.6.1). We also describe how bootstrap resampling is used to determine the uncertainty on $\langle M_\star \rangle$. The stellar mass growth of the BCGs is then determined by comparing the $\langle M_\star \rangle$ of the BCGs in the lowest redshift bin to that in the highest bin and by fitting the evolution of $\langle M_\star \rangle$ as described in Section 3.2.6.2.

3.2.1 Deriving the halo masses of the redMaPPer clusters

Throughout the thesis we use the richnesses of the clusters as a proxy for their M_h. In order to avoid underestimating the halo masses of the clusters it is important to correct the clusters' richness estimates for the galaxies missed due to the depth of the survey. The richnesses are corrected using $\lambda/S(z)$, where $S(z)$ is a scale factor used to correct the richness estimates for the survey depth (hereafter the corrected richnesses, see Section 2.2.2.1). However, as noted in Section 2.2.2.1, restricting the sample to $z \leq 0.35$ means that this correction is small (~ 1).

The halo mass-richness relation of Rykoff et al. (2012) is used to determine the M_h of the redMaPPer clusters at their observed redshifts:

$$\ln\left(\frac{M_{200}}{10^{14}\,\mathrm{M}_\odot}\right) = 1.72 + 1.08\ln(\lambda/60) \tag{3.1}$$

where M_{200} is the mass of the cluster at its virial radius (r_{200})[1] and λ is the corrected richness of the cluster. The resulting M_h distribution of the redMaPPer clusters is shown in Fig 3.1. The clusters span a halo mass range of $\sim (0.17 - 2.20) \times 10^{15}\,\mathrm{M}_\odot$.

3.2.2 The M_h completeness of the redMaPPer catalogue

During the construction of the evolutionary sequence of the redMaPPer clusters, we have to take into account the completeness (in terms of richness) of the catalogue. The redMaPPer algorithm has determined this completeness for five redshift slices (see figure 22 of R14). The richness completeness of the redMaPPer clusters is not the same for the redshift range $0.08 \leq z \leq 0.55$ as the

[1] Assume that a cluster can be approximated by a sphere. r_{200} is the radius at which the average density inside the sphere is ~ 200 times that of the Universe's critical density at that redshift.

catalogue becomes incomplete for low mass (low richness) clusters towards higher redshifts. This will ultimately influence the M_h range of the redMaPPer clusters from which we can investigate the $M_\star$ evolution of the BCGs. Briefly, (see R14 for more details) the algorithm used the full original cluster catalogue and randomly sampled the galaxy clusters to generate a model cluster distribution that had the same richness and redshift distributions as the original catalogue. These model clusters were then randomly distributed throughout the 10 000 deg^2 of sky that is used by the redMaPPer catalogue. The algorithm was then re-run and used to determine how many of the original clusters were detected as function of richness and redshift.

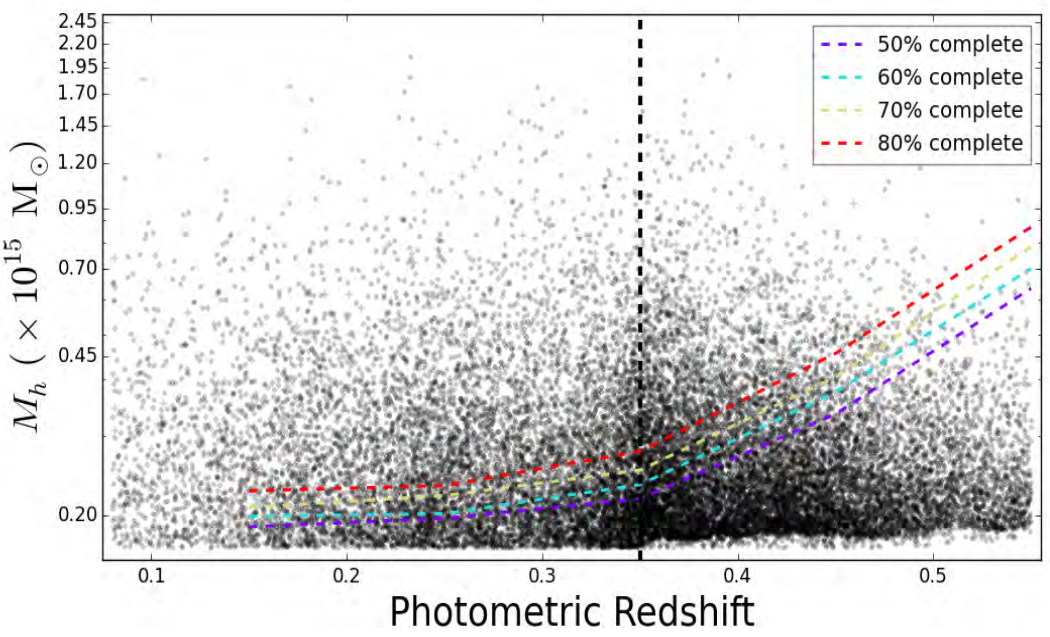

FIGURE 3.1: Completeness of the redMaPPer catalogue as a function of M_h and redshift. The dashed lines indicate the best fit to the mean of the five redshift bins used by the redMaPPer algorithm to determine the completeness (see their figure 22). At low redshifts the catalogue is complete down to clusters with $M_h \sim 0.2 \times 10^{15}\,\mathrm{M}_\odot$. At $z > 0.35$ (black dashed line) however the algorithm is only able to detect the most massive clusters due to the magnitude limit of the survey and is therefore incomplete for low mass clusters.

We illustrate the measured completeness of the redMaPPer catalogue as a function of M_h in Fig 3.1. The dashed lines in Fig 3.1 represent the best fit through the mean redshift of each of the five redshift bins used by the redMaPPer algorithm to determine the completeness of the catalogue as a function of richness (values have been taken from figure 22 of R14). At $z \lesssim 0.35$ (black dashed line) the catalogue is 50% complete for clusters with $M_h \gtrsim 0.2 \times 10^{15}\,\mathrm{M}_\odot$. At $z > 0.35$ the magnitude limit of the survey becomes a problem and due to this the algorithm is only able to

detect the brightest galaxies at high redshifts. Since fainter galaxies are missed by the algorithm, the catalogue is incomplete for low mass clusters at these high redshifts.

Assume for a moment that we ignore the M_h completeness of the redMaPPer catalogue. If we were to use the catalogue *as is* to study the stellar mass build-up of the BCGs, we would underestimate the mass growth of these massive galaxies. This is due to the fact that the high-z clusters in redMaPPer are more massive than their lower$-z$ counterparts. The $M_\star - M_h$ relation shows that more massive BCGs are located in more massive clusters (Edge 1991; Burke et al. 2000; Brough et al. 2008; Whiley et al. 2008; Stott et al. 2012), and therefore the redMaPPer BCGs at high redshifts are more massive than those at lower redshifts. In order not to underestimate the stellar mass growth of the BCGs, it is important to take the M_h completeness of the redMaPPer catalogue into account as we will show in Section 3.3. As we have described in Section 2.2.2, we use the volume limited sample ($z \leq 0.35$) of the redMaPPer catalogue for the remainder of the thesis.

3.2.3 The halo mass growth of the redMaPPer clusters

Within the hierarchical formation scenario, large-scale structures (such as clusters and groups) are assembled through the accretion of smaller sub-structures. Numerous studies, e.g. Fakhouri et al. (2010) have used N-body simulations to investigate how the mass of dark matter halos changes due to the accretion of smaller halos. We use the mean mass accretion rates (MMARs, given by Eq 3.2) of Fakhouri et al. (2010) to determine what the halo mass of a redMaPPer cluster will be at any redshift. This step is vital in order to construct the evolutionary sequence of redMaPPer clusters across redshift.

Fakhouri et al. (2010) used the Millennium (Springel et al. 2005) and Millennium-II (Boylan-Kolchin et al. 2009) simulations to determine how dark matter halos with $10^{10} \lesssim M_h \lesssim 10^{15}$ evolve over a redshift range of $0 \leq z \leq 15$. The merger history of a simulated halo (at $z = 0$) is used to identify the most massive progenitor of the halo at an earlier 'snapshot'. This process is repeated backwards in time to construct the main branch of the halo's merger tree. The mass evolution of a given dark matter halo can then be studied since the mass accretion history of the halo can be traced back in time through the main branch.

They used this approach to determine the mean value of the mass accretion rates ($\dot{M}_h$) as a function of z for a set of dark matter halos that span a wide range of halo masses. They found that the mass evolution of a halo with mass M_h at redshift z can be described by the following:

$$\langle \dot{M}_h \rangle_{\rm mean} = 46.1\,{\rm M}_\odot {\rm yr}^{-1} \left(\frac{M_h}{10^{12}\,{\rm M}_\odot} \right)^{1.1} \times (1 + 1.11z)\sqrt{\Omega_m(1+z)^3 + \Omega_\Lambda} \tag{3.2}$$

3.2.4 Constructing an evolutionary sequence of redMaPPer clusters

We divide the clusters/BCGs into four equal sized redshift bins with a width of 0.067. The bin width is chosen as such for two reasons: firstly, it is larger than the typical uncertainty on the z_{phot} of the clusters (~ 0.02) which reduces the chances that clusters will be scattered in and out of adjacent redshift bins. Secondly, it is small enough to ensure we have multiple bins, each with a robust number of clusters, so that the BCG mass evolution can be studied. The bin width was varied between 0.06 and 0.09 with steps of 0.01 but found that it has no influence on the measured stellar mass evolution of the BCGs.

We construct an evolutionary sequence for the redMaPPer clusters at $z = 0.35$ by identifying their low-z descendants. We evolve these high-z clusters forward in time by using the Fakhouri et al. (2010). MMARs (given by Eq 3.2) and determine what their corresponding M_h will be at different redshifts. The descendants of these high-z redMaPPer clusters are identified as follows:

1. Choose the upper M_h limit of the clusters in the lowest redshift bin ($z = 0.08$). This limit is set by the M_h that the clusters in the highest redshift bin ($z = 0.35$) will have at $z = 0.08$.

2. Find the corresponding M_h limit in the highest redshift bin ($z = 0.35$) given the accretion rates from Fakhouri et al. (2010) All clusters above this limit are excluded since their descendants will be more massive than the clusters included in our sample in the lowest redshift bin.

3. Determine the lower M_h limit of the clusters in the highest redshift bin ($z = 0.35$).

4. Find the corresponding M_h limit in the lowest redshift bin ($z = 0.08$). All clusters below this limit are excluded from the analysis as these clusters will not have any progenitors in the highest redshift bin.

For the evolutionary sequence construction of the clusters in the redMaPPer catalogue, we only consider clusters above the 50% M_h completeness limit. This is done to maximize the number of clusters in the evolutionary sequence. We have tested whether the measured mass growth of the BCGs is sensitive to our choice of M_h completeness ($60\% - 80\%$) and found that it is not.

Various studies, for example Lidman et al. (2012); Lin et al. (2013); Oliva-Altamirano et al. (2014) have constructed an evolutionary sequence for the clusters in their samples by only applying a lower M_h cut. This approach inevitably includes high-z clusters that are already too massive to have any low-z descendants within the same samples. That said, we want to test whether or not this will influence the derived mass growth of the BCGs. More specifically, if an *upper* M_h limit is applied during the evolutionary sequence construction, will it influence the BCG mass growth derived when no upper M_h limit is applied? We test this by using the method outlined above to construct an evolutionary sequence of clusters with an applied upper M_h limit. We repeat the method to construct an evolutionary sequence of clusters with no upper M_h limit imposed. The clusters in the two evolutionary sequences are represented by the blue points in Fig 3.2. For each evolutionary sequence, we present a summary of the selected clusters in Table 3.1. A total of 5432 clusters form part of the evolutionary sequence where no upper M_h limit was imposed. This number decreased to 4543 when an upper M_h limit was imposed.

TABLE 3.1: Summary of the clusters that form part of the evolutionary sequence of the redMaPPer clusters. These clusters have been identified using the MMARs of Fakhouri et al. (2010). For each redshift bin the number of clusters are stated along with their corresponding M_h range.

No upper M_h limit			**With upper M_h limit**		
z	M_h **range** ($\times 10^{15}\,\mathrm{M}_\odot$)	N_{clus}	z	M_h **range** ($\times 10^{15}\,\mathrm{M}_\odot$)	N_{clus}
$0.08 - 0.15$	> 0.29	329	$0.08 - 0.15$	$0.29 - 0.73$	303
$0.15 - 0.21$	> 0.26	789	$0.15 - 0.21$	$0.26 - 0.63$	730
$0.21 - 0.28$	> 0.24	1572	$0.21 - 0.28$	$0.24 - 0.53$	1361
$0.28 - 0.35$	> 0.22	2742	$0.28 - 0.35$	$0.22 - 0.42$	2149
		Total = 5432			Total = 4543

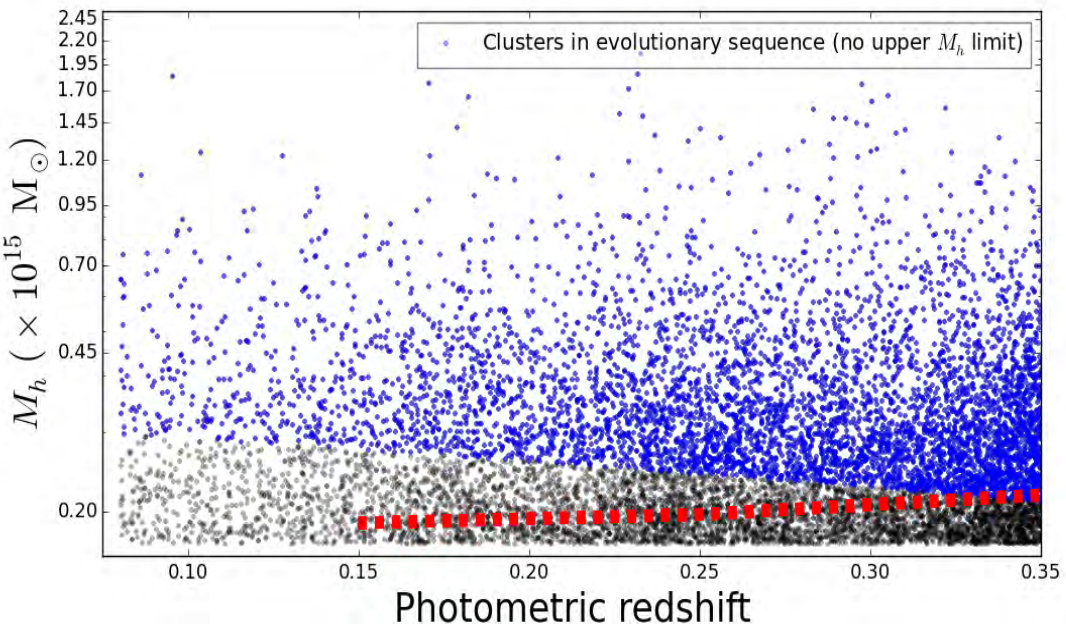

(a) No upper M_h limit is imposed.

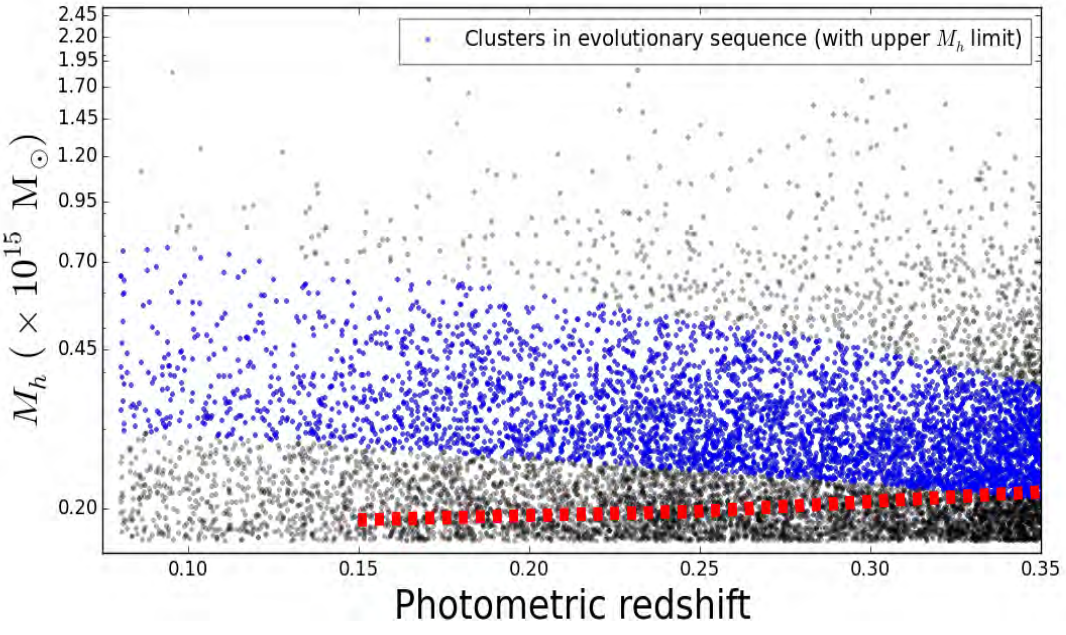

(b) Upper M_h limit is imposed.

FIGURE 3.2: The evolutionary sequence of redMaPPer clusters at $z \leq 0.35$ when no upper M_h limit is imposed (top panel) and when an upper M_h limit is imposed (bottom panel). In each panel the red dashed line indicates the 50% M_h completeness limit while the blue points represent the clusters that are included in the evolutionary sequences.

3.2.5 Deriving stellar masses for the redMaPPer galaxies

The redMaPPer catalogue does not supply any stellar mass estimates for the galaxies. Since we are interested in the stellar mass build-up of BCGs, we first have to derive them for these massive galaxies. For this purpose we use the `kcorrect` code[2] (Blanton & Roweis 2007).

We refer the reader to Blanton & Roweis (2007) for a detailed description of how the software determines the estimates for the stellar masses of galaxies. In short, SED fitting is used to derive the $M_\star$ of the galaxies by fitting their observed `Model_Mag` magnitudes (in the u, g, r, i and z-bands) against a range of spectral templates from Bruzual & Charlot (2003) while the Chabrier (2003) initial mass function (IMF) is assumed. The best-fitting stellar template is determined through χ^2- minimization, whereafter a mass-to-light ratio is determined from this template and used to convert the luminosity of the galaxy to stellar mass.

The resulting stellar masses of the redMaPPer galaxies are hereafter referred to as the `kcorrect` stellar masses. In order to verify that we ran the `kcorrect` code correctly, we compare the `kcorrect` stellar masses of the redMaPPer galaxies against those given in the MPA-JHU value-added galaxy catalogue[3,4] (Brinchmann et al. 2004). The MPA-JHU catalogue contains stellar mass estimates for $\sim$ 930 000 galaxies in SDSS derived using the `kcorrect` code. We use the stellar masses derived using the `Model_Mag` magnitudes and we refer to these hereafter as the MPA-JHU stellar masses.

The following had to be taken into account before the stellar mass comparison could be made:

(i) The MPA-JHU catalogue only contains galaxies with spectroscopic information. The spectroscopic redshifts (z_{spec}) of the galaxies were therefore used by the `kcorrect` code to determine their stellar masses. For the redMaPPer galaxies on the other hand we use the photometric redshift (z_{phot}) of the cluster as the estimate of the redshift of each galaxy, since z_{spec} are not available.

(ii) The MPA-JHU catalogue has used DR7 photometry to determine the $M_\star$ with the `kcorrect` code. The masses of the galaxies in the redMaPPer catalogue however have been determined

[2] http://howdy.physics.nyu.edu/index.php/Kcorrect
[3] Max-Planck Institute for Astronomy and Johns Hopkins University; http://www.mpa-garching.mpg.de/SDSS/
[4] Updates are also available at http://home.strw.leidenuniv.nl/∼jarle/SDSS/

using DR8 photometry. As described in Section 2.1 the differences in the algorithms used may change the magnitudes somewhat.

We make a uniform choice to use the z_{phot} of the cluster in determining the masses of all galaxies (both BCGs and other cluster members) because z_{spec} are not always available. In this comparison we use galaxies with z_{spec} within 0.01 of z_{phot}. This ensures that the `kcorrect` stellar masses of the redMaPPer BCGs, determined using z_{spec} and z_{phot}, are comparable. We can therefore compare the `kcorrect` stellar masses of the BCGs (derived using z_{phot}) against their corresponding MPA-JHU stellar masses (derived using z_{spec}). We further require that the BCGs' i-band magnitudes, given in the redMaPPer and MPA-JHU catalogues, are within 0.01 of one another. This in turn allows us to compare the `kcorrect` stellar masses of the BCGs (derived using DR8 photometry) against their corresponding MPA-JHU stellar masses (derived using DR7 photometry).

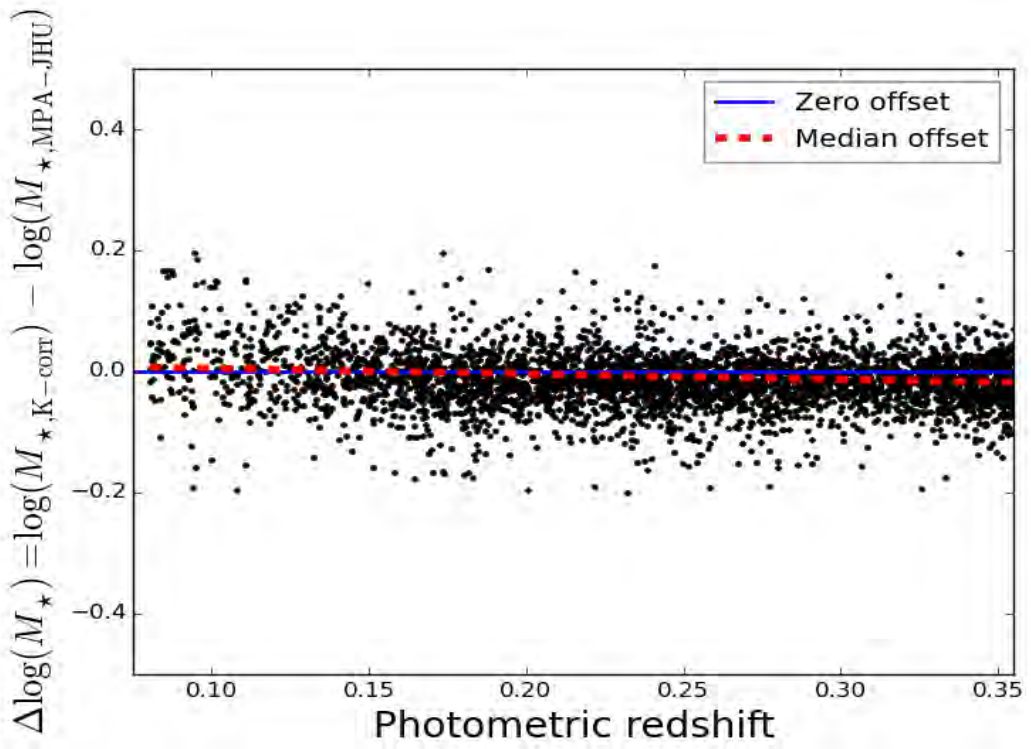

FIGURE 3.3: For a subsample of 10 237 BCGs, we compare the `kcorrect` and MPA-JHU stellar mass estimates. A stellar mass offset of $\sim$ 1% is observed between the two catalogues at high redshift. This offset is considered negligible as it is smaller than the scatter in the data, indicating that we ran the `kcorrect` code correctly.

Using the criteria above we construct a subsample of $\sim$10 000 BCGs from the redMaPPer catalogue and compare their `kcorrect` stellar masses with their corresponding MPA-JHU stellar masses

(see Fig 3.3). There is a slight trend observable in the median mass offset (red dashed line) with redshift. At low redshift ($z \sim 0.1$) no offset in stellar mass is detected, while the stellar masses differ by $\sim 1\%$ at high redshift ($z \sim 0.3$). This offset is small compared to the scatter ($\sigma = 0.09$) and is therefore considered negligible with redshift. This indicates that we ran the `kcorrect` code correctly.

3.2.6 Defining the mass growth factor

We now continue on to the main aim of this chapter, measuring the mass growth of the BCGs as a function of redshift. In order to do this we first need to calculate the average stellar masses of the BCGs in the redshift bins along with their associated uncertainties (Section 3.2.6.1). We describe the techniques used to measure the mass growth of the BCGs in Section 3.2.6.2. The simplest way is to take the ratio of the average BCG masses over some period of interest. We compare this simple method to the results obtained from fitting the evolving masses as a function of redshift.

3.2.6.1 Calculating the average stellar masses of the BCGs and their associated uncertainties

The average stellar mass of the BCGs, denoted $\langle M_\star \rangle$, in the i-th redshift bin are given by:

$$\langle M_\star \rangle_i \; = \; \frac{\sum_{j=1}^{\mathrm{N_{BCGs}}} (M_\star)_j}{\mathrm{N_{BCGs}}} \quad \text{with} \;\; 0.08 \leq z_i \leq 0.35 \tag{3.3}$$

where $(M_\star)_j$ is the stellar mass of the j-th BCG and $\mathrm{N_{BCGs}}$ is the number of BCGs in the i-th redshift bin.

Let $\sigma_{M_\star}$ represent the uncertainty on $\langle M_\star \rangle$, which is determined through bootstrap resampling with 1000 realizations. For each realization, a new sample of BCGs is created that has the exact same number of BCGs as the original BCG sample in redshift z_i. The new sample of BCGs is created by randomly selecting BCGs from the original sample. Any given BCG can be selected more than once. We then determine $\langle M_\star \rangle$ of the BCGs for each realization. Thereafter we determine $\langle M_\star \rangle$ of

the BCGs in z_i by averaging the results from these 1000 realizations and the standard deviation is taken as the estimate of the uncertainty.

3.2.6.2 Calculating the mass growth factor

The simplest way to estimate the stellar mass growth factor (MGF) of BCGs between two redshift bins is as follows:

$$\mathrm{MGF} = \frac{\langle M_\star \rangle (z_1)}{\langle M_\star \rangle (z_2)} \quad \text{with } z_1 < z_2 \tag{3.4}$$

where $\langle M_\star \rangle$ denotes the average stellar mass of the BCGs at redshifts z_1 and z_2. The uncertainty on the MGF is determined through the standard propagation of errors.

$$\sigma_{\mathrm{MGF}} = \mathrm{MGF} \times \sqrt{A^2 + B^2 + E} \tag{3.5}$$

$$\text{with } A = \frac{\sigma_{M_\star}(z_1)}{\langle M_\star \rangle (z_1)},\ B = \frac{\sigma_{M_\star}(z_2)}{\langle M_\star \rangle (z_2)},\ E = -2\frac{\sigma_{M_\star}(z_1 z_2)}{\langle M_\star \rangle (z_1)\langle M_\star \rangle (z_2)}$$

where $\sigma_{M_\star}$ is the uncertainty on the average stellar mass of the BCGs at redshifts z_1 and z_2. The E-term is set to zero since the BCGs' average stellar masses in the two redshift bins are independent of each other.

This simple method is commonly used in the literature to derive the mass growth of BCGs over a redshift range of interest. The disadvantage to this, however, is that only the first and last redshift bins are considered and consequently not all the available information is used (see e.g. Lidman et al. 2012; Lin et al. 2013). To improve on this method we use all the available redshift information and fit straight lines to the evolving BCG stellar masses as a function of redshift and then determine the MGF (hereafter referred to as $\mathrm{MGF_{fit}}$). The method we followed is described below.

We fit two models to the $\langle M_\star \rangle$ of the BCGs (and their uncertainties) and compare them using the log-likelihood ratio (LLR) test. The first model we consider is simply a best-fit straight line to the data (hereafter alternative model). The second model assumes no mass growth, fixing the slope to zero (hereafter null model). We use the chi-square (χ^2) goodness of fit test to investigate whether the observed $\langle M_\star \rangle$ evolution of the BCGs, is consistent with the values expected from each model.

The test statistic, χ^2 is expressed as:

$$\chi^2 = \sum_{i=1}^{4} \frac{(\langle M_\star \rangle_{i,\mathrm{obs}} - \langle M_\star \rangle_{i,\mathrm{exp}})^2}{\sigma^2_{i,\mathrm{obs}}} \tag{3.6}$$

where $\langle M_\star \rangle_{i,\mathrm{obs}}$ is the average stellar mass of the BCGs in the i-th redshift bin (as determined from the redMaPPer catalogue). The associated uncertainty on this value is given by $\sigma_{i,\mathrm{obs}}$. Similarly $\langle M_\star \rangle_{i,\mathrm{exp}}$ denotes the expected average stellar masses of the BCGs, as derived from each model. The closer the χ^2-value of a model is to 1 per degree of freedom (dof), the better the model fits the data.

The LLR test compares the goodness of fit of two models. This test is used in cases where one of the models (the null model) is a special case of the other. The two competing models are fitted separately to the data, whereafter the likelihood of each fit is determined. The LLR test statistic (denoted by D) is given by the following:

$$D = -2 \times \log\left(\frac{\text{likelihood of null model}}{\text{likelihood of alternative model}}\right) \tag{3.7}$$

If it is assumed that the test statistic has an χ^2-distribution, then the likelihood ratio can be compared against a critical value to decide whether the null model is accepted or rejected (in favour of the alternative model).

We use the `scipy.stats.chi2.cdf`[5] routine in `Python`[6] to determine the likelihoods of the two models. This routine requires the χ^2-value (see Eq 3.6) and dof of each model fitted to the data. The alternative model has two free parameters and therefore has two dof. Similarly, the null model has only one dof since it only has one free parameter. To determine which model best fit the observed data, we compare D against $\chi^2_{\mathrm{crit}} = 3.84$, which is the critical χ^2-value with $2 - 1 = 1$ dof at the 95% significance level. The null model is rejected when D is larger than χ^2_{crit}.

[5] http://docs.scipy.org/doc/scipy/reference/generated/scipy.stats.chi2.html
[6] https://www.python.org/

3.3 Results – BCG mass growth from $z = 0.35 - 0.08$

In this section we investigate the stellar mass evolution of the BCGs over $0.08 \leq z \leq 0.35$. In order to fairly compare the stellar masses of these BCGs with one another, we constructed an evolutionary sequence of clusters and assumed that the BCGs in these clusters are progenitors/descendants of one another. We show the stellar mass evolution of the BCGs, with and without progenitor bias taken into account, in Fig 3.4. We derive the mass growth factor for the BCGs in each case using both the methods described above and present a summary of these results in Table 3.2.

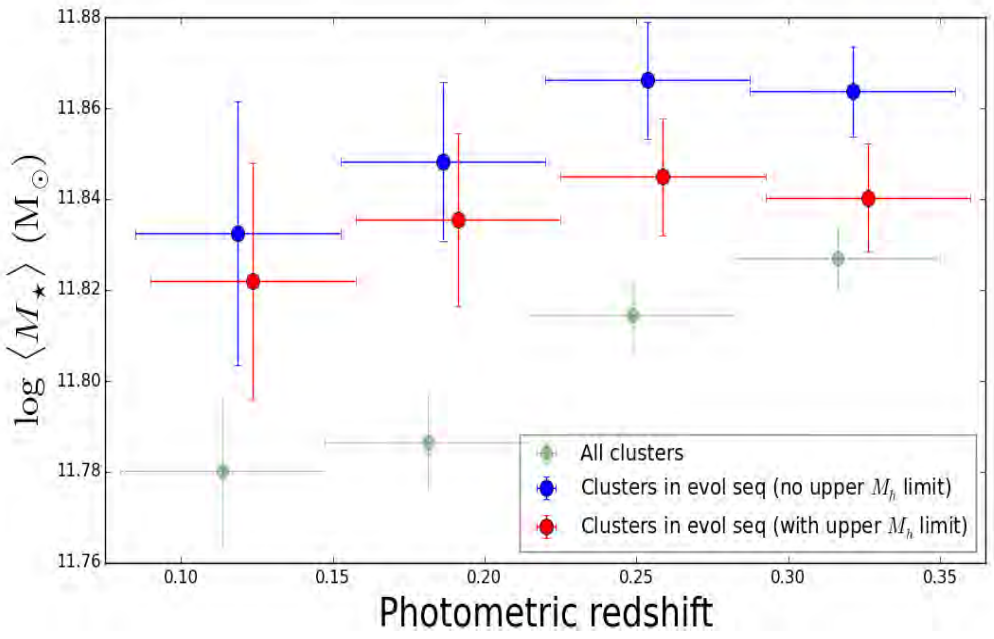

FIGURE 3.4: The stellar mass evolution of the BCGs over $0.08 \leq z \leq 0.35$. The horizontal uncertainties indicate the width of the redshift bins. The blue and red points have been offset in redshift for clarity. See text for details.

TABLE 3.2: MGFs for the BCGs in the following cases: (i) all clusters (regardless of completeness) and (ii) clusters that form part of the two evolutionary sequences. We also indicate the cases where progenitor bias has been corrected for.

	MGF			**Corrected for progenitor bias?**
	Method 1 - Ratio of lowest to highest redshift:			
All	0.89 ± 0.01			No
Only apply lower M_h limit	0.94 ± 0.02			Yes
Apply both upper and lower M_h limit	0.97 ± 0.03			Yes
	Method 2 - Line fitting:			
	Alternative model	*Null model*	D (Eq 3.7)	
All	0.88 ± 0.01 ($\chi^2 = 0.76$)	1.0 ($\chi^2 = 15.02$)	14.26	No
Only apply lower M_h limit	0.94 ± 0.02 ($\chi^2 = 1.77$)	1.0 ($\chi^2 = 0.55$)	1.22	Yes
Apply both upper and lower M_h limit	0.98 ± 0.03 ($\chi^2 = 0.37$)	1.0 ($\chi^2 = 0.70$)	0.32	Yes

We find at the 95% confidence level that the zero-slope line (where no mass growth is assumed) is favoured over the line with a non-zero slope. This results in $\mathrm{MGF_{fit}} = 0.98 \pm 0.03$ (also see Fig 3.5). The simple method also gives a value consistent with one ($\mathrm{MGF} = 0.97 \pm 0.03$).

3.4 Discussion

Our results imply that is important to take the M_h growth of the clusters into account when the BCG stellar mass evolution is investigated, i.e. consider the BCGs that form part of the evolutionary sequences. This is our preferred method with which we determine the stellar mass growth of the BCGs.

We continue to show what happens in the case where we do not take the evolution of the clusters' halo masses into account, i.e. consider *all* BCGs. Both of the methods indicate that a non-zero

slope is favoured (MGF $= 0.89 \pm 0.01$ and $\mathrm{MGF_{fit}} = 0.88 \pm 0.01$). However, both these slopes suggest negative growth (i.e. shrinking), which is a non-physical result. This highlights what we have already shown, i.e. that it is important to take the growth of the clusters' M_h into account when the stellar mass evolution of BCGs is investigated. It is of interest to explore the physical reasons behind the observed negative growth. One reason may be related to the different volumes probed across our redshift range of interest, where the volume at $z = 0.08$ is smaller than that probed at $z = 0.35$. As a results we have fewer high mass clusters in our sample at low redshift (in comparison to higher redshift). Because the stellar mass of the BCG is known to correlate with the halo mass of its host cluster, it is not surprising that the high redshift BCGs have higher stellar mass estimates compared to their low redshift counterparts.

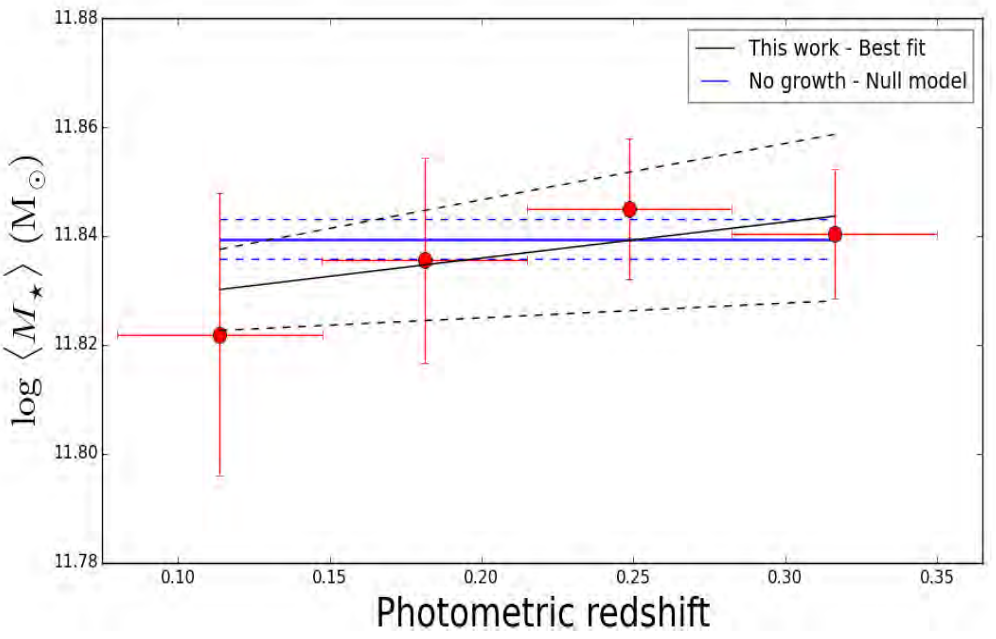

FIGURE 3.5: Taking progenitor bias into account, we find the ratio of BCG masses in the first and last redshift bins is MGF $= 0.97 \pm 0.03$, consistent with no growth. To test what influence using all the available information as a function of redshift have on our claim of no growth, we use least-square fitting to find the best-fitting straight line to the data (solid black line). We also fit a straight line assuming no mass growth for the BCGs (blue line) and compare the two models. The zero-slope line is preferred at the 95% confidence level. See text for details.

Consider the average stellar mass evolution if all BCGs, regardless of M_h completeness, are considered (green points in Fig 3.4). In this case progenitor bias is not taken into account and the sample therefore contains clusters at low redshift that do not have any high-z progenitors. Now consider the mass growth of the BCGs in the case where progenitor bias has been taken into account (i.e. BCGs

in the two evolutionary sequences shown in Fig 3.2). The BCGs in the evolutionary sequence constructed without an upper M_h limit (blue points) are, on average, more massive than those in the sequence where an upper M_h limit is also applied (red points). This is because the upper M_h limit excludes some of the high mass clusters that are otherwise included in the first evolutionary sequence where no upper M_h limit is applied.

We compare the mass growth of the BCGs in the following two cases: when (i) all clusters are considered regardless of completeness (green points in Fig 3.4) and (ii) only the clusters in the evolutionary sequence, constructed with a lower M_h limit (blue points) are included. The BCGs in the evolutionary sequence are, on average, more massive, at any given redshift, because we exclude clusters that are less massive than the descendants of the high-z clusters. This causes the average M_h of the clusters in the evolutionary sequence to be larger than if all clusters are considered. Taking the $M_\star - M_h$ relation into account, it is not surprising that the BCGs in the evolutionary sequence are, on average, more massive than if all BCGs are considered. This trend is also observed if all BCGs are compared to those in the evolutionary sequence constructed by also applying an upper M_h limit (compare green and red points). If progenitor bias is not taken into account the mass growth of these massive galaxies will be underestimated.

For all three cases shown in Fig 3.4, we observe a reduction in the BCGs' stellar masses towards lower redshifts. This has also been observed by other works in the literature, e.g. Lidman et al. (2012); Oliva-Altamirano et al. (2014), and although we consider a reduction in mass to be unphysical, perhaps mass loss mechanisms such as stripping need to be explored in future work. Another possible reason for this observed reduction in mass may be related to whether or not the `kcorrect` code took stellar remnants (e.g. white dwarfs, black holes and neutron stars) into consideration when the stellar masses of the BCGs have been determined. This is important to consider because the $M_\star$ of a stellar population evolves with time. As the stellar population ages and stars go supernova etc, this will reduce the luminosity (and the stellar mass) of the stellar population. We test this idea by investigating how much the $M_\star$ of a BCG may change, over the ~ 3 Gyr time period spanned by our redshift range of interest ($0.08 \leq z \leq 0.35$), in the case where stellar remnants are also taken into consideration. For this purpose we use figure 3 of Courteau et al. (2014) which shows the $M_\star$ evolution of a single stellar population (SSP) that have been derived using a Chabrier (2003)

IMF, along with the fraction of stellar mass found in remnants. For this simple test we assume that a BCG can be approximated with a SSP. Assuming this SSP formed at $z = 2$ (corresponding to an age of $\sim$ 10 Gyr), we find that the mass of the living stars has decreased by $\sim 0.9\%$ from $z = 0.35 - 0.08$[7], while the mass in the stellar remnants increased by $\sim 1.2\%$. These small changes indicate that taking the remnant mass into account will make little difference to the stellar mass estimates for these galaxies, which are mostly composed of old stellar populations.

During the course of our analysis in Chapter 2 we investigated the SDSS photometry of the BCGs in our sample. In particular we remeasured the total magnitudes of these galaxies using large aperture photometry (with `qphot`) and compared these magnitudes against those given in SDSS (see Section 2.3.1.4 for details). This analysis showed that SDSS underestimates the total magnitudes of all the BCGs, however those in the lowest redshift bin are affected the most. Their total magnitudes are underestimated by 0.15 mag. Consequently, we need to allow for this additional uncertainty when the mass growth of the BCGs is determined. That said, the total stellar mass growth of the BCGs can be $\mathrm{MGF_{fit}} = 0.98^{+0.15}_{-0.03}$, where the random uncertainty on the MGF has been increased by combining the 15% uncertainty with the other uncertainties by adding it in quadrature.

Now, we compare the derived BCG mass growth results to those given in the literature (Section 3.4.1). Our derived BCG mass growth results however depend on the techniques used to derive the stellar masses of the BCGs and the methods used to study the mass growth of these massive galaxies. In Section 3.4.2 - 3.4.4 we investigate two factors that may influence the $M_\star$ estimates of the BCGs and we use a different M_h proxy to construct the evolutionary sequence of clusters. We discuss how each of these influence the derived stellar mass evolution of the BCGs and find that our results are robust.

3.4.1 Comparison to the literature

We show a comparison of the stellar mass evolution of the BCGs in our sample to that found in the literature in Fig 3.6. In this section we only consider observational studies undertaken in 2014

[7] A galaxy formed at $z = 2$ has an age of 10 Gyr by present day. We can determine what the age of the galaxy will be at $z = 0.35$ and 0.08 by subtracting their corresponding lookback times from 10 Gyr, i.e. the age of the galaxy will be 6 (9) Gyr at $z = 0.35\,(0.08)$. From figure 3 we obtain the 0.9% mass difference by comparing the stellar masses of the SSP at these two ages.

and earlier, while later observational works and theoretical models are discussed in Section 6.2. A summary of the derived mass growth factors are also given in Table 3.3. The studies from which these values were obtained are discussed hereafter.

Lidman et al. (2012) studied the stellar mass evolution of BCGs since $z \sim 1$. They used near-IR data from the SpARCS[8] (Muzzin et al. 2009; 2012; Wilson et al. 2009; Demarco et al. 2010) survey to construct a sample of 12 BCGs between $0.8 < z < 1.6$. They supplemented these BCGs with those studied in Stott et al. (2008; 2010) to construct a sample of 160 BCGs across $0.03 < z < 1.63$. The clusters in Lidman's sample have a halo mass range of $(0.12 - 2.5) \times 10^{15}\,\mathrm{M}_{\odot}$. Using a method similar to ours to correct for progenitor bias, they measure a mass growth factor of 0.96 ± 0.20 from $z = 0.40$ to $z = 0.20$ (blue squares in Fig 3.6). When they did not correct for progenitor bias, they found MGF $= 0.88 \pm 0.09$ from $z = 0.45 - 0.17$ (green points in Fig 3.6). Within the uncertainties of these measurements the BCGs experienced the same mass growth whether progenitor bias was accounted for or not. Due to these large uncertainties the authors could not decisively say whether or not it is important to take progenitor bias into account when investigating the stellar mass evolution of BCGs. In comparison to Lidman et al. (2012), our results decisively show that progenitor bias has to be taken into account otherwise it will cause the mass growth of the BCGs to be underestimated. This is because our sample is ~ 68 times larger than that of Lidman et al. (2012), causing the uncertainties on our derived MGFs to be small enough to make the distinction as to whether progenitor bias is important or not.

Although small, Lidman's sample is currently the only observational sample with which the mass growth of BCGs can be investigated from $z \sim 2$ to the present. This sample however is at some disadvantage since the clusters in the sample have all been selected from different surveys, such as the SpARCS, ROSAT BCS[9], eBCS[10] (Ebeling et al. 2000), XBACS[11] (Ebeling et al. 1996) and MACS[12] (Ebeling et al. 2001) surveys. These surveys use different techniques to locate clusters, i.e. the SpARCS survey detect clusters by looking for over-densities of red-sequence galaxies while the clusters in the remaining surveys have been detected through X-ray emission. The galaxies

[8]Spitzer Adaptation of the Red-Sequence Cluster Survey, http://www.faculty.ucr.edu/∼gillianw/SpARCS/
[9]The ROentgen SATellite Brightest Cluster Sample, http://www.ifa.hawaii.edu//∼ebeling/clusters/BCS.html
[10]The extended Brightest Cluster Sample.
[11]The X-ray Brightest Abell Clusters Survey, http://www.ifa.hawaii.edu//∼ebeling/clusters/XBACs.html
[12]The MAssive Cluster Survey, http://www.ifa.hawaii.edu/∼ebeling/clusters/MACS.html

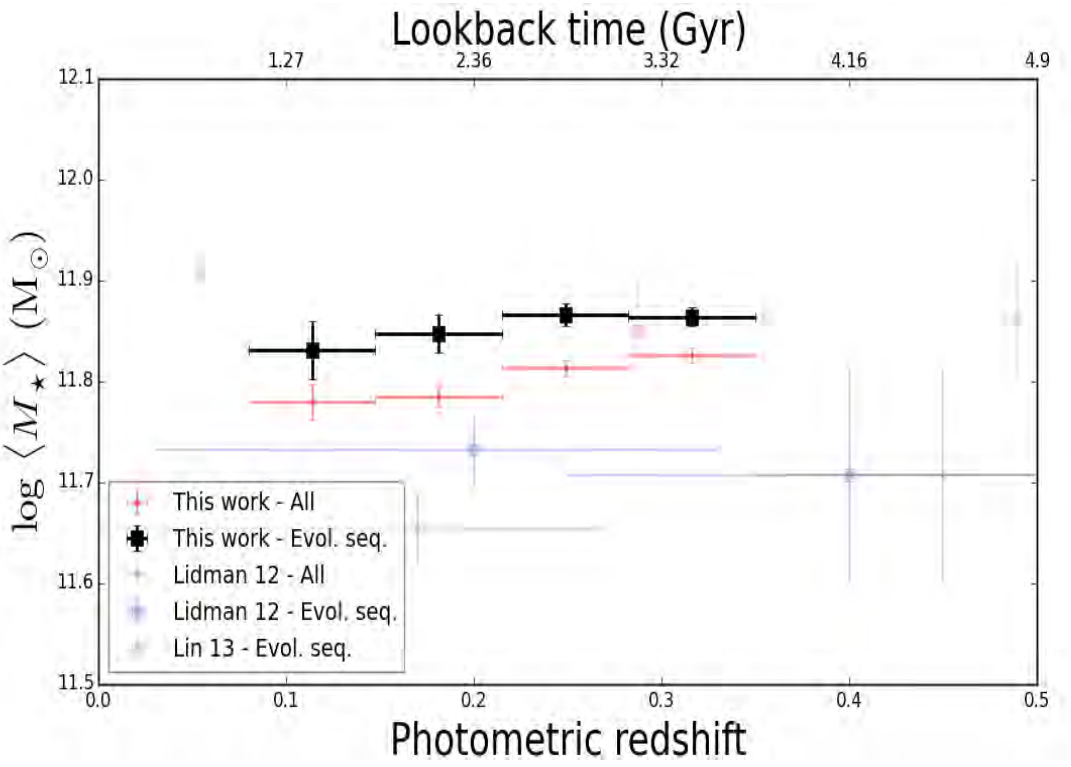

FIGURE 3.6: The stellar mass evolution of BCGs over $0.08 \leq z \leq 0.35$. The mass growth represented by the points have been derived by considering all the clusters. In contrast the mass growth represented by the squares has been derived by taking progenitor bias into account (i.e. only considered clusters that are progenitor/descendants of one another). The vertical uncertainties on our results are derived from bootstrap resampling while the horizontal uncertainties indicate the width of the redshift bins. Comparisons from Lidman et al. (2012) and Lin et al. (2013) are also given. The uncertainties on Lidman's masses are representative of the average uncertainty on $M_\star$.

identified as the BCGs might be different depending on the technique used to locate the clusters. The mass growth of the BCGs may be unreliable if the wrong galaxies are identified as the BCGs.

Lin et al. (2013) studied the stellar mass growth of BCGs between $z = 1.5$ and the present day. They use clusters with a present day halo mass range of $(0.24 - 0.45) \times 10^{15}\,\mathrm{M}_\odot$ that have been selected from the Spitzer IRAC Shallow Cluster Survey (ISCS; Eisenhardt et al. 2008). Extensive spectroscopic follow up observations of the AGES[13] survey (Kochanek et al. 2012) have been used to derive the halo masses of the ISCS clusters via velocity dispersions. The majority of the high redshift ISCS clusters however do not have velocity dispersion estimates and therefore have no halo masses estimates. In order to infer M_h of the clusters in their sample, Lin et al. (2013) relied on luminosity ranking (as done by Yang et al. 2007; 2009; Rozo et al. 2009). The volume probed by the ISCS survey at $z < 0.1$ is too small to contain any clusters in the halo mass range that the Lin study

[13]The AGN and Galaxy Evolution Survey, http://www.naic.edu/∼ages/

is interested in. They therefore turned to the extended version of the low redshift cluster sample presented in Vikhlinin et al. (2009) where X-ray temperature is used as the halo mass proxy since all these clusters have been observed with Chandra. With the help of a high resolution cosmological simulation, Lin et al. (2013) used an empirical method where cluster masses have been derived based on the ranking of cluster luminosity. For a more detailed description of this method we refer the reader to Lin et al. (2013). Over the redshift interval $0.5 \leq z \leq 1.5$ they found that the BCGs have MGF $= 2.28 \pm 0.62$. At $z < 0.5$, however, they found that the mass growth of the BCGs slowed down (MGF $= 1.11 \pm 0.30$; magenta squares in Fig 3.6).

The clusters in the Lin et al. (2013) sample have a lower halo mass range than those in our sample. The BCGs in these clusters are therefore less massive than those in our sample. If only the clusters in the Lin et al. (2013) sample with redshifts closest to our redshift range of interest ($0.08 \leq z \leq 0.35$) are considered, we find that these BCGs have MGF $= 1.14 \pm 0.30$ from $z = 0.29 - 0.05$. When compared with our derived $\mathrm{MGF_{fit}}$ of $0.98^{+0.15}_{-0.03}$, it seems that the BCGs in both samples experienced the same mass growth factor (within the uncertainties), regardless of the fact that the BCGs in our sample are more massive.

Using the GAMA[14] survey, Oliva-Altamirano et al. (2014) studied the stellar mass evolution of BCGs over the last three billion years of the Universe ($0.09 \leq z \leq 0.27$). They analysed a sample of 883 galaxies that have been selected from the GAMA Galaxy Group Catalogue ($\mathrm{G^3C}$; Robotham et al. 2011). These galaxies are located in halos that span a wide halo mass range ($10^{12} - 10^{15}\,\mathrm{M_\odot}$). They separate groups and clusters with a single halo mass cut of $M_h = 10^{14}\,\mathrm{M_\odot}$. For the purpose of this discussion, we will only focus on the mass growth of the BCGs that they have derived from the clusters. Taking the growth of the dark matter halos of the clusters into account (i.e. constructing an evolutionary sequence), they found that the BCGs did not experience any significant mass growth (MGF $= 0.93 \pm 0.09$) from $z = 0.27 - 0.09$.

Although the M_h range of clusters in the Oliva-Altamirano et al. (2014) sample are not given we can comment on a few things. The Oliva-Altamirano et al. (2014) sample is constructed from GAMA while our sample is constructed using SDSS data. The high spectroscopic completeness of GAMA allows galaxies to be reliably associated with clusters. Over a similar redshift range, the

[14]GAMA include reprocessed imaging from the SDSS (*ugriz*).

SDSS survey probes a larger volume of the sky than GAMA. The number density of high mass clusters are low because they are so rare. Considering this together with the volume probed by each survey, we can conclude that the redMaPPer catalogue includes more high mass clusters than G^{3}C. GAMA is therefore missing the high mass end of the clusters' halo mass distribution and as a direct result the high mass end of BCGs' stellar mass distribution is also missing. However we find consistent mass growth factors between the two studies, within the uncertainties, so it is not possible to know whether the inclusion of more high mass clusters has had an impact.

TABLE 3.3: Comparison of our derived BCG mass growth factor to those given in the literature. Column 1 indicates the redshift range over which the mass growth has been determined, while Column 2 gives the halo mass ranges of the clusters. Columns 3 and 4 indicate the MGFs derived if all clusters and only clusters that form part of the evolutionary sequence are considered. The last column is the reference to the work from which the results are obtained.

z	M_h **range** ($\times 10^{15}\,\mathrm{M}_\odot$)	**All**	**Evol. seq.**	**Ref.**
$0.35 - 0.08$	$0.17 - 2.20$	0.88 ± 0.01	$0.98^{+0.15}_{-0.03}$	This work
$0.40 - 0.20$	$0.12 - 2.50$	0.88 ± 0.09	0.96 ± 0.20	Lidman et al. (2012)
$0.29 - 0.05$	$0.24 - 0.45$	–	1.14 ± 0.30	Lin et al. (2013)
$0.27 - 0.09$	$0.10 - 1.00$	–	0.93 ± 0.09	Oliva-Altamirano et al. (2014)

3.4.2 The influence of using a constant mass-to-light ratio to derive the BCG stellar masses

Constant mass-to-light (M/L) conversions have historically been widely used in the literature to derive stellar mass estimates for galaxies based on luminosities (e.g. van der Marel 1991; Cappellari et al. 2006; Edwards & Patton 2012). It is therefore instructive to understand how our results, derived using the more sophisticated technique of stellar population model-fitting, compare with these.

For this section we will use a constant M/L to determine stellar mass estimates for the BCGs in the redMaPPer catalogue and use the method outlined in Section 3.2 to remeasure the mass growth of these massive galaxies. We retrieve the k-corrected absolute r-band (M_R) magnitudes of BCGs from the `kcorrect` code. These absolute magnitudes are then converted into luminosities by using the distance modulus. To convert these luminosities into stellar masses, we use typical M/L ratios for BCGs in the R-band from the literature. Cappellari et al. (2006) typically find M/L values of 5.8 for luminous galaxies with $-25 \leq M_R \leq -22$. van der Marel (1991) in turn find that elliptical galaxies have $\mathrm{M/L_R}$ of 4.7 (on average). We take the average of these two values and use $\mathrm{M/L}_R = 5.3$ to convert the luminosities of the BCGs to stellar masses as done by Edwards & Patton (2012).

The stellar mass estimates of the BCGs as derived by using the `kcorrect` code and a constant $\mathrm{M/L}_R$ are shown in Fig 3.7. Using a constant M/L results, on average, in a higher mass than `kcorrect`. Eq 3.4 is used to determine the MGF for the BCGs in the following three cases: (i) all clusters; (ii) the clusters that form part of the evolutionary sequences that have been constructed with and (iii) without an upper M_h limit. The results are presented in Table 3.4. For comparison we also state the MGFs that have been derived using the `kcorrect` stellar masses. In each case we find that the MGF are consistent within the uncertainties. This suggests that the method used to derive the $M_\star$ estimates of the BCGs has little to no effect on their measured mass growth.

Additionally, we also use the colour-based relation of Taylor et al. (2011) to derive stellar mass estimates for the BCGs in our sample. We refer the reader to Taylor et al. (2011) for more detail. Briefly, they determined how well the $g-i$ colours of galaxies can be used to estimate M/L (compared to those obtained using stellar population model-fitting). Fitting the empirical relation for GAMA galaxies, they find

$$\log\left(M_\star/\mathrm{M}_\odot\right) = 1.15 + 0.7(g-i) - 0.4M_\mathrm{i} \tag{3.8}$$

where M_i is the absolute magnitude of each BCG in the restframe i-band. They find that this relation is able to derive M/L estimates to a accuracy of ~ 0.1 dex using (restframe) g and i-band photometry alone.

Using Eq 3.8 we obtain stellar masses for our BCGs and compare these against their corresponding

`kcorrect` stellar mass estimates in Fig 3.8. The $M_\star$ estimates obtained by using the Taylor et al. (2011) colour-based relation are on average more massive than those derived with `kcorrect`. Furthermore, we used the mass estimates from Eq 3.8 and derived the MGFs of the BCGs in the three above-mentioned cases (results are presented in Table 3.4). In each case we find the MGFs to be consistent (within the uncertainties) to those obtained using stellar masses from `kcorrect` and the constant M/L, supporting our conclusion that the method used to derive the $M_\star$ estimates of the BCGs has little to no effect on the measured mass growth of these massive galaxies.

TABLE 3.4: Comparison of the MGFs using the $M_\star$ estimates, derived from a constant M/L ratio and the `kcorrect` code. The MGFs have been determined by considering (i) all the clusters and (ii) only the clusters that form part of the evolutionary sequence (constructed with and without an upper M_h limit).

z	**All**	**Imposing lower M_h limit**	**Impose upper M_h limit**	$M_\star$ **derived using**
	0.88 ± 0.01	0.93 ± 0.03	0.96 ± 0.03	M/L
$0.35 - 0.08$	0.88 ± 0.01	0.94 ± 0.02	0.98 ± 0.03	`kcorrect`
	0.87 ± 0.01	0.94 ± 0.02	0.97 ± 0.03	Taylor et al. (2011)

3.4.3 Contamination from neighbouring objects

As mentioned early in Chapter 2 we found examples where obvious, bright objects around the BCGs were not detected by SDSS. This is potentially problematic for our project since the magnitudes of the BCGs are used to derive their $M_\star$. If the bright contamination around the BCGs is not corrected, we may end up overestimating the mass growth of these massive galaxies.

We quantified how many of the BCGs in our sample suffered from the bright contamination problem by redoing the object detection around the BCGs with the `SExtractor` software (see Section 2.3.2). We found that $\sim 1\%$ of the BCGs in the sample suffered from this problem. The fraction

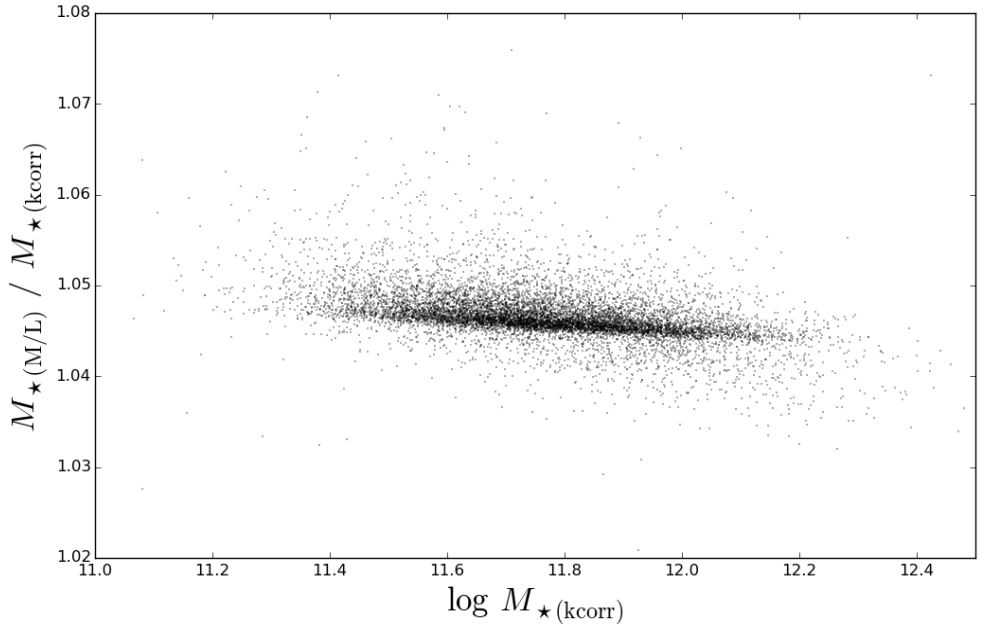

FIGURE 3.7: Comparison of the BCGs' stellar mass estimates as derived by using the `kcorrect` code and a constant M/L_R of 5.7. It is clear the mass estimates derived by using a constant M/L are on average more massive than those derived with `kcorrect`.

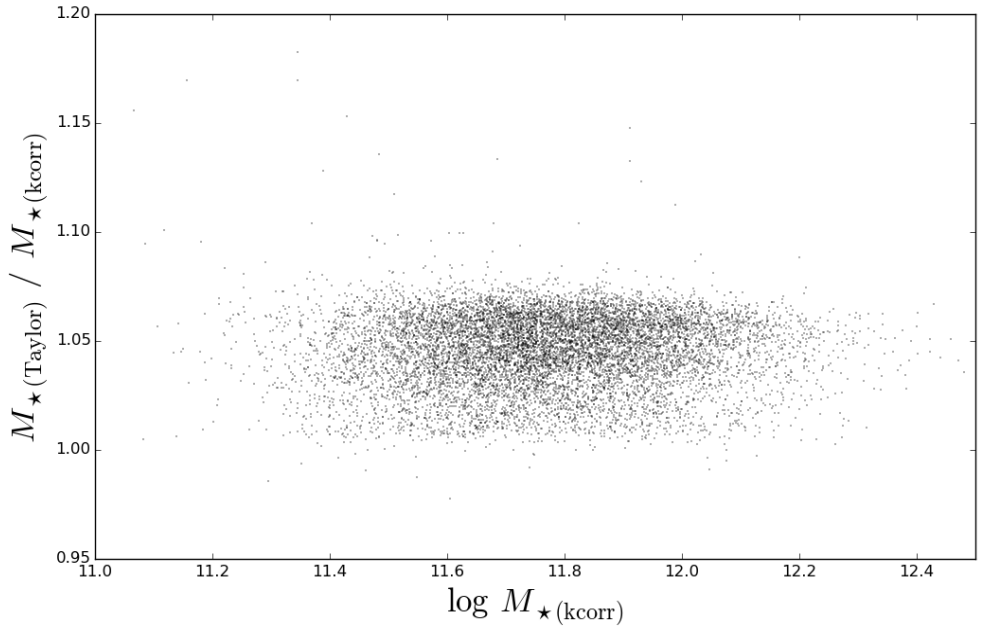

FIGURE 3.8: Comparison of the BCGs' stellar mass estimates as derived by using the `kcorrect` code and the colour-based relation of Taylor et al. (2011). The mass estimates derived by using the colour-based relation (Eq 3.8) are on average more massive than those derived with `kcorrect`.

of BCGs, per redshift bin, that suffer from this contamination (denoted $f_{\text{bright cont}}$) is summarised in Table 3.5. We used the method outlined in Cameron (2011) to determine the uncertainties on $f_{\text{bright cont}}$ and we refer the reader to Section 4.2.1 for details. In the worst cases, i.e. where the neighbouring object is both bright and close, we find that the magnitudes of the BCGs are biased by 0.08 mag (corresponding to an 8%[15] bias in mass). Therefore the maximum stellar mass bias on the average is negligible.

TABLE 3.5: The fraction of BCGs that were found to have a neighbouring bright object, undetected by SDSS. The uncertainties have been derived using the method described in Cameron (2011).

z	**Fraction of BCGs** ($f_{\text{bright cont}}$)
$0.08 - 0.15$	0.009 ± 0.003
$0.15 - 0.21$	0.008 ± 0.002
$0.21 - 0.28$	0.013 ± 0.002
$0.28 - 0.35$	0.010 ± 0.001

3.4.4 The SZ-effect as M_h proxy

Estimates for the halo masses of clusters are derived using observables (or mass tracers) that correlate with the mass. These relate to hot gas content, galaxy content and galaxy dynamics, etc. Each of these methods has its own set of biases. For example, in a dynamically unrelaxed or merging system, mass proxies such as velocity dispersion, X-ray temperature and richness, will likely overestimate the M_h of the cluster. However the amount by which each of these proxies will overestimate the halo mass will vary (due to the different scaling of the relevant observables with mass).

[15] Using the standard definition to convert from magnitude to flux, we determine how a magnitude offset (Δm) translates to a change in stellar mass. It follows that $\Delta m = 1.086(\Delta M_\star/M_\star)$, where $(\Delta M_\star/M_\star)$ represents the corresponding change in stellar mass. A magnitude offset of 0.01, for example, then corresponds to a 1% change in stellar mass.

In this section we specifically look at two mass proxies, the galaxy content (richness, using the redMapper catalogue) and hot gas content (SZ-effect, using the *Planck* catalogue[16]). There is some evidence that clusters from galaxy-selected surveys may have cooled a higher fraction of their hot gas content into galaxies (Hicks et al. 2007) which may also have implications for how BCGs have built up their stellar mass in such systems.

By combining the large public SZ catalogues, such as *Planck*, with optical photometry of the BCGs from SDSS we can study the mass growth of these massive galaxies in SZ-selected clusters. Such a study has already been performed by Inagaki et al. (2015) who essentially used the same data as we use here, however they used a different method to select galaxy clusters and their BCGs and also used a slightly different method for constructing an evolutionary for their BCGs.

For examining the SZ-effect we use the latest version of the *Planck* SZ cluster catalogue (PSZ1; Planck Collaboration et al. 2014b), where clusters have been detected using the SZ-effect. We refer the reader to Planck Collaboration et al. (2014b) for a detailed description of the PSZ1 catalogue. Briefly, the catalogue contains 1227 cluster candidates which span $M_h = (0.07 - 1.64) \times 10^{15}\,\mathrm{M}_\odot$ and covers a redshift range of $0.01 \leq z \leq 0.97$. The redshifts of the clusters have been assigned either by cross-matching to external catalogues, or through extensive photometric and spectroscopic follow-up observations of the PSZ sources by the *Planck* satellite.

Throughout this section we only consider the 947 galaxy clusters that have been labelled as confirmed systems in the PSZ1 catalogue ('validation' flag values ≥ 10). We further restrict ourselves to systems that have reported redshifts and lie in the redMaPPer footprint (203 clusters). These clusters were identified using the method outlined in Rozo et al. (2015). Using the positions of the PSZ1 clusters, a radius of $1\,\mathrm{Mpc} + \delta_x$[17] has been used to identify matches for these clusters in redMaPPer.

For these 203 overlapping clusters, we compare their PSZ1 and redMaPPer redshifts. It is immediately apparent that some of these overlapping clusters do not have comparable redshifts in the two catalogues. We quantify this by considering the redshifts between the PSZ1 and redMaPPer catalogues to be consistent if they agree within 3σ (with σ the clusters' redshift uncertainties as given

[16] http://www.cosmos.esa.int/web/planck

[17] δ_x is the position uncertainty that is provided in the PSZ1 catalogue for each cluster and is typically ~ 4 arcmin.

in redMaPPer; see Rozo & Rykoff 2014; Rozo et al. 2015). Using this requirement, we find that 173 of the overlapping clusters have consistent redshifts. The origins of the redshift conflicts for the 30 remaining clusters are beyond the scope of this analysis. We do however refer the interested reader to Rozo et al. (2015) who performed a detailed comparison of the redMaPPer and PSZ1 cluster catalogues. Within this study they search for reasons that might explain the redshift conflicts and try to assign the correct redshifts to the clusters. For the remainder of this section these 30 redshift outliers are excluded from our analysis.

We replace the richness halo mass estimates of the 173 matched clusters with their SZ-mass ($M_{\rm SZ}$) estimates from the PSZ1 catalogue. Following the method outlined in Section 3.2, we construct an evolutionary sequence for the 173 clusters using their $M_{\rm SZ}$ estimates. All these clusters have $\geq 50\%$ completeness in redMaPPer. We only apply a lower M_h limit, to ensure a sufficient number of clusters across our redshift range. We highlight the 56 clusters that form part of this evolutionary sequence with red points in Fig 3.9. A summary of the matched clusters is presented in Table 3.6.

Using $M_{\rm SZ}$ as the mass proxy of the clusters, we derive the mass growth of the BCGs (using Eq 3.4) in the following two cases: (i) when all clusters and (ii) only the clusters in the evolutionary sequence are considered. These results are summarised in Table 3.7. For comparison we also give the derived MGFs of the two cases when richness was used as the M_h proxy. We note that there is only one cluster that forms part of the evolutionary sequence in the lowest redshift bin. We therefore measured the MGF of the BCGs over $z = 0.35 - 0.21$ since there are enough clusters in these two redshift bins with which the BCG mass growth can be measured, MGF $= 1.08 \pm 0.11$. This compares well with the MGF derived by Inagaki et al. (2015, MGF $= 1.08 \pm 0.06$), despite the different methods used.

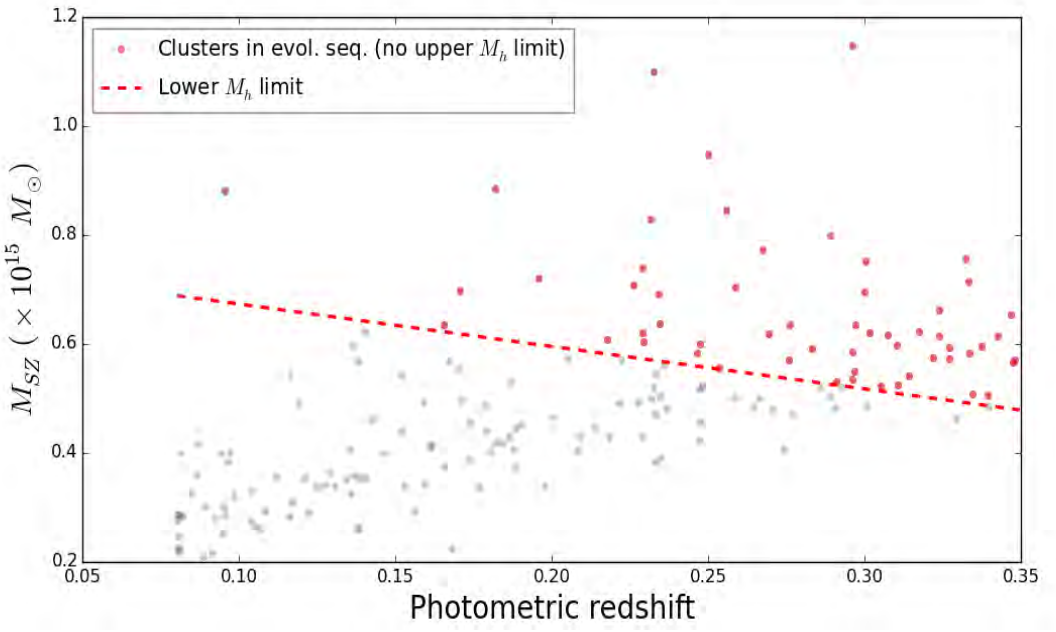

FIGURE 3.9: For the 173 redMaPPer clusters that have $M_{\rm SZ}$ estimates in the PSZ1 catalogue, we follow the method outlined in Section 3.2 to construct an evolutionary sequence by only applying a lower M_h limit.

TABLE 3.6: Number of clusters per redshift bin in the full matched PSZ1-redMaPPer sample and the subsample of clusters selected as an evolutionary sequence.

	All clusters	**No upper M_h limit**	
z	$N_{\rm clus}$	M_h **range** ($\times 10^{15}\,{\rm M}_\odot$)	$N_{\rm clus}$
$0.08-0.15$	53	≥ 0.63	1
$0.15-0.21$	37	≥ 0.59	4
$0.21-0.28$	43	≥ 0.53	19
$0.28-0.35$	40	≥ 0.48	32
	Total = 173		Total = 56

TABLE 3.7: Derived MGFs using 2 mass proxies for all clusters (173) and only clusters (56) in the evolutionary sequence. Column 1 gives the redshift interval over which the MGF of the BCGs has been determined.

z	M_h **proxy**	**All**	**Imposing lower** M_h **limit**
$0.35 - 0.21$	$M_{\rm SZ}$	1.08 ± 0.11	1.14 ± 0.16
	Richness	0.97 ± 0.01	1.01 ± 0.04
Inagaki et al. (2015)			
$0.4 - 0.2$	$M_{\rm SZ}$	–	1.08 ± 0.06

We have tested whether the properties used to select the clusters (and the associated biases) have an influence on the stellar mass evolution of the BCGs. Using two mass proxies, we find consistent mass growth for the BCGs within the uncertainties. This may suggest that the galaxy and hot gas content of the clusters do not influence the mass evolution of the BCGs.

In summary: In this chapter we have shown that the BCGs did not increase their stellar masses in the ~ 3 Gyr spanned by $z = 0.35 - 0.08$, however allowing for the additional uncertainty that the SDSS magnitudes of the BCGs are underestimated in the lowest redshift bin, we find that the total stellar mass growth of the BCGs can be $0^{+15\%}_{-3\%}$. This result was shown to be robust against changes in the methods use to derive the stellar masses of the BCGs and the clusters' halo masses. The contamination of neighbouring objects has also been found to have a negligible effect on the mass growth. Importantly, we also showed that progenitor bias must be taken into account when the mass growth of BCGs is investigated. If this is not done, then it seems as if the BCGs are somehow losing stellar mass with decreasing redshift (which is non-physical).

Chapter 4

The importance of mergers in the stellar mass build-up of BCGs between $0.08 \leq z \leq 0.35$

> "May the road rise up to meet you. May the wind always be at your back. May the sun shine warm upon your face, and rains fall soft upon your fields. And until we meet again, may God hold you in the palm of His hand."
>
> An old Irish blessing

4.1 Introduction

In the ΛCDM dominated Universe, structures are believed to grow hierarchically through the accretion of smaller sub-structures (Spergel et al. 2003; 2007). Mergers in turn are thought to play a very significant role in the stellar mass assembly of massive early-type galaxies (Toomre & Toomre 1972; van Dokkum 2005; Bell et al. 2006a). To obtain accurate, quantitative estimates of the galaxy merger rates has proven to be rather difficult and results vary greatly between studies.

Two techniques are commonly used in the literature to estimate the galaxy merger rate with cosmic time. The first technique uses the number density of morphologically disturbed galaxies (with strong asymmetries, double nuclei, or prominent tidal tails; e.g. Le Fèvre et al. 2000; Conselice et al. 2003; Lavery et al. 2004; Lotz et al. 2006; 2008; McIntosh et al. 2008; Liu et al. 2009; 2015) as a measurement of the galaxy interaction rate. The second technique on the other hand uses the incidence of dynamically close galaxy pairs (e.g. Zepf & Koo 1989; Burkey et al. 1994; Carlberg et al. 2000; Patton et al. 2000; Lin et al. 2004; Bell et al. 2006b; Masjedi et al. 2006; Kartaltepe et al. 2007; Edwards & Patton 2012; López-Sanjuan et al. 2012; Burke & Collins 2013; Keenan et al. 2014).

In this chapter, we are particularly interested in the importance of mergers in the stellar mass build-up of BCGs with cosmic time. Predictions from numerical simulations and SAMs suggests that BCGs formed in two 'phases'. At $z \geq 2$ star formation is found to dominate the BCG's mass growth and at later times ($z \leq 1$) the mass growth is dominated by multiple dry mergers of smaller galaxies (e.g. De Lucia & Blaizot 2007; Naab et al. 2009; Laporte et al. 2013). The simulations however differ in their predicted mass growth and the importance of mergers therein. De Lucia & Blaizot (2007) find that the BCGs increase their stellar masses by a factor of ~ 4 from $z = 1 - 0$, mainly through minor mergers[1]. Laporte et al. (2013) on the other hand predict a BCG mass growth factor closer to 2 over the same redshift range, however both major and minor mergers are found to contribute towards the mass growth of these massive galaxies.

Observational evidence has also indicated that BCGs are experiencing mergers (e.g. Bernardi et al. 2007; Lauer et al. 2007; von der Linden et al. 2007; McIntosh et al. 2008; Liu et al. 2009; 2015; Rasmussen et al. 2010; Brough et al. 2011). Several studies, for example Liu et al. (2009; 2015); Edwards & Patton (2012); Lidman et al. (2012); Burke & Collins (2013); Burke et al. (2015), have shown that BCGs accumulate a large portion of their stellar masses through dry mergers that take place at $z < 1$. These studies indicate that BCGs increase their stellar masses by factors that range between $\sim 1.8 - 2.5$ (Lidman et al. 2012; Burke & Collins 2013; Ascaso et al. 2014) and suggest that major mergers are the dominant mass contributor (rather than minor mergers).

[1]Works in the literature typically define minor mergers as mergers with stellar mass ratios of >1:4−1:20 (e.g. Edwards & Patton 2012; Burke & Collins 2013; Burke et al. 2015).

The discrepancies between observations and simulations regarding the mass growth of BCGs are quite apparent. This may be because mergers do not contribute significantly to the stellar mass growth of the BCGs if a significant fraction of the merging mass ends up in the ICL. The Laporte et al. (2013) simulation predicts that $30 - 50\%$ of a companion galaxy's mass will be distributed into the ICL during a merger event (also see Conroy et al. 2007b; Puchwein et al. 2010). This brings the model's predicted BCG mass growth over $0 < z < 1$ into better agreement with the observed mass growth estimates of Lidman et al. (2012); Burke & Collins (2013) in the same redshift range. Observational studies on the other hand have also shown that the ICL experienced significant mass growth over $0 < z < 1$ (a factor of $4 - 5$ growth; e.g. Krick & Bernstein 2007; Burke et al. 2012; 2015). If we are to believe that the majority of the merging mass ends up in the ICL, then this presents us with a scenario that the ICL is being built-up through galaxies that are interacting with the BCGs. Consequently it is clear that the growth and build-up of BCGs and the ICL are linked, however it is not clear to what extent merger events contribute towards this.

In this chapter we use the incidence of close galaxy pairs to investigate the role of major mergers in the stellar mass build-up of BCGs over $0.08 \leq z \leq 0.35$. We begin by defining the pair fraction and also discuss the selection criteria used to construct the close pair sample. We then describe the method used to measure the stellar mass growth of the BCGs due to major mergers (Section 4.2). The results are given in Section 4.3, whereafter we compare to studies in the literature.

4.2 Method – The pair fraction and mass growth of BCGs

In this section we describe the general method we used to measure (i) the pair fraction of BCGs and (ii) the stellar mass growth of the BCGs due to the major mergers. We do this for two cases. The complete method used to measure the BCG pair fraction is quite complicated. It is therefore useful to start with the simpler case, where only photometry is used. This is used in studies (such as Edwards & Patton 2012) that do not have spectroscopy available. We then proceed to the more complicated case, where spectroscopy is used. We begin this section by defining what close companion galaxies are and how the BCG pair fraction (and the associated uncertainty) is determined.

4.2.1 Definition of the pair fraction

When a merger candidate sample is constructed by just using photometry, the sample will inevitably suffer from contamination due to line-of-sight projection effects. Studies, for example Edwards & Patton (2012), correct for this by applying a 50% contamination correction to their pair fraction, estimated using the Millennium Simulation (Springel et al. 2005). We will apply this same contamination correction to our results and compare to studies in the literature.

Studies in the literature typically use physical separation distances of 20 kpc (e.g. Hsieh et al. 2008; Brough et al. 2011; Robotham et al. 2014), 30 kpc (e.g. Patton et al. 2000; Lin & Mohr 2004; Kartaltepe et al. 2007; McIntosh et al. 2008; Liu et al. 2009; Robaina et al. 2010; Lidman et al. 2013; Keenan et al. 2014) or 50 kpc (e.g. Lin & Mohr 2004; Edwards & Patton 2012; López-Sanjuan et al. 2012; Robotham et al. 2014; Burke & Collins 2013; Burke et al. 2015) to look for close pairs. We construct a close pair sample from the redMaPPer catalogue (consisting of galaxies with $P_{\rm RSM} > 0$) by using a physical separation distance ($r_{\rm sep}$) of 50 kpc[2] at the photometric redshift of the cluster. The galaxies within this search radius are referred to as companions. We are however only interested in companions that are massive enough to be considered major merger candidates, i.e. have stellar mass ratios of (1:1 - 1:4)[3].

We will however not detect every single companion within this search radius, simply because companions that are very close to the BCGs will be missed. This is the case if the separation distance between the two galaxies is smaller than the sizes of the BCGs[4]. When the companion is on top or behind the BCG, it will not be detected. Seeing smears out the light of a galaxy and makes it appear larger. This could make it appear that a companion is on top of the BCG and consequently, it will not be detected. Seeing has little effect on galaxies that are much larger than the seeing (most of our sample), however BCGs that are smaller or comparable to the seeing (those in our highest redshift bin) may be smeared out and close companions may therefore be hidden.

[2] At $z = 0.08\,(0.35)$, 50 kpc roughly corresponds to $34''\,(10'')$ on the sky.

[3] Between $0.08 \leq z \leq 0.20$, we are complete for mergers with mass ratios down to (1:6). However, in order to use the whole redshift range of our sample, we choose to only consider major mergers. See Appendix B for details.

[4] Loosely defined as the radius where the light of BCG begins to dominate and makes it difficult to distinguish any close-by objects.

Almost all of the studies that are mentioned above did not impose an explicit lower $r_{\rm sep}$ limit during their close pairs selection, however an inner radius cut is implicitly applied to these samples since the sizes of galaxies are not zero. Patton et al. (2000); Lin & Mohr (2004); Lin et al. (2008); Kartaltepe et al. (2007); Hsieh et al. (2008); López-Sanjuan et al. (2012); Lidman et al. (2013); Keenan et al. (2014) are exceptions as they impose a minimum separation distance (typically between $5 - 10$ kpc). In order to fairly compare the pair fractions from different observational studies and simulations, it is necessary to specify a lower $r_{\rm sep}$ limit so that the pair selection is reproducible.

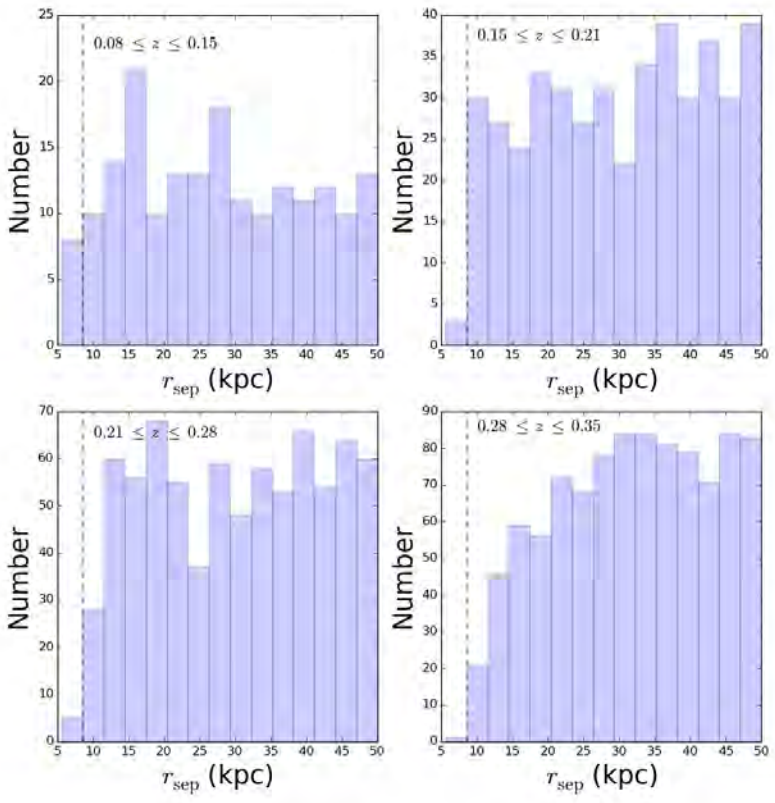

FIGURE 4.1: The physical separation distribution of the close pairs in our sample in four redshift slices. The number of close pairs decreases at $r_{\rm sep} \leq 7$ kpc (dashed line) due to the BCG sizes (main cause in first three slices), while seeing causes the light of the BCGs to be smeared out in last redshift slice, hiding nearby companions. See text for details.

In order to obtain the lower $r_{\rm sep}$ limit for our close pair sample, we consider the distribution of the physical separation distances of our close pair sample in Fig 4.1. Consider the first three redshift slices ($0.08 \leq z \leq 0.28$). Moving in from large radii, the number of observed close pairs drastically

decreases in the first radius bin ($r_{\rm sep} \sim 7$ kpc) as opposed to the remaining bins where the number of pairs stays roughly constant. This is not observed in the last redshift slice, since the number of observed close pairs gradually decreases from $r_{\rm sep} \leq 25$ kpc. Although both the BCG sizes and seeing effects are applicable to the four redshift slices, the BCG sizes are the main cause for the decreasing number of pairs. For the remaining redshift slice, seeing causes the BCGs' light to be smeared out, causing close companions to be missed. From this redshift slice we would choose the minimum $r_{\rm sep}$ value to be 25 kpc as this is where the number of pairs starts to gradually decline. This cut however would result in a very small close pair sample. We therefore turn to the first three redshift slices and obtain a minimum $r_{\rm sep}$ value of 7 kpc. We apply this inner radius cut to all four redshift slices, however any results obtained from the last redshift slice will be treated with caution. We will determine what effect the applied minimum radius has on the measured pair fraction in Section 4.3.1.

We define the pair fraction of the BCGs, denoted $\langle f_{\rm pair} \rangle$, in the i-th redshift bin as

$$\langle f_{\rm pair} \rangle_i \; = \; \frac{(\mathrm{N_{BCGs}\,with}\; \geq 1\,\mathrm{true\,companion})_i}{(\mathrm{N_{BCGs}})_i} \quad \mathrm{with}\;\; 0.08 \leq z_i \leq 0.35 \tag{4.1}$$

where ($\mathrm{N_{BCGs}\,with}\; \geq 1\,\mathrm{true\,companion}$) is the number of BCGs with one (or more) true companion, selected within $7 \leq r_{\rm sep} \leq 50$ kpc of the BCG. Since we do not know which companions will merge, we set the number of BCGs with 1 or more true companions to the number of BCGs with observed companions that are possible major merger candidates. $\mathrm{N_{BCGs}}$ is the total number of BCGs in this particular redshift bin that form part of the evolutionary sequence (as derived in Chapter 3). In Section 4.3.1 we test how the pair fraction is influenced if we consider all the BCGs in the sample (regardless of the cluster M_h completeness).

In the case where spectroscopic information is available for some of the sample, we rewrite Eq 4.1 to measure the pair fraction of the BCGs by taking the spectroscopic completeness of the sample into account, to convert the observed (incomplete) numbers to the 'true' numbers. This is done as follows:

$$\langle f_{\rm pair} \rangle_i \; = \; \frac{(\sum_{j=1}^{N_{\mathrm{BCGs},i}} C_j\,\mathrm{of\,N_{BCG}\,with}\; \geq 1\,\mathrm{obs.\,companion})_i}{(\mathrm{N_{BCGs}})_i} \quad \mathrm{with}\;\; 0.08 \leq z_i \leq 0.35 \tag{4.2}$$

where C_j is the applied correction for spectroscopic incompleteness (used in Section 4.2.2) of the j-th companion belonging to the j-th BCG in the i-th redshift bin. For the photometric case we assume that $C_j = 1$ for each close pair.

Let $\sigma_{f_{\rm pair}}$ represent the uncertainty on the pair fraction of the BCGs. The uncertainty on $\langle f_{\rm pair} \rangle$ represents the 68.3% (1σ) binomial confidence limit and is calculated using the beta confidence interval as described by Cameron (2011). The beta distribution for k successes and n trials is defined as

$$B(a, b) = \frac{(a + b - 1)!}{(a - 1)!(b - 1)!} p^{a-1} q^{b-1} \tag{4.3}$$

where $a = k + 1$, $b = n - k + 1$ and $q = 1 - p$.

The lower and upper bounds (p_l, p_u) at confidence level $c = 1 - \alpha$ are given by:

$$\int_0^{p_l} B(a, b)dp = \alpha/2 \text{ and } \int_{p_u}^1 B(a, b)dp = \alpha/2 \tag{4.4}$$

This technique is now commonly used in the literature (see e.g. López-Sanjuan et al. 2014; Galloway et al. 2015; Davies et al. 2016; Moffett et al. 2016; Rees et al. 2016, and others). It is more robust for the extreme cases of fractions that are close to zero and one. The binomial confidence limits can be calculated by using the standard library routines in PYTHON (see Appendix A of Cameron 2011, for details). We tested how well the binomial confidence limits compares to another popular technique that is commonly used in the literature, the Gehrels (1986) approach. To give an example, for a fraction of 7/12, both techniques estimate an uncertainty of 0.13. For a fraction of 7/100, the Gehrels (1986) approach estimate an uncertainty that is a factor of two higher than that determined by the Cameron (2011) method. We prefer the latter method since our derived pair fractions are quite small (close to 0).

Where we do not use spectroscopic information, we assume a similar contamination correction to Edwards & Patton (2012). Using the Millennium Simulation, they found a contamination correction[5] of 50% has to be applied to their results in order to eliminate the contributions made by

[5]This correction is applicable to BCGs with companions within 50 kpc and stellar mass ratios down to 1:20. The correction is therefore for major and minor merger candidates.

projection effects. We call the pair fraction derived in this way the *photometric pair fraction*.

4.2.2 Close pair selection criteria using spectroscopy

With our close pair sample we can do a better job of estimating the contamination level by using spectroscopy. We only have spectroscopy for a fraction of the galaxies in our sample. The correction for this spectroscopic incompleteness is fairly involved and outlined over the next few sections. We use a relative velocity difference (Δv) to eliminate galaxies from our sample that have been included due to projection effects.

4.2.2.1 Identifying possible merger candidates

We have identified close galaxy pairs by searching for photometric galaxies that are within $7 \leq r_{\rm sep} \leq 50$ kpc from the BCGs. Spectroscopy is used in our analysis to correct for line-of-sight projections (due to fore-/background galaxies). The spectroscopic redshifts of the galaxies are also used to determine whether the photometrically identified companion galaxies are bound to their host BCGs. We require the galaxies to have $\Delta v \leq 300\,{\rm km\,s^{-1}}$ in order for them to be considered potential merger candidates (also used by Burbidge 1975; Kitzbichler & White 2008; Ellison et al. 2013). This value was obtained by Patton et al. (2000) who used close pair statistics to study the pair fraction of field galaxies. A relative velocity cut of 500 $\rm km\,s^{-1}$ is also commonly used in the literature (see e.g. Lin et al. 2004; 2008; López-Sanjuan et al. 2012; Robotham et al. 2014). We will test how the pair fraction depends on our choice of Δv (see Section 4.3.1).

We retrieve the spectroscopic redshifts (if available) of the galaxies in the close pairs from SDSS DR12[6] (Alam et al. 2015). In each pair, the relative velocity difference between the companion and BCG is determined as follows:

$$\Delta v = \frac{c \times (z_{\rm com} - z_{\rm BCG})}{1 + z_{\rm BCG}} \tag{4.5}$$

where c is the speed of light (in $\rm km\,s^{-1}$) and $z_{\rm com/BCG}$ is the SDSS spectroscopic redshift of the companion and BCG.

[6] http://www.sdss3.org/dr12/

In summary: Our final close pair sample consists of 3113 major merger candidate pairs for which the BCG is at most a factor of four more massive than the companion. These pairs have been selected by a physical separation of $7 \leq r_{\rm sep} \leq 50$ kpc. We use a $\Delta v \leq 300$ km s^{-1} cut to select pairs that may potentially merge.

4.2.2.2 Investigating the spectroscopic completeness of the close pairs

Not every galaxy in the close pair sample has a spectroscopic redshift. This can simply be due to the fact that the galaxies did not meet the selection criteria of SDSS's spectroscopic surveys (see Table 4.1) or fiber collision problems caused them not to be targeted for spectroscopy. Fiber collisions take place because the minimum separation of the SDSS spectroscopic fibers is 55″ (in a single mask) and if two objects are within 55″ of each other, then only one of them will be observed[7] (Zehavi et al. 2002; Blanton et al. 2003). Our close pair sample is therefore spectroscopically incomplete which in turn will cause close pairs to be missed because one or more galaxies in these pairs have no spectroscopy. It is therefore necessary to correct any derived results for this spectroscopic incompleteness. We do this by determining how the spectroscopic completeness of our close pair sample changes as a function of the selection criteria of the SDSS spectroscopic surveys. Through this approach we assign each galaxy in our close pair sample a spectroscopic weight, with which the pair fraction is determined later.

We begin to derive the correction for spectroscopic incompleteness (hereafter C-correction) by first considering the three spectroscopic surveys in SDSS: the Main Galaxy Sample (MGS; Strauss et al. 2002), the Luminous Red Galaxy (LRG; Eisenstein et al. 2001) sample and the Baryon Oscillation Spectroscopic Survey (BOSS; Ahn et al. 2012). Each of these surveys used different selection criteria to determine which galaxies would be targeted for spectroscopic follow-up observations. The selection criteria for each of these surveys are summarised in Table 4.1. We also consider the angular separation ($r_{\rm ang}$) of the galaxies in the close pairs since fiber collisions also influence the spectroscopic completeness of the close pair sample.

[7]Note: repeat observations mean that many galaxies closer than 55″ are observed in practice.

TABLE 4.1: Summary of the selection criteria used in the MGS, LRG and BOSS sample to target galaxies for spectroscopy. Column 2 and 3 respectively give the magnitude limit and galaxy colour selection of each survey. Due to the transition of the 4000 Å break from the g to r-band at $z \sim 0.4$, both the LRG and BOSS surveys have to use two different selection criteria to select galaxies for spectroscopic follow-up below and above this redshift.

	Sample	**Magnitude (mag)**	**Colour**
`MGS`		$r_{\rm petro} < 17.77$	
`LRG`	Cut I ($z < 0.4$)	$r_{\rm petro} \leq 19.2$	$(g-r)$
	Cut II ($z > 0.4$)	$r_{\rm petro} \leq 19.5$	$(r-i)$
`BOSS`	LOWZ ($z < 0.4$)	$r_{\rm cmod} \leq 19.6$	$(g-r)$
	CMASS ($z > 0.4$)	$i_{\rm cmod} \leq 19.9$	$(r-i)$

The correction for spectroscopic incompleteness we apply to our close pair sample is determined as a function of four variables: the r-band Petrosian magnitude ($r_{\rm petro}$), $(g-r)$ and $(r-i)$ colours of the galaxies along with the pairs' angular separation distances[8]. The C-correction is given as:

$$C = \frac{N_{\rm pairs\,in\,spec.\,sample}(r_{\rm petro}, g-r, r-i, r_{\rm ang})}{N_{\rm pairs\,in\,phot.\,sample}(r_{\rm petro}, g-r, r-i, r_{\rm ang})} \tag{4.6}$$

where $N_{\rm pairs\,in\,spec.\,sample}$ and $N_{\rm pairs\,in\,phot.\,sample}$ respectively indicates the number of pairs in the spectroscopic and photometric samples.

The C-correction as a function of the angular separation distance

Consider the $r_{\rm ang}$ of the close pairs in our sample which have spectroscopy from the SDSS's MGS, LRG or BOSS samples. We show the spectroscopic completeness of the pairs (derived using Eq 4.6)

[8]There may be other factors that affect spectroscopic completeness, for example the surface brightness limit of the survey, which has not been considered here.

as a function of $r_{\rm ang}$ in Fig 4.2. It follows that the spectroscopic completeness of the close pairs is fairly constant with $r_{\rm ang}$, suggesting that we do not need to correct the close pair sample for separation distance.

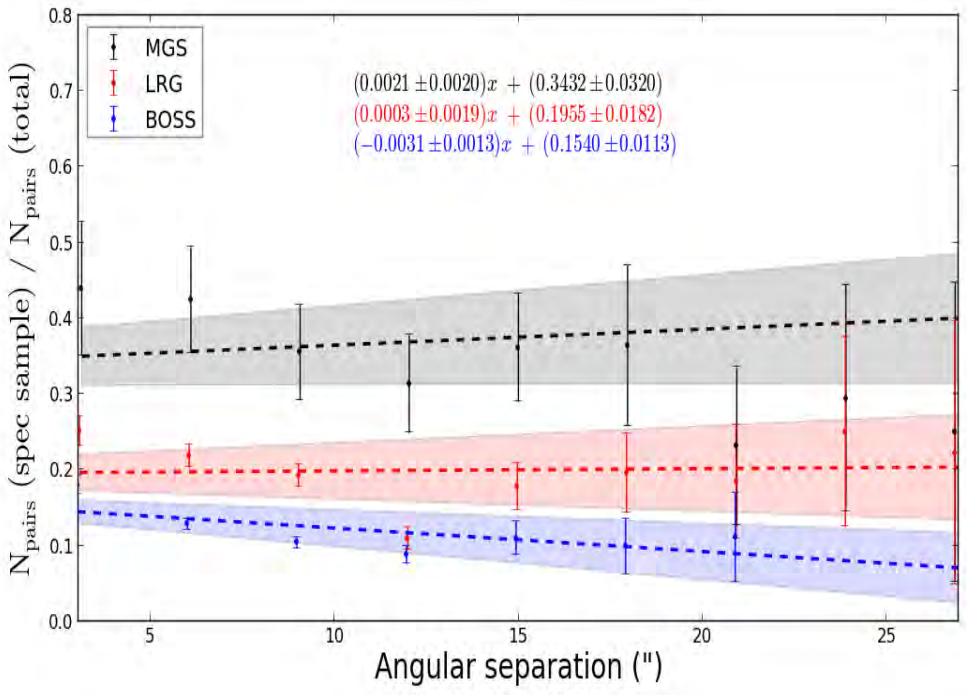

FIGURE 4.2: The spectroscopic completeness of the close pairs in the MGS (black), LRG (red) and BOSS (blue) surveys as a function of the angular separation (in arcsec). The dashed lines are the least-square best-fitting lines to the respective surveys while the shaded regions indicate the 1σ uncertainties. The spectroscopic completeness of the pairs is consistent with a zero slope within 2σ, suggesting that no correction is needed for the pair separation.

The C-correction as a function of $(g-r)$, $(r-i)$ and $r_{\rm petro}$

Since no correction is needed for $r_{\rm ang}$, the C-correction is now only dependent on three variables, i.e. the $r_{\rm petro}$ magnitudes, the $(g-r)$ and $(r-i)$ colours.

We determine the C-correction as function of these three variables by constructing a three-dimensional cube where each of the three variables represent an axis (see Fig 4.3). The galaxies in our close pair sample are divided into $r_{\rm petro}$ magnitude slices of ~ 1.4 mag to ensure a smooth C-correction transition between the voxels. The $(g-r)$ vs. $(r-i)$ colour diagram of the galaxies in each magnitude slice is then plotted. Thereafter, Eq 4.6 is used to determine the C-correction of each voxel.

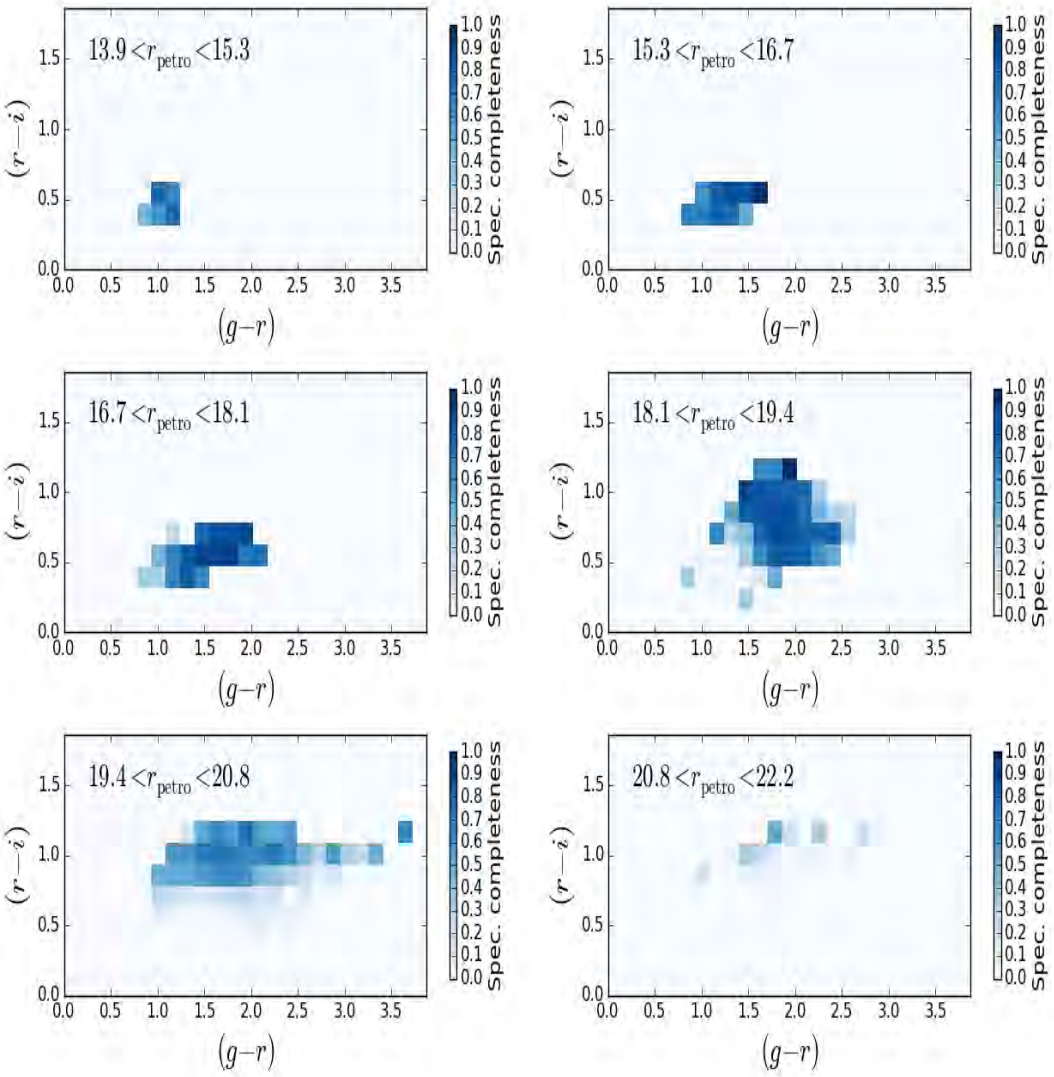

FIGURE 4.3: The spectroscopic completeness of our pair sample as a function of $(g-r)$ and $(r-i)$ colours for six $r_{\rm petro}$ magnitude slices for the close pairs in the MGS, LRG and BOSS surveys. The colour bar to the right of each panel represents the value of the C-correction for each voxel. At $r_{\rm petro} \gtrsim 20.8$ mag (last panel) the spectroscopic completeness of the sample drops to ~ 0. See text for more details.

Since the close pairs in the MGS, LRG and BOSS surveys are considered together to construct Fig 4.3, we expect the spectroscopic completeness of our pair sample to drop around $i_{\rm cmod} \leq 19.9$ mag since this is the magnitude limit of the BOSS survey (see Table 4.1). For BCGs this magnitude roughly corresponds to 20.8 in the r-band. Not surprising, this is exactly where we see the drop in the

spectroscopic completeness of our pair sample (refer to last panel of Fig 4.3). Consequently, for any galaxy with a magnitude fainter than $r_{\rm petro} \gtrsim 20.8$ we set the C-correction equal to zero. Without spectroscopy we cannot determine which fraction of these galaxies are bound to their host BCGs or included in the sample due to projection effects. We do not attempt to address this problem in our analysis and simply require that only galaxies with $m_{\rm i} \leq 19.9$ mag be included in our close pair sample. This is done to ensure that we have a close pair sample with a high spectroscopic completeness. With the C-correction in hand we continue to calculate the pair fraction by using Eq 4.2.

Not every companion in the close pair sample will merge with the BCGs. We use merger timescales ($t_{\rm merge}$) to determine how many companions will actually merge with their host BCGs by $z = 0$. We now continue on to the main aim of the chapter, measuring the stellar mass growth of the BCGs due to major mergers.

4.2.3 The mass growth of BCGs

The stellar mass growth of the BCGs, due to major mergers, is determined as follows. We first derive the merger timescale of each companion in the close pair sample. Merger timescales are dependent on the separation distance, relative velocity and mass ratios of galaxies. Kitzbichler & White (2008) used the Millennium Simulation (Springel et al. 2005) to determine merger timescales as a function of stellar mass and projected separation for galaxy pairs with $r_{\rm sep} \leq 50\,{\rm kpc}$ and $\Delta v \leq 300\ \ {\rm km\,s^{-1}}$. For galaxy pairs that satisfy these criteria, Kitzbichler & White (2008) found an average merger timescale of

$$\langle t_{\rm merge} \rangle = 2.2\,{\rm Gyr}\,\frac{r_{\rm sep}}{50\,{\rm kpc}}\left(\frac{M_{\star,{\rm com}}}{5.5\times10^{10}\,{\rm M_\odot}}\right)^{-0.3}\left(1+\frac{z}{8}\right) \tag{4.7}$$

where $M_{\star,{\rm com}}$ is the total stellar mass of the companion at its observed redshift (which we determine from `kcorrect`), $r_{\rm sep}$ is the physical separation distance (in kpc) and z is the photometric redshift of the cluster.

Thereafter, we calculate the average merger rate, $\langle R_{\rm merge} \rangle$, of the sample, i.e. the number of mergers per BCG per Gyr, as follows:

$$\langle R_{\rm merge} \rangle = \frac{\langle f_{\rm pair} \rangle}{\langle t_{\rm merge} \rangle} \tag{4.8}$$

where $\langle t_{\rm merge} \rangle$ is the average merger timescale of the companions in the sample. The uncertainty on $\langle R_{\rm merge} \rangle$ is determined using the standard propagation of errors. Various works (e.g. Conroy et al. 2007a; Bertone & Conselice 2009; Conselice 2009; Kauffmann et al. 2010) have commented that the merger timescales estimated using the Kitzbichler & White (2008) equations are significantly longer than the estimate from dynamical friction or the orbital period (e.g. Binney & Tremaine 1987; Bell et al. 2006b). We will test what effect this claim has on the measured mass growth.

Semi-analytical models, for example Conroy et al. (2007b); Puchwein et al. (2010); Laporte et al. (2013) have shown that $30 - 80\%$ of the companion's stellar mass ends up in the ICL during a merger with the BCG. During a merger, we assume that 50% of the companion's stellar mass is transfered to the BCG ($f_{\rm mass} = 0.5$; also used by Liu et al. 2009; 2015; Burke & Collins 2013; Lidman et al. 2013). To account for this possible range of $f_{\rm mass}$ values, we assign an uncertainty of 20% to our assumed $f_{\rm mass}$ value of 50% (i.e. $f_{\rm mass} = 0.5 \pm 0.2$). This uncertainty is propagated through to the measured fractional mass growth. In order to calculate how much mass (ΔM) major mergers add to a BCG from redshift z_i down to $z = 0$, we use the following:

$$\Delta M_{z=z_i-0} = \langle R_{\rm merge} \rangle \times T_{\rm LB} \times \langle M_{\star,\,\rm com} \rangle_{z_i} \times f_{\rm mass} \tag{4.9}$$

where $T_{\rm LB}$ and $\langle M_{\star,\,\rm com} \rangle_{z_i}$ respectively gives the lookback time and the average stellar mass of the companions at z_i.

The fractional mass increase (F) of the BCGs (due to major mergers) with respect to their stellar masses at $z = 0$, denoted $\langle M_{\star,\,\rm BCG} \rangle_{z=0}$, is calculated as follows:

$$F = \frac{\Delta M_{z=z_i-0}}{\langle M_{\star,\,\rm BCG} \rangle_{z=0}} \tag{4.10}$$

with

$$\langle M_{\star,\,\rm BCG} \rangle_{z=0} = \langle M_{\star,\,\rm BCG} \rangle_{z_i} + \Delta M_{z=z_i-0} \tag{4.11}$$

where $\langle M_{\star,\,\mathrm{BCG}}\rangle_{z_i}$ the average stellar mass of the BCGs at redshift z_i. The uncertainty on F is determined using the standard propagation of errors.

4.3 Results and Discussion

4.3.1 The redshift evolution of the pair fraction

Several studies in the literature, e.g. Le Fèvre et al. (2000); Kartaltepe et al. (2007); de Ravel et al. (2009); López-Sanjuan et al. (2012); Keenan et al. (2014) parameterized the evolution of the pair fraction with the following power-law function:

$$\langle f_{\mathrm{pair}}\rangle(z) = \langle f_{\mathrm{pair},0}\rangle \times (1+z)^m \tag{4.12}$$

For the following discussion we only consider the pair fraction that has been derived by considering the BCGs that form part of the evolutionary sequence. Unless stated otherwise we identify possible major merger candidates using $\Delta v \leq 300$ km s^{-1} and measure the pair fraction (within $7 \leq r_{\mathrm{sep}} \leq 50$ kpc) using the C-correction.

First let us consider the photometric pair fraction (see Fig 4.4). As explained earlier, using photometry will inevitably include projection effects into the close pair sample. The resulting pair fraction can be seen as an upper limit since the pair fraction will be higher than in the case where a correction for contamination was applied. Let us now apply a 50% contamination correction and compare the resulting pair fraction to that derived using the C-correction. Applying a 50% contamination correction reduces the photometric pair fraction to $\sim 10\%$, while the C-correction results in a pair fraction of $\sim 6\%$. The C-correction therefore results in a pair fraction which is $\sim 4\%$ lower than that obtained using the 50% contamination correction, suggesting that our C-correction is larger than the 50% contamination correction often assumed. Subsequently, the pair fraction will likely be overestimated if one only applies a contamination correction of 50%.

In Chapter 2 we have shown that SDSS did not detect some obvious bright objects around the BCGs. Approximately 1% of the BCGs in our sample suffered from this bright contamination

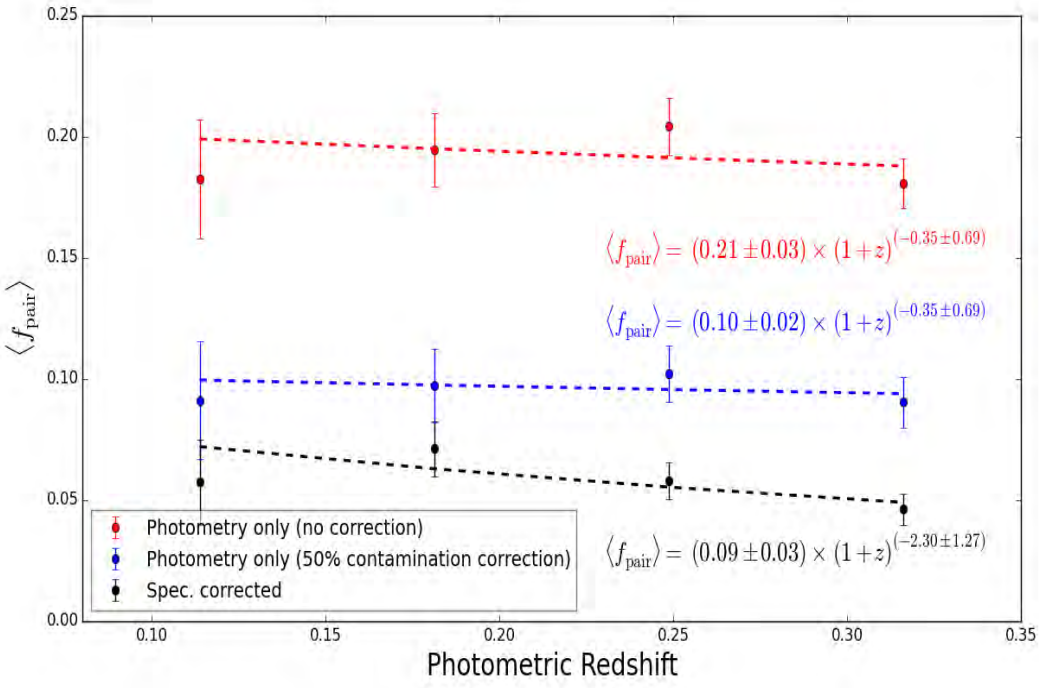

FIGURE 4.4: The photometric pair fraction derived within $7 \leq r_{\rm sep} \leq 50$ kpc. For comparison we also show $\langle f_{\rm pair} \rangle$ derived by (i) applying a 50% contamination correction (blue symbols) and (ii) using the C-correction (black symbols) to measure the pair fraction. The dashed lines represent the best-fitting power-law through the observed pair fractions. See text for details.

problem. We lack spectroscopic information for these objects and can therefore only investigate the influence of these 'extra', bright objects on the photometric BCG pair fraction. These bright objects have a negligible influence on the photometric BCG pair fraction since it increases by less than 0.5% if they are included.

In Section 2.2.2 we explained that the redMaPPer catalogue does not necessarily only contain galaxies that are located on the red-sequence, i.e. galaxies on the blue cloud might also be included. We test whether the redMaPPer catalogue only includes red galaxies by using a method similar to that of Lu et al. (2009) to separate the red-sequence galaxies from their blue counterparts. We refer the reader to Lu et al. (2009) for details. However, very briefly, we obtain the width of the red-sequence of the clusters by fitting a single Gaussian against the galaxies with high probabilities of being red-sequence cluster members ($P_{\rm RSM} > 0.9$). The galaxies within 2σ of the red-sequence are considered to be part of the red-sequence while those below this limit are classified as blue galaxies. Using these criteria we find that not all the galaxies in the redMaPPer catalogue with $P_{\rm RSM} > 0$ are located on

the red-sequence, since a small fraction (7%) of these galaxies are blue. Using these colour cuts, we queried the SDSS DR8 database and found that ~ 200 blue galaxies have not been included in the redMaPPer catalogue. This in turn suggests that the catalogue does not include all the companions that may possibly merge with the BCGs. Including these 200 'missed' blue companion galaxies into the close pair sample and remeasuring the photometric pair fraction, results in an increase of less than 1%. We refer the interested reader to Appendix C for a more detailed discussion.

Several studies in the literature use luminosity ratios[9], rather than stellar mass, to identify potential major merger candidates (e.g. Liu et al. 2009; 2015; Edwards & Patton 2012; Burke & Collins 2013; Keenan et al. 2014; Burke et al. 2015, and others). We test whether it has any effect on the measured pair fraction if we use luminosity (rather than stellar mass) to identify potential major merger candidates in the redMaPPer catalogue. By using luminosity, we add an additional $\sim 4\%$[10] to the close pairs that have been selected using stellar mass ratios. We find that the luminosity selected major mergers have no perceivable effect on the BCG pair fraction (measured using stellar mass ratios).

As mentioned earlier, galaxies with small separation distances may be missed during the construction of the close pair sample. It is therefore advisable to impose a lower $r_{\rm sep}$ limit when close pairs are identified in order to allow for fair comparisons to simulations and other observational studies. For our close pair sample, we determined a minimum $r_{\rm sep}$ value of 7 kpc. If we compare the pair fraction, derived within $7 < r_{\rm sep} \leq 50$ kpc to that measured without the inner radius cut, we find that the total pair fraction decreases by 0.3% at most.

Next, we investigate what effect our choice of velocity difference had on the measured pair fraction. When we remeasure the pair fraction by using $\Delta v \leq 500$ km s^{-1} to identify possible major merger candidates, we find that it only increases $\langle f_{\rm pair} \rangle$ by $\sim 0.03\%$ (result not shown).

We now investigate how our measured pair fraction (where only BCGs part of evolutionary sequence has been considered, Section 3.2.4) compares to that derived if *all* BCGs in the redMaPPer catalogue are considered. We find that the pair fractions are consistent within the uncertainties. This in turn

[9] Major mergers have luminosity ratios of 1:4 or less.
[10] These pairs are spread out over the redshift range of interest.

suggests that the pair fraction of BCGs, involved in major mergers, does not depend on the halo mass of their host cluster.

In summary: Considering BCGs that form part of the cluster evolutionary sequence, we searched for possible major merger candidates within a search radius of $7 < r_{\rm sep} \leq 50$ kpc. Thereafter we determined the BCG pair fraction using the C-correction. Our results suggest that the major merger pair fraction increases with decreasing redshift. Our results do not depend sensitively on the choice of $r_{\rm sep}$, Δv or whether luminosity (rather than stellar mass) is used to identify major mergers candidates.

4.3.1.1 Comparison to the literature

In Fig 4.5 we show the comparison of our measured pair fraction against values obtained from the literature. We compare against the results of studies conducted in clusters and the field. The majority of the studies discussed hereafter have derived pair fractions within $r_{\rm sep} \leq 30$ kpc. We have therefore chosen to only show the pair fraction we obtained by considering close pairs within the same physical separation distance.

We note that the BCG pair fraction within 30 kpc increases more drastically with decreasing redshift than the pair fraction within 50 kpc. This implies that $\langle f_{\rm pair} \rangle$ is dependent on the search radius. This is a direct result of the fact that the number of companions decreases with search radius, therefore decreasing the number of mergers.

Studies done in clusters:

Both McIntosh et al. (2008) and Liu et al. (2009) have studied the BCG pair fraction (over $0.01 \leq z \leq 0.12$) by searching for close pairs within 30 kpc. McIntosh et al. (2008) studied the major merger fraction of massive red galaxies in groups with $M_h \geq 2.5 \times 10^{13}\,M_{\odot}$. While many of their galaxies are in halos of similar masses to our clusters, their sample also includes lower mass groups. Both these studies further restricted their samples to only consider close pairs where both the BCG and companion show signs of morphological distortions (i.e. diffuse tails and asymmetries in the inner isophotes). These distortions indicate that the galaxies are in the process of merging. By only

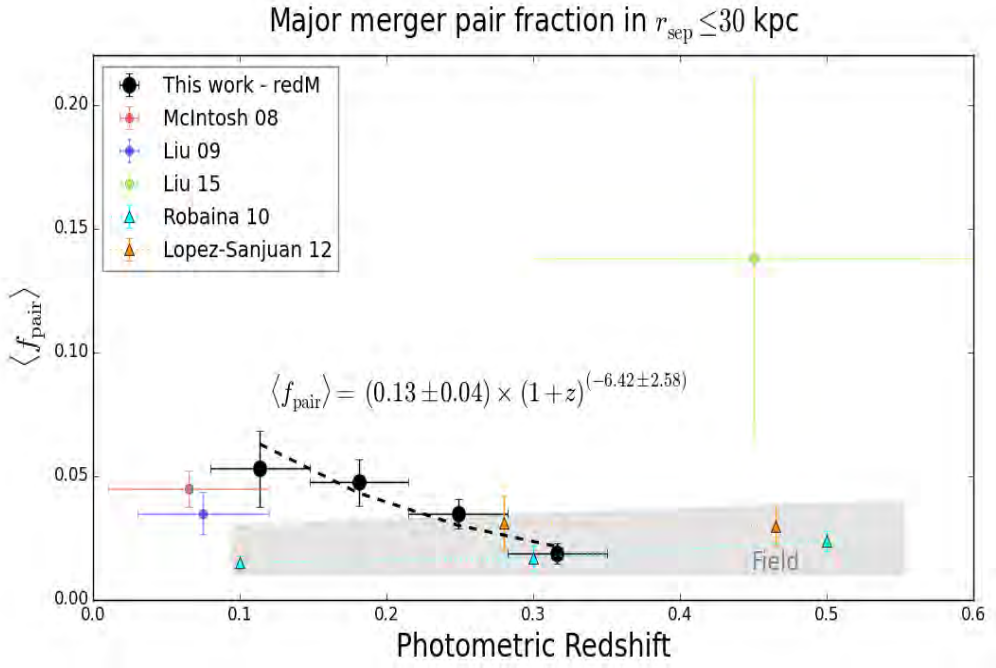

FIGURE 4.5: Literature comparison of the major merger pair fraction $r_{\rm sep} \leq 30$ kpc. The dashed line represents the best-fitting power-law through our measured pair fractions. The points indicate values obtained from studies done in clusters while the shaded region represents the values obtained from studies done in the field. We only indicate the pair fractions of two field studies (represented by triangles) as examples, chosen because they defined major mergers in the same way as we do in this thesis. The pair fractions from the literature are plotted at the average redshifts of the samples while the horizontal error bars indicate the width of the redshift bins. See text for details.

considering major mergers (luminosity ratios $\leq$ 1:4), McIntosh et al. (2008) found that 38 of their 845 close pairs were morphologically distorted, giving $\langle f_{\rm pair} \rangle = 0.04 \pm 0.01$, assuming Poisson errors (red point). Similarly, Liu et al. (2009) found $\langle f_{\rm pair} \rangle = 0.03 \pm 0.01$ (18/515) by assuming Poisson errors (blue point).

Only our first redshift bin overlaps with the redshift range used in the above-mentioned studies ($z \leq 0.12$). We measure a pair fraction of 0.05 ± 0.01 at $z \sim 0.11$, which is consistent within the uncertainties to that above. The main difference between our study and that of McIntosh et al. (2008); Liu et al. (2009) is the technique used to select mergers: morphological distortions vs. close pairs. Mergers identified through morphological distortions are in the final stages of merging. Galaxies in these pairs are typically expected to merge within $\sim$ 0.2 Gyr (e.g. Patton et al. 2002; Hernández-Toledo et al. 2005; Lotz et al. 2011). The close pair technique on the other hand selects mergers that are in various stages of the merging process (early to final stages). For major merger pairs with a separation distance of $\sim$ 50 kpc, Lotz et al. (2011) estimate a merger timescale

of roughly 0.6 Gyr. For pairs with $r_{\rm sep} \sim 30$ kpc, $t_{\rm merge}$ decreases to 0.33 Gyr (Lotz et al. 2011). The merger timescales of the pairs in our sample is therefore longer (on average) than those in McIntosh et al. (2008); Liu et al. (2009). It is therefore not unreasonable that our pair fraction is higher than that of McIntosh et al. (2008); Liu et al. (2009).

Another reason that may explain our high pair fraction is the fact that we impose a velocity difference to identify potential major merger candidates. We are not able to measure the three dimensional velocities of galaxies and the only way close galaxy pairs can be identified is to determine their line-of-sight velocities (by using spectroscopy). By imposing a velocity difference, one is able to identify pairs of galaxies that are potentially gravitationally bound to one another (as illustrated in Fig 1.7). The velocity cut however may still cause false-positive pairs to be introduced in the sample, subsequently making our pair fraction higher (in comparison to McIntosh et al. 2008; Liu et al. 2009).

In a later study, Liu et al. (2015) extended their analysis to investigate the role of major mergers in the mass growth of BCGs between $0.3 \leq z \leq 0.6$. Using the same methodology as in Liu et al. (2009), they find that 4 of their 29 BCGs have morphological distortions, giving $\langle f_{\rm pair} \rangle = 0.45 \pm 0.07$, assuming Poisson errors (green point). No comparison to the other studies is possible due to the difference in redshift ranges. We include this study for completeness, but note that it is limited by small number statistics.

Field studies:

There are numerous studies over the years that have investigated the close pair fraction of galaxies in the field (e.g. Carlberg et al. 2000; Patton et al. 2000; Lin et al. 2004; 2008; Kartaltepe et al. 2007; Hsieh et al. 2008; Bundy et al. 2009; de Ravel et al. 2009; Jogee et al. 2009; Robaina et al. 2010; López-Sanjuan et al. 2012; Keenan et al. 2014; Robotham et al. 2014). For this discussion, we do not attempt to make a detailed comparison of clusters galaxies and those in the field. We rather use this comparison to show the different pair fractions that are observed between these two environments. The shaded region in Fig 4.5 represent the range of pair fractions in the field. We only indicate the pair fractions of two field studies as examples.

Jogee et al. (2009); Robaina et al. (2010); Keenan et al. (2014); Robotham et al. (2014) investigated the close pair fraction of field galaxies with $M_\star \geq (2-5) \times 10^{10}\,\mathrm{M}_\odot$ over $0.1 \leq z \leq 1.2$. The close pairs were selected to be within $r_{\mathrm{sep}} \leq 30$ kpc and $\Delta v \leq 500$ $\mathrm{km\,s^{-1}}$, although Keenan et al. (2014) also imposed a lower r_{sep} limit of 7 kpc on their close pair sample selection. These studies all considered major mergers, although the major merger definition differed slightly from study to study. Jogee et al. (2009); Robaina et al. (2010) used stellar mass ratios of (1:4), while Robotham et al. (2014) used a mass ratio of (1:3). Keenan et al. (2014) in turn used luminosity ratios of (1:4) to define major mergers. The results from these studies suggested that the pair fraction experienced a very mild evolution since $z \sim 1$.

The studies of Lin et al. (2008); López-Sanjuan et al. (2012) used $10 \lesssim r_{\mathrm{sep}} \lesssim 50$ kpc and $\Delta v \leq 500$ $\mathrm{km\,s^{-1}}$ to identify close galaxy pairs in the field between $0.2 \leq z \leq 0.9$. The galaxies in these studies had $M_\star \geq 10^{11}\,\mathrm{M}_\odot$. Both these studies only considered major mergers, however López-Sanjuan et al. (2012) used stellar mass ratios of (1:4) to identify major mergers, while Lin et al. (2008) used luminosity ratios of (1:4) instead. These studies continued to separate the red and blue galaxies in their samples, whereafter they investigated the pair fraction for each of these galaxy population. López-Sanjuan et al. (2012) found that the major merger rate for blue galaxies decreased rapidly with decreasing redshift, while this evolution was slower for red galaxies. Lin et al. (2008) observed the same trend for their blue galaxies, however they found that the red galaxy pair fraction increased with decreasing redshift. The same results were observed by other studies that separated red (ETGs) and blue (LTGs) galaxies (e.g. Bundy et al. 2009; de Ravel et al. 2009). More interesting though is the fact that they found that the major merger fraction of ETGs was higher than that of LTGs. Robotham et al. (2014) found a similar result, i.e. the major merger pair fraction of high mass galaxies was higher than for lower mass galaxies. Liu et al. (2009) in turn found that the pair fraction (specifically for major mergers) increased with halo mass.

A direct comparison between our observed $\langle f_{\mathrm{pair}} \rangle$ and that measured in the field is beyond the scope of this work. It is however useful to indicate how the pair fraction of field galaxies evolve with redshift, since it can be used to determine whether the redshift evolution of major mergers in galaxy clusters follow the same pattern as those in the field. The results of all the above-mentioned field studies indicate that little to no evolution took place in $\langle f_{\mathrm{pair}} \rangle$ since $z \sim 1$. Our results on

the other hand suggest that the major merger pair fraction in clusters increases with decreasing redshift, a result that was also found by Lin et al. (2008) for the red galaxies in their field sample.

4.3.2 Mass growth due to mergers

We used the method outlined in Section 4.2.3 to determine the fractional mass growth that major mergers have contributed towards the stellar mass growth of a present day BCG since a given redshift. This mass growth has been derived under the assumption that half of the stellar mass of the companion is accreted onto the BCG ($f_{\rm mass} = 0.5 \pm 0.2$). The fractional mass growth results are summarised in Table 4.2. Major mergers increased the stellar mass of a present day BCG by $24 \pm 14\%$ (on average) since $z = 0.32$.

Various works have commented that the Kitzbichler & White (2008) merger timescales are significantly longer than the estimate from dynamical friction or the orbital period (e.g. Conroy et al. 2007a; Bertone & Conselice 2009; Conselice 2009; Kauffmann et al. 2010). What effect does this claim have on the fractional mass growth we measured, since we used Kitzbichler & White (2008) to derive $t_{\rm merge}$ estimates for our close pairs? The average merger timescale of our close pairs at $z = 0.32$ is $t_{\rm merge}$ of 0.77 ± 0.55 Gyr. This uncertainty is large enough to encompass differences with other methods (see Table 4.2) and is propagated through to the measured fractional mass growth.

TABLE 4.2: Summary of the fractional mass growth that major mergers have contribute towards the stellar mass growth of a present day BCG since a given redshift. The average merger timescales of the close pairs at the given redshifts are also indicated, where the uncertainty is determined using the standard propagation of errors.

z	F **(Eq 4.10)** **(%)**	$\langle t_{\rm merge} \rangle$ **(Gyr)**
0.11	13 ± 8	0.79 ± 0.53
0.18	20 ± 12	0.69 ± 0.52
0.25	24 ± 15	0.63 ± 0.50
0.32	24 ± 14	0.77 ± 0.55

We also investigate what effect the 'extra' bright objects (that have not been detected in SDSS) may have on our measured fractional mass growth of the BCGs since $z = 0.32$. In Chapter 3, we found that contamination from these 'extra' bright objects would bias the BCG stellar masses by 8% in the worst case. If we assume that these bright objects will all bias their host BCGs' stellar masses with this percentage when they merge, we find that our measured BCG fractional mass growth of $24 \pm 14\%$ increases by less than 2%. We conclude that these bright objects have a negligible effect on the BCGs' fractional mass growth.

4.3.2.1 Comparison to the literature

In Fig 4.6 we show the comparison of our measured BCG fractional mass growth (due to major mergers within $7 \leq r_{\rm sep} \leq 50$ kpc, black points) to that derived from studies in the literature. For all the studies we only show the fractional mass growth due to major mergers, assuming $f_{\rm mass} = 0.5$.

Using morphological distortions as an indication of mergers, Liu et al. (2009) found that major mergers would increase a present day BCG's stellar mass by $15 \pm 10\% \, (f_{\rm mass}/0.5)$ on average from $z = 0.7$ (blue point) at a mean rate of $2.5 \pm 1.7\% \, (f_{\rm mass}/0.5)$ per Gyr. Liu et al. (2015) in turn found that major mergers, on average, contributed $35 \pm 15\% \, (f_{\rm mass}/0.5)$ to the stellar mass build-up of a present BCG since $z = 0.6$ (green point).

In a separate study, Burke et al. (2015) used close pairs (identified within 50 kpc) to study the stellar mass build-up of BCGs over $0.18 < z < 0.9$. Their sample included mergers down to stellar mass ratios of 1:20 and they are therefore considered both major and minor mergers. They found that these mergers increased the BCGs' stellar masses by a factor of 1.2 since $z = 0.9$. They estimate that $\sim 32\%$ of the total merging mass is locked up in major mergers (with mass ratios of 1:2−1:5, cyan point). Extending this analysis out to $0.8 < z < 1.4$, Burke & Collins (2013) found that major mergers (mass ratios of 1:1−1:2) contributed $53 \pm 30\%$ to the stellar mass growth of BCGs since $z \sim 1$ (grey point), while the remainder of the mass growth was contributed by minor mergers (mass ratios of >1:3−1:20).

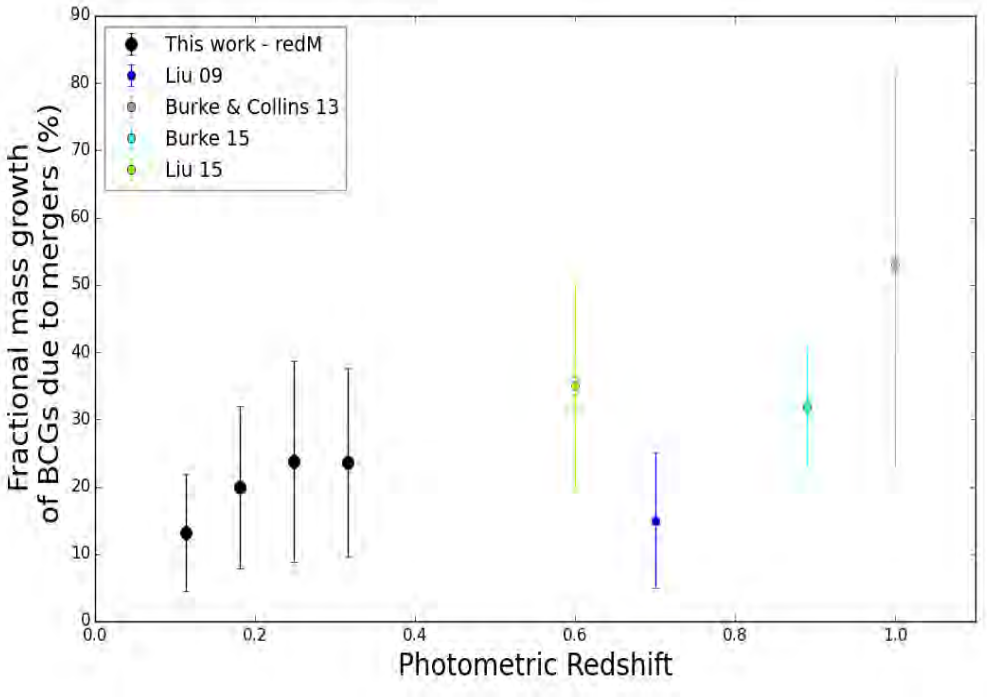

FIGURE 4.6: Comparison of our measured fractional mass growth that a present day BCG will experience (on average) due to major mergers since a given redshift. The mass growths have been measured from the redshift they are plotted at, down to $z = 0$ (assuming $f_{\rm mass} = 0.5$). See text for details.

The recent simulation of Laporte et al. (2013) predicts that major and minor mergers will change the BCGs' stellar masses by factors of 1.4 ± 0.3 and 2.9 ± 0.6 over $0.0 < z < 0.3$ and $0.0 < z < 1.0$ respectively. They also predict that anything between 30% and 80% of the accreted mass will end up in the ICL during mergers. This ICL prescription causes the predicted mass growth to be in better agreement with what is observed (e.g. Lidman et al. 2012; Lin et al. 2013; Bai et al. 2014). Simulations with no ICL prescription, for example De Lucia & Blaizot (2007); Tonini et al. (2012), predict a mass growth factor of ~ 4 between $z = 1 - 0$.

In summary: Using our sample of close galaxy pairs (identified within $7 \leq r_{\rm sep} \leq 50$ kpc), we find that major mergers contributed $24 \pm 14\%$ (on average) towards the stellar mass growth of a present day BCG since $z = 0.32$, assuming that half of the merging mass was accreted onto the BCGs. We will combine the results from both this chapter and that of Chapter 3 in Chapter 6 to form a complete picture regarding the importance of mergers in the stellar mass build-up of BCGs.

Chapter 5

Investigating the BCG pair fraction between $0.4 \leq z \leq 0.5$ using SALT observations

"May the Sun bring you new energy by day, may the Moon softly restore you by night, may the rain wash away your worries, may the breeze blow new strength into your being, may you walk gently through the world and know its beauty all the days of your life."

Apache blessing

5.1 Introduction

In this chapter we extend our study of the mass growth of BCGs out to moderately high redshifts, by investigating the pair fraction of BCGs between $0.4 \leq z \leq 0.5$.

We cannot use SDSS data to investigate the BCG pair fraction at these moderately high redshifts, because the spectroscopic completeness of SDSS drops significantly around $z = 0.4$. Spectroscopic information plays a crucial role in determining whether galaxies in close pairs are bound to one another. We therefore use the Southern African Large Telescope (SALT; Buckley et al. 2006; O'Donoghue et al. 2006) to obtain spectroscopic observations for a sample of close pairs between $0.4 \leq z \leq 0.5$. These pairs, in turn, are used to investigate the BCG pair fraction. This chapter is outlined as follows: the sample of close pairs are described in Section 5.2. This is followed by a description of the observational setup used by SALT to observe these pairs (Section 5.3). Thereafter, the spectroscopic data reduction is described (Section 5.4) and this is followed by the results in Section 5.5. We show the reduced SALT spectra of the close pairs in Section 5.6.

5.2 Sample description – Identification of BCGs and major merger candidates

Only in this chapter do we use the Gaussian Mixture Brightest Cluster Galaxy (GMBCG[1]; Hao et al. 2010) catalogue to identify BCGs that are involved in major mergers. The reasoning behind this is, at the start of this PhD, we initially used GMBCG as the parent catalogue from which we selected close pairs to be targeted by SALT for follow-up spectroscopic observations. However, when we investigated the GMBCG catalogue in detail, we found it difficult to reproduce the BCG magnitudes (by directly querying the SDSS database). Consequently, we decided to use the redMaPPer catalogue for the remainder of this PhD instead. However, at the time the SALT proposals were submitted, the GMBCG catalogue was still in use, and so the close pairs observed with SALT have been selected from the GMBCG catalogue.

We refer the reader to Hao et al. (2010) for a more detailed description of the GMBCG catalogue. Briefly, the catalogue spans a redshift range of $0.1 < z < 0.55$ and contains 55 000 clusters that have been optically identified from SDSS DR7[2] (Abazajian et al. 2009) by searching for overdensities of red-sequence galaxies. The catalogue provides the positions of the BCGs along with the

[1] http://home.fnal.gov/∼jghao/gmbcg_sdss_catalog.html
[2] http://classic.sdss.org/dr7/

photometric redshifts of their host clusters. For the remainder of the chapter we will only consider the 13 272 clusters in the redshift range of interest ($0.4 \leq z \leq 0.5$, with a median redshift of $z = 0.45$). Using the BCG positions we queried the DR7 database and retrieved all companions within: (i) a physical radius of 50 kpc and (ii) 1.5 magnitudes (in the i-band) of the BCGs. This resulted in 4814 close pairs. We also retrieved the spectroscopic redshifts (if available) of the galaxies in these close pairs from SDSS DR12[3] (Alam et al. 2015).

Hereafter, the close pairs observed with SALT are referred to as the SALT sample. We submitted two SALT proposals for the purpose of obtaining spectroscopic redshifts ($z_{\rm spec}$) for the galaxies in close pairs between $0.4 \leq z \leq 0.5$. In order for a close pair to make it into our SALT sample, it had to be observable with SALT during the semester of observations. We further restricted the SALT sample to only include close pairs where either the BCG or companion (in each pair) had a $z_{\rm spec}$ in SDSS. SALT observations will then be used to determine the $z_{\rm spec}$ of the remaining galaxy for the purpose of determining whether these galaxies are potential merger candidates or not.

Only 16 of the close pairs satisfied these criteria and we successfully observed 12 of these close pairs. The close pairs in the SALT sample (with corresponding proposal codes) are summarised in Table 5.1. The pairs in 2013-2-RSA-008 were observed between 2013 November and 2014 April, while those in 2014-1-RSA_OTH-009 were observed between 2014 May and October (PI: Groenewald). The SALT telescope is queue-scheduled, meaning that observations of a particular galaxy pair could be obtained on different nights throughout an observing semester.

[3]http://www.sdss.org/dr12/

TABLE 5.1: Description of the 12 close pairs in the SALT sample that span a redshift range of $0.4 \leq z \leq 0.5$ (see photometric redshifts of the clusters in Column 5). The pair ID and coordinates of the galaxies in these pairs are indicated as well as the corresponding proposal codes in which these pairs were observed.

Pair ID		**RA (deg)**	**DEC (deg)**	**Cluster $z_{\rm phot}$**	**Proposal code**
337	BCG	190.404850	−0.668280	0.458 ± 0.044	2013-2-RSA-008
	Com	190.406416	−0.667039		
5501	BCG	128.317079	0.108010	0.473 ± 0.018	2013-2-RSA-008
	Com	128.316370	0.108480		
5919	BCG	153.259460	0.812003	0.437 ± 0.027	2013-2-RSA-008
	Com	153.259030	0.809660		
22105	BCG	27.261019	−0.639814	0.417 ± 0.030	2013-2-RSA-008
	Com	27.261605	−0.639844		
22258	BCG	346.949880	0.948270	0.454 ± 0.036	2013-2-RSA-008
	Com	346.949133	0.947189		
23941	BCG	186.754036	0.765942	0.418 ± 0.040	2013-2-RSA-008
	Com	186.753290	0.767780		
24097	BCG	148.316850	1.272180	0.401 ± 0.026	2013-2-RSA-008
	Com	148.316048	1.272079		
431	BCG	206.032182	1.948250	0.470 ± 0.035	2014-1-RSA_OTH-009
	Com	206.031830	1.948720		
5680	BCG	223.098640	0.949810	0.477 ± 0.025	2014-1-RSA_OTH-009
	Com	223.099826	0.950909		
5905	BCG	210.260650	0.275680	0.486 ± 0.026	2014-1-RSA_OTH-009
	Com	210.258767	0.275656		
24726	BCG	218.763280	3.109750	0.411 ± 0.023	2014-1-RSA_OTH-009
	Com	218.763793	3.111125		
52685	BCG	357.091165	0.741055	0.422 ± 0.030	2014-1-RSA_OTH-009
	Com	357.088710	0.741300		

5.3 The spectroscopic observations with SALT

The Robert Stobie Spectrograph (RSS; Burgh et al. 2003) on SALT was used to obtain longslit spectroscopy for the galaxies in the SALT sample. A slit with a width of 2″ was centered on the BCG in each pair and aligned in such a way that both the BCG and companion are observed in a single observation. This allows us to determine the relative velocities between these two galaxies by using the same wavelength calibration (see example shown in Fig 5.1). The RSS observations are conducted using the PG900 grating which covers the main optical features that we are interested in (e.g. the K, H-bands and the 4000 Å break) over $4500 - 7500$ Å. This grating allows us to reach a spectral resolution of 8 Å at 5800 Å (corresponds to a velocity resolution of ~ 85 km s^{-1}).

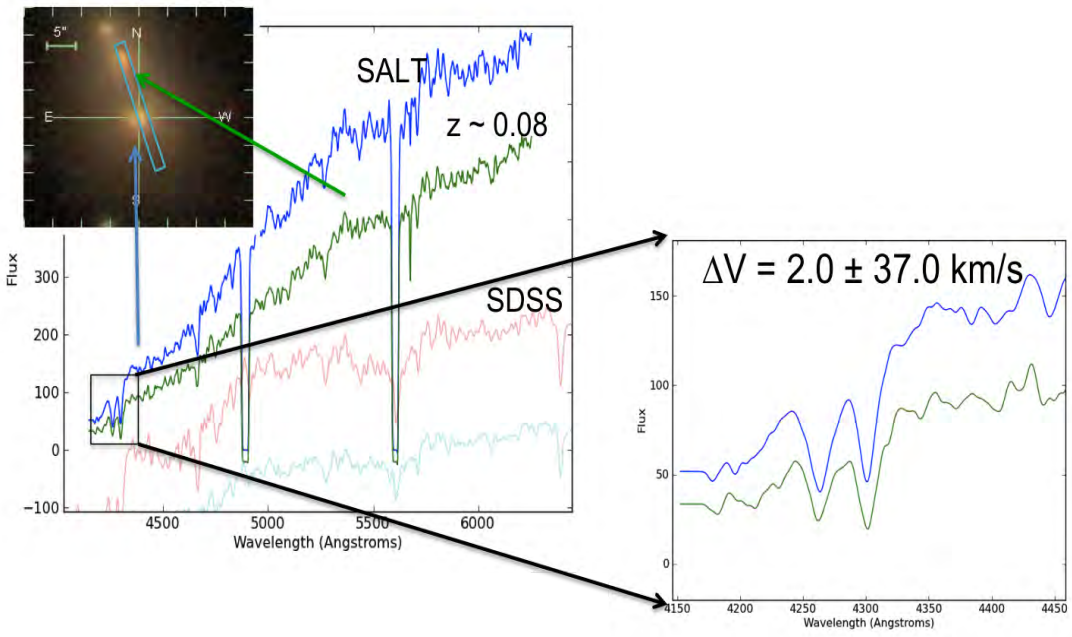

FIGURE 5.1: Example of a close pair (located at $z \sim 0.08$) obtained from the pilot sample with known redshifts that was observed with the SALT telescope. The BCG (blue) and companion (green) are centred in a slit with a width of 2″ and observed in a single observation. The SALT spectra of both galaxies are shown and for comparison the SDSS spectra are also given (BCG/companion shown in red/cyan). The spectroscopic redshifts of the galaxies are determined using the Calcium II H and K-bands. The velocity difference between these gravitationally bound galaxies were determined to be $\Delta V = 2 \pm 37$ km s^{-1}, which is in close agreement with the SDSS measurement.

The SALT telescope is only able to observe objects within certain 'visibility windows' because of the fixed elevation angle of the primary mirror. The close pairs in the SALT sample are equatorial

objects and can be observed for $\sim$ 53 minute intervals with SALT (hereafter observation blocks/tracks). After each track, the tracker on SALT has to be reset and the BCG re-acquired. Each close pair in the SALT sample was observed for a total of 106 minutes. This was split over two observation blocks, where each observation block consisted of 2×20 minute exposures.

5.4 Spectroscopic data reduction

Basic reductions, i.e. gain and cross-talk correction as well as bias subtraction are performed with the `PySALT`[4] package (Crawford et al. 2010) as part of the automated reduction pipeline of SALT. We clean all the science images of cosmic rays by using the `LACosmic`[5] package (van Dokkum 2001). Wavelength calibrations are then performed with standard `IRAF` tasks, i.e. `identify`, `reidentify`, `fitcoords` and `transform`. Thereafter, the one-dimensional spectra of the galaxies in the close pairs are extracted with the `apall` task.

5.4.1 Determining the spectroscopic redshifts

The spectroscopic redshift of each galaxy in the SALT sample is obtained by fitting each galaxy's observed SALT spectrum against the 'Early-type' SDSS galaxy spectral template[6] (hereafter reference spectrum). The rest wavelengths of the Calcium II H and K absorption lines in the reference spectrum are shifted to match those in the galaxy's observed SALT spectrum. The rest wavelengths ($\lambda_{\rm rest}$) of these absorption lines are 3933.7 and 3968.5 Å respectively. Since $\lambda_{\rm rest}$ and the observed wavelengths ($\lambda_{\rm obs}$) of these absorption lines are known, we can determine the spectroscopic redshift of each galaxy as follows:

$$\lambda_{\rm obs} = \lambda_{\rm rest}(1 + z) \tag{5.1}$$

We shift this redshift value with increments of 0.001 and visually inspect the fit. If this results in a sub-optimal fit, we reduce the increments with 1/10 and repeat the process. This is continued until no offset can be detected when the increments are reduced further. This increment value is then

[4] http://pysalt.salt.ac.za/
[5] http://www.astro.yale.edu/dokkum/lacosmic/
[6] http://classic.sdss.org/dr7/algorithms/spectemplates/index.html

taken as the uncertainty on z (σ_z). This method gives comparable uncertainties to using standard cross-correlation techniques for measuring redshifts, for example the `rvsao/xcsao` package (Kurtz et al. 1992) in `IRAF`.

The velocity (v) of each galaxy, with the corresponding uncertainty (σ_v), are determined from:

$$\begin{aligned} v &= z_{\rm spec} \times c \\ \sigma_v &= \sigma_z \times c \end{aligned} \tag{5.2}$$

where c is the speed of light in $\mathrm{km\,s^{-1}}$.

The reduced SALT spectra of the BCGs and companions in the SALT sample are shown in Fig 5.5. A summary of the spectroscopic redshifts of the galaxies in the SALT sample is given in Table 5.2. We are able to verify the SALT spectroscopic redshifts for 12 galaxies (BCGs or companions) since they have spectroscopic redshifts in SDSS. Using $\Delta z = z_{\rm SALT} - z_{\rm SDSS}$, we measure a median redshift offset of $(-9 \pm 20) \times 10^{-4}$, where the uncertainty is given by the standard deviation (see panel a of Fig 5.2). This translates to a velocity difference of (-270 ± 602) $\mathrm{km\,s^{-1}}$. For illustrative purposes we show the difference between the SALT and SDSS velocities of these galaxies in panel b of Fig 5.2.

This analysis shows that there are some differences between the SDSS and SALT spectroscopic redshifts. This could be because the wavelength scale of SDSS is based on heliocentric vacuum wavelengths[7] while the wavelengths from SALT are not. Converting the SALT wavelengths from air to vacuum[8] and also applying a heliocentric correction only reduces the above offset by $20 - 30$ $\mathrm{km\,s^{-1}}$. Another reason for the differences may be related to the fact that we have only used one reference spectrum to derive the SALT redshifts while SDSS on the other hand has used an automated approach to be able to measure the spectroscopic redshifts of thousands of objects. One more reason could be that the wavelength calibration we used is offset from that used by SDSS. If this is the case, then the *same offset* applies to *both* the BCG and companion in each close pair. This in turn makes Δv for each pair robust. Internally we are able to measure the SALT spectroscopic redshifts with an accuracy of 85 $\mathrm{km\,s^{-1}}$.

[7] https://www.sdss3.org/dr9/spectro/spectro_basics.php
[8] For details see http://classic.sdss.org/dr7/products/spectra/vacwavelength.html

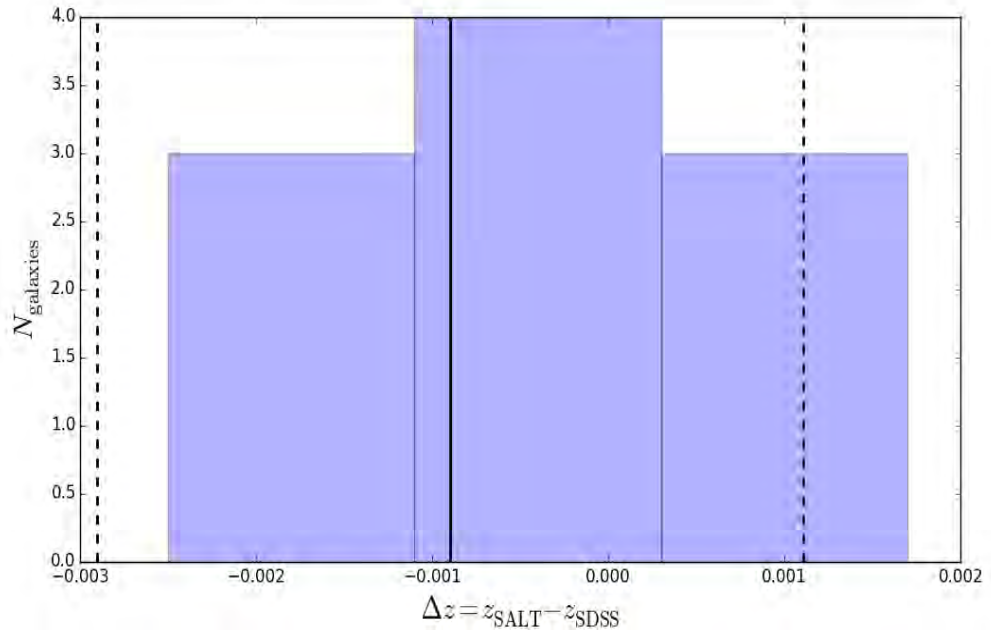

(a) For the galaxies in the SALT sample, we show the difference between the SALT and SDSS spectroscopic redshifts (if available). The solid and dashed lines respectively indicate the median offset and 1σ uncertainty (as given by the standard deviation).

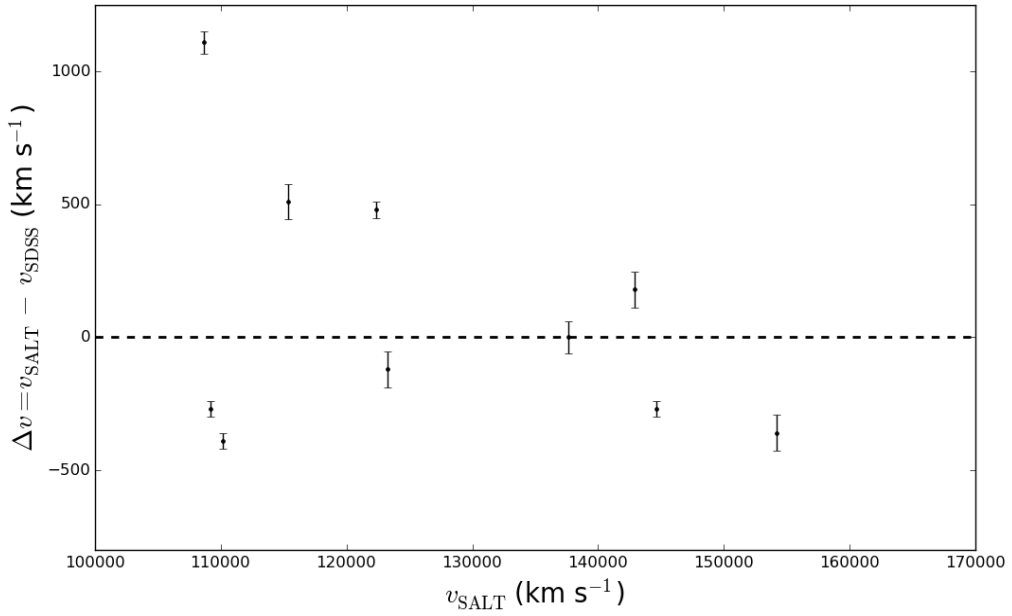

(b) The difference between the SALT and SDSS velocities of the galaxies in the SALT sample. The dashed line indicate the zero offset.

FIGURE 5.2

TABLE 5.2: Summary of the SDSS (if available) and SALT spectroscopic redshifts of the galaxies in the SALT sample. For each close pair the velocity difference, physical separation distance and the estimated merger timescale (derived using Kitzbichler & White 2008, see Eq 4.7) are given. A pair is considered to be a potential merger candidate if $\Delta v \leq 300$ km s^{-1}.

Pair ID		$z_{\rm SDSS}$	$z_{\rm SALT}$	Δv (**km s^{-1}**)	**Pot. merger?**	$r_{\rm sep}$ (**kpc**)	$T_{\rm merge}$ (**Gyr**)
337	BCG	0.4587 ± 0.0001	0.4587 ± 0.0002	21 ± 85	Yes	40.19	1.23
	Com	–	0.4586 ± 0.0002				
5501	BCG	–	0.4754 ± 0.0002	1017 ± 85	No	17.61	–
	Com	0.4748 ± 0.0001	0.4704 ± 0.0002				
5919	BCG	0.4063 ± 0.0001	0.4079 ± 0.0002	4517 ± 85	No	47.28	–
	Com	–	0.4291 ± 0.0002				
22105	BCG	0.3584 ± 0.0001	0.3571 ± 0.0001	685 ± 42	No	11.89	–
	Com	–	0.3602 ± 0.0001				
22258	BCG	0.3686 ± 0.0001	0.3673 ± 0.0002	307 ± 85	No	25.70	–
	Com	–	0.3687 ± 0.0002				
23941	BCG	–	0.5274 ± 0.0001	2612 ± 42	No	37.97	–
	Com	0.5153 ± 0.0002	0.5141 ± 0.0001				
24097	BCG	0.3648 ± 0.0001	0.3639 ± 0.0001	198 ± 42	Yes	15.17	0.39
	Com	–	0.3648 ± 0.0001				
431	BCG	–	0.5377 ± 0.0001	39 ± 42	Yes	11.87	0.38
	Com	0.5432 ± 0.0001	0.5379 ± 0.0001				
5680	BCG	0.4830 ± 0.0001	0.4821 ± 0.0002	40 ± 85	Yes	33.65	0.89
	Com	–	0.4819 ± 0.0002				
5905	BCG	–	0.4760 ± 0.0001	61 ± 42	Yes	38.87	1.03
	Com	0.4757 ± 0.0001	0.4763 ± 0.0001				
24726	BCG	0.3829 ± 0.0001	0.3846 ± 0.0002	152 ± 85	Yes	28.29	0.72
	Com	–	0.3839 ± 0.0002				
52685	BCG	–	0.4114 ± 0.0002	106 ± 85	Yes	48.14	1.62
	Com	0.4113 ± 0.0001	0.4109 ± 0.0002				

5.5 The pair fraction and mass growth of the BCGs due to major mergers

5.5.1 Estimating the pair fraction of the BCGs

In order for a pair to be considered as a potential merger candidate, we require the relative velocity difference between the galaxies to be 300 $\mathrm{km\,s^{-1}}$ or less. From Table 5.2 it follows directly that seven of the 12 close pairs in the SALT sample are potential merger candidates, giving a pair fraction of $\langle f_{\mathrm{pair}} \rangle_{\mathrm{SALT}} = 0.58^{+0.12}_{-0.14}$. The uncertainties on the pair fraction are 1σ values, calculated using the method of Cameron (2011), as described in Section 4.2.1.

Before we derive the BCG pair fraction, we have to ask whether the close pairs in the SALT sample are representative of those in the photometric pair sample. The following selection criteria have been used to select the SALT close pairs: (i) $r_{\mathrm{sep}} \leq 50$ kpc, $\Delta m_{\mathrm{i}} \leq 1.5\,\mathrm{mag}$ and (ii) one galaxy in each close pair had to have a SDSS z_{spec}. We continue to show that the SALT pairs are not different from those in the photometric pair sample since the same r_{sep} and Δm_{i} criteria have been used in both samples to select pairs. The only difference between the SALT and photometric pair samples is the SDSS z_{spec} requirement. We are not worried that the BCGs will not have a spectroscopic redshift in SDSS. Since these massive galaxies are bright and red galaxies, they are very likely to be observed by the SDSS spectroscopic surveys due to the selection criteria of these surveys. The number of pairs observed with SALT should therefore be representative of the number of pairs in the photometric sample.

We can therefore assume that the fraction of potential merger pairs in the SALT sample is representative of the fraction of potential merger pairs found in the photometric pair sample (selected from the GMBCG catalogue). We can thus derive the BCG pair fraction in this redshift range by

rewriting Eq 4.2 as follows:

$$\begin{aligned}\langle f_{\rm pair}\rangle &= \frac{\rm N_{BCGs}\,with\ \geq 1\,companion}{\rm N_{BCGs}} \times \langle f_{\rm pair}\rangle_{\rm SALT} \\ &= \frac{4814}{13272} \times \frac{7}{12} \\ &= 0.36^{+0.004}_{-0.004} \times 0.58^{+0.12}_{-0.14} \\ &= 0.21^{+0.04}_{-0.05}\end{aligned} \tag{5.3}$$

where we assumed that the C-correction of these pairs is unity. The spectroscopic completeness of the pairs in the SALT sample does not depend on the same properties used to derive the C-correction in Chapter 4. Here we are using the fraction of pairs that are potential merger candidates, based on our spectroscopic sample, to correct the photometric pair fraction. This is a slightly higher correction than the 50% we assumed for the photometric sample in Chapter 4 but is consistent within the uncertainties.

The uncertainty on each fraction in Eq 5.3 is the 68.3% binomial confidence limit, calculated using the method of Cameron (2011). The uncertainty on the pair fraction is determined through the standard propagation of errors. This is done as follows:

$$\sigma_{f_{\rm pair}} = \langle f_{\rm pair}\rangle \times \sqrt{A^2 + B^2 + D} \tag{5.4}$$

$$\text{with } A = \frac{\sigma_{f_{\rm pair,SALT}}}{\langle f_{\rm pair}\rangle_{\rm SALT}},\ B = \frac{\sigma_{f_{\rm pair,phot}}}{\langle f_{\rm pair}\rangle_{\rm phot}},\ D = -2\frac{\sigma_{f_{\rm pair,SALT},f_{\rm pair,phot}}}{\langle f_{\rm pair}\rangle_{\rm SALT}\langle f_{\rm pair}\rangle_{\rm phot}}$$

where $\sigma_{f_{\rm pair}}$ is the uncertainty on the pair fractions of the SALT and photometric samples. The D-term is set to zero since the pair fractions in the two samples are independent of each other.

5.5.2 Estimating the mass growth of the BCGs due to major mergers

We use the method outlined in Section 4.2.3 to estimate the mass growth of the BCGs due to major mergers since $z \sim 0.45$. Using the Kitzbichler & White (2008) merger timescales estimates (Eq 4.7), we find that the mergers in the SALT sample have $t_{\rm merge}$ that range from 0.38 to 1.62 Gyr with a mean value of 0.89 ± 0.42 Gyr, where the uncertainty is given by the standard deviation. This

results in a average major merger rate of

$$\begin{aligned}\langle R_{\rm merge}\rangle &= \frac{\langle f_{\rm pair}\rangle}{\langle t_{\rm merge}\rangle} \\ &= \frac{0.21^{+0.04}_{-0.05}}{0.89 \pm 0.42} \\ &= 0.24^{+0.12}_{-0.13} \text{ mergers per BCG per Gyr at } z \sim 0.45\end{aligned} \tag{5.5}$$

The uncertainty on $\langle R_{\rm merge}\rangle$ has been determined using the standard propagation of errors.

Using the methods outlined in Sections 3.2.5 - 3.2.6, we find that the average stellar masses of the BCGs and their close companions in the SALT sample are respectively given as $\langle M_{\star,\,\rm BCG}\rangle = 4.74 \times 10^{11}\,{\rm M}_{\odot}$ and $\langle M_{\star,\,\rm com}\rangle = 3.64 \times 10^{11}\,{\rm M}_{\odot}$. The stellar masses have been determined using the method outlined in Section 3.2.5. Mergers that involve these companions will add the following amount of mass to the BCGs between $z = 0.45 - 0$:

$$\begin{aligned}\Delta M_{z=0.45-0} &= \langle R_{\rm merge}\rangle \times T_{\rm LB} \times \langle M_{\star,\,\rm com}\rangle_{z=0.45} \times f_{\rm mass} \\ &= 0.24^{+0.12}_{-0.13} \times 4.51 \times (3.64 \times 10^{11}\,{\rm M}_{\odot}) \times 0.5 \pm 0.2 \\ &= (1.96^{+1.26}_{-1.32}) \times 10^{11}\,{\rm M}_{\odot}\end{aligned} \tag{5.6}$$

The fractional mass increase of the BCGs, with respect to their stellar masses at $z = 0$, is:

$$\begin{aligned}F &= \frac{\Delta M_{z=0.45-0}}{\langle M_{\star,\,\rm BCG}\rangle_{z=0.45} + \Delta M_{z=0.45-0}} \\ &= \frac{(1.96^{+1.26}_{-1.32}) \times 10^{11}\,{\rm M}_{\odot}}{4.74 \times 10^{11}\,{\rm M}_{\odot} + (1.96^{+1.26}_{-1.32}) \times 10^{11}\,{\rm M}_{\odot}} \\ &= 0.29 \pm 0.17\end{aligned} \tag{5.7}$$

The uncertainty on F has been determined using the standard propagation of errors. A present day BCG will therefore have increased it stellar mass by $29 \pm 17\%$ on average over the last ~ 5 Gyr via major mergers.

Several studies in the literature have used luminosity, instead of mass to search for potential major merger candidates (e.g. McIntosh et al. 2008; Liu et al. 2009; 2015; Edwards & Patton 2012, among others). In Chapter 4 we have shown that it makes no difference to the estimated pair fraction and

merger-inferred mass growth of the BCGs if luminosity, rather than mass selected major merger candidates are considered. We confirm this for the SALT sample by investigating how much the average major merger (selected via luminosity) contributes towards the mass growth of the BCGs since $z \sim 0.45$. The average magnitude difference of the companions in the SALT sample is ~ 0.28 mag in the i-band, corresponding to a (1:1.3) luminosity ratio. The same fractional mass change is measured as in the case where mass selected major mergers are considered (i.e. $F = 29 \pm 17\%$ from $z = 0.45 - 0$).

5.5.3 Comparison to the literature

In Chapter 4 we performed a detailed comparison of our measured BCG pair fraction and fractional mass growth to other studies in the literature. We will not repeat that discussion here, however we supplement that discussion with a comparison of our SALT results to that of Liu et al. (2015). Their redshift range is the closest to the redshift range we probed with the SALT observations (i.e. $0.4 \leq z \leq 0.5$). For the purposes of comparison we derive the BCG pair fraction using close pairs within 30 kpc. Using Eq 5.3 we find $\langle f_{\rm pair} \rangle = 0.09^{+0.06}_{-0.03}$ (magenta point in Fig 5.3).

Liu et al. (2015) used a sample of 29 clusters to investigated the stellar mass assembly of BCGs via major mergers from $0.3 \leq z \leq 0.6$ (with a median value of $z \sim 0.43$). These clusters were selected from the Cosmological Evolutionary Survey (COSMOS[9]; Scoville et al. 2007). The catalogue used by Liu et al. (2015) does not provide information regarding the BCG candidates of the clusters, however the clusters' centres and photometric redshifts are supplied. Using a search radius of 1 Mpc from the cluster centre, Liu et al. (2015) defined the BCG as the brightest galaxy within this aperture. Combining the COSMOS data with high-resolution imagining from HST, they define major merger candidates as BCGs that show morphological distortions[10] due to close companions that have magnitude differences of 1.5 and are within a projected separation distance of ≤ 10 kpc. They find that four of the BCGs in their sample are involved in major mergers, giving a pair fraction of $\langle f_{\rm pair} \rangle = 0.14 \pm 0.07$, assuming Poisson errors (green point in Fig 5.3). For their

[9] http://irsa.ipac.caltech.edu/data/COSMOS/

[10] Liu et al. (2009) find that 3.5% of close pairs are morphologically distorted between $0.03 \leq z \leq 0.12$. McIntosh et al. (2008) find a similar morphologically distorted pair fraction at $z < 0.12$. The same pair fraction was also measured by Conselice et al. (2009) out to $z = 0.2$.

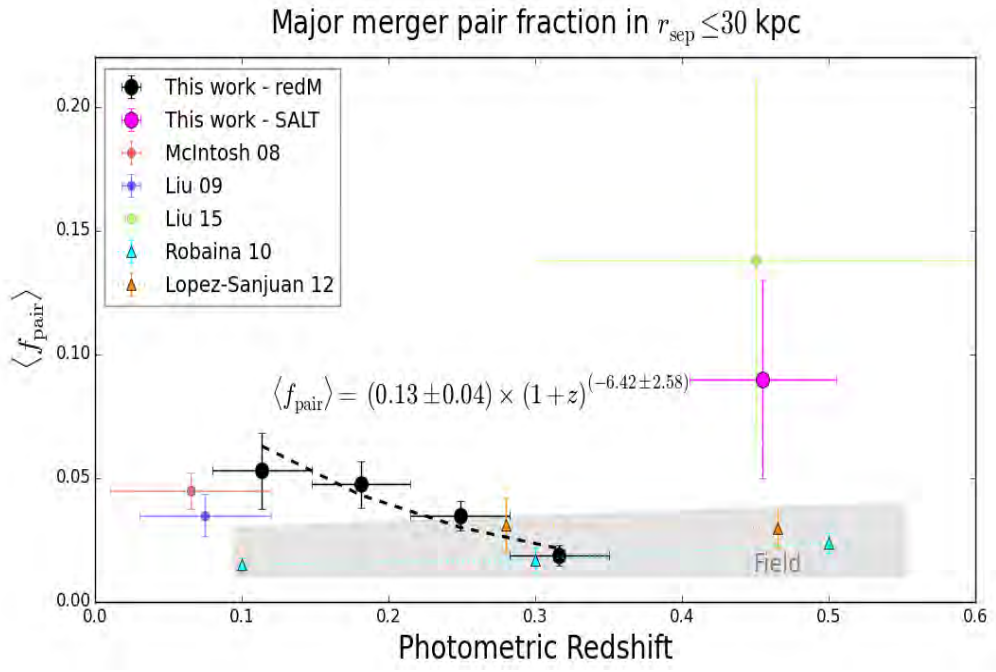

FIGURE 5.3: Literature comparison of the major merger pair fraction $r_{\rm sep} \leq 30$ kpc. The dashed line represents the best-fitting power-law through our measured pair fractions (using the redMaPPer catalogue). The points indicate values obtained from studies done in clusters while the shaded region represents the values obtained from studies done in the field. We only indicate the pair fractions of two field studies (triangles) as examples, chosen because they defined major mergers in the same way as we do in this thesis. The pair fractions from the literature are plotted at the average redshifts of the samples while the horizontal error bars indicate the width of the redshift bins. See text for details.

pairs, they find an average merger timescale of 0.25 Gyr using Kitzbichler & White (2008) in the same way as described above. This results in a major merger rate of 0.55 ± 0.27 merger per Gyr at $z \sim 0.43$. Using the assumption that 50% of the companion's mass is accreted onto the BCG during a merger, they find that a present day BCG has increased (on average) its luminosity or mass by $\sim (35 \pm 15)\%$ since $z = 0.6$ (green point in Fig 5.4).

A direct comparison between our results and that of Liu et al. (2015) must be treated with caution due to the differences between the two studies. This is due to the main difference between the studies, the technique used to select mergers: morphological distortions vs. close pairs. We measure a BCG pair fraction of $0.09^{+0.06}_{-0.03}$ between $0.4 \leq z \leq 0.5$ (within $r_{\rm sep} = 30$ kpc). This is lower than that found by Liu et al. (2015), however the pair fractions are still consistent within the uncertainties.

In order to determine the amount by which a present day BCG has increased its stellar mass since

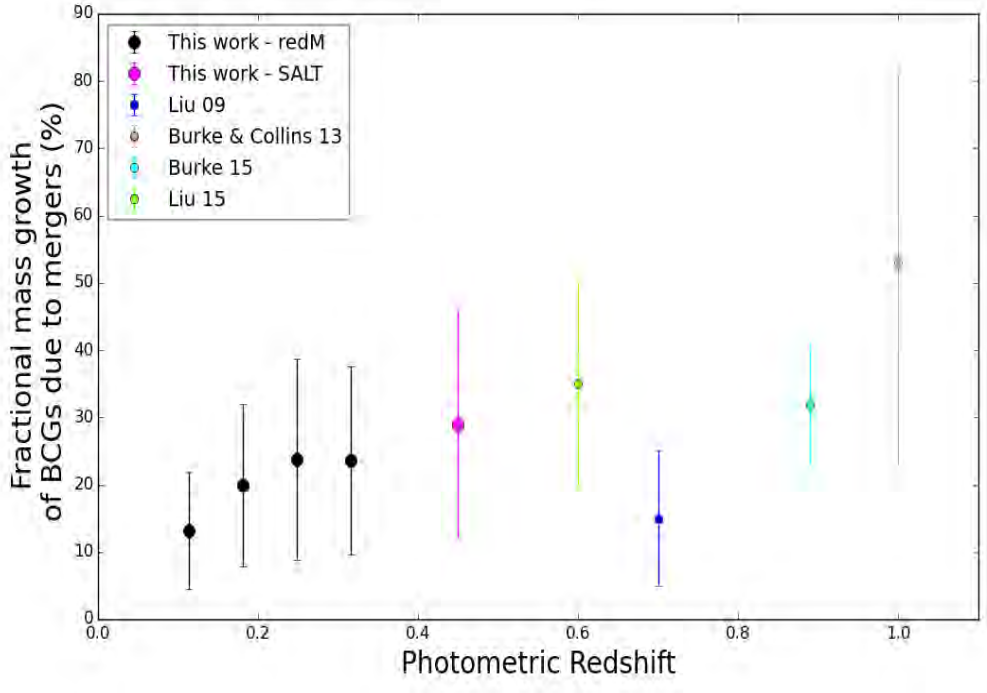

FIGURE 5.4: Comparison of our measured fractional mass growth that a present day BCG will experience (on average) due to major mergers since a given redshift. The mass growths have been measured from the redshift they are plotted at, down to $z = 0$ (assuming $f_{\rm mass} = 0.5$). See text for detail.

$z \leq 0.6$, Liu et al. (2015) used an evolving major merger rate of $(1+z)^{5.2\pm2.4}$. We in turn assumed that the major merger rate is constant with redshift. We find that major mergers, on average, have increased the stellar mass of a present day BCG by $29 \pm 17\%$ since $z = 0.45$ (magenta point in Fig 5.4), with a mean rate of $(6 \pm 4)\%$ per Gyr. This is in close agreement with Liu et al. (2015) who measured a mean mass growth rate of $\sim (6 \pm 3)\%$ per Gyr, despite the differences in assumed evolution.

Caution must be used when the BCG pair fraction, as derived from the GMBCG catalogue is compared to that measured from redMaPPer. This is because when we compared the clusters in both catalogues, we only found $\sim 8\%$ of the clusters overlapped. This suggests that the two catalogues identify different clusters, consequently causing different galaxies to be identified as the BCGs in the two catalogues. As a result the parent photometric samples will be different, leading to different pair fractions. We do not attempt to reconcile the differences between these two studies. We can however make the tentative statement that the trend in the observed major merger pair fraction

(from redMaPPer and SALT) suggests that major mergers continue to play an important role in the stellar mass build-up of BCGs at $z = 0.5$ and lower.

Although the parent photometric samples of the redMaPPer catalogue and the SALT sample may be different, we find these two samples to have very similar mean mass growth rates, i.e. the mean rate by which major mergers will increase the stellar mass of a present day BCG per Gyr. In Chapter 4 we find that major mergers contribute $24 \pm 14\%$ to the stellar mass of a present day BCG from $z = 0.32$, with a mean mass growth rate of $7 \pm 4\%$ per Gyr. This is in very close agreement to the mean mass growth rate of $6 \pm 4\%$ per Gyr derived above using the SALT data. Using the latter growth rate, we find that major mergers will contribute $25 \pm 14\%$ towards the mass growth of a present day BCG since $z = 0.32$ (in very close agreement to the redMaPPer major merger-inferred mass growth result above).

In summary: We used spectroscopic observations from SALT to investigate the importance of major mergers in the stellar mass build-up of BCGs since $z \sim 0.5$. We are not able to use SDSS data for this analysis since the spectroscopic completeness of the survey drops significantly around $z = 0.4$. We find that 2787 BCGs (21% of the total) are involved in major mergers between $0.4 \leq z \leq 0.5$ (with a median value of $z \sim 0.45$). Using merger timescales, we are able to predict how much mass these major mergers have contributed towards the stellar mass growth of a present day BCGs over the last ~ 5 Gyr of their lifetimes. We find that major mergers contribute between $29 \pm 17\%$ to the stellar mass growth of a BCG since $z \sim 0.45$ (on average). This in turn suggest that major mergers have played some role in the stellar mass assembly of a present day BCG over the last 5 Gyr.

5.6 The reduced SALT spectra of the close pairs

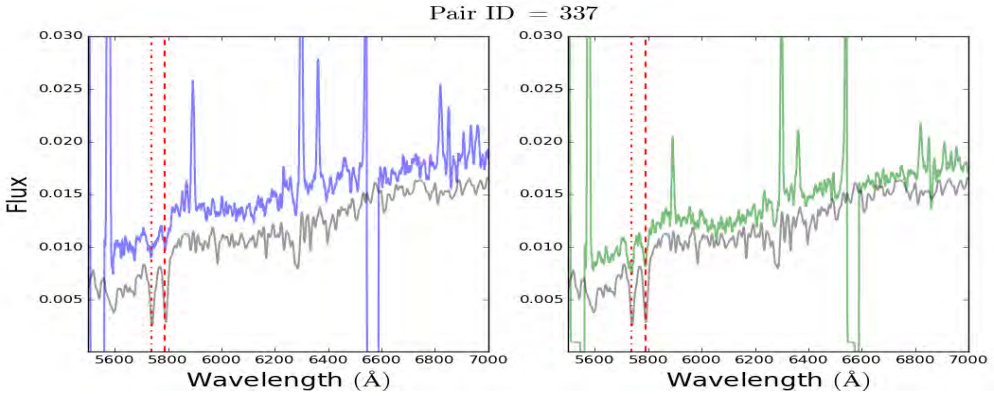

(a) BCG: $z_{\rm spec} = 0.4587 \pm 0.0002$, Comp: $z_{\rm spec} = 0.4586 \pm 0.0002$, $\Delta v = 21 \pm 85\,{\rm km\,s^{-1}}$, Potential merger.

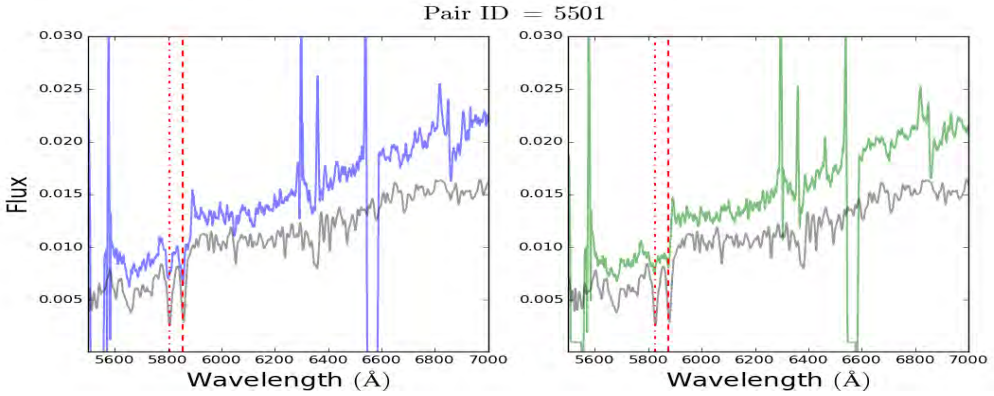

(b) BCG: $z_{\rm spec} = 0.4754 \pm 0.0002$, Comp: $z_{\rm spec} = 0.4704 \pm 0.0002$, $\Delta v = 1017 \pm 85\,{\rm km\,s^{-1}}$, Not a potential merger.

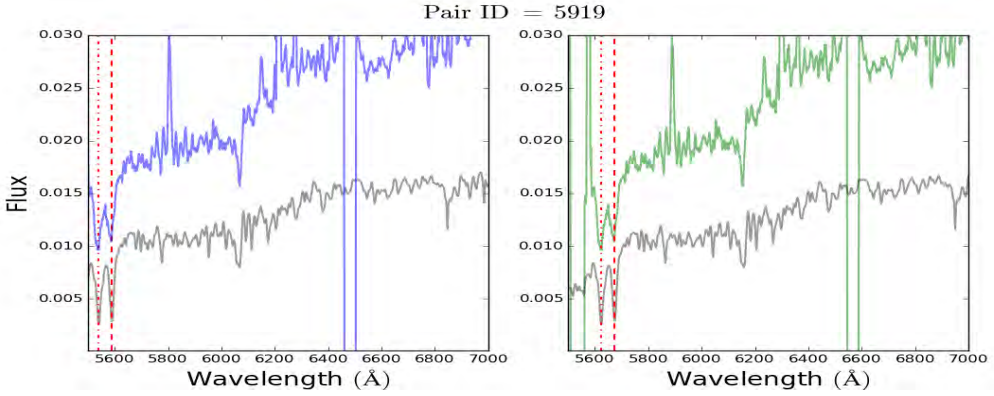

(c) BCG: $z_{\rm spec} = 0.4079 \pm 0.0002$, Comp: $z_{\rm spec} = 0.4291 \pm 0.0002$, $\Delta v = 4517 \pm 85\,{\rm km\,s^{-1}}$, Not a potential merger.

FIGURE 5.5: For each pair we show the reduced SALT spectra of the BCG in blue (left panel) and that of the companion in green (right panel). The SDSS reference spectrum is shown in grey. The observed wavelengths of the Calcium II H and K absorption lines are respectively indicated with the red dashed-dotted and dashed lines. For each close pair we also state the measured SALT $z_{\rm spec}$ of the BCG and companion, their relative velocity difference and comment whether the pair is potentially gravitationally bound.

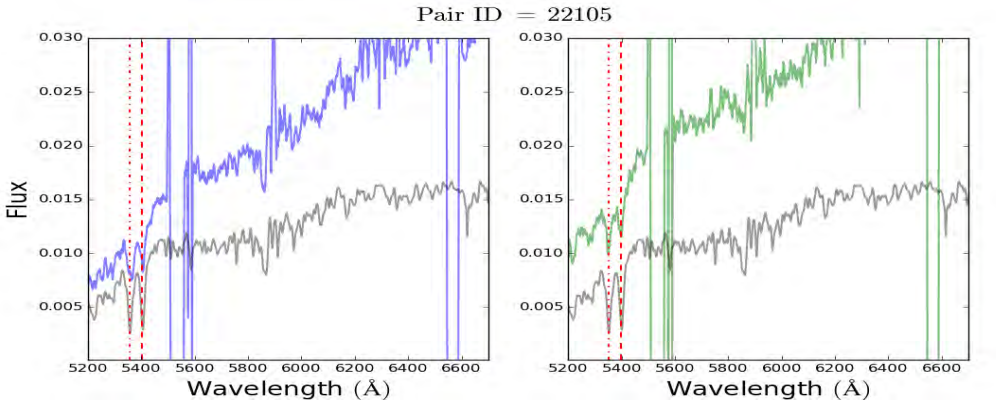

(a) BCG: $z_{\rm spec} = 0.3571 \pm 0.0001$, Comp: $z_{\rm spec} = 0.3602 \pm 0.0001$, $\Delta v = 685 \pm 42\,{\rm km\,s^{-1}}$, Not a potential merger.

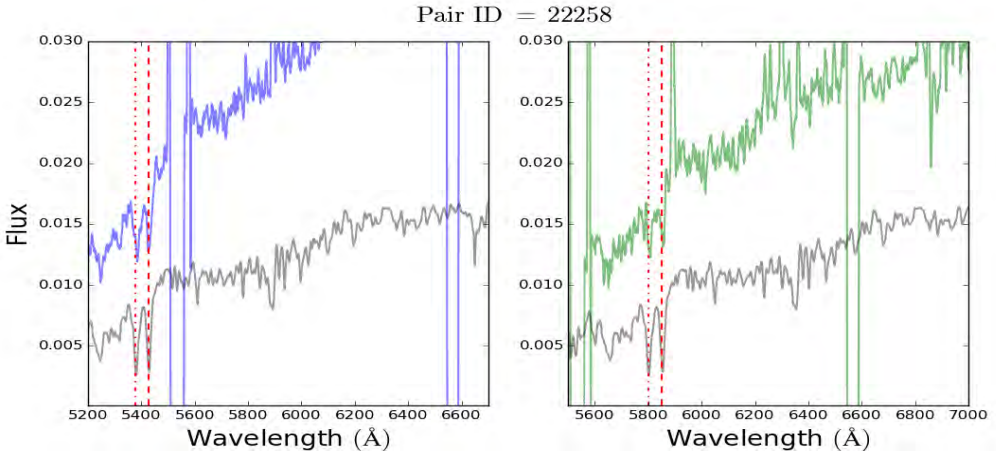

(b) BCG: $z_{\rm spec} = 0.3673 \pm 0.0002$, Comp: $z_{\rm spec} = 0.3687 \pm 0.0002$, $\Delta v = 307 \pm 85\,{\rm km\,s^{-1}}$, Not a potential merger.

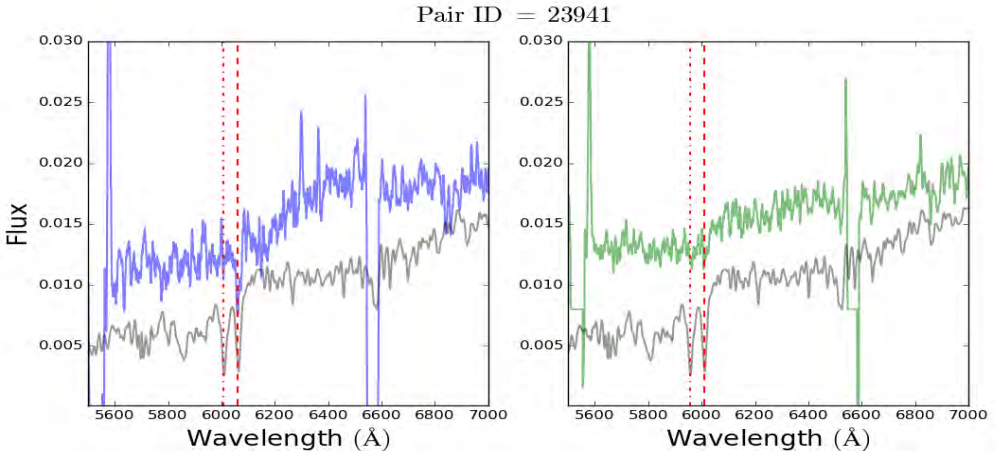

(c) BCG: $z_{\rm spec} = 0.5274 \pm 0.0001$, Comp: $z_{\rm spec} = 0.5141 \pm 0.0001$, $\Delta v = 2612 \pm 42\,{\rm km\,s^{-1}}$, Not a potential merger.

FIGURE 5.5: – Continued.

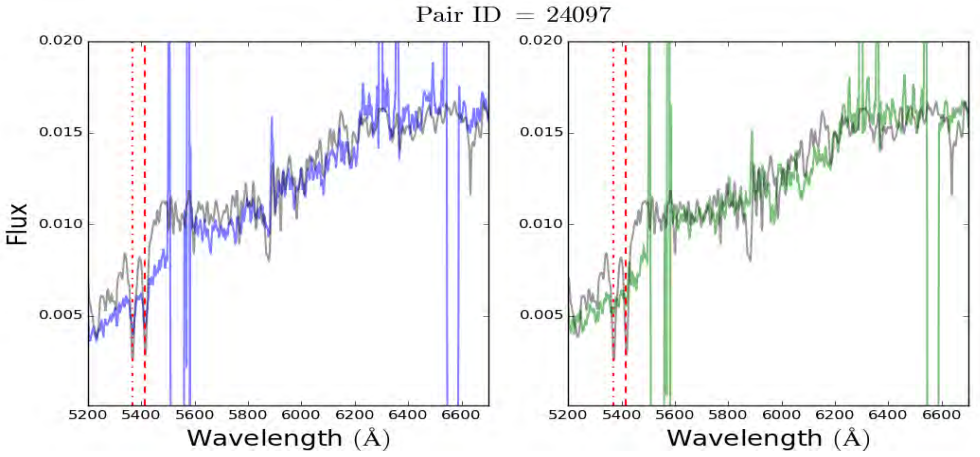

(a) BCG: $z_{\rm spec} = 0.3639 \pm 0.0001$, Comp: $z_{\rm spec} = 0.3648 \pm 0.0001$, $\Delta v = 198 \pm 42\,{\rm km\,s^{-1}}$, Potential merger.

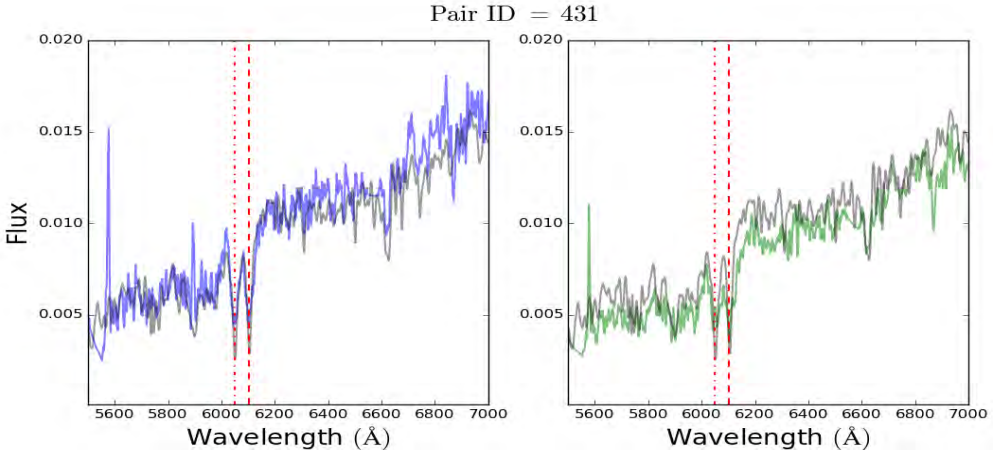

(b) BCG: $z_{\rm spec} = 0.5377 \pm 0.0001$, Comp: $z_{\rm spec} = 0.5379 \pm 0.0001$, $\Delta v = 39 \pm 42\,{\rm km\,s^{-1}}$, Potential merger.

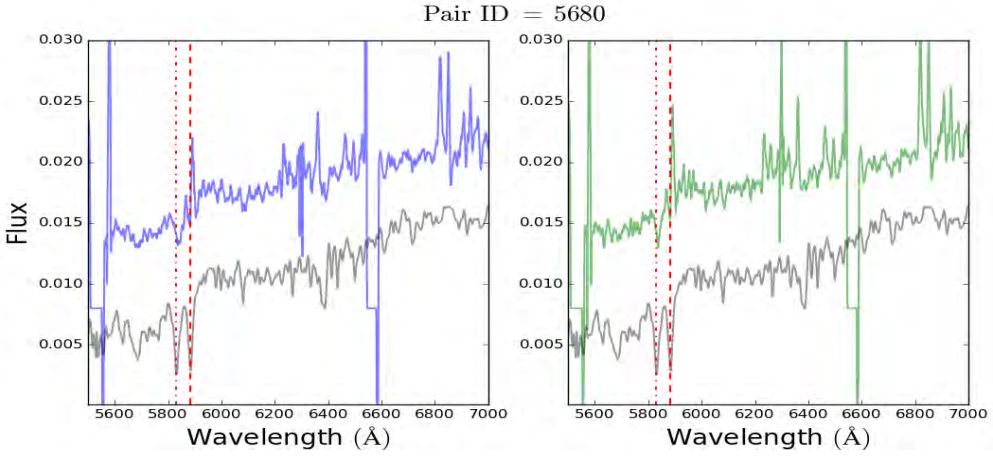

(c) BCG: $z_{\rm spec} = 0.4821 \pm 0.0002$, Comp: $z_{\rm spec} = 0.4819 \pm 0.0002$, $\Delta v = 40 \pm 85\,{\rm km\,s^{-1}}$, Potential merger.

FIGURE 5.5: – Continued.

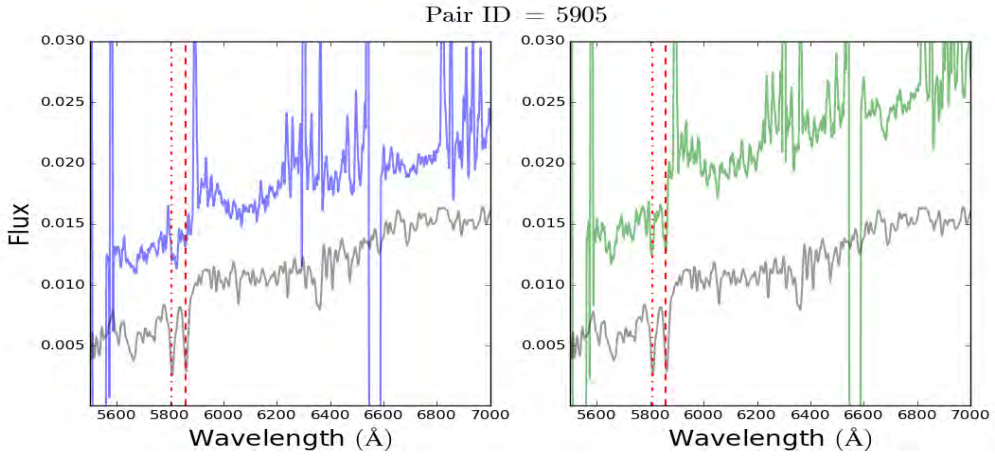

(a) BCG: $z_{\rm spec} = 0.4760 \pm 0.0001$, Comp: $z_{\rm spec} = 0.4763 \pm 0.0001$, $\Delta v = 61 \pm 42\,{\rm km\,s^{-1}}$, Potential merger.

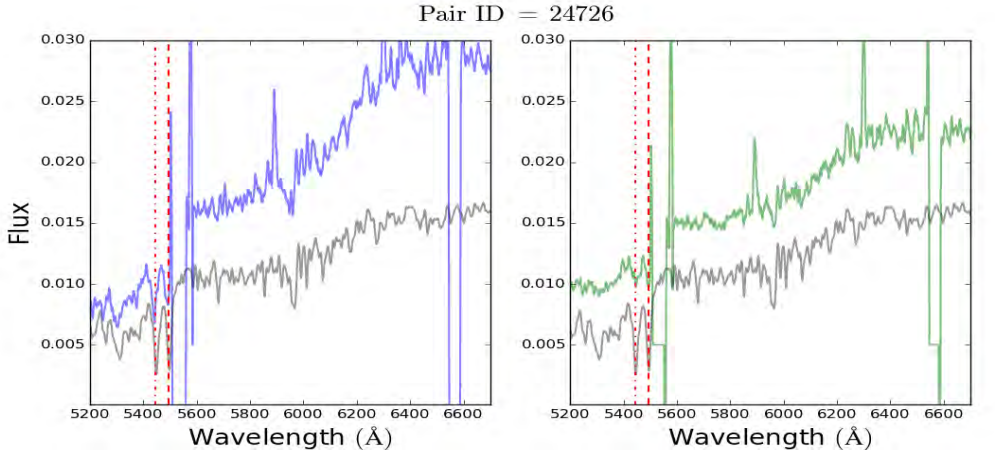

(b) BCG: $z_{\rm spec} = 0.3846 \pm 0.0002$, Comp: $z_{\rm spec} = 0.3839 \pm 0.0002$, $\Delta v = 152 \pm 85\,{\rm km\,s^{-1}}$, Potential merger.

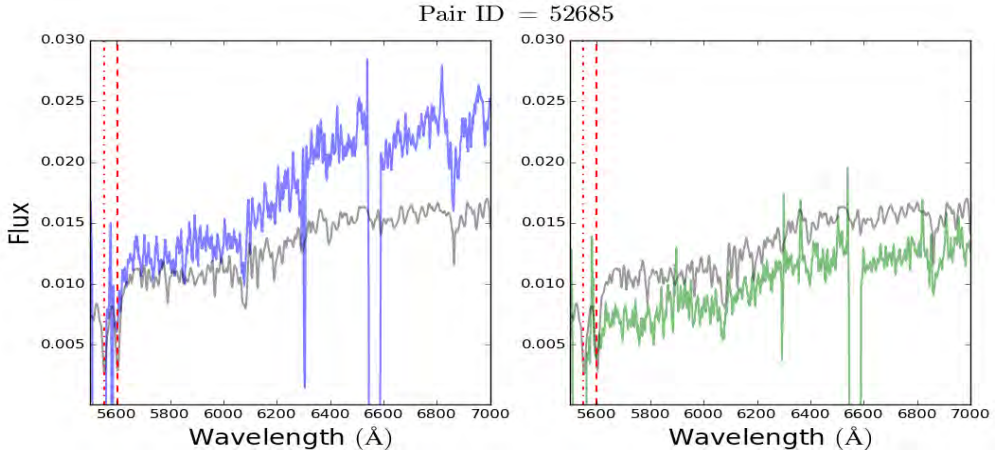

(c) BCG: $z_{\rm spec} = 0.4114 \pm 0.0002$, Comp: $z_{\rm spec} = 0.4109 \pm 0.0002$, $\Delta v = 106 \pm 85\,{\rm km\,s^{-1}}$, Potential merger.

FIGURE 5.5: – Continued.

Chapter 6

Discussion and Conclusions

"You can't just throw a Carroll and Ostlie at a merger tree and hope for the best!"

Eric Bell

Sydney, Feb. 2015

6.1 Introduction

The main aim of this thesis is to study the stellar mass growth of BCGs between $0.08 \leq z \lesssim 0.50$ by paying special attention to the role that major mergers play in the stellar mass growth of these massive galaxies. We have investigated the BCGs' mass growth using two independent methods.

In the first method we only considered the stellar masses of the BCGs themselves and investigated how these evolved as a function of redshift (Chapter 3). This approach allowed us to study the total stellar mass growth of the BCGs. This in turn gave us an insight into the past mass growth of the BCGs where both SF and mergers contributed towards the mass growth, however the fraction of mass each mechanism contributed is not known.

In the second method we used close pairs as a diagnostic of mergers and determined how much these mergers contributed towards the BCGs' stellar mass build-up between $0.08 \leq z \lesssim 0.50$ (Chapters 4

and 5). This approach on the other hand enabled us to investigate the BCGs' future mass growth because the BCGs and their close companions will only merge some time in the future[1].

In this chapter we summarise the main science results we obtained during our analysis and attempt to put the past and future mass growth of the BCGs together in order to form a coherent picture regarding the stellar mass build-up of these massive galaxies over the last 5 Gyr. This chapter is outlined as follows. The main science results from Chapter 3 are summarised in Section 6.2 whereafter the results are compared to those in the literature. We do the same for the results from Chapters 4 and 5 in Section 6.3. In Section 6.4 we discuss how we combine the BCGs' past and future mass growth and discuss the implications of this on our current understanding of galaxy formation and evolution. We draw conclusions in Section 6.5 and comment on future work in Section 6.6.

6.2 Chapter 3 – The stellar mass evolution of BCGs over $0.08 \leq z \leq 0.35$

In order to investigate the stellar mass evolution of BCGs, we determine how the observed $\langle M_\star \rangle$ of the BCGs evolve with redshift. This is done for two cases. In the first case we consider all the BCGs (clusters) in our sample and find negative mass growth for the BCGs, i.e. these massive galaxies are somehow losing mass (or shrinking) as the redshift decreases, which is a non-physical result (see Section 3.3). This highlights the need to take the halo mass growth of the BCGs' host clusters into account when the stellar mass build-up of these massive galaxies is studied. We take this into consideration in our analysis and use evolving M_h limits to select clusters in an evolutionary sequence, assume that the BCGs in these clusters are progenitors/descendants of one another. We also find that SDSS is underestimating the total magnitudes of the BCGs in the lowest redshift bin. We corrected for this and find that the BCGs in the evolutionary sequence increased their stellar masses by $0.98^{+0.15}_{-0.03}$ from $z = 0.35 - 0.08$, however the log-likelihood ratio test slightly favoured a result with no slope at the 95% confidence level (Section 3.3).

[1]This approach is independent of the method of Chapter 3, even though they use the same clusters and photometric data, since the total stellar mass growth depends solely on the photometry of the BCG; the present method, however, has only a weak dependence on the BCG mass (and the companion mass, see Section 4.2.1) and is largely governed by the pair fraction and its completeness correction.

We continue to compare our result to those obtained from the literature. The literature comparison in Section 3.4.1 only includes observational works published prior to 2014 and we therefore expand this comparison here to include the results from more recent observational works along with predictions from theoretical models. We summarise the results of this literature comparison in Table 6.1 and Fig 6.1.

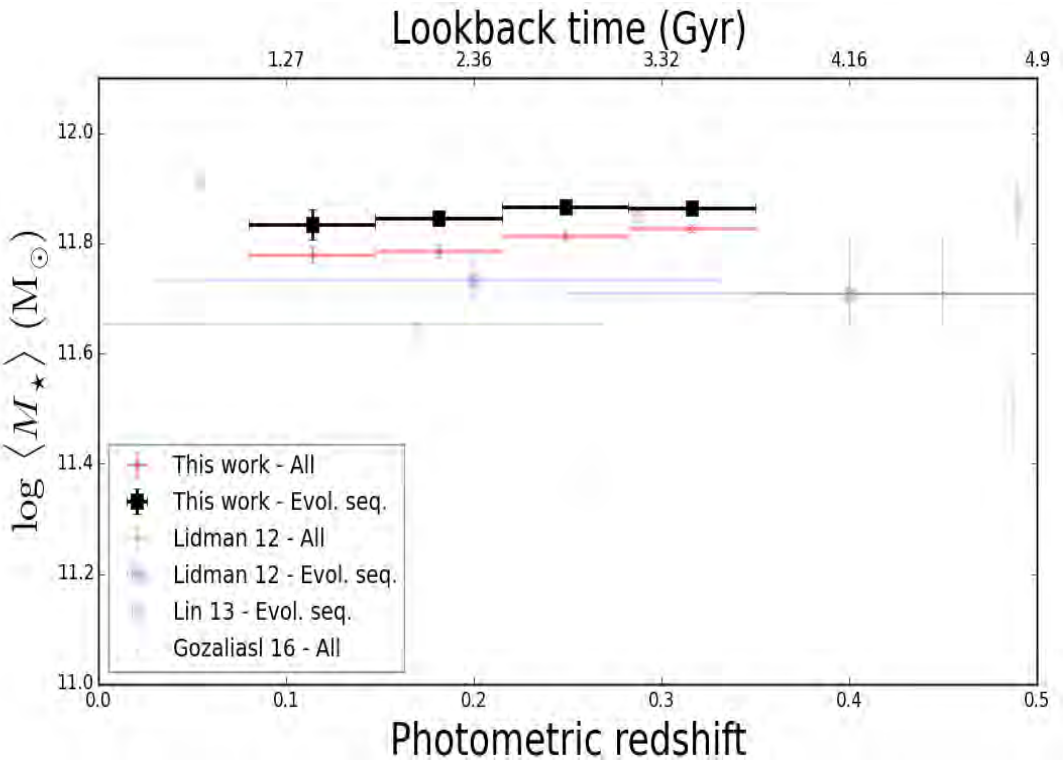

FIGURE 6.1: The stellar mass evolution of BCGs over $0.08 \leq z \leq 0.35$. The mass growth represented by the points has been derived by considering all the clusters. In contrast the mass growth represented by the squares has been derived by taking progenitor bias into account (i.e. only considering clusters that are progenitor/descendants of one another). The vertical uncertainties on our results are derived from bootstrap resampling while the horizontal uncertainties indicate the width of the redshift bins. Comparisons from Lidman et al. (2012) and Lin et al. (2013) are also given. The uncertainties on Lidman's masses are representative of the average uncertainty on $M_\star$.

6.2.1 Discussion

Observational studies

We have already discussed Lidman et al. (2012), Lin et al. (2013) and Oliva-Altamirano et al. (2014) in great detail in Chapter 3, specifically highlighting the differences between these studies and ours. We will not repeat the discussion here, although we refer the reader to Table 6.1 for a

summary of the results from these studies. In short, these studies found that the BCGs did not experience any mass growth over the redshift range of interest ($0.08 \leq z \leq 0.35$).

Recently, Gozaliasl et al. (2016) studied the stellar mass growth of brightest group galaxies (BGGs) over $0.04 < z < 1.3$. Using the XMM-LSS[2] (Pierre et al. 2004), COSMOS[3] (Finoguenov et al. 2007) and AEGIS[4] (Davis et al. 2007) surveys, they constructed a sample of 407 groups with a halo mass range of $12.85 \leq \log(\frac{M_h}{\mathrm{M}_\odot}) \leq 14.02$. They simply identified the BCG as the brightest, red-sequence cluster member (although the band used for this choice is not specified). In order to measure the mass growth of the BGGs, they only considered the groups within the halo mass range of $\log(M_h) = 13.50 - 14.5\,\mathrm{M}_\odot$. These groups were split up into five equally spaced redshift bins, whereafter they determined the average stellar masses of the BGGs in each bin. Using line-fitting they found that the mean stellar mass of BGGs gradually grow by a factor of 1.5 ± 0.3 from $z = 0.9 - 0.2$. It is important to note however that these authors did not take the halo mass growth of their groups into account when they determined the BGG stellar mass growth. They also comment that their observed BGG mass growth is consistent with what Lidman et al. (2012) measures for the mass growth of BCGs in more massive halos over the same redshift range (specifically MGF $= 1.8 \pm 0.3$ for the case where the M_h growth was taken into account). The BGG mass growth factor is however in closer agreement to what Lidman et al. (2012) measures for the mass growth of BCGs in the case where the cluster' M_h growth is not accounted for (MGF $= 1.55 \pm 0.18$).

Over our redshift range of interest Gozaliasl et al. (2016) find that the BGGs will grow by a factor of 1.13 ± 0.22 from $z = 0.3 - 0.1$ (gray points in Fig 6.1). Although they measure some mass growth for the BGGs over this redshift, their measurements are also consistent with no growth, given their large uncertainties. Although the authors do not explicitly apply an evolution correction for the evolving M_h limit, they note that doing so would make very little difference to the clusters included in their sample, and so are approximately consistent with accounting for the group's halo mass growth. This study also probes a lower halo mass range than we do (our clusters span a halo mass range of $14.23 \leq \log(\frac{M_h}{\mathrm{M}_\odot}) \leq 15.34$).

[2]XMM Large Scale Structure Survey, http://vela.astro.ulg.ac.be/themes/spatial/xmm/LSS/index_e.html
[3]Cosmological Evolution Survey, http://cosmos.astro.caltech.edu/
[4]All-Wavelength Extended Groth Strip International Survey, http://aegis.ucolick.org/

Zhang et al. (2016) investigated the stellar mass evolution of BCGs from $z \sim 1$ using the Dark Energy Survey[5] Science Verification data (DES SV; Sánchez et al. 2014). Their sample consisted of 106 X-ray selected clusters and groups from the DES XMM Cluster Survey, spanning a halo mass range of $13.48 \leq \log(\frac{M_h}{\mathrm{M}_\odot}) \leq 15.30$. The BCGs were identified as the brightest red-sequence galaxies, closest to the X-ray emission centres of the clusters (note: band used to select BCG is not mentioned). Using the Millennium Simulation, they identified descendants for the clusters in their observed sample at $z = 1$, for the purpose of constructing an evolutionary sequence for their groups/clusters. They find that the BCGs increased their stellar masses by MGF $= 1.07 \pm 0.22$ from $z = 0.3 - 0.1$. Zhang et al. (2016) probes a lower halo mass range than we do, although there is overlap in the M_h ranges. Since the Zhang et al. (2016) sample includes lower mass clusters, we directly test what influence these less massive clusters have on the derived mass growth of the BCGs. Directly comparing our derived MGF to that of Zhang et al. (2016) over the redshift range of interest, we find that the BCGs in both studies experienced the same mass growth within the uncertainties. Therefore, as far as we can tell, the mass growth of BCGs appears independent of the range of parent halo masses probed (provided they form an evolutionary matched sample).

Bellstedt et al. (2016) studied the stellar mass evolution of BCGs since $z = 1$. Their sample consisted of 98 BCGs with a redshift range of $0.2 < z < 0.6$ and were selected from the RELICS[6] survey. They supplemented these BCGs with those studied in Lidman et al. (2012) to construct a sample of 132 BCGs across $0.04 < z < 1.63$. The clusters in Bellstedt et al. (2016)'s sample have a halo mass range of $14.08 \leq \log(\frac{M_h}{\mathrm{M}_\odot}) \leq 15.40$. They use a method similar to Lidman et al. (2012) to correct for progenitor bias, measuring a mass growth factor of 0.86 ± 0.13 from $z = 0.32$ to $z = 0.18$ for their BCGs. Within the uncertainties, they measure a mass growth factor that is consistent with ours.

The Bellstedt et al. (2016) sample is at some disadvantage since the clusters in the sample have all been selected from different surveys, such as the SPT[7] (Carlstrom et al. 2011), ACT[8] (Swetz et al.

[5]http://www.darkenergysurvey.org/
[6]REd Lens Infrared Cluster Survey.
[7]South Pole Telescope.
[8]Atacama Cosmology Telescope.

2011), ROSAT BCS[9] (Ebeling et al. 1998), MACS[10] (Ebeling et al. 2001) and SPT[11] (Carlstrom et al. 2011) surveys, to name a few. The different surveys use different techniques to locate clusters, i.e. the SpARCS survey detects clusters by looking for overdensities of red-sequence galaxies, while those in SPT have been discovered through the Sunyaev-Zelodvich effect (Zeldovich & Sunyaev 1969; Sunyaev & Zeldovich 1970). These various selection mechanisms may lead to physically different clusters entering the samples (even with nominally the same mass range for each proxy), possibly leading to different measured BCG evolution.

In their independent study, Bai et al. (2014) found that the BCGs' stellar masses have grown by a factor of 1.5 from $z = 0.5 - 0$. Their sample consisted of 37 clusters ($0.3 \leq z \leq 0.9$) that were selected from the first Red-sequence Cluster Survey (RCS; Gladders & Yee 2005), spanning a halo mass range of $13.84 \leq \log(\frac{M_h}{\mathrm{M}_\odot}) \leq 15.30$. The BCGs were selected to be the brightest red-sequence galaxy in each cluster. They supplemented their sample at low redshift ($0.03 \leq z \leq 0.13$) with the BCGs from Gonzalez et al. (2005). Using a method similar to ours, Bai et al. (2014) constructed an evolutionary sequence for their clusters and used these clusters to investigate the mass growth of the BCGs. Unfortunately Bai et al. (2014) does not explicitly mention how they have derived the stellar masses of the BCGs and we will therefore not place too much emphasis on the results of this study.

On the other hand, there are earlier studies that have indicated that there is little to no evolution in the stellar masses of BCGs in both optically selected clusters out to $z = 0.8$ (Whiley et al. 2008) and in X-ray selected clusters as far back as $z \sim 1.5$ (Collins et al. 2009; Stott et al. 2010; 2011). For the BCGs in X-ray selected clusters out to $z \sim 1$, the measured mass growth is small since it is found that these massive galaxies already have $90 - 95\%$ of their final stellar masses in place at these high redshifts. The reason for the 'no growth' result lies in the manner in which the different studies compared their low and high redshift BCGs. Whiley et al. (2008), for example, have matched their clusters according to the halo masses they had at their observed redshifts while studies such as Lidman et al. (2012); Lin et al. (2013); Oliva-Altamirano et al. (2014); Zhang et al.

[9]The ROentgen SATellite Brightest Cluster Sample, http://www.ifa.hawaii.edu/∼ebeling/clusters/BCS.html
[10]The MAssive Cluster Survey, http://www.ifa.hawaii.edu/∼ebeling/clusters/MACS.html
[11]South Pole Telescope.

(2016) took the growth of the dark matter haloes into account when deriving the mass growth of the BCGs.

Theoretical models

De Lucia & Blaizot (2007) used a semi-analytic model, based on the Millennium simulation (Springel et al. 2005), to study the formation and evolution of central cluster galaxies within dark matter. For detailed information on these model, we refer the interested reader to De Lucia & Blaizot (2007). Assuming these central galaxies to be synonymous with BCGs, they find a predicted mass growth factor of 1.48 ± 0.42 from $z = 0.35$ down to $z = 0$ for these massive galaxies. Although this predicted MGF is higher than our observed MGF, we find them to be consistent within the uncertainties.

Tonini et al. (2012) on the other hand used an updated version of the Croton et al. (2006) semi-analytical model to study the mass build-up of BCGs with cosmic time (refer to Tonini et al. 2012, for details). Like the De Lucia & Blaizot (2007) model, this SAM is also based on the Millennium simulation and predicts a MGF $= 0.95 \pm 0.17$ from $z = 0.40 - 0.02$ for BCGs, which is in excellent agreement with our observational MGF (i.e. 0.98 ± 0.03).

TABLE 6.1: Comparison of our derived BCG mass growth factor to those given in the literature. Column 1 indicates the redshift range over which the mass growth has been determined, while Column 2 gives the halo mass ranges of the clusters. Columns 3 and 4 indicate the MGFs derived if all clusters and only clusters that form part of the evolutionary sequence are considered. The last column is the reference to the work from which the results are obtained.

z	M_h **range** ($\times 10^{15}\,\mathrm{M}_\odot$)	**All**	**Evol. seq.**	**Ref.**
$0.35 - 0.08$	$0.17 - 2.20$	0.88 ± 0.01	$0.98^{+0.15}_{-0.03}$	This work
$0.40 - 0.20$	$0.12 - 2.50$	0.88 ± 0.09	0.96 ± 0.20	Lidman et al. (2012)
$0.29 - 0.05$	$0.24 - 0.45$	–	1.14 ± 0.30	Lin et al. (2013)
$0.27 - 0.09$	$0.10 - 1.00$	–	0.93 ± 0.09	Oliva-Altamirano et al. (2014)
$0.30 - 0.10$	$0.03 - 0.32$	1.13 ± 0.22	–	Gozaliasl et al. (2016)
$0.30 - 0.10$	$0.03 - 2.00$	–	1.07 ± 0.22	Zhang et al. (2016)
$0.32 - 0.18$	$0.12 - 2.50$	–	0.86 ± 0.13	Bellstedt et al. (2016)

Continued on Next Page ...

Table 6.1 – Continued

z	M_h **range** ($\times 10^{15}\,\mathrm{M}_\odot$)	**All**	**Evol. seq.**	**Ref.**
$0.50 - 0.00$	$0.07 - 2.00$	–	1.5	Bai et al. (2014)
$0.35 - 0.00$	–	–	1.48 ± 0.42	De Lucia & Blaizot (2007)
$0.40 - 0.02$	–	–	0.95 ± 0.17	Tonini et al. (2012)

In summary: By only considering the stellar masses of the BCGs themselves, we find that these massive galaxies have not experienced any mass growth between $0.08 \leq z \leq 0.35$, in the case where we take the halo mass growth of the clusters into account. This is supported by studies in the literature that also take this into consideration.

6.3 Chapters 4 & 5 – The role of major mergers in the stellar mass build-up of BCGs from $z \lesssim 0.5$

In order to examine the importance of major mergers in the stellar mass build-up of BCGs, we consider close pairs as a diagnostic of mergers. We construct a sample of potential major merger candidates (with stellar mass ratios down to 4:1) by identifying close galaxy pairs within a physical separation distance of $7 \leq r_{\mathrm{sep}} \leq 50$ kpc. By calculating the merger timescales of the companion galaxies, we determine which of the companions will merge with their host BCGs. We find that major mergers, on average, increase the stellar mass of a present day BCG by $24 \pm 14\%$ since $z = 0.32$, assuming that half of the merging mass is accreted onto the BCGs (Section 4.3.2). Using spectroscopic observations from the SALT telescope, we are able to extend this analysis out to moderately high redshifts ($0.4 \leq z \leq 0.5$). Here we find that major mergers increase the stellar mass of a present day BCG by $29 \pm 17\%$ (on average) since $z = 0.45$ (assuming that 50% of the companions' stellar masses are distributed throughout the ICL, Section 5.5.2).

6.3.1 Discussion

For the purpose of this discussion we treat the results from Chapters 4 and 5 as independent studies and compare them as we do with other works in the literature. The results from both these chapters suggest that major mergers played some role in the stellar mass assembly of present day BCGs since $z \sim 0.5$. Since we have already performed a detailed comparison of our results against those in the literature in Section 4.3.2.1 and 5.5.3, we will not repeat the comparisons here. In Fig 6.2 we show the comparison of our measured BCG fractional mass growth results against studies in the literature.

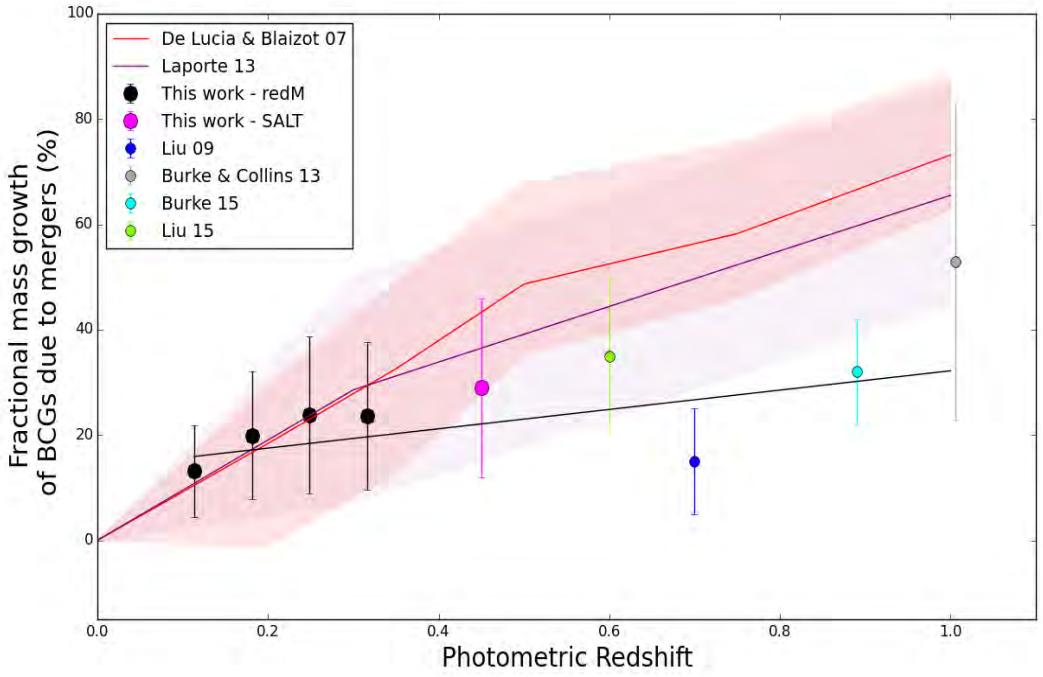

FIGURE 6.2: Comparison of our measured BCG fractional mass growth against values obtained from studies in the literature. The studies shown as large points are observational studies while the predictions from the De Lucia & Blaizot (2007); Laporte et al. (2013) SAMs are indicated with the red and purple solid lines, where the shaded regions represent the uncertainties. The black solid line indicate the best-linear fit (obtained using least-square fitting) to the observational studies. See text for details.

At $z \gtrsim 0.5$ it seems that the mass growth predictions of the De Lucia & Blaizot (2007); Laporte et al. (2013) semi-analytical models (represented by the red and purple solid line respectively) are higher than what is observed, indicating that the observed BCG mass growth does not increase like predicted. At lower redshifts, however, the observed and predicted BCG mass growths are in

agreement. The source of the mass growth discrepancy at high redshifts may lie in the manner in which the SAMs take the efficiency of mergers into account, specifically the fraction of the accreted mass that ends up in the ICL. The SAM of Laporte et al. (2013) on the other hand predicts a mass growth that is in better agreement with what is observed. This may be because this SAM includes an ICL prescription which is lacking in De Lucia & Blaizot (2007). This illustrates the need to take the stellar mass growth of the ICL into account when the BCG stellar mass growth is investigated.

6.4 Combining the science results from Chapters 3 & 4

The total stellar mass growth of the BCGs has been investigated over $0.08 \leq z \leq 0.35$. The mass growth due to major mergers on the other hand has been calculated from the BCGs' observed redshifts ($z = 0.32$) down to $z = 0$. We therefore need to place the results on the same timescale in order for a fair comparison to be made. We do this by calculating how much mass major mergers will contribute (on average) towards the mass growth of the BCGs between two adjacent redshift bins, z_0 and z_1. This is done by rewriting Eq 4.9 as follows:

$$\Delta M_{z_1-z_0} = \langle R_{\rm merge} \rangle_{z_1} \times (\Delta T_{\rm LB})_{z_1-z_0} \times \langle M_{\star,\,\rm com} \rangle_{z_1} \times f_{\rm mass} \tag{6.1}$$

where $\langle R_{\rm merge} \rangle_{z_1}$ is the average merger rate at z_1, $(\Delta T_{\rm LB})_{z_1-z_0}$ is the difference in lookback time between z_1 and z_0 and $\langle M_{\star,\,\rm com} \rangle_{z_1}$ is the average stellar mass of the companions at z_1. Here we again assume $f_{\rm mass} = 0.5 \pm 0.2$.

In Fig 6.3, we combine the total mass growth of the BCGs over $0.08 \leq z \leq 0.35$ (red points) with the mass growth that the BCGs will experience over the same redshift range due to major mergers as calculated from Eq 6.1. Each blue point represents the mass added to the BCGs due to major mergers between z_1 and z_0 and is given by

$$\langle M_{\star,\,\rm BCG} \rangle_{z_0} = \langle M_{\star,\,\rm BCG} \rangle_{z_1} + \Delta M_{z_1-z_0} \tag{6.2}$$

For the starting redshift z_1, $\langle M_{\star,\,\mathrm{BCG}}\rangle_{z_1}$ is the average stellar mass of the BCGs at redshift z_1 as calculated in Chapter 3. For the remaining redshift bins, we set $\langle M_{\star,\,\mathrm{BCG}}\rangle_{z_1}$ equal to $\langle M_{\star,\,\mathrm{BCG}}\rangle_{z_0}$ that has been derived in the previous redshift bin.

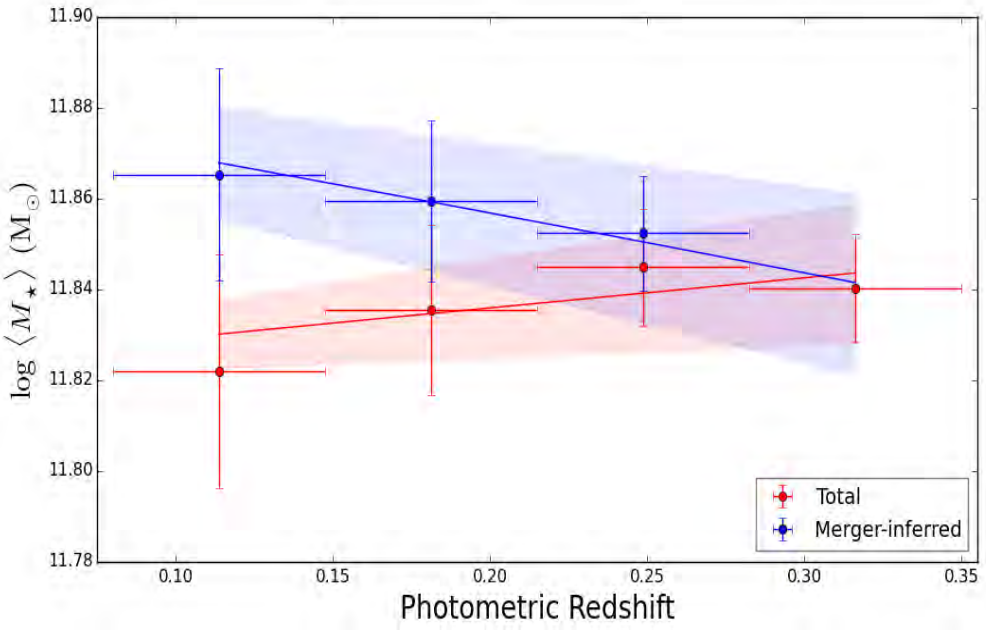

FIGURE 6.3: Comparison between the total stellar mass growth of BCGs between $0.08 \leq z \leq 0.35$ and the mass growth due to major mergers over the same redshift range. Each blue point represents the mass growth that BCGs will experience due to major mergers between two adjacent redshift bins (calculated using Eq 6.1). The solid lines indicates the best linear fit to the data points (shaded regions represent the uncertainties on the mass growth results). The total stellar mass growth of the BCGs is $0^{+15\%}_{-3\%}$, allowing for the additional uncertainty of the BCGs' SDSS magnitudes being underestimated in the lowest redshift bin. Major mergers contribute a fractional mass increase of $24 \pm 14\%$ from $z = 0.32 - 0$.

To determine how much mass major mergers have added to the BCGs between two adjacent redshift bins, we used an evolving merger rate (but assumed constant within each redshift bin) as a function of redshift. It is therefore an assumption of our method that this is a good enough approximation to the real merger rate of the Universe. Adding up the stellar masses, contributed via major mergers, between $z = 0.32 - 0.11$ results in a fractional mass increase of $22 \pm 11\%$ (with respect to the BCG stellar mass at $z = 0.11$) since $z = 0.32$ (calculated using Eq 6.1). This agrees within the uncertainties with the merger-inferred mass growth we measured from $z = 0.32 - 0$, assuming a single constant merger rate over this redshift range.

The measured total stellar mass growth of the BCGs from $z = 0.35 - 0.08$ is found to be $0^{+15\%}_{-3\%}$,

while the merger-inferred mass growth is given by $24 \pm 14\%$. Although the total stellar mass growth is formally below the merger-inferred mass growth, these two results are consistent within the uncertainties, since we accounted for the fact that SDSS underestimated the magnitudes of the BCGs in the lowest redshift bin.

6.4.1 Discussion – The stellar mass growth of BCGs and the ICL over the last five billion years

6.4.1.1 *The BCG stellar mass build-up*

We first investigated the total stellar mass growth of the BCGs from $z = 0.32 - 0.08$ and found that these massive galaxies have not experienced any mass growth over this redshift range ($0^{+15\%}_{-3\%}$). We also investigated the role of major mergers in the stellar mass build-up of BCGs and found that these mergers contributed $24 \pm 14\%$ (on average) towards the mass growth of a present day BCG since $z = 0.32$.

A BCG acquires stellar mass through two mechanisms, namely SF and mergers. This can be represented as follows:

$$(M_\star)_{\rm total} = (M_\star)_{\rm SF} + (M_\star)_{\rm mergers} \tag{6.3}$$

where two types of mergers contribute towards the stellar mass build-up of BCGs, i.e. major and minor mergers.

First consider the mass growth that BCGs experience due to SF. As previously described in Section 1.4.1.3, it is rare to find BCGs in the local Universe that are actively forming stars (less than 1%; e.g. Liu et al. 2012; Fraser-McKelvie et al. 2014). These starbursts have also been found to only increase the BCGs' stellar masses by $\sim 1 - 3\%$ (e.g. Sarazin & O'Connell 1983; Cardiel et al. 1995; Pipino et al. 2009; Liu et al. 2012; Loubser et al. 2016). Considering this in conjunction with our measured major merger mass growth suggests that mergers are the dominant mechanism through which the stellar mass of a BCGs can grow at low redshift.

Now consider the mass growth that BCGs experience due to mergers (both major and minor). We first take a look at the role of *minor* mergers. The stellar mass ratio that is used by studies in the literature to distinguish major and minor mergers is rather subjective. Minor mergers are typically defined in the literature as mergers with stellar mass ratios of >1:4−1:20 (e.g. Edwards & Patton 2012; Burke & Collins 2013; Burke et al. 2015). There is currently no consensus between observational studies regarding the relative contributions of major and minor mergers to the stellar mass build-up of BCGs. Rasmussen et al. (2010); Brough et al. (2011); Bildfell et al. (2012); Lidman et al. (2013) find that major merger dominate, whereas others (Edwards & Patton 2012; Burke & Collins 2013; Burke et al. 2015) find that minor mergers are more important. We are not able to comment on the relative importance of minor mergers because our sample is not complete for these systems (see Section 4.2.1 and Appendix B).

We now turn to *major* mergers. Our results show that major mergers will contribute $24 \pm 14\%$ (on average) to the stellar mass build-up of a present day BCG since $z = 0.32$. Combined with the total stellar mass growth of $0^{+15\%}_{-3\%}$, this suggests that major mergers provide enough stellar mass to the BCGs during merger events to explain the observed total stellar mass growth of the BCGs since $z = 0.32$, assuming 50% of the companion's stellar mass is distributed into the ICL. Together the total and merger-inferred stellar mass growth results imply that mergers are the dominant mechanism through which a BCGs' stellar mass can grow at low redshift ($z \leq 0.35$).

6.4.1.2 *The ICL stellar mass build-up*

Galaxies merging with BCGs have been proposed as a mechanism through which the stellar mass of the ICL grows. Observations and simulations of the ICL suggest that the stellar mass of the ICL has increased by a factor of $4 - 5$ since $z = 1$ (e.g. Krick & Bernstein 2007; Murante et al. 2007; Rudick et al. 2011; Burke et al. 2012; 2015). The N-body simulations of Murante et al. (2007); Conroy et al. (2007b); Puchwein et al. (2010) predict that $30 - 80\%$ of the BCGs' merging mass should be distributed into the ICL in order to reproduce the distribution observed in nearby clusters. Combined with the number of mergers that BCGs are expected to experience, one is faced with a scenario where the ICL is being built up through galaxies that are interacting with BCGs. If we are to believe the model predictions that the majority of the stellar masses accreted

on to BCGs during mergers are distributed throughout the ICL, then this could explain why the stellar masses of the BCGs remain relatively unchanged (or only slightly increase) with decreasing redshift. Apart from the above-mentioned mechanism, tidal stripping of satellite galaxies are also thought to contribute towards the ICL growth. We continue to investigate whether mergers are the dominant mechanism through which the ICL increases its stellar mass from $z = 0.3 - 0$. This is done by determining whether major mergers have transferred enough stellar mass to the ICL between $z = 0.3$ and the present day in order to explain the ICL's stellar mass growth between these two redshifts. We denote the amount of stellar mass added to the ICL due to mergers as $(\Delta M_{\star})_{\rm mergers}$ and the stellar mass growth of the ICL between two redshift bins by $(\Delta M_{\star})_{\rm ICL}$. If $(\Delta M_{\star})_{\rm ICL} \gg (\Delta M_{\star})_{\rm mergers}$, it implies that mergers are not the dominant mass contributor of the ICL. We investigate this idea by combining values from the literature with our own measurements.

We investigate the stellar mass growth of the ICL from $z = 0.3 - 0$ as follows. From the literature we were not able to obtain a stellar mass estimate of the ICL at either $z = 0.3$ or $z = 0$. DeMaio et al. (2015) on the other hand investigated the ICL stellar mass build-up in four clusters at $0.44 \leq z \leq 0.57$ (with a median redshift of $z = 0.5$) that span a halo mass range of $0.6 - 2.6 \times 10^{15}\,{\rm M}_{\odot}$. They measured the ICL luminosities of these clusters within a radius of 110 kpc from their centres (see their table 6). Because their M_h range overlaps with ours, we use their ICL luminosities in our analysis to investigate the stellar mass growth of the ICL from $z = 0.3 - 0$. We do this by taking the average of their measured ICL luminosities, denoted $\langle L^{\star} \rangle_{\rm ICL}\,(z = 0.5)$, as a proxy of the ICL's average stellar mass at $z = 0.5$, denoted $\langle M_{\star} \rangle_{\rm ICL}\,(z = 0.5)$. We then use the predicted stellar mass growth factor (f) of the ICL from Contini et al. (2014, see their figure 6)[12] to determine $\langle M_{\star} \rangle_{\rm ICL}\,(z = 0)$ and $\langle M_{\star} \rangle_{\rm ICL}\,(z = 0.3)$. This method is described below.

$$(\Delta M_{\star})_{\rm ICL} = \langle M_{\star} \rangle_{\rm ICL}\,(z = 0) - \langle M_{\star} \rangle_{\rm ICL}\,(z = 0.3) \tag{6.4}$$

[12]They investigated the ICL growth in clusters by updating the De Lucia & Blaizot (2007) semi-analytical model to include various implementations for modeling the formation of the ICL, more specifically through the stellar stripping of satellite galaxies and mergers with the BCGs (assuming that 20% of the companion's stellar mass ends up in the ICL during a merger event with the BCG).

with

$$\begin{aligned}\langle M_\star \rangle_{\rm ICL}\,(z=0) &= \frac{\langle M_\star \rangle_{\rm ICL}\,(z=0.5)}{f_{z=0.5-0}} \\ &= \frac{\langle L^\star \rangle_{\rm ICL}\,(z=0.5) \times (M_\star)_{L^\star}}{f_{z=0.5-0}}\end{aligned} \tag{6.5}$$

where $\langle L^\star \rangle_{\rm ICL}\,(z=0.5)$ denotes the average ICL luminosity of the clusters at $z=0.5$ and has a value of $7.4\,L^\star$ (obtained from DeMaio et al. 2015). $(M_\star)_{L^\star}$ is the stellar mass of a $L^\star$ galaxy and is $(M_\star)_{L^\star} \sim 5 \times 10^{10}\,{\rm M}_\odot$.

$$\langle M_\star \rangle_{\rm ICL}\,(z=0.3) = \langle M_\star \rangle_{\rm ICL}\,(z=0)\ \times\ f_{z=0.3-0} \tag{6.6}$$

where $f_{z=0.5-0}=0.5$ and $f_{z=0.3-0}=0.75$. These are the predicted stellar mass growth factors of the ICL between $z=0.5-0\,(z=0.3-0)$ from Contini et al. (2014). Substituting these values into the relevant equations above, we find $(\Delta M_\star)_{\rm ICL} \sim 2 \times 10^{11}\,{\rm M}_\odot$.

During our analysis we assumed that 50% of the companion's stellar mass is accreted onto the BCG during a merger. Our results suggest that major merger distributed about $(\Delta M_\star)_{\rm mergers} \sim 2 \times 10^{11}\,{\rm M}_\odot$ of stellar mass into the ICL between $z=0.3-0$. From this we find that $(\Delta M_\star)_{\rm ICL} \sim (\Delta M_\star)_{\rm mergers}$. This implies that major mergers are enough to explain the stellar mass growth of the ICL between $0 \leq z \leq 0.3$. This result also indicates that our assumption of 50% mass transfer to the ICL is enough to grow the ICL and therefore argues against a higher mass transfer fraction.

6.5 Conclusions

The main aim of this thesis was to investigated the stellar mass build-up of BCGs between $0.08 \leq z \leq 0.35$. We conclude the following from our analysis:

- We find that major mergers, on average contribute $24 \pm 14\%$ towards the stellar mass growth of a present day BCG since $z=0.32$ (Section 4.3.2), while the total stellar mass growth is given by $0^{+15\%}_{-3\%}$ (Section 3.3). Although the total stellar mass growth is formally lower than

that measured from major mergers, we find that these two mass growth results are consistent within the uncertainties.

- When we investigated the total stellar mass growth of the BCGs, we have shown that it is important to take the halo mass growth of the clusters into account. If this is not done then one runs the risk of obtaining the non-physical result that the BCGs are somehow losing stellar mass towards the present day (i.e. shrinking). To our knowledge, we are the first to successfully make this distinction due to the uncertainties on our measurements being small enough (Section 3.3).

- Our results also suggest that the stellar mass growth of BCGs appears to be independent of the range of parent halo masses probed (providing these clusters are descendants/progenitors of each other, Section 3.4.1 and 6.2.1).

- Our findings show that major mergers contribute enough stellar mass to the BCGs to explain their observed total stellar mass growth between $0.08 \leq z \leq 0.35$. This leaves no room for SF to contribute towards the mass growth of these massive galaxies (at least in our redshift range of interest). This is supported by various works (e.g. Sarazin & O'Connell 1983; Cardiel et al. 1995; Pipino et al. 2009; Liu et al. 2012; Fraser-McKelvie et al. 2014; Loubser et al. 2016) who find star formation in BCGs to be a rare occurrence in the local Universe and these starbursts only add $1-3\%$ to the total stellar mass growth of BCGs.

- We investigated whether mergers are the dominant mechanism through which the ICL increases its stellar mass from $z = 0.3-0$. Using the predicted stellar mass growth factor of Contini et al. (2014) we find that the ICL has increased its stellar mass by $(\Delta M_{\star})_{\rm ICL} \sim 2\times10^{11}\,{\rm M}_{\odot}$ between $z = 0.3$ and 0. Our results on the other hand suggest that major mergers distributed about $(\Delta M_{\star})_{\rm mergers} \sim 2\times10^{11}\,{\rm M}_{\odot}$ of stellar mass into the ICL between $z = 0.3-0$ (assuming $f_{\rm mass} = 0.5$). Our findings imply that mergers are enough to explain the stellar mass growth of the ICL between $0.0 \leq z \leq 0.3$. Mergers are therefore the dominant mass contributor to the ICL stellar mass build-up (at least from $z \leq 0.3$).

6.6 Plans for Future Research

- One of the lingering questions from this thesis is the contribution of minor mergers to the mass build-up of BCGs. For this purpose we propose to use the GAMA survey because it (i) has a high spectroscopic completeness and (ii) is two magnitudes deeper than the spectroscopic SDSS samples. Since GAMA goes to fainter magnitudes we can explore potential mergers between BCGs and companions with luminosity ratios down to 1:20. The high spectroscopic completeness on the other hand is necessary to determine which of these pairs will merge.

- Extending our wavelength coverage to the near-IR will allow us to investigate the importance of mergers in the stellar mass build-up of BCGs out to $z \sim 1$ (over the last 8 Gyr). Available data from KIDS[13] (de Jong et al. 2015), RCS-1 (Gladders & Yee 2005) and UKIDSS[14] (Dye et al. 2006) will therefore be integrated into our future dataset.

- The selection criteria used throughout this thesis to construct our potential merger candidate sample have been derived by studying merging field galaxies (see Patton et al. 2000). This criteria may therefore not be applicable to study mergers in clusters (although it has been used for this purpose, see e.g. Edwards & Patton 2012; Burke & Collins 2013). We propose to investigate this idea further by using N-body simulations (such as the Millennium Simulation; Springel et al. 2005) to investigate merger events in simulated cluster environments, thereby allowing us to obtain appropriate $r_{\rm sep}$ and Δv values for mergers that take place in clusters.

[13] Kilo Degree Survey, http://kids.strw.leidenuniv.nl/
[14] UKIRT Infrared Deep Sky Survey, http://www.ukidss.org/

Appendix A

The SDSS cutouts for clusters in the redMaPPer catalogue

We present the SDSS cutouts for a subsample of 200 clusters in the redMaPPer catalogue. Each cluster's cutout has a physical size of 0.7×0.7 Mpc (at the cluster's photometric redshift) and is centered on the BCG (circled in cyan). The galaxies that the redMaPPer algorithm has identified as cluster members (with $P_{\rm RSM} > 0$) are circled in red and are brighter than the $0.2L^{\star}$ magnitude limit of redMaPPer. Each cluster's redMaPPer ID, photometric redshift and optical richness (λ) are also indicated. This size of the stamp covers a significant part of the clusters at all redshifts, ensuring (1) we have enough area around the BCG to measure its total magnitude and (2) we will detect all neighbouring objects within 50 kpc. The cutouts are divided into four equally spaced redshift bins, whereafter they are sorted according to optical richness (high to low).

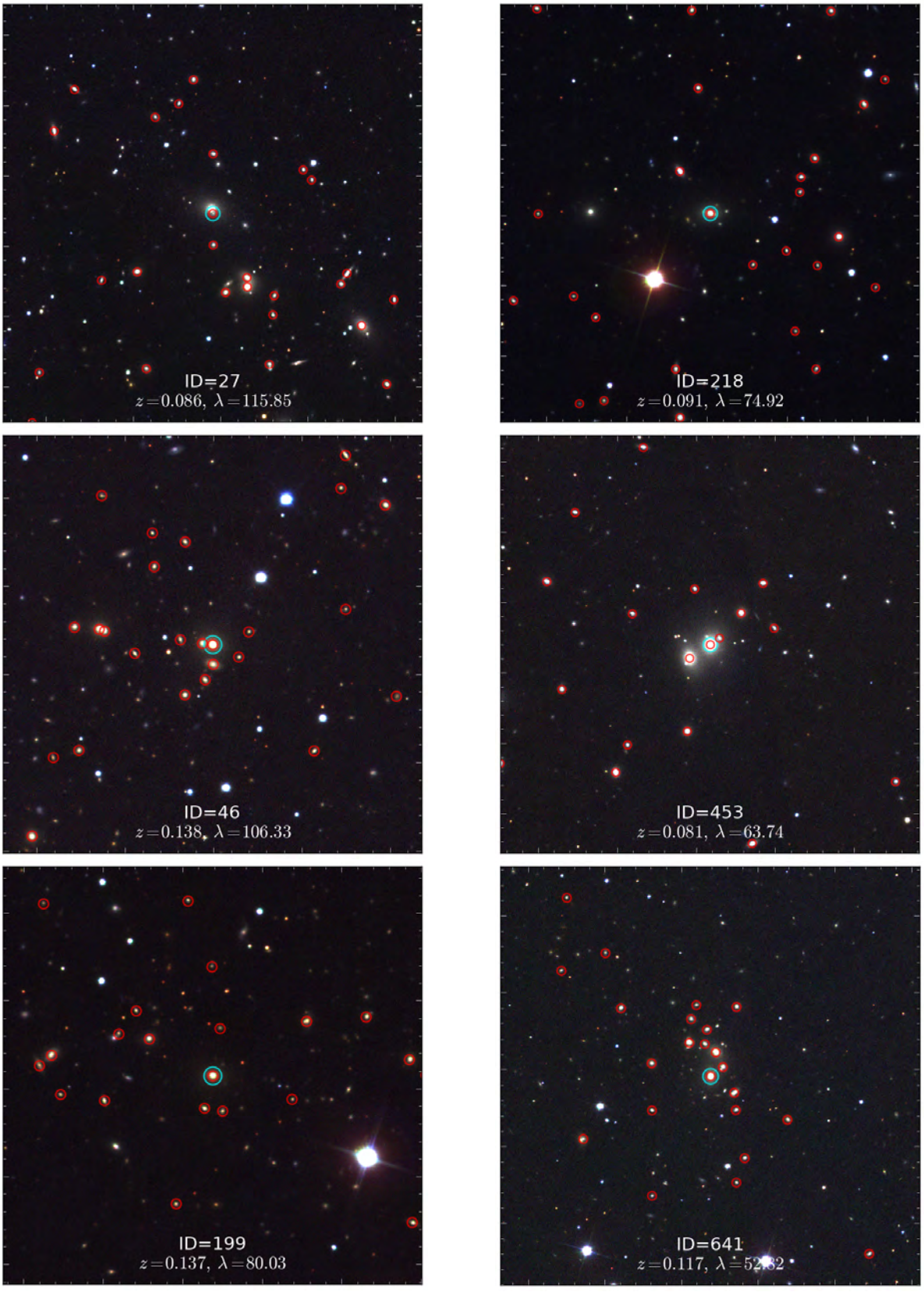

FIGURE A.1: Examples of SDSS cutouts for 50 clusters between $0.08 \leq z \leq 0.15$.

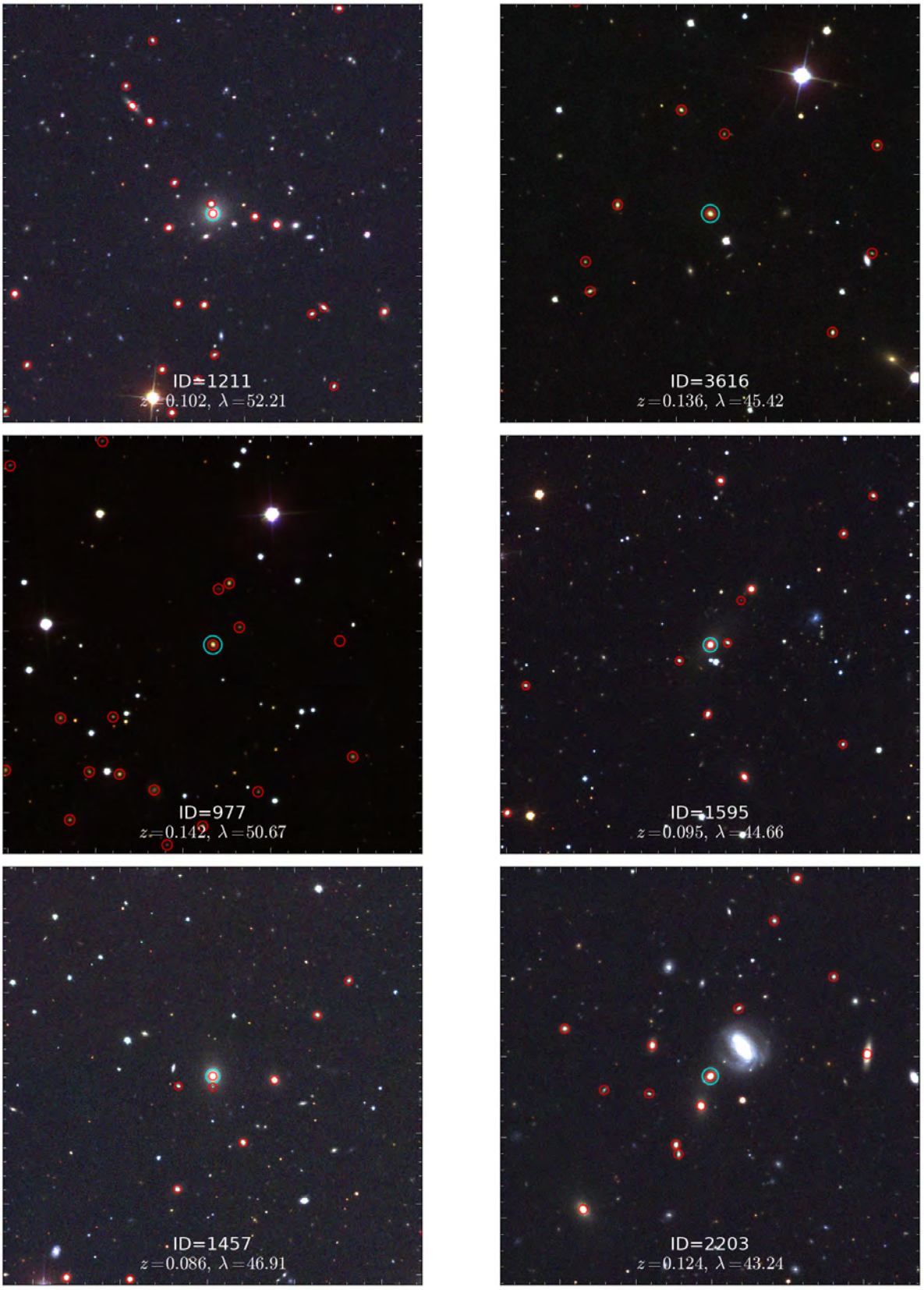

FIGURE A.1: – Continued.

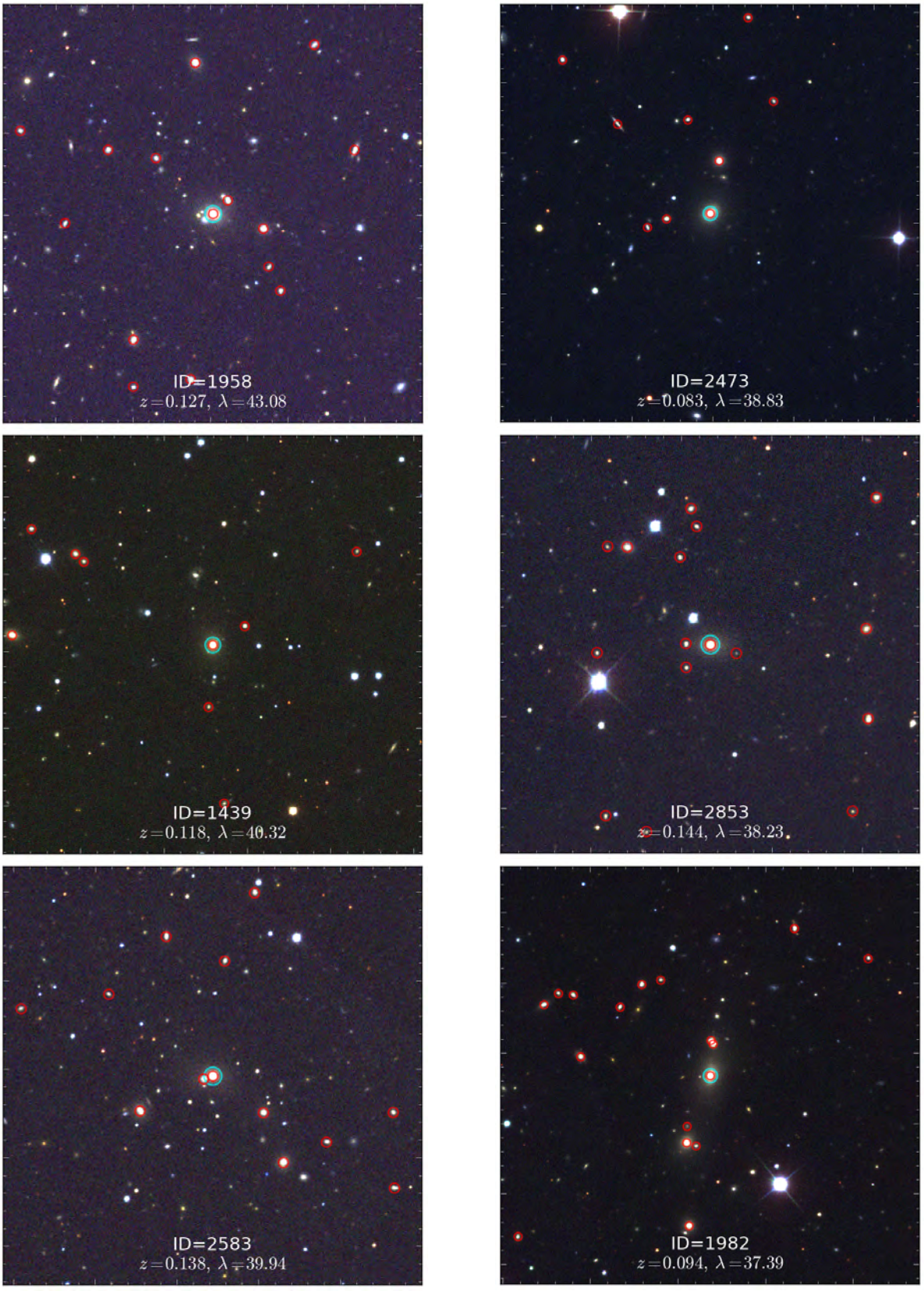

FIGURE A.1: – Continued.

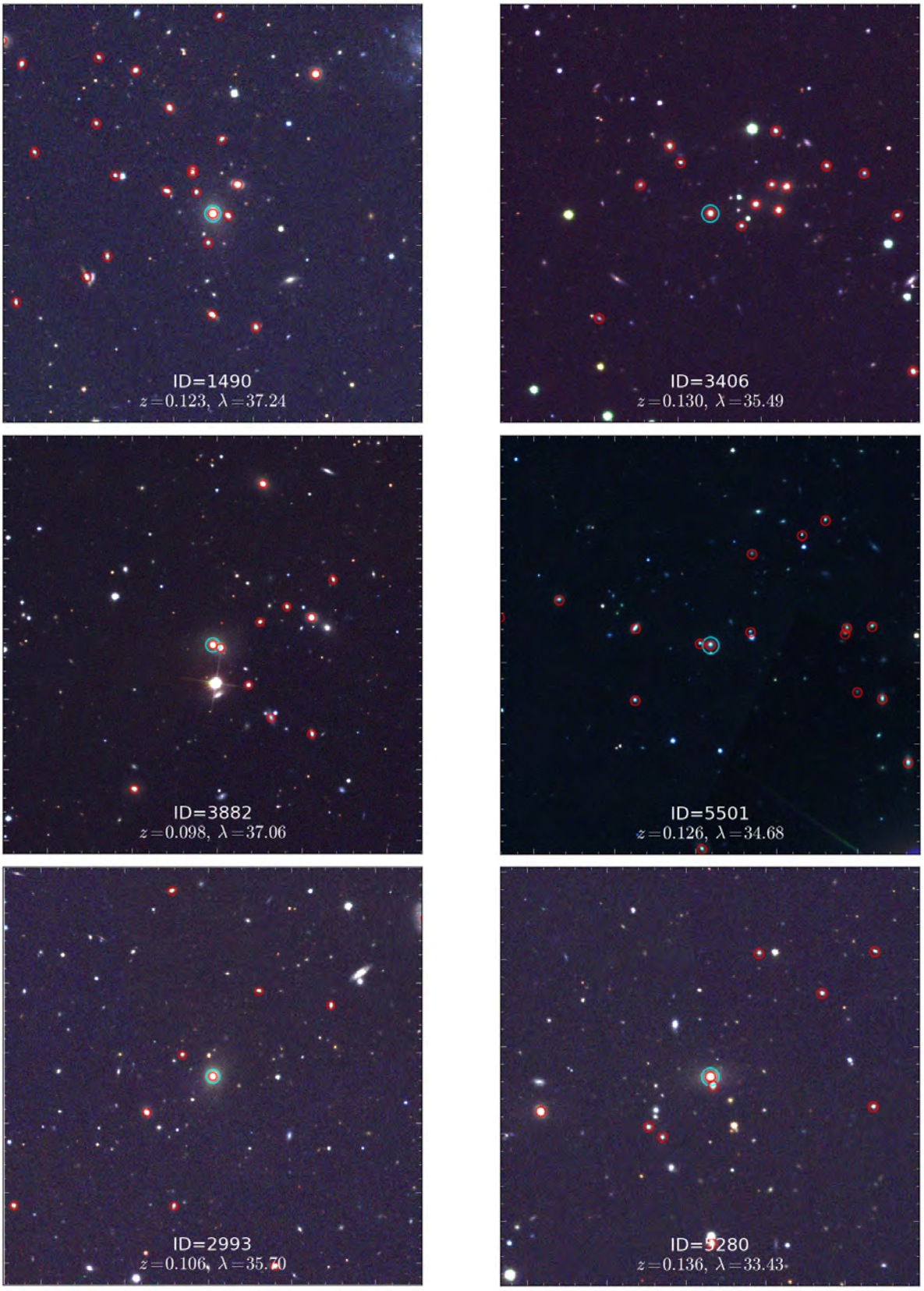

FIGURE A.1: – Continued.

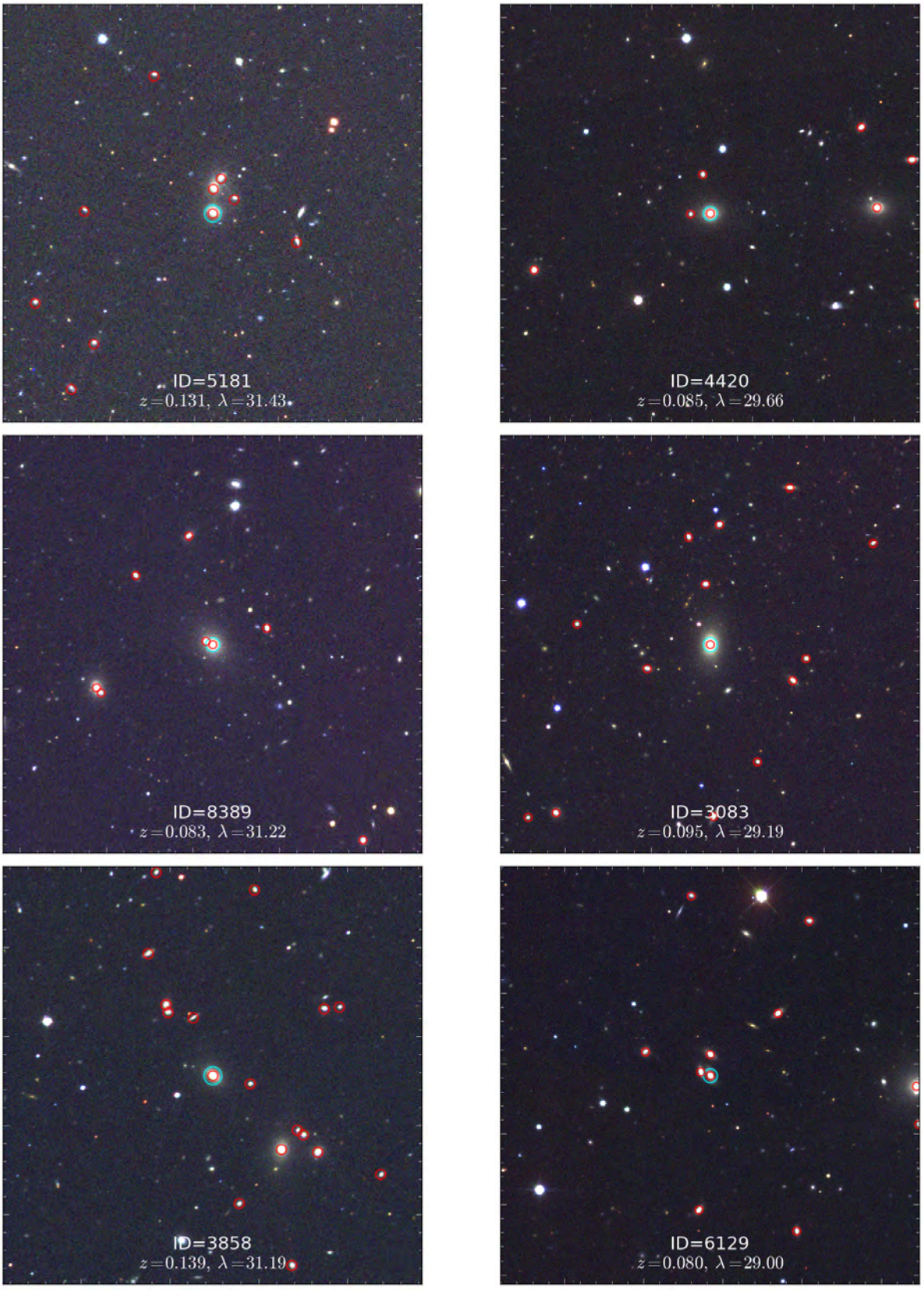

FIGURE A.1: – Continued.

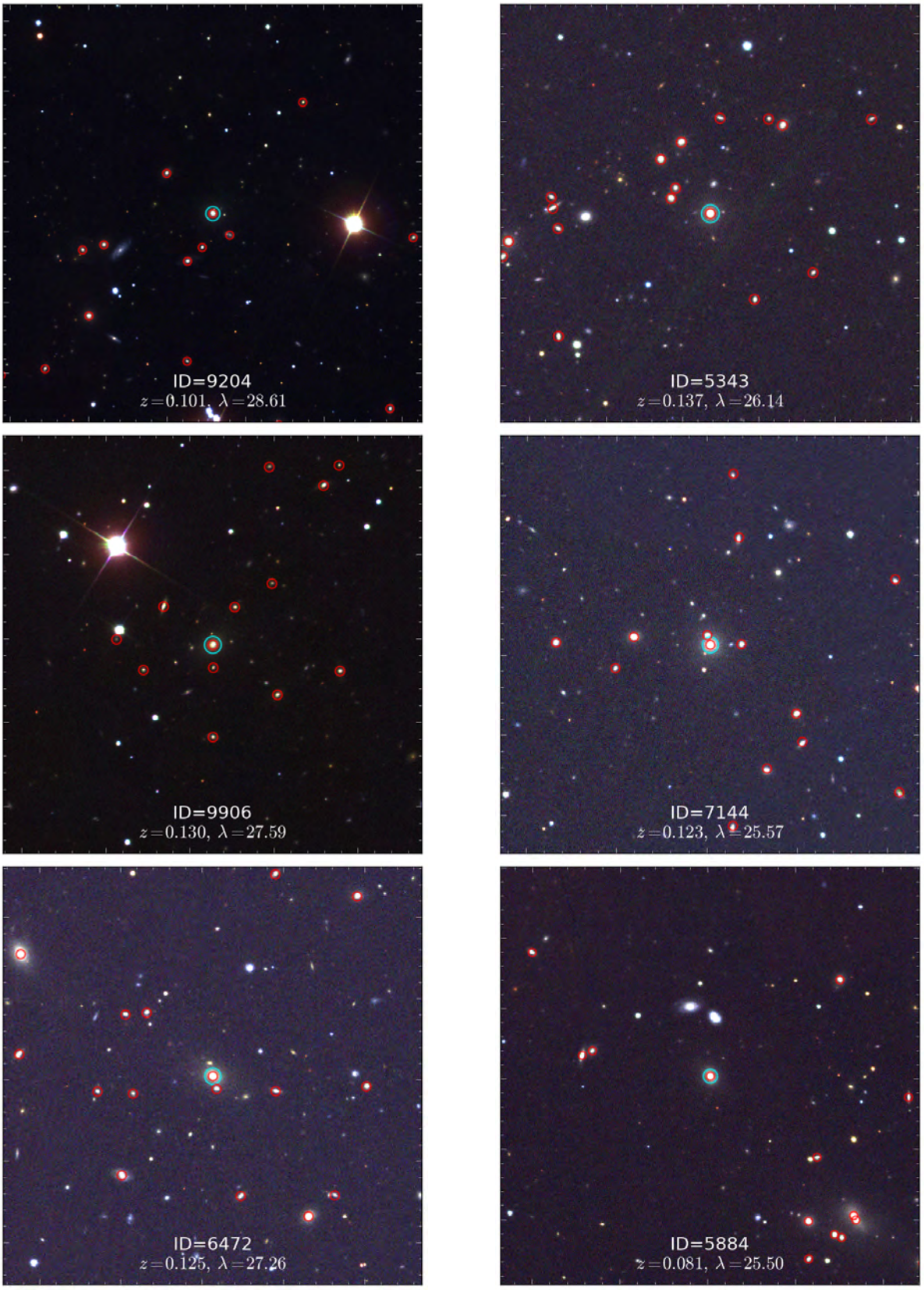

FIGURE A.1: – Continued.

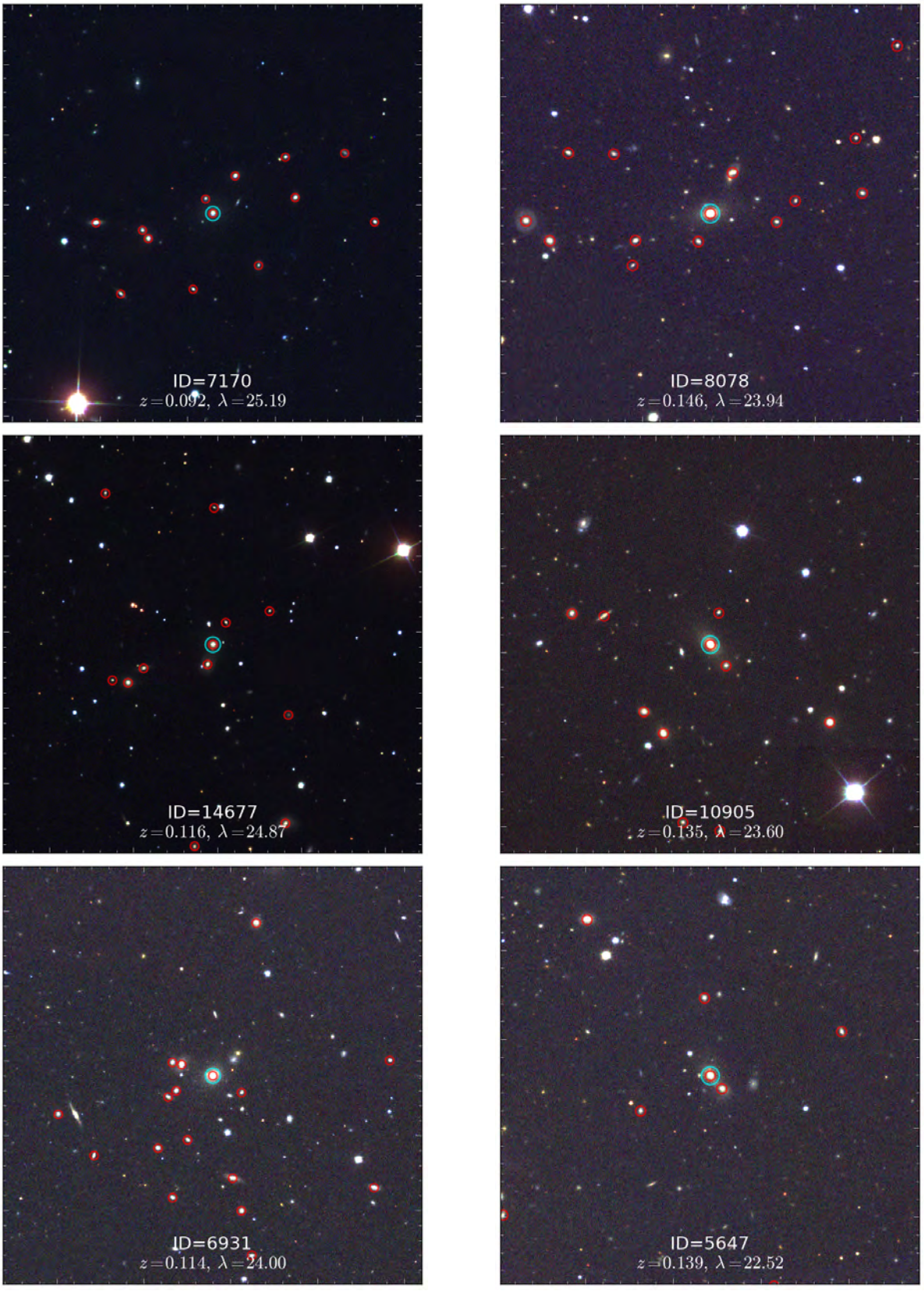

FIGURE A.1: – Continued.

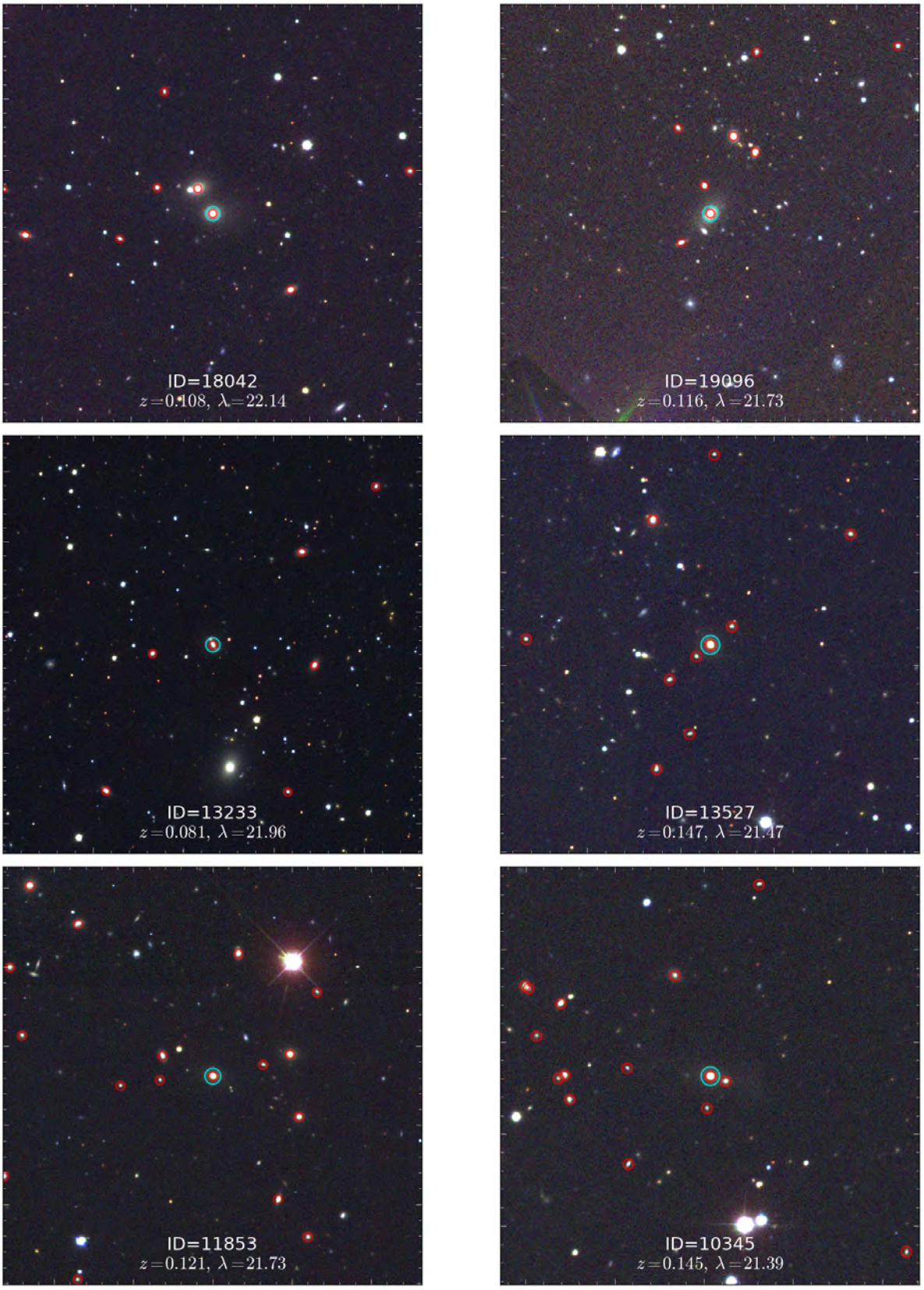

FIGURE A.1: – Continued.

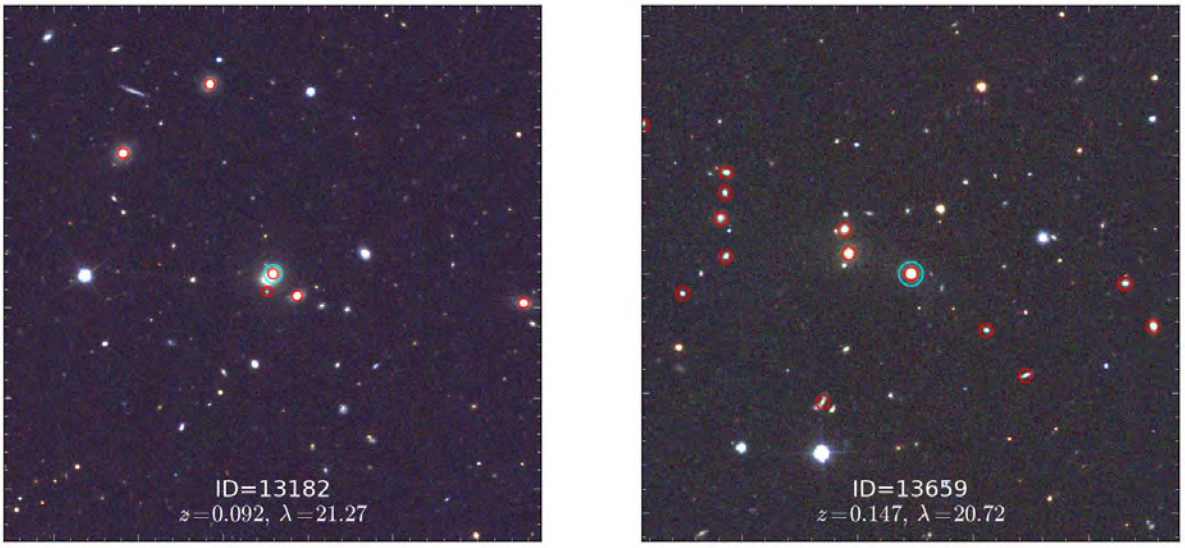

FIGURE A.1: – Continued.

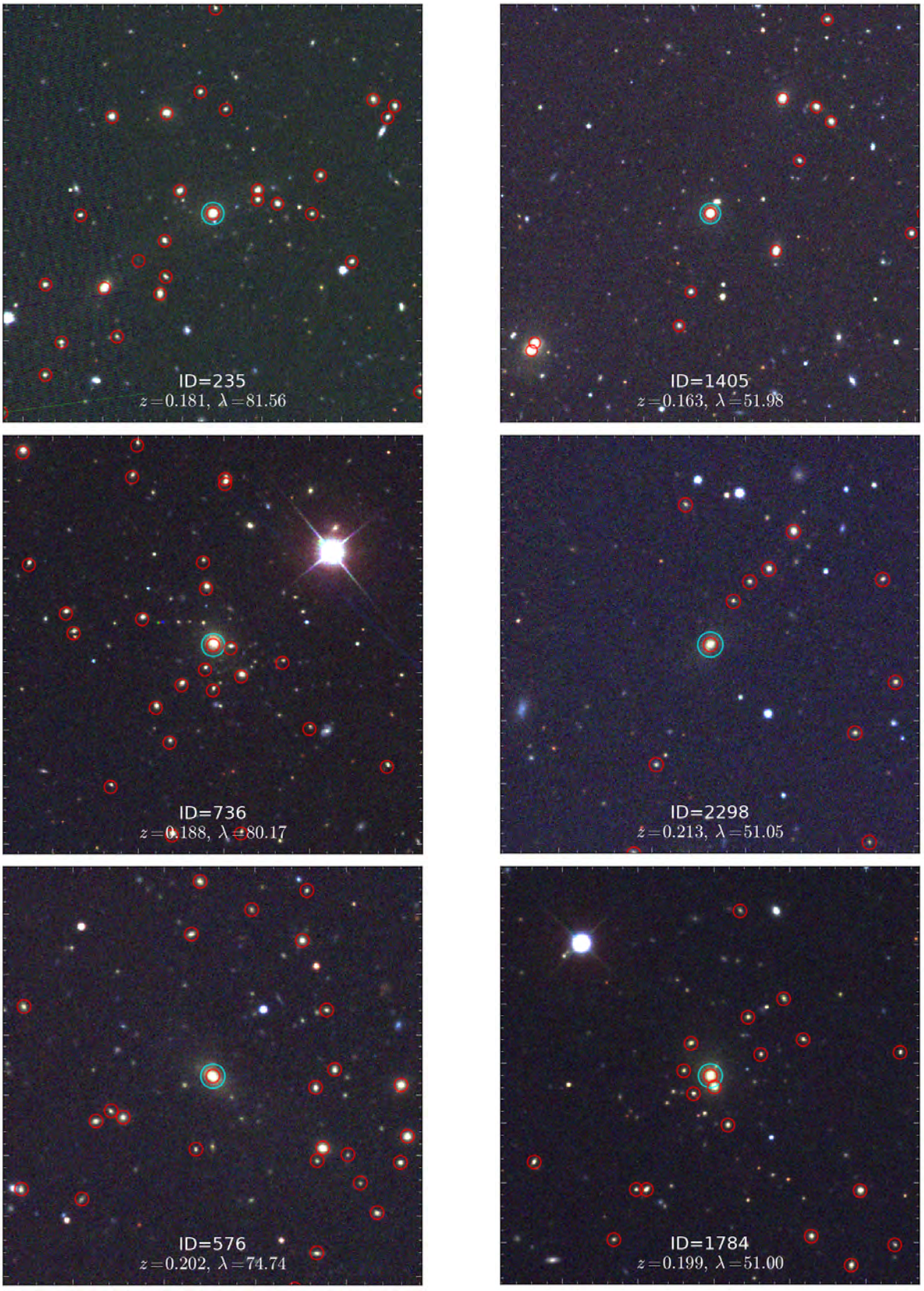

FIGURE A.2: Examples of SDSS cutouts for 50 clusters between $0.15 < z \leq 0.22$.

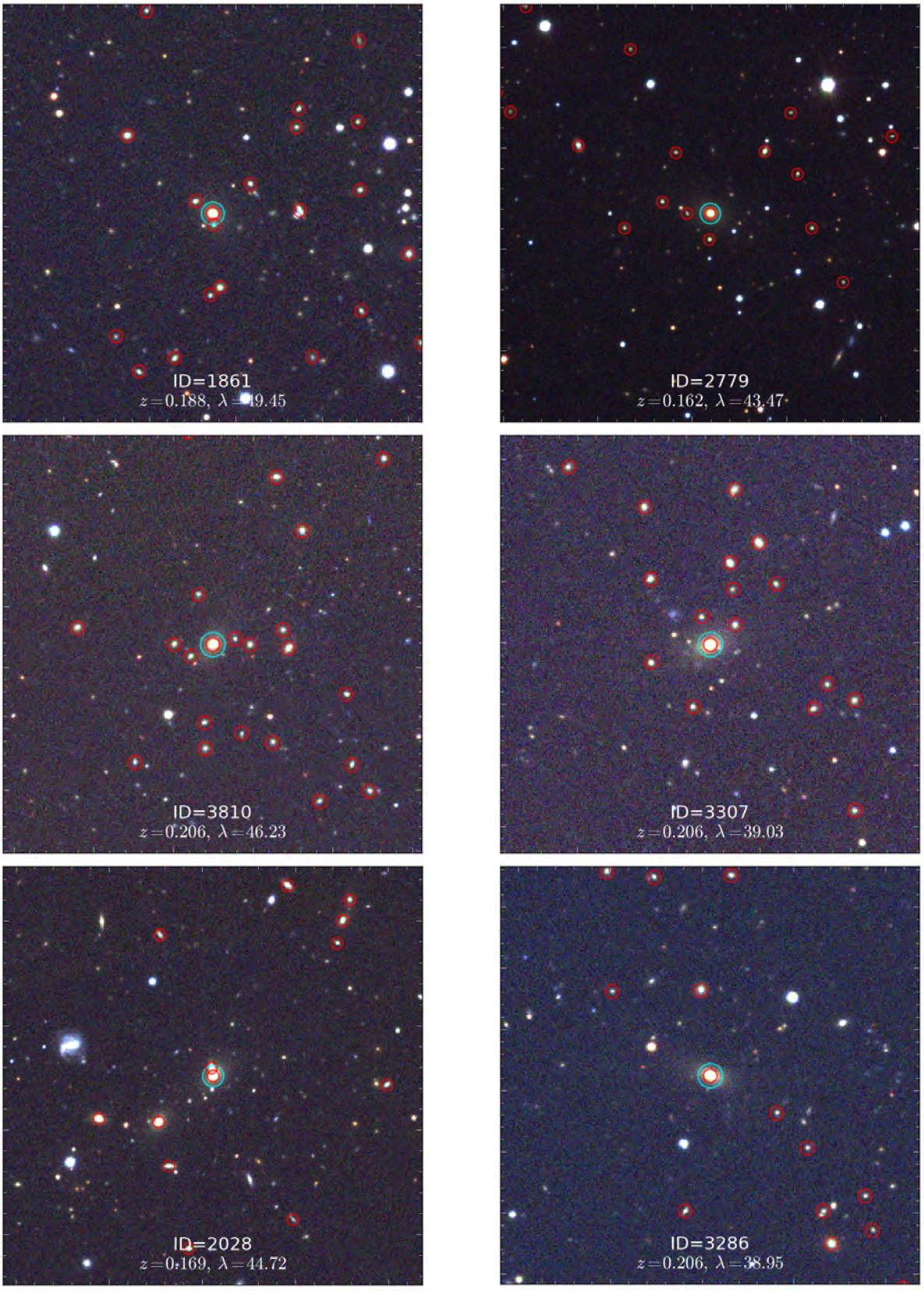

FIGURE A.2: – Continued.

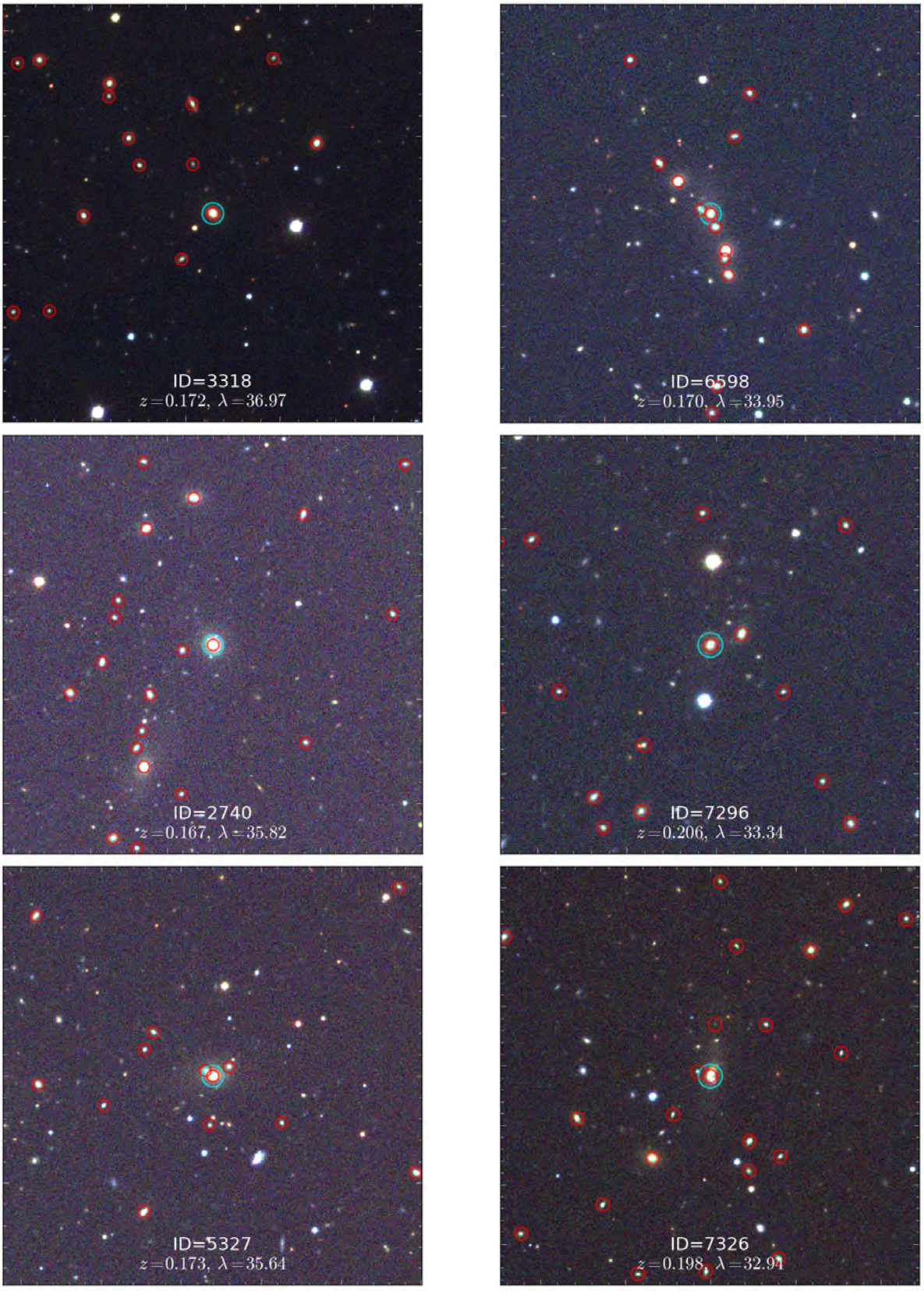

FIGURE A.2: – Continued.

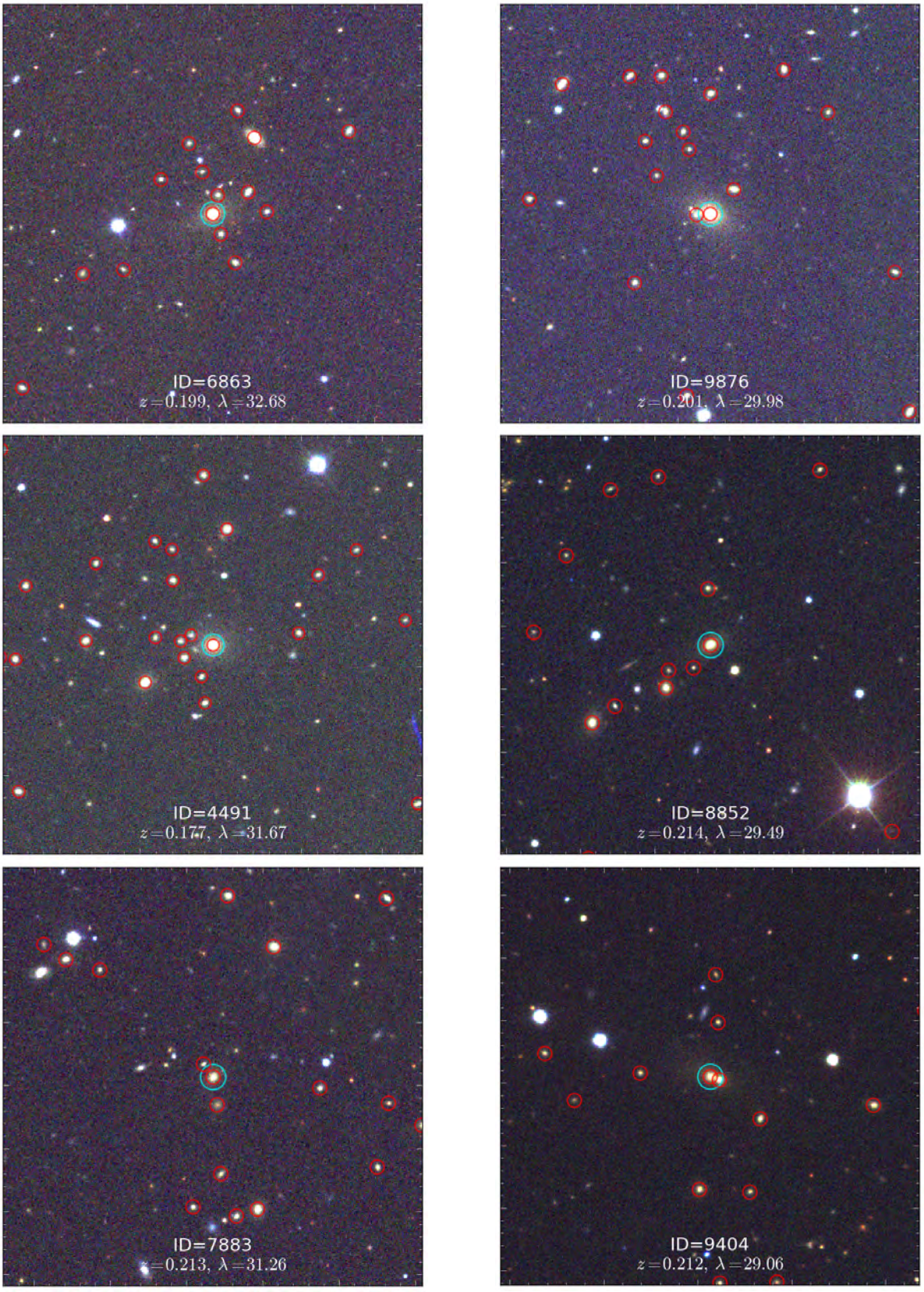

FIGURE A.2: – Continued.

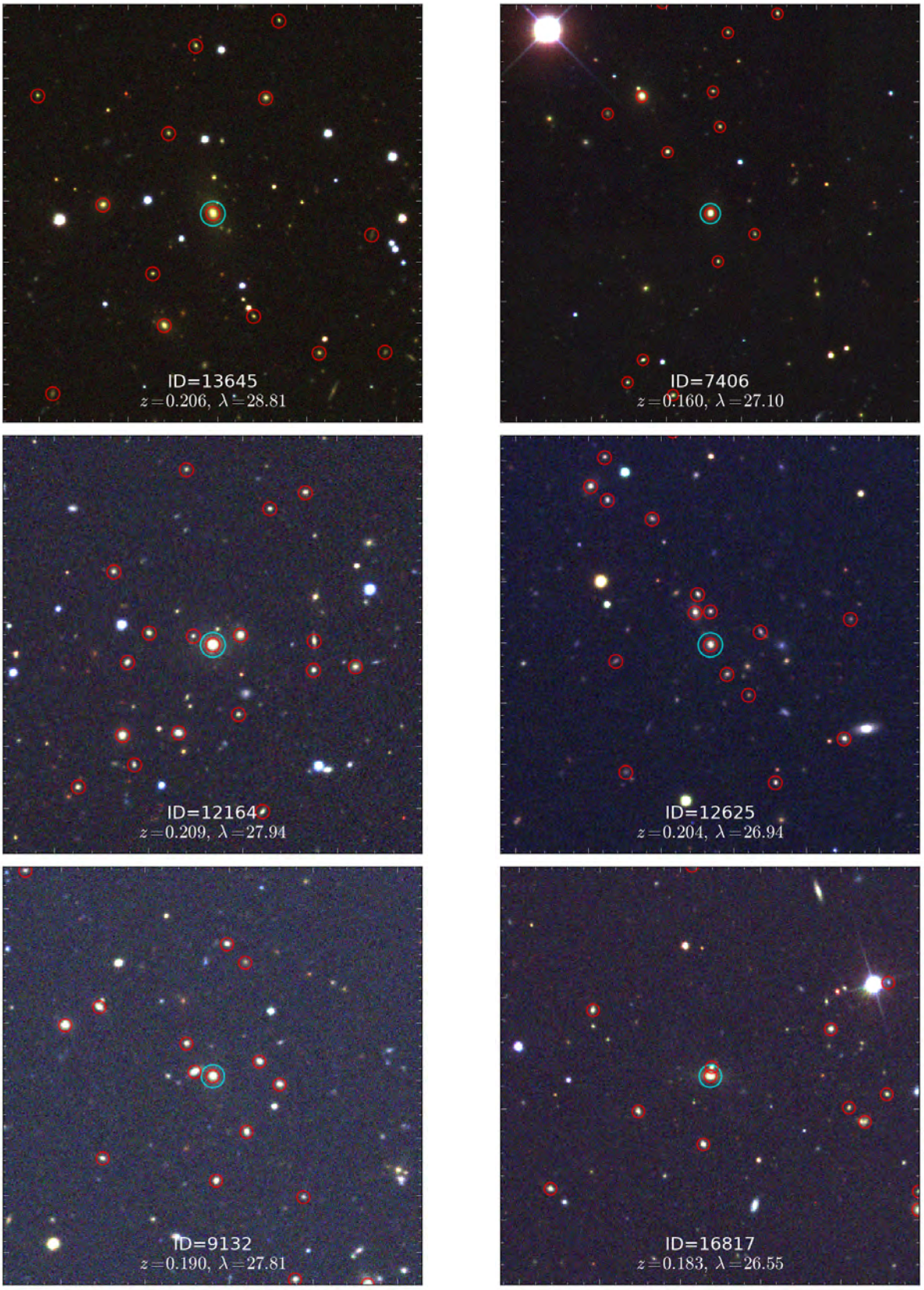

FIGURE A.2: – Continued.

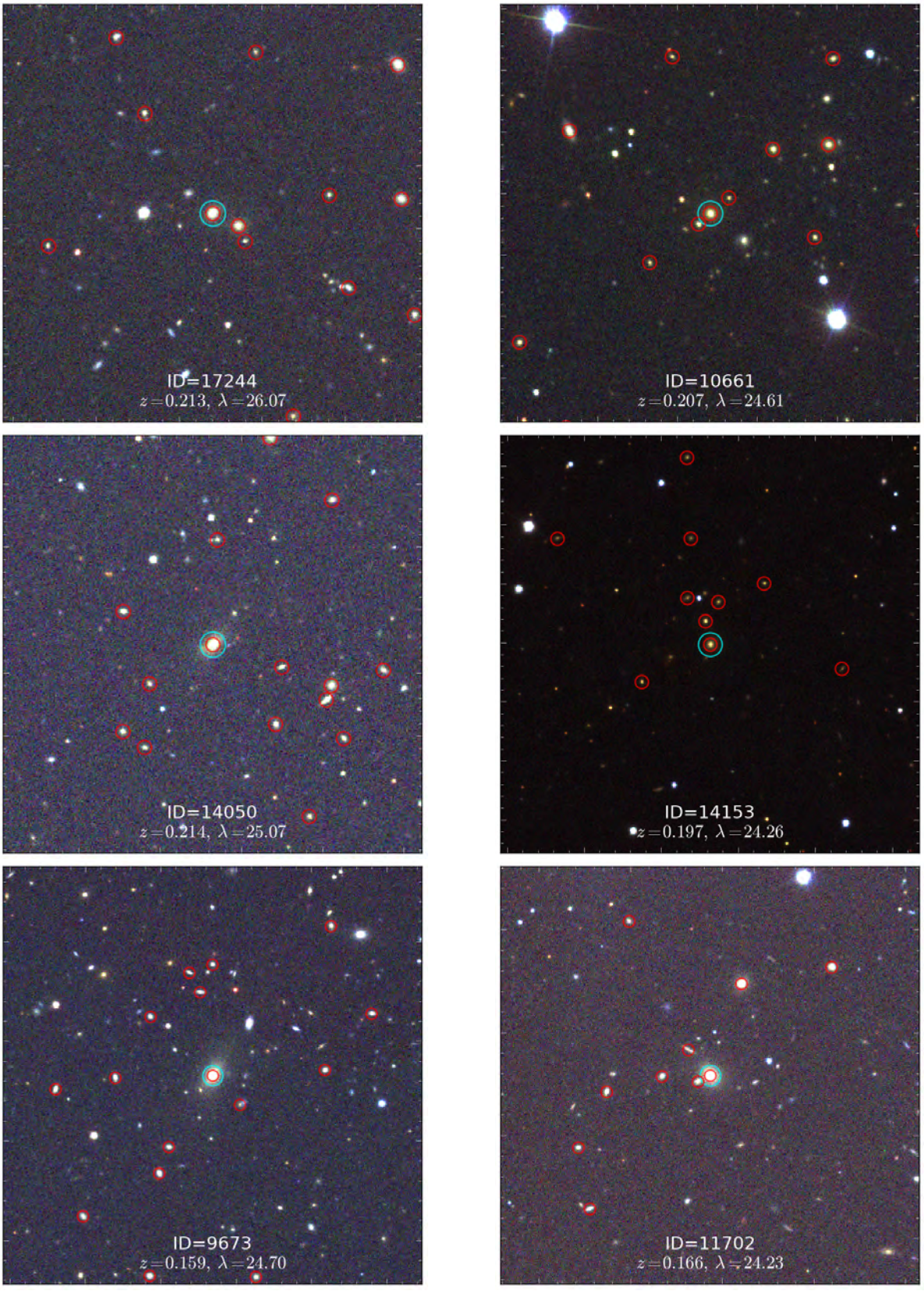

FIGURE A.2: – Continued.

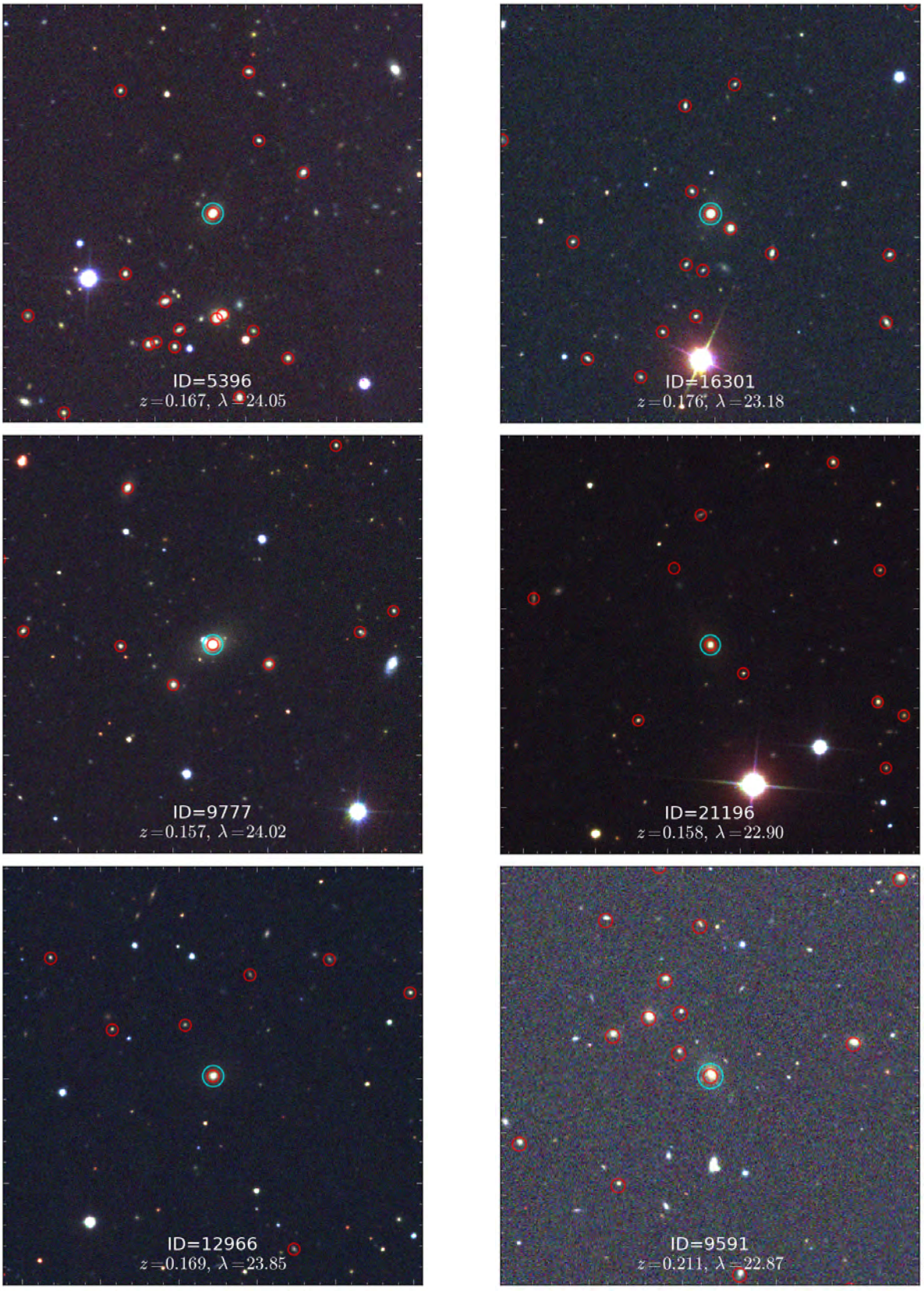

FIGURE A.2: – Continued.

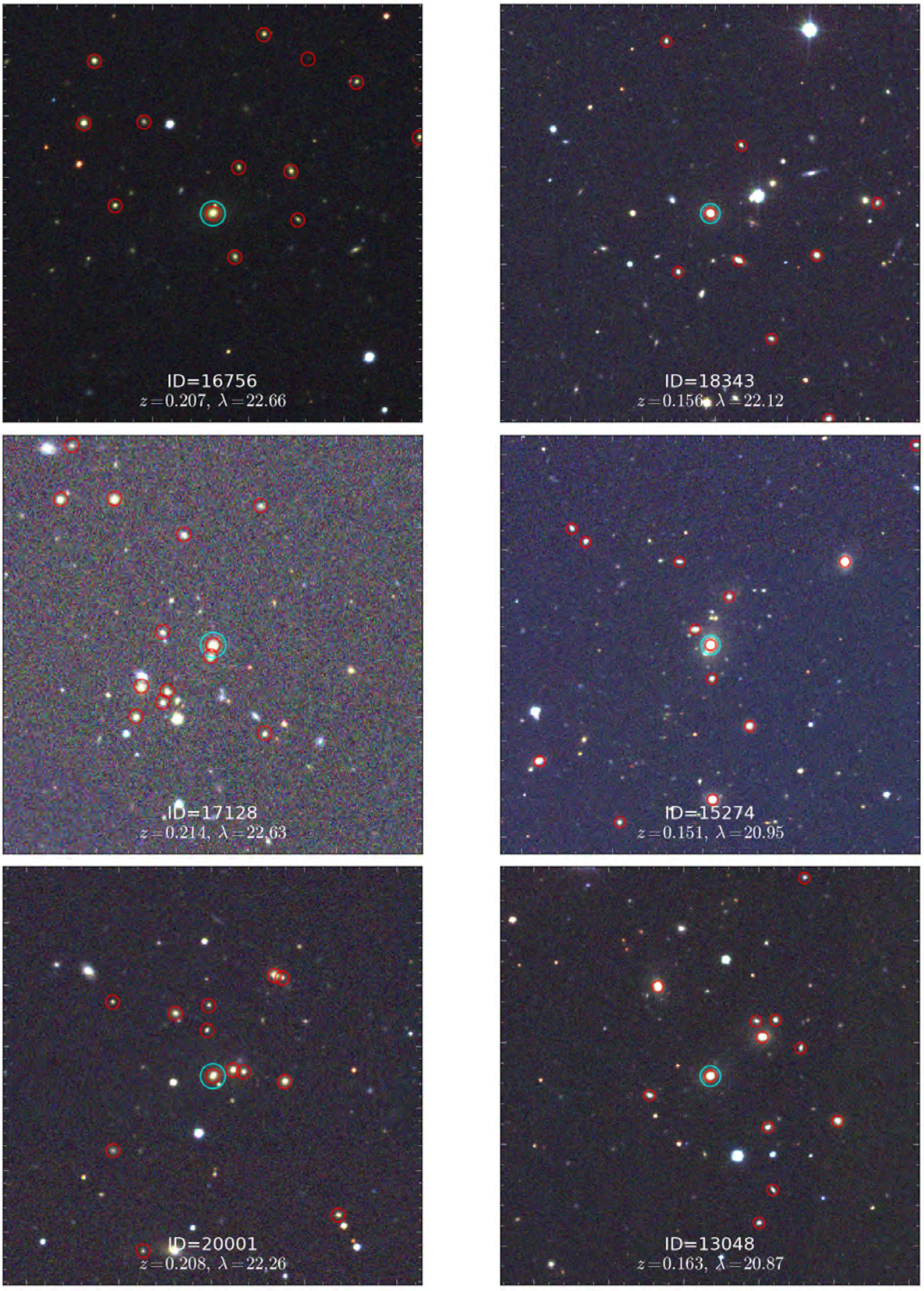

FIGURE A.2: – Continued.

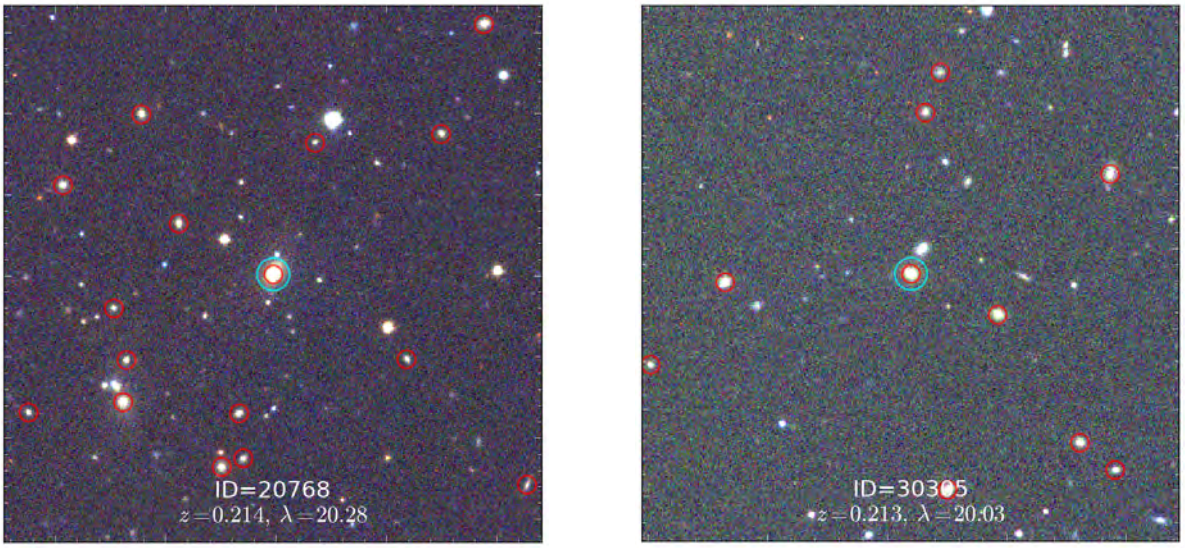

FIGURE A.2: – Continued.

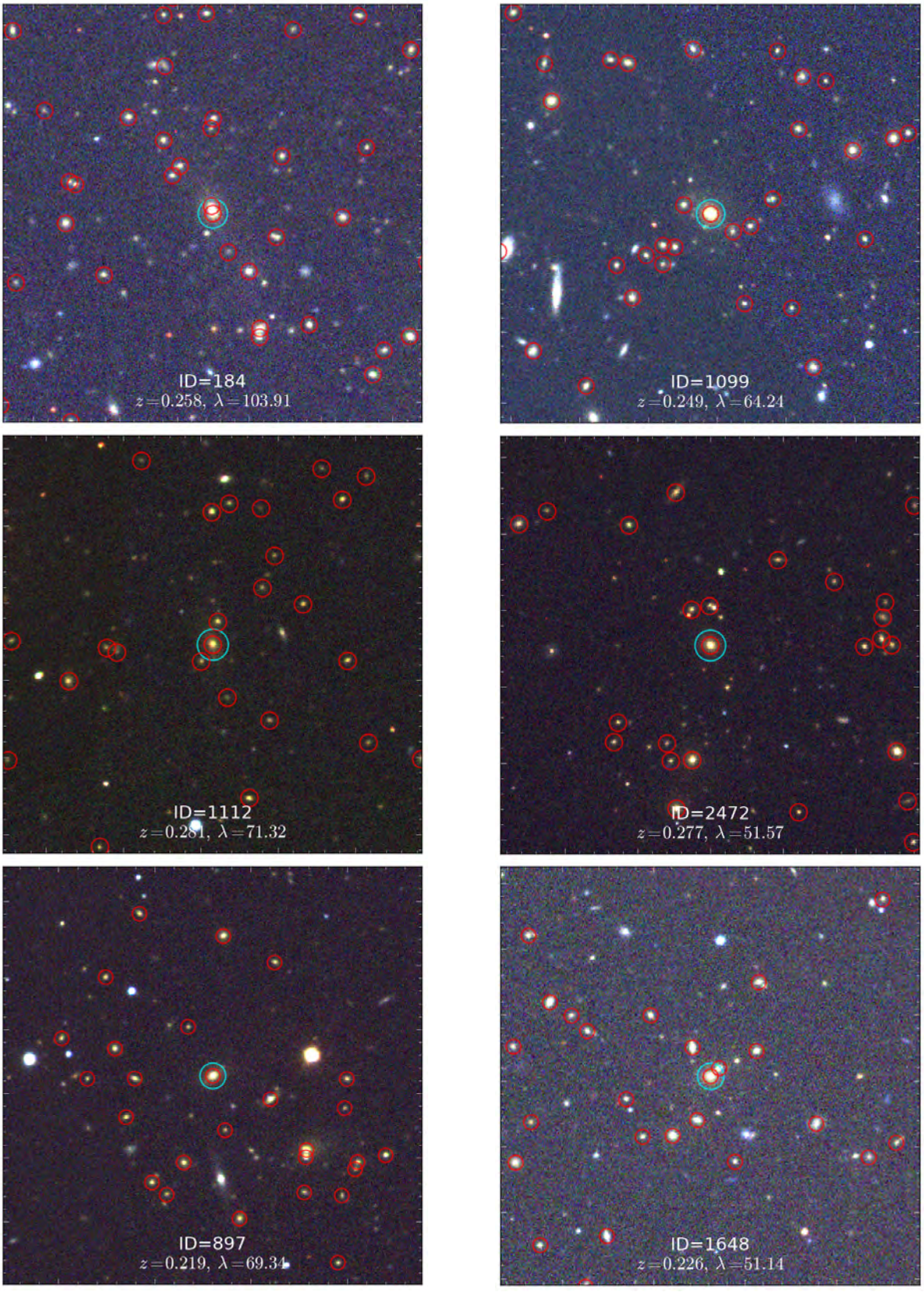

FIGURE A.3: Examples of SDSS cutouts for 50 clusters between $0.22 < z \leq 0.28$.

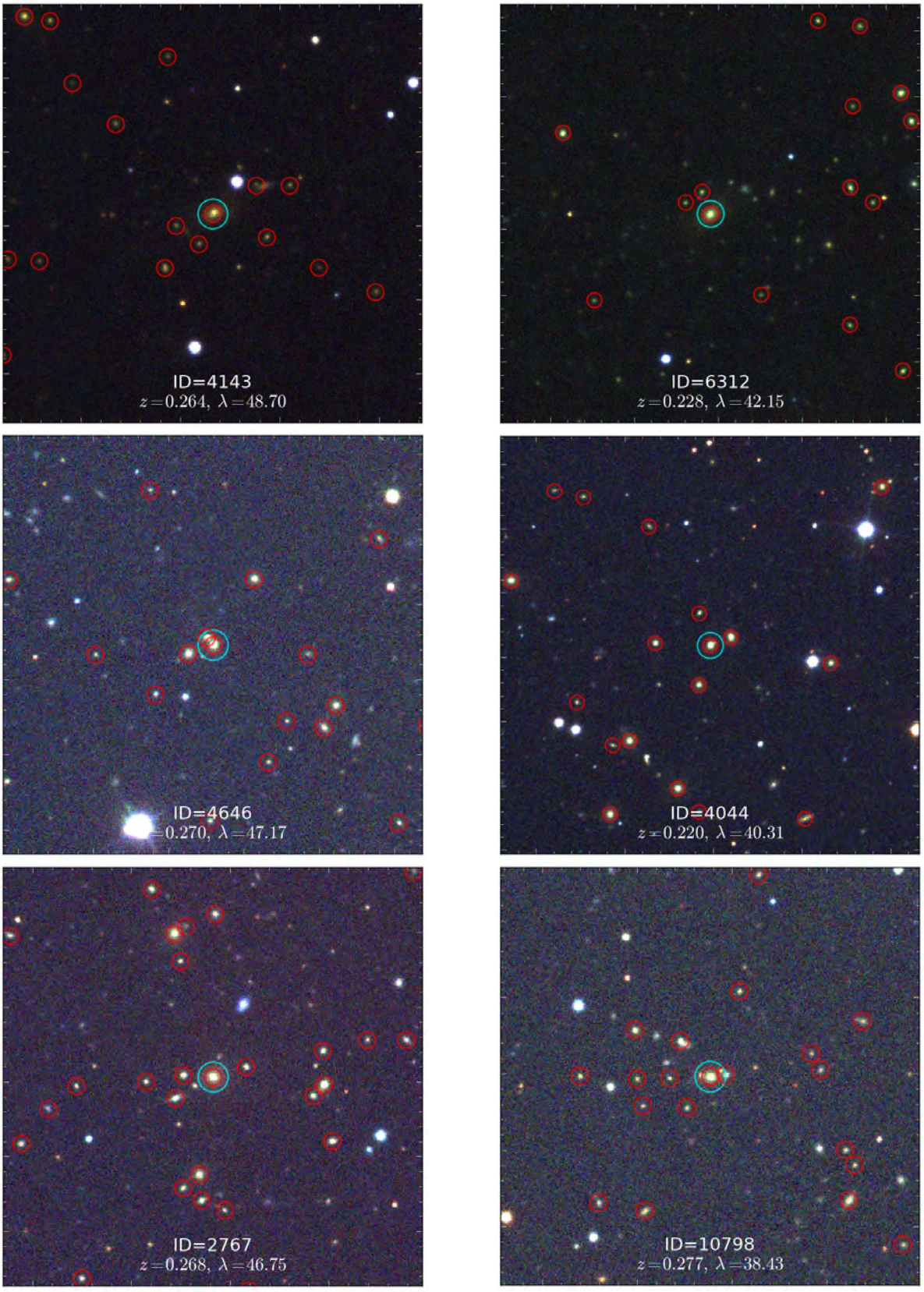

FIGURE A.3: – Continued.

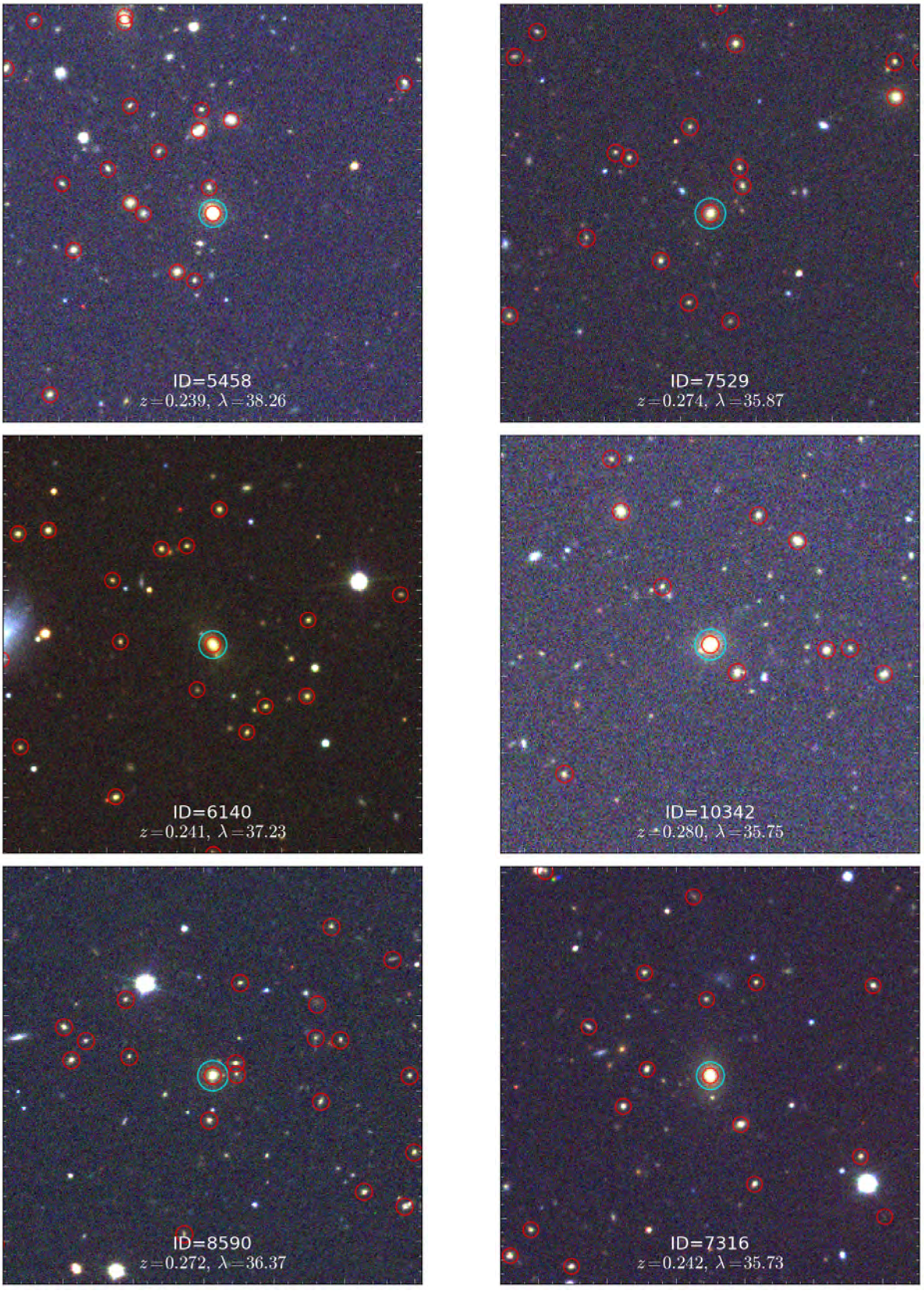

FIGURE A.3: – Continued.

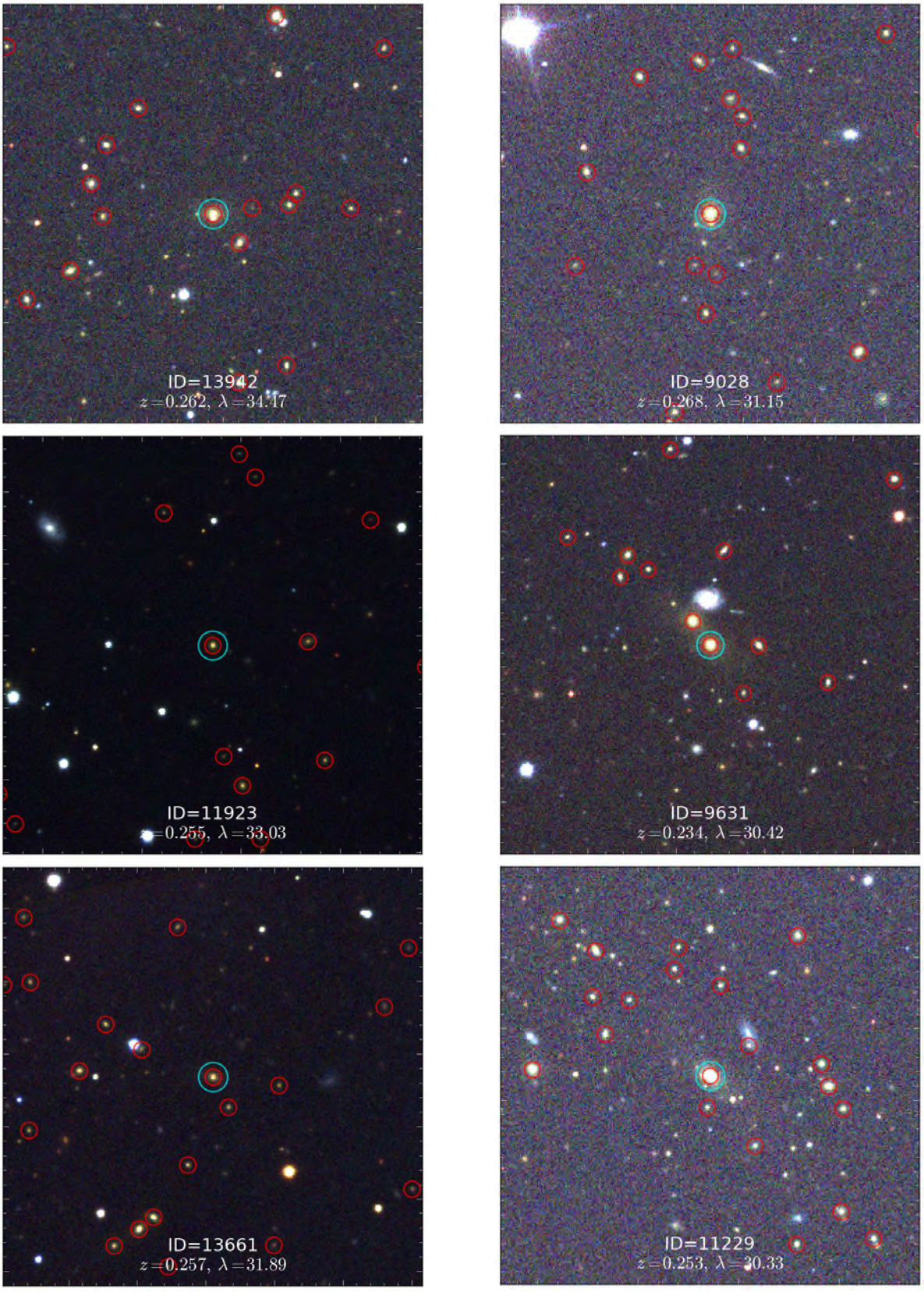

FIGURE A.3: – Continued.

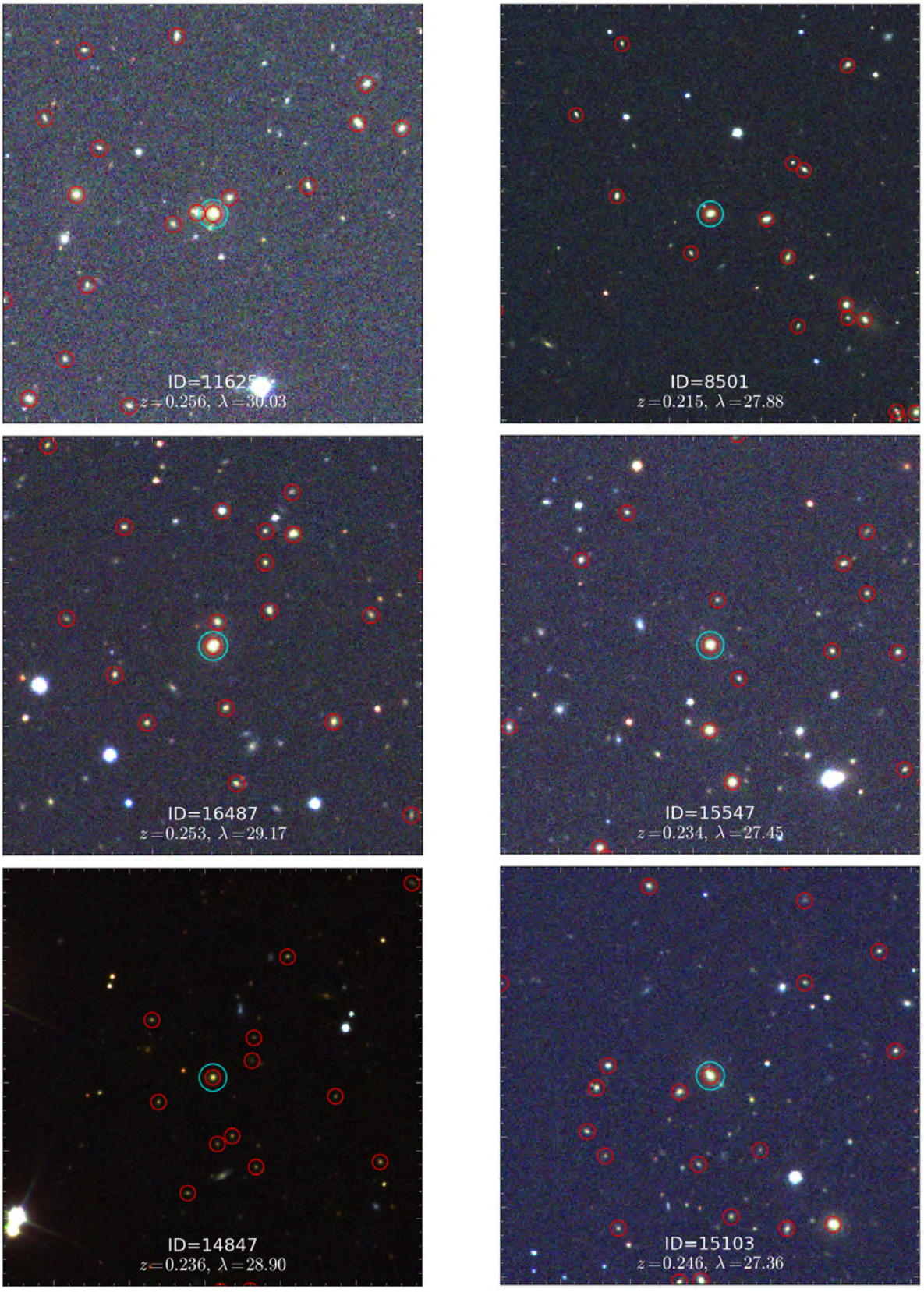

FIGURE A.3: – Continued.

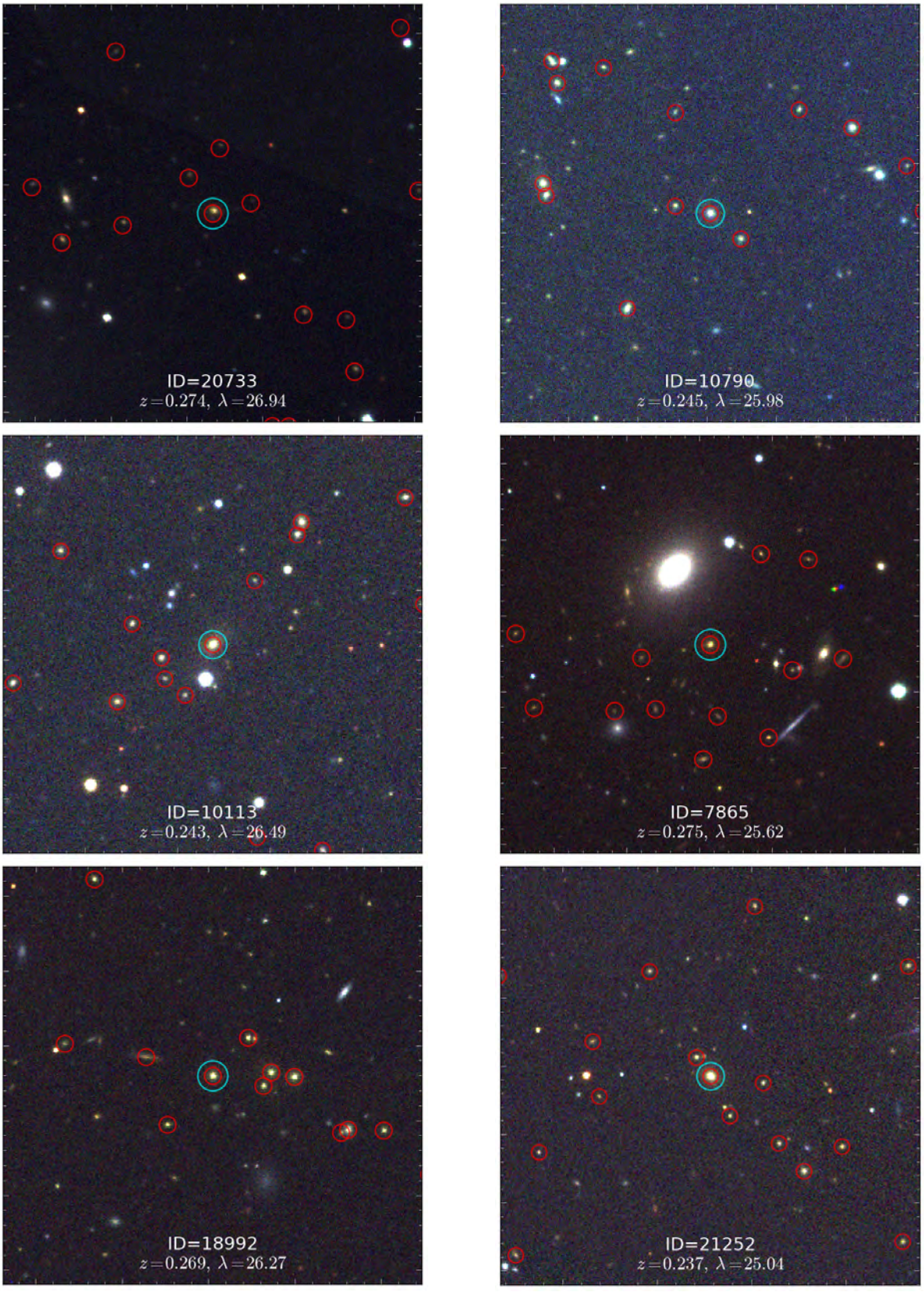

FIGURE A.3: – Continued.

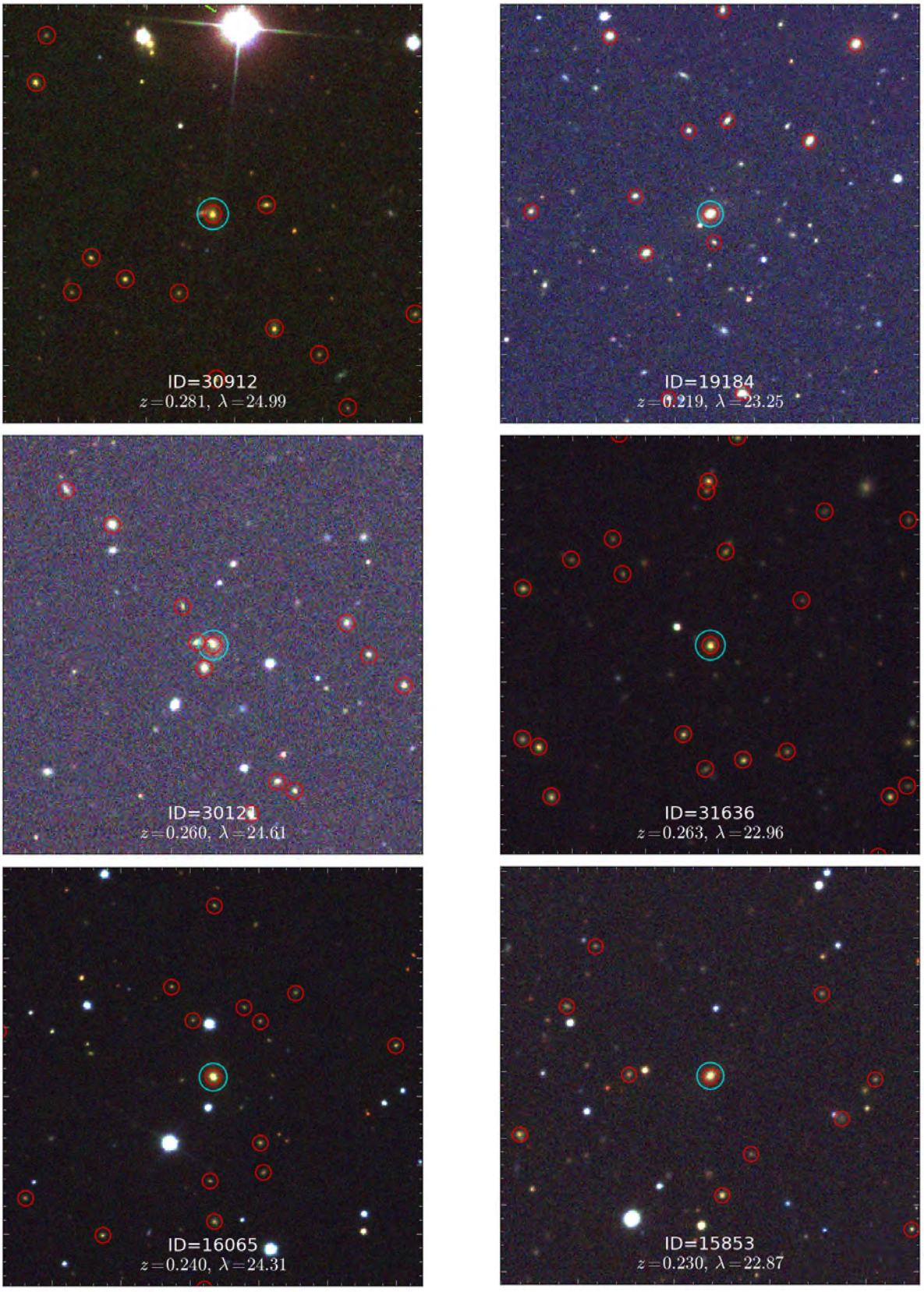

FIGURE A.3: – Continued.

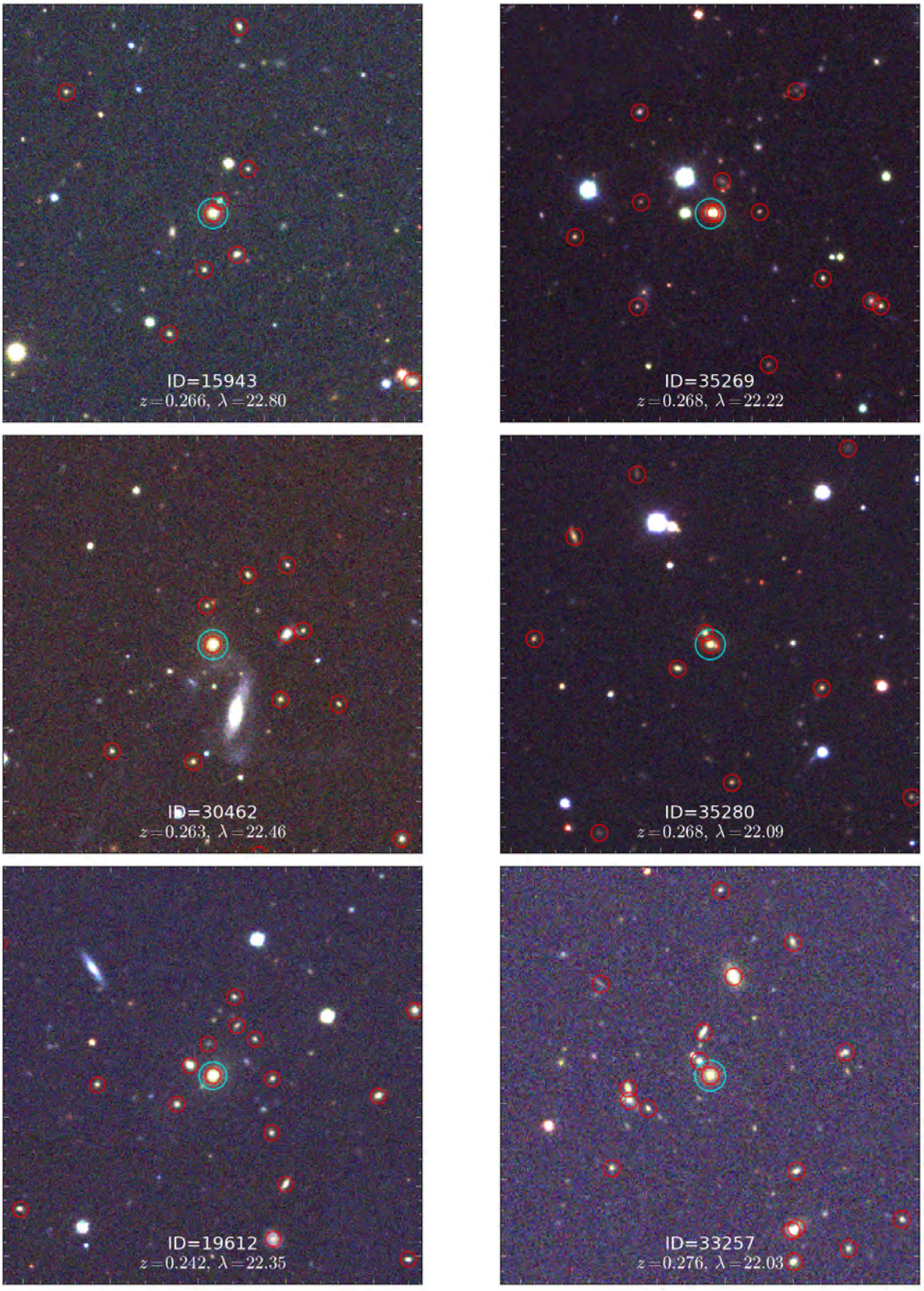

FIGURE A.3: – Continued.

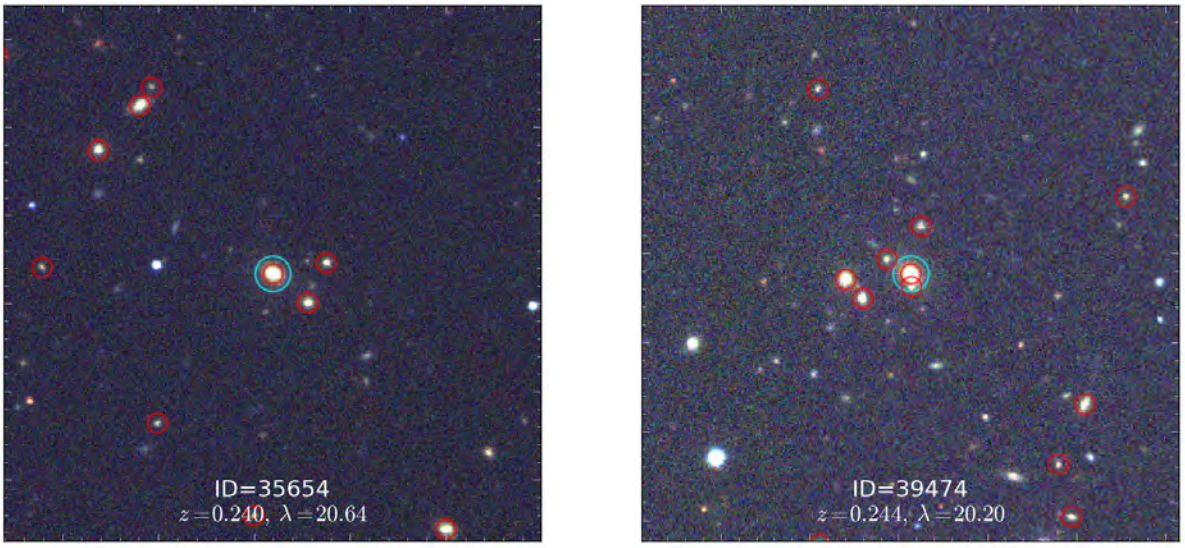

FIGURE A.3: – Continued.

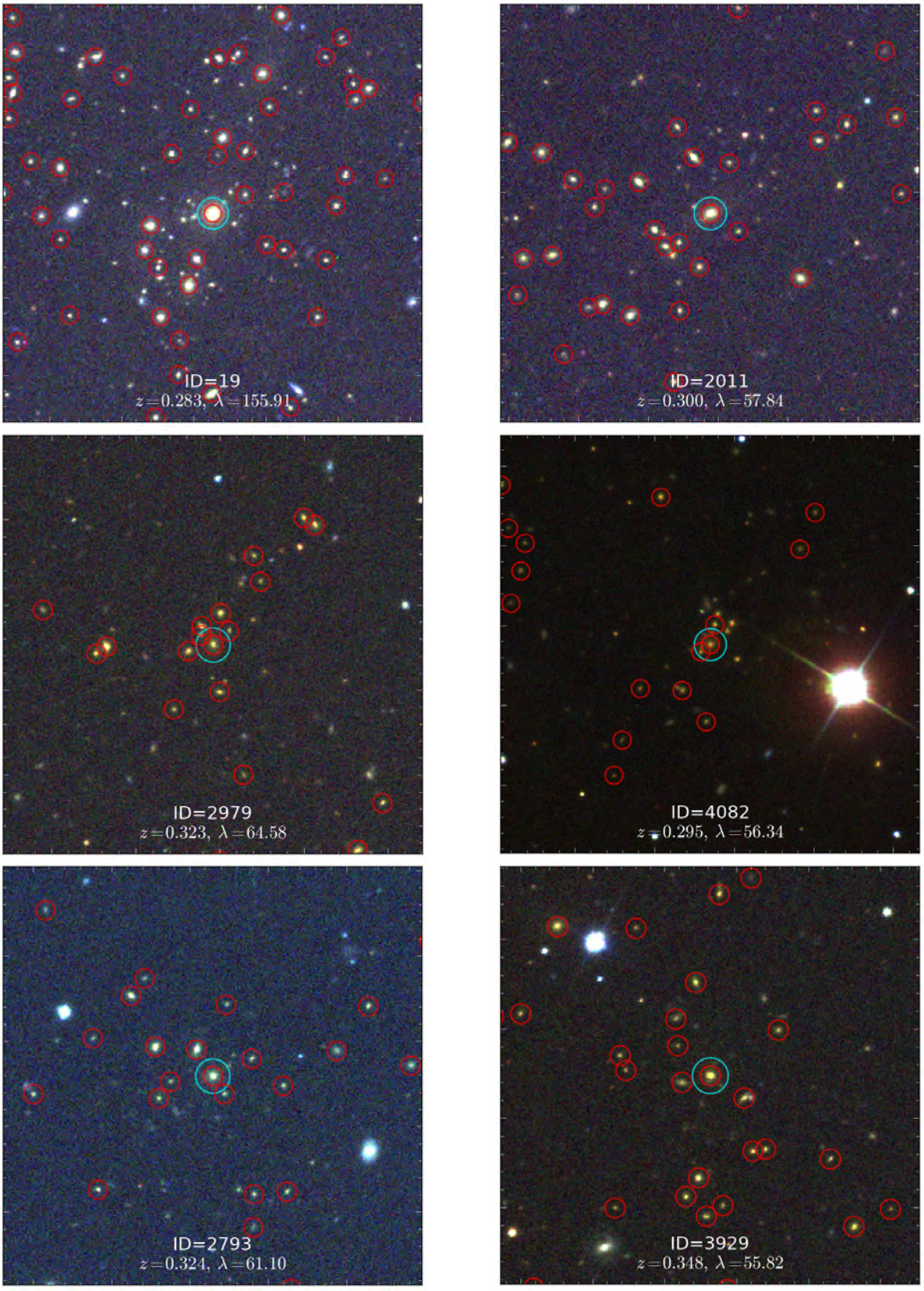

FIGURE A.4: Examples of SDSS cutouts for 50 clusters between $0.28 < z \leq 0.35$.

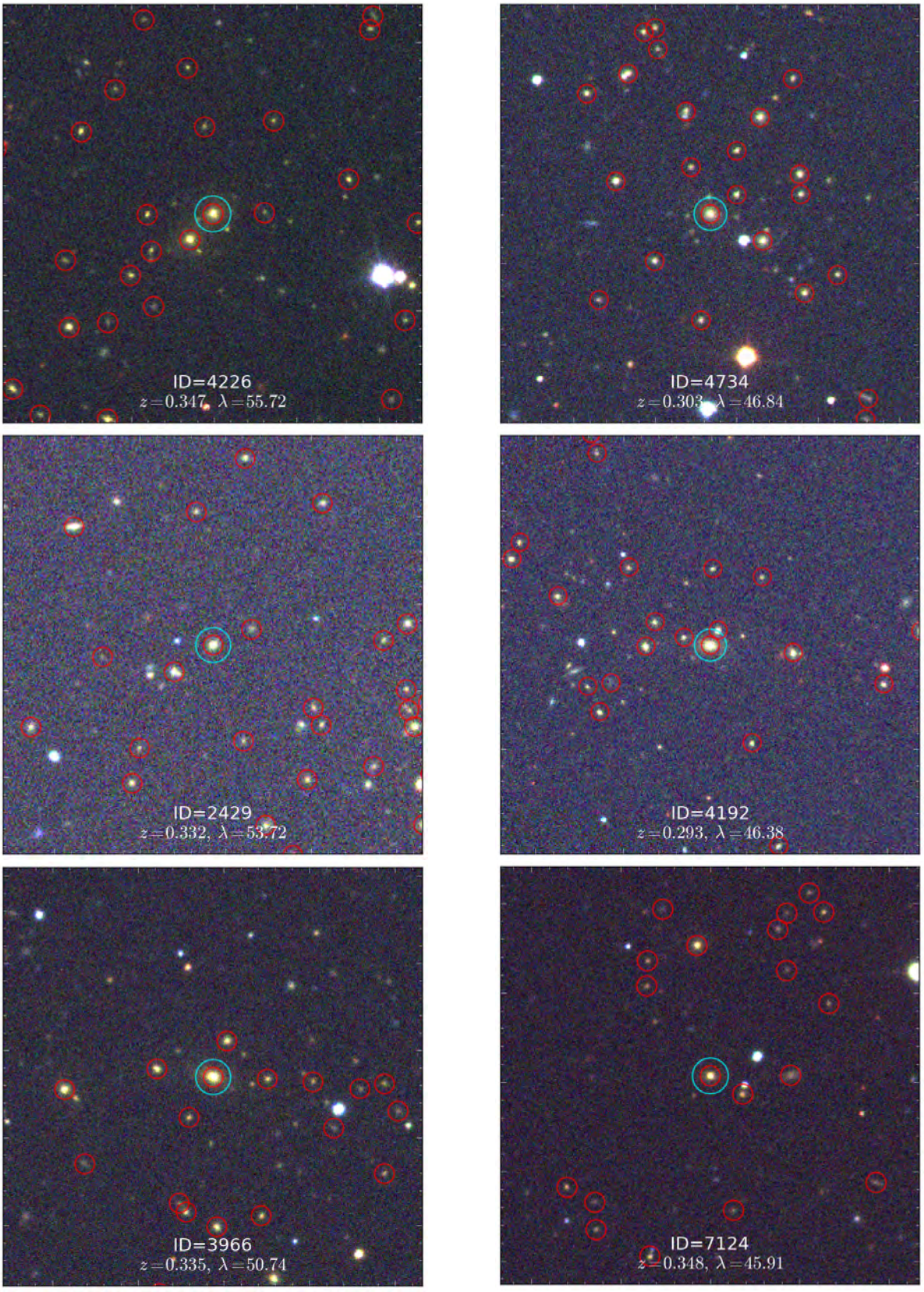

FIGURE A.4: – Continued.

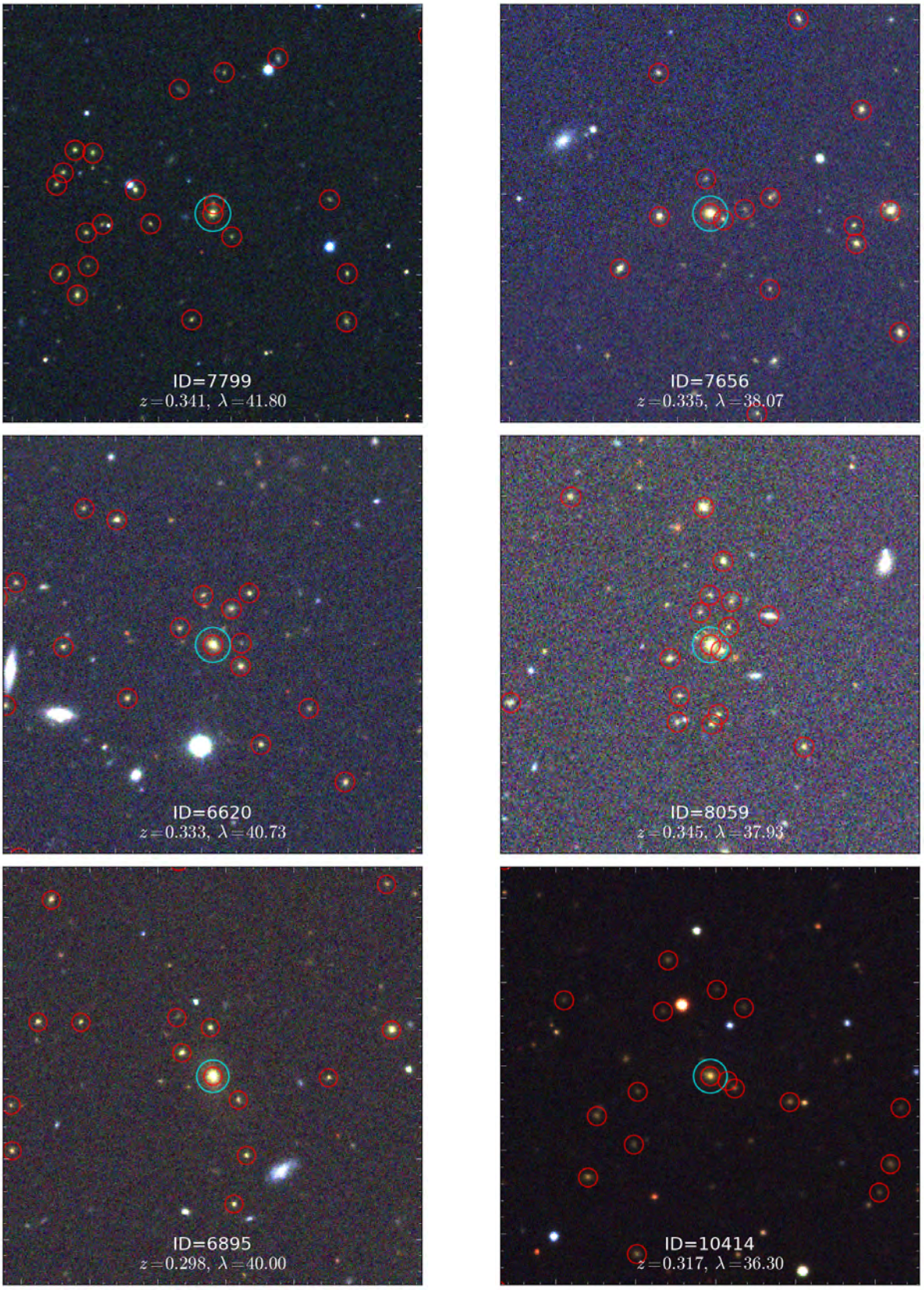

FIGURE A.4: – Continued.

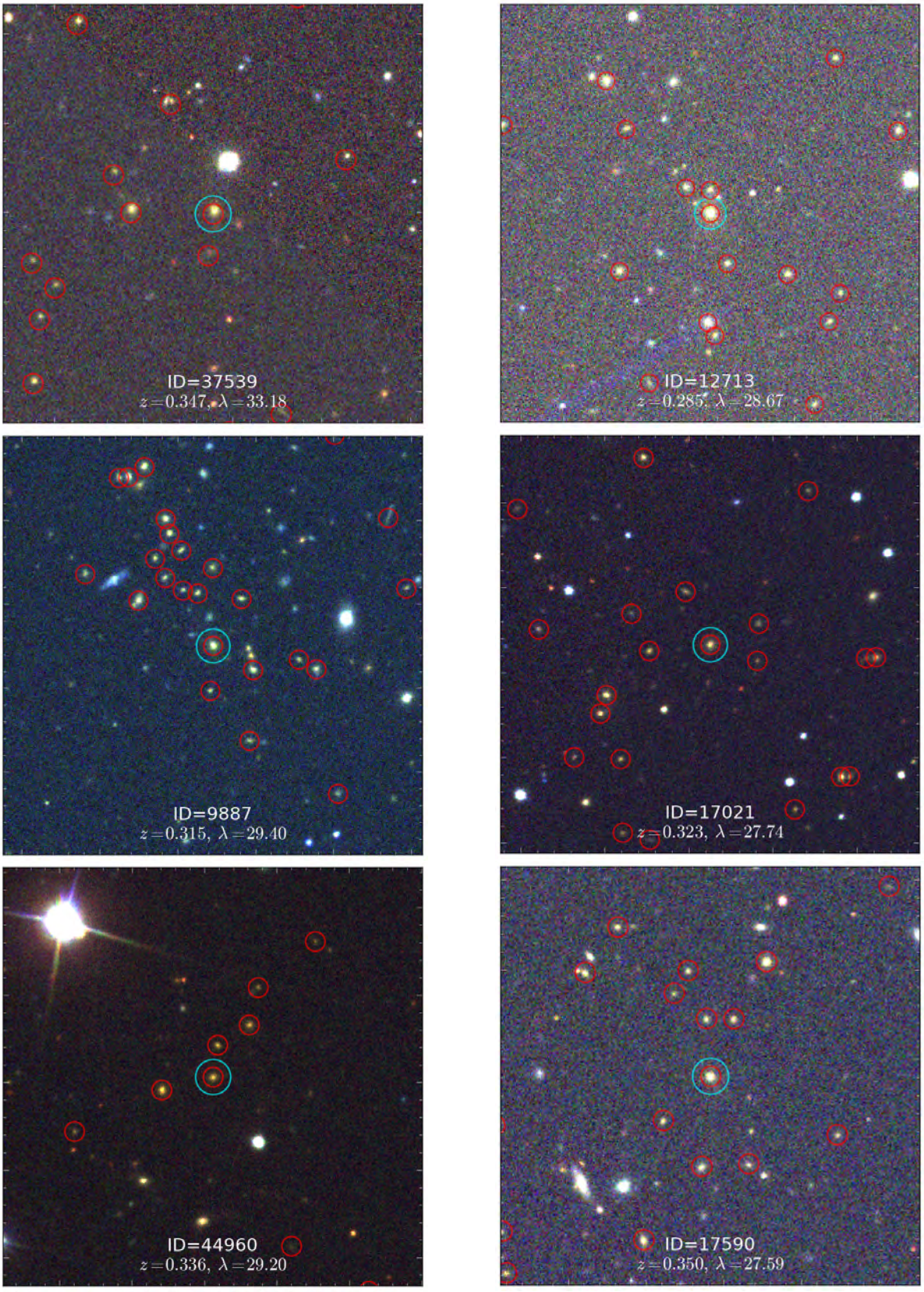

FIGURE A.4: – Continued.

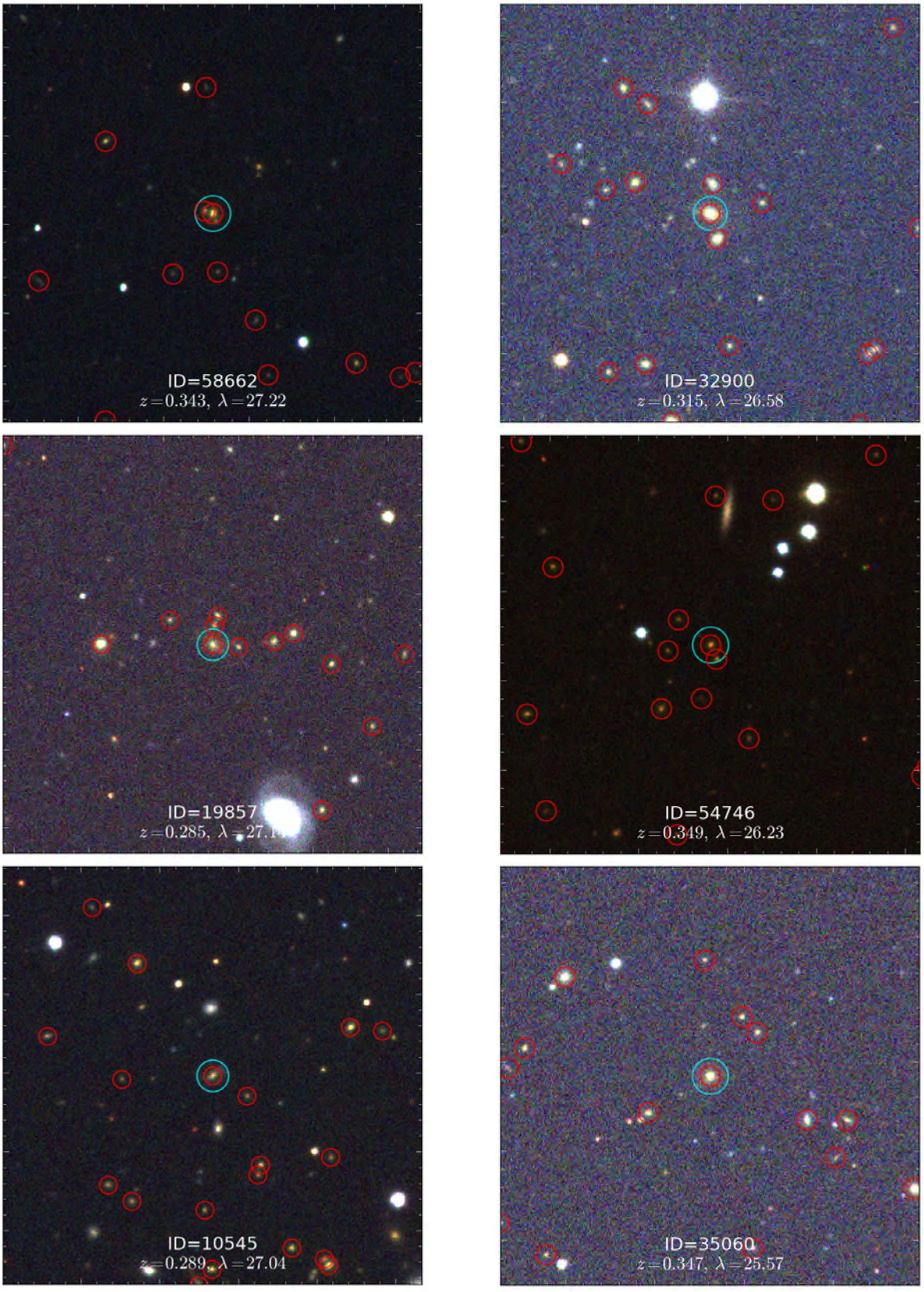

FIGURE A.4: – Continued.

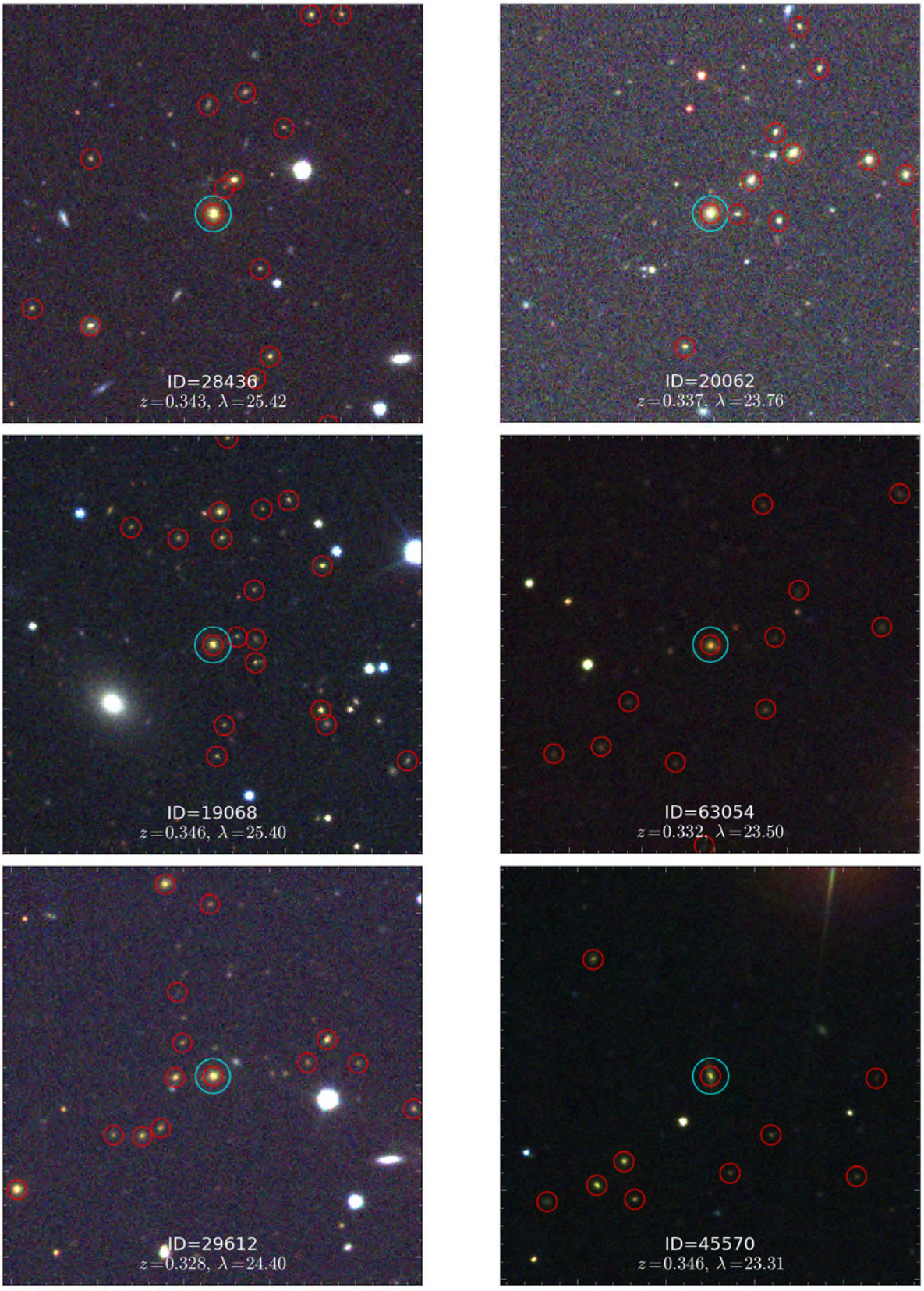

FIGURE A.4: – Continued.

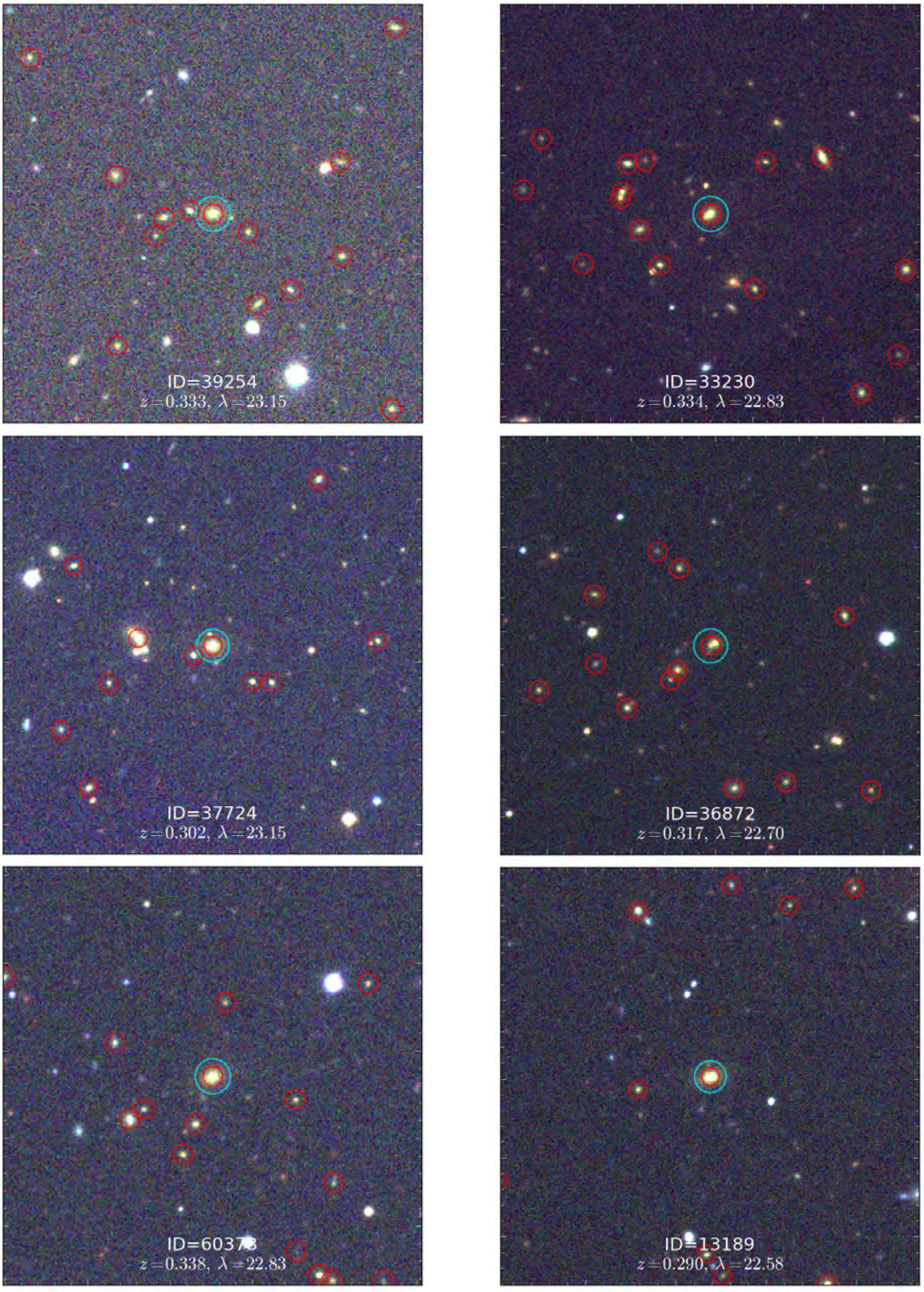

FIGURE A.4: – Continued.

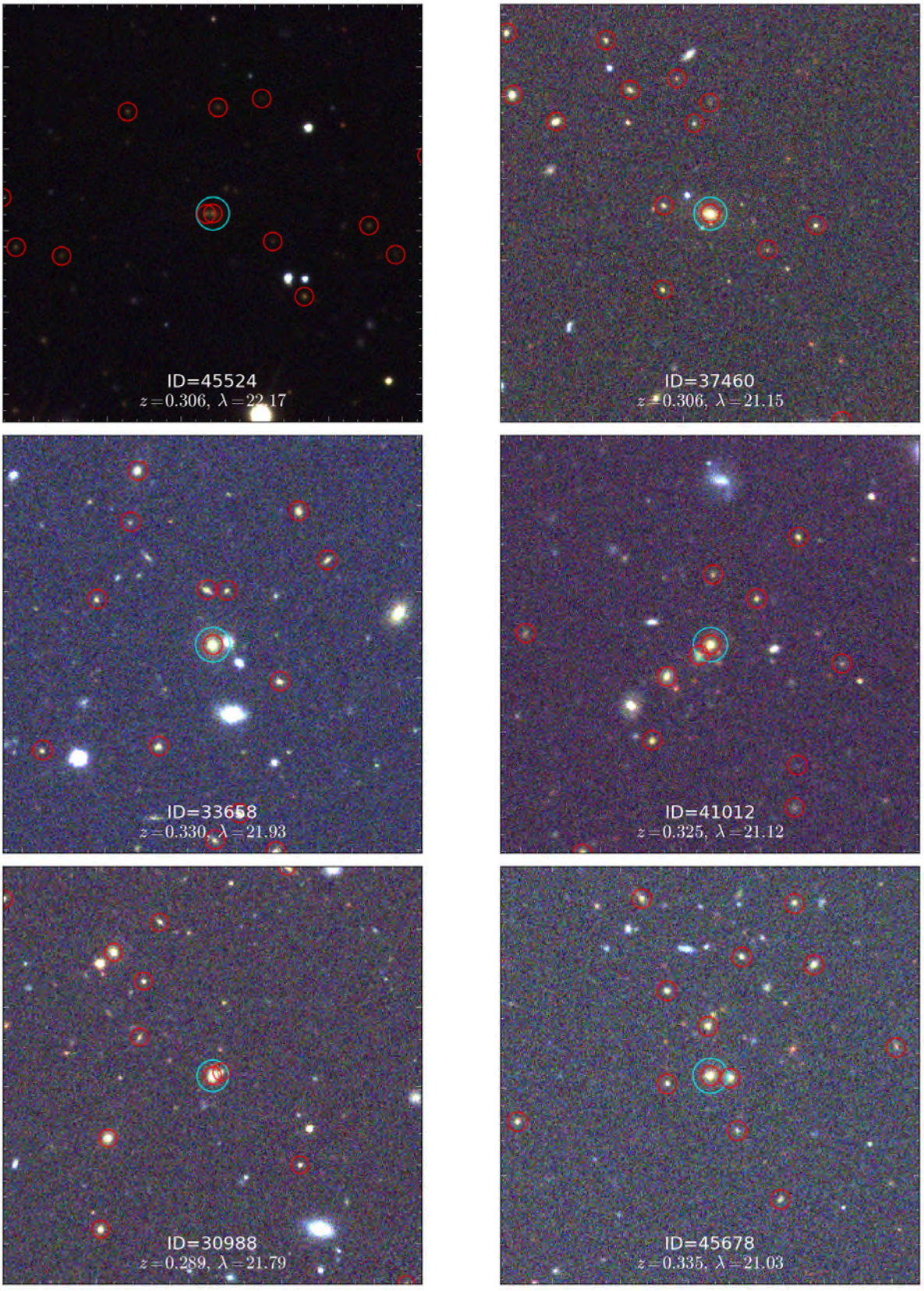

FIGURE A.4: – Continued.

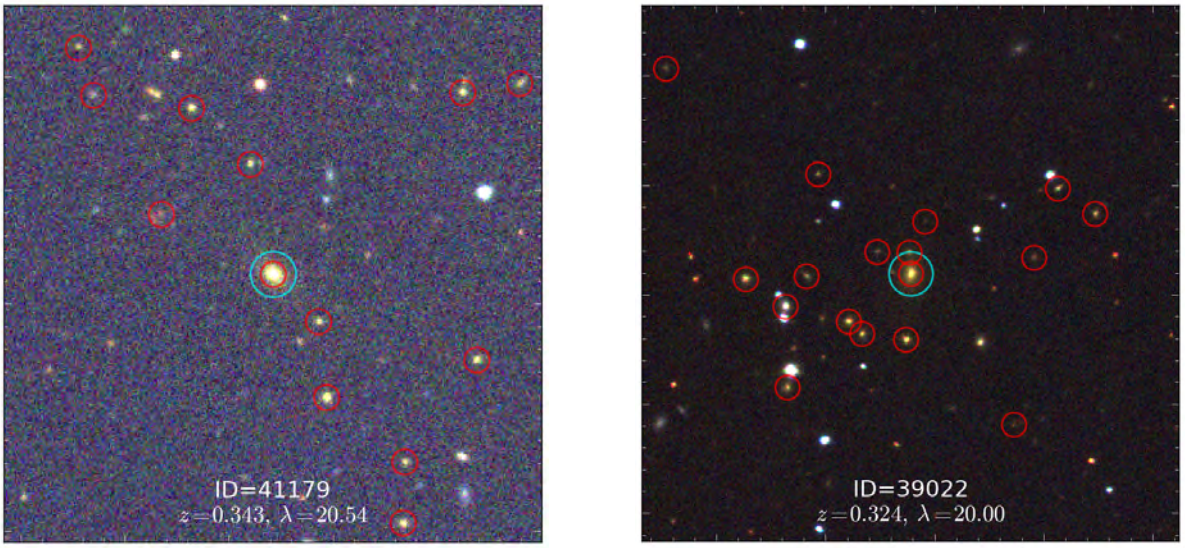

FIGURE A.4: – Continued.

Appendix B

The completeness limit of SDSS and correcting for Malmquist bias

B.1 The completeness limit of SDSS for galaxies

SDSS is a relatively shallow survey and has a 95% completeness for point sources at a magnitude limit of 21.3 magnitudes in the i-band. Since galaxies are used in this project, we need to determine the completeness of SDSS for galaxies. If we were to search for close pairs beyond the magnitude limit where SDSS is complete for galaxies, we run the risk of underestimating the pair fraction of the BCGs. In order to determine what this magnitude limit is for SDSS imaging in the i-band, we proceed as follows.

The Stripe 82 (S82[1]; Adelman-McCarthy et al. 2007) survey covers an area of 275 deg^2 on the celestial equator of SDSS ($-50.8^\circ \leq$ RA $\leq 58.6^\circ$ and $-1.26^\circ \leq$ DEC $\leq 1.26^\circ$). This area has been surveyed multiple times, with the result that S82 imaging are ~ 2 magnitudes deeper than any single-pass scan of SDSS. S82 is therefore able to detect more faint galaxies than SDSS would in the same region of sky. For an SDSS region on the celestial equator, we compare the galaxy number counts from this region as observed with both SDSS and S82 (see Fig B.1). At $m_{\rm i} = 21.5$ mag, SDSS is able to observe 95% of S82's observed galaxy number counts (hereafter 95%

[1] http://cas.sdss.org/stripe82/en/

completeness limit). The completeness limit of SDSS continues to decrease as the magnitudes become fainter. Consequently, we restrict our close pair sample to only contain galaxies that are brighter than $m_{\rm i} = 21.5$ magnitudes.

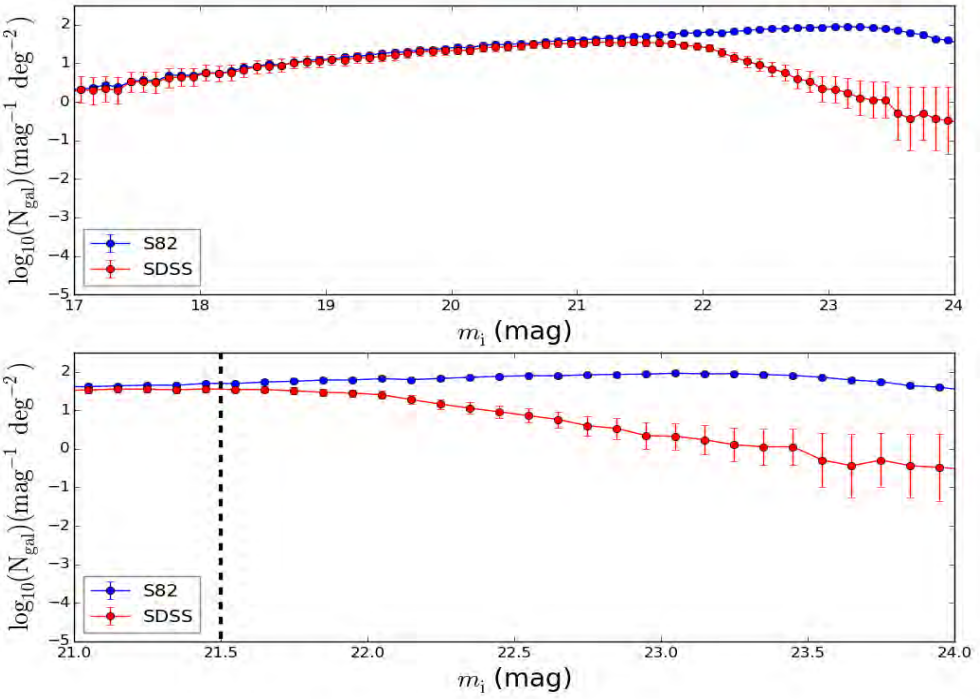

FIGURE B.1: Deriving the completeness limit of SDSS for galaxies. Top panel: For a region on the celestial equator of SDSS, we compare the galaxy number counts as observed by SDSS DR8 (red) and S82 (blue). Bottom panel: Zoomed version of top panel. At $m_{\rm i} = 21.5$ mag (dashed line), SDSS observed 95% of the galaxy number counts that were observed with S82. As the i-band magnitude becomes fainter, the SDSS completeness limit decreases.

B.2 Correcting for Malmquist bias

To ensure that our sample has a high spectroscopic completeness with which the BCG pair fraction could be determined, we further restricted our close pair sample to only include galaxies brighter than the BOSS magnitude limit ($m_{\rm i} \leq 19.9$ mag). However, we cannot include all the galaxies that are brighter than this magnitude limit in our close pair sample. The reason is Malmquist bias (Malmquist 1920); in any flux limited sample, the bias will cause more intrinsically brighter (or more massive) galaxies to be included at higher redshifts. Consequently, we cannot directly compare the

total, observed number of close pairs at low redshifts ($z \sim 0.1$) to those at high redshifts ($z \sim 0.3$) because we will only be seeing the brighter close companions at high redshifts. We correct for this bias by imposing a magnitude difference (Δm_i) on our sample of close pairs to ensure that mergers between BCGs and companions within the same stellar mass range are considered at all redshifts. The imposed magnitude difference is a trade off between maximizing both the redshift range and number of close pairs that may potentially merge.

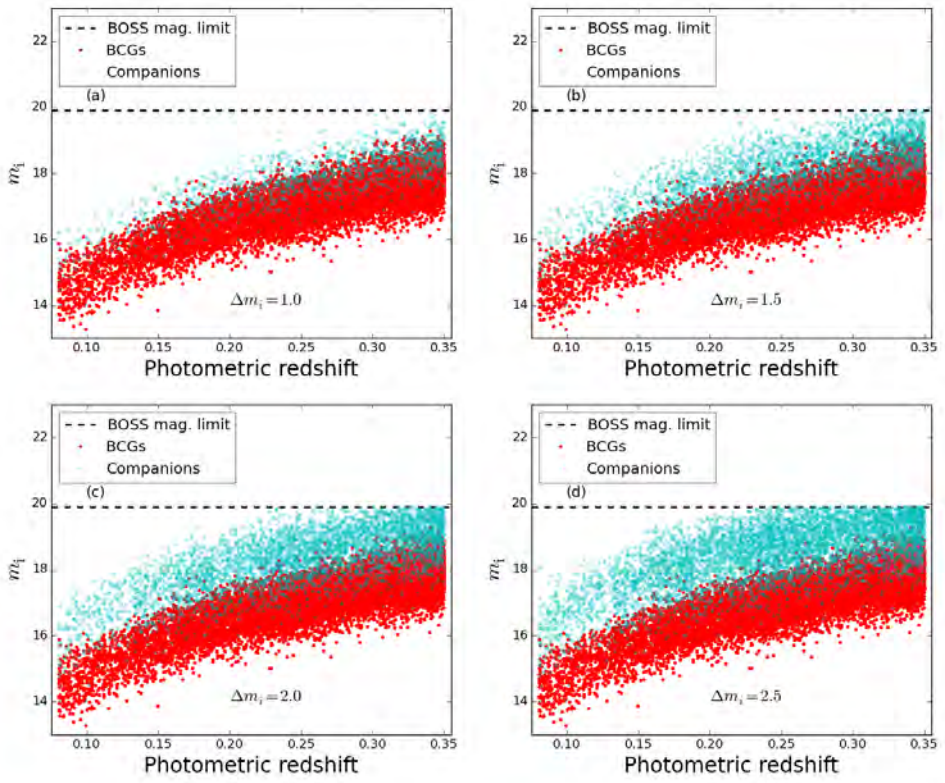

FIGURE B.2: Correcting the close pair sample for Malmquist bias. The *i*-band magnitudes of the BCGs (red) and companions (cyan) in the close pairs are shown as a function of the clusters' photometric redshifts. The dashed line at $m_i = 19.9$ mag in each panel indicates the magnitude limit of the BOSS survey. To correct for Malmquist bias, we impose a magnitude difference on the close pairs. See text for details.

We start off by imposing $\Delta m_i = 1$ mag on the pair sample (see panel a in Fig B.2). Although the whole redshift range ($0.08 \leq z \leq 0.35$) is used and no companion galaxies are excluded from the sample by the BOSS magnitude limit, the number of close pairs that may potentially be involved in mergers is small (~ 1336 pairs). Imposing a magnitude difference of 1.5 causes $\leq 1\%$ of the close

pairs to be excluded from the sample due to the galaxies being fainter than the BOSS magnitude limit. The percentage of pairs that are excluded due to this magnitude limit only increases as the imposed magnitude difference increases. For example, imposing $\Delta m_i = 2.0$ (2.5) mag, causes about 4 (11%) of the close pairs to fall out of our pair sample. This in turn means that we cannot use the whole redshift range to investigate the BCG pair fraction with these stellar mass ratios because we cannot fairly compare the low-z and high-z mergers. In this thesis we choose to impose a $\Delta m_i = 1.5$ mag on the close pairs to account for Malmquist bias. The whole redshift range can then be used to investigate the BCG pair fraction. This is also the stellar mass range that is the least influenced by the BOSS magnitude limit (less than 1% of the close pairs are excluded). We refer to close pairs with $\Delta m_i = 1.5$ mag or less as major mergers (see e.g. Lin et al. 2008; Keenan et al. 2014). This imposed magnitude difference of 1.5 also translates to a stellar mass ratio of 1:4. If we repeat the above stated analysis by replacing the magnitude differences with stellar mass ratios, we find that we are complete for mergers with mass ratios of 1:4 or less (over the whole redshift range). We refer to mergers with stellar mass ratios of (4:1) or less as major mergers (see e.g. Jogee et al. 2009; López-Sanjuan et al. 2012; Robotham et al. 2014). We find that it makes no difference to the measured pair fraction of the BCGs if we use mass or luminosity selected close pairs, since the pair fractions are consistent within the uncertainties. For this project however we will use stellar mass ratios to identify potential major merger candidates.

Appendix C

Investigating colour bimodality in the redMaPPer cluster catalogue

In Section 2.2.2 we explained that the redMaPPer catalogue does not necessarily only contain galaxies that are located on the red-sequence, i.e. galaxies on the blue cloud might also be included (but the sample is almost certainly not complete for blue galaxies, by design). We test this by separating the red-sequence galaxies from their blue counterparts by using a method similar to that of Lu et al. (2009). Very briefly, the width of the red-sequence is obtained by using a single Gaussian fitting. Any galaxies bluer than the lower 2σ limit are classified as blue while those above this limit are considered to be part of the red-sequence.

This empirical colour cut method (that is based on the red-sequence) will allow us to identify the red-sequence galaxies within our close pair sample along with any potential blue galaxies (see Section C.1 for details). We must understand what we are measuring: this should be either purely red galaxies or red plus *all* the blue galaxies (i.e. the total cluster population). We therefore have to ensure that all possible blue galaxies that may merge with the BCGs are included in our analysis. We do this by determining what number of blue galaxies has been 'missed' during the construction of the catalogue (Section C.2). This will present us with an upper limit to the number of blue galaxies that may potentially be involved in mergers with the BCGs. After we separate the galaxies by

colour, we proceed to investigate what influence the different galaxy populations may have on the BCG pair fraction in Section C.3.

C.1 Separating the red and blue galaxies in the redMaPPer catalogue

We begin by constructing colour-magnitude diagrams (CMDs) for the galaxies in our pair sample. This is shown in Fig C.1, where the $(g-r)$ colours of the galaxies in various redshift bins are plotted against their observed i-band magnitudes. All the galaxies in our pair sample have $z \leq 0.35$ and we use the $(g-r)$ colours in the CMDs since the 4000 Å break is spanned by this colour.

For each redshift bin we construct a composite CMD to define the best-fitting colour-magnitude relation (CMR). An initial CMR fit is obtained by considering all the galaxies in the pair sample (illustrated as red points in Fig C.1). To obtain a more accurate CMR fit, we only consider galaxies (i) that have high probabilities of being red-sequence galaxies ($P_{RSM} \geq 0.9$) and (ii) are within 0.2 mag[1] of the initial CMR fit. Due to the fact that the photometry becomes more uncertain at faint magnitudes, we further require that the galaxies be brighter than the magnitudes represented by the green dashed lines. These magnitudes are chosen in such a way that the slope of the CMR fit does not change if the limit is moved to fainter magnitude.

The galaxies in our pair sample that satisfy these three criteria are divided into magnitude bins of 0.5 mag. For each magnitude bin we determine the mean of the colour-distribution. Using a straight line, we fit the means as a function of magnitude to obtain the best-fitting CMR for a particular redshift slice. We examine the fit more closely by subtracting the best-fitting CMR from the observed relation, whereafter the relative position of each galaxy is plotted with respect to the best-fitting CMR. An example of this is shown in Fig C.2 where the galaxies within $0.15 \leq z \leq 0.19$ (represented in third panel of Fig C.1) are considered. The residuals of the distribution are represented by the histogram in the right-hand panel.

[1]We use a wide colour slice to ensure that we do not lose any potential red-sequence galaxies due to uncertainties in the $(g-r)$ colour.

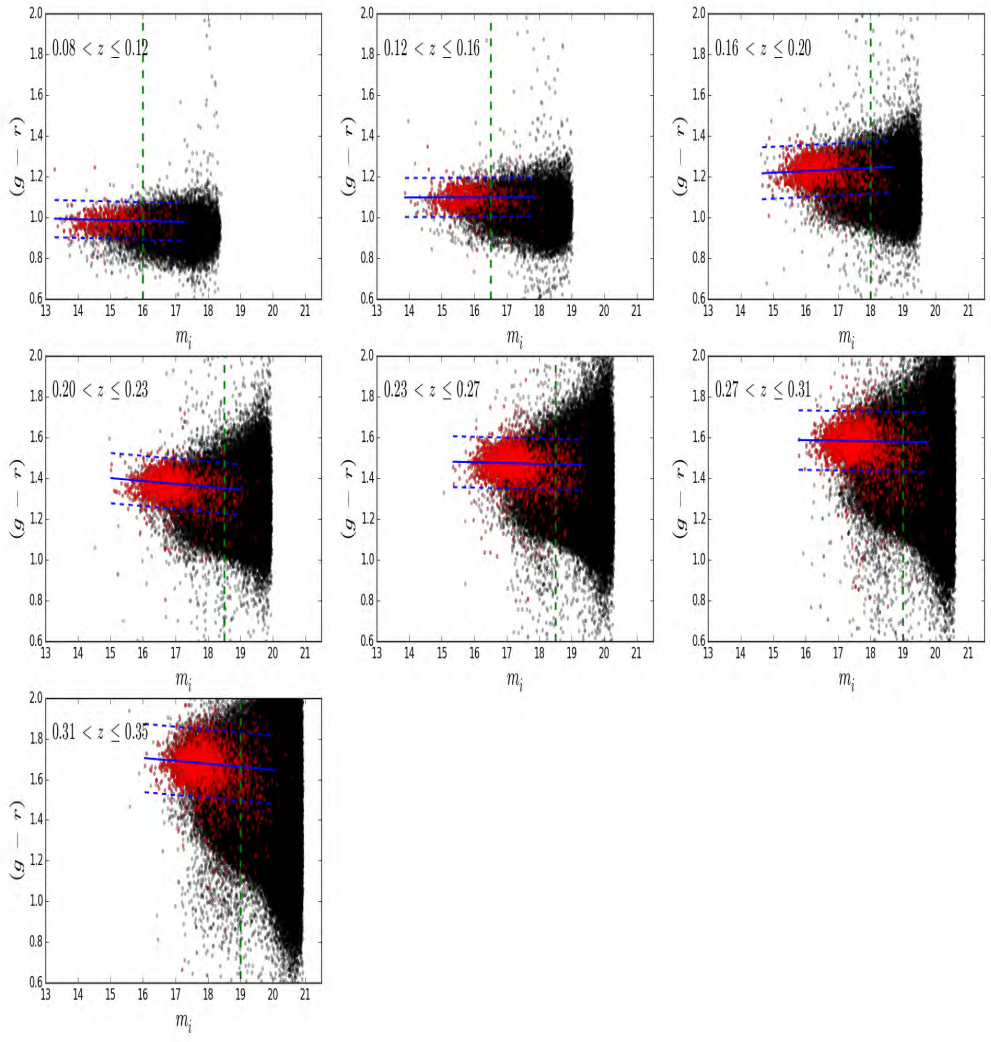

FIGURE C.1: The composite CMDs of galaxies in the close pair sample for various redshift bins. The red points represent the location of the galaxies in the close pair sample with respect to those in the original redMaPPer catalogue (black points). The central line represent the best-fitting colour-magnitude relation (CMR) while the upper and lower lines represent the 2σ limits. The dashed green lines represent the magnitudes where the slope of the CMR fit does not change.

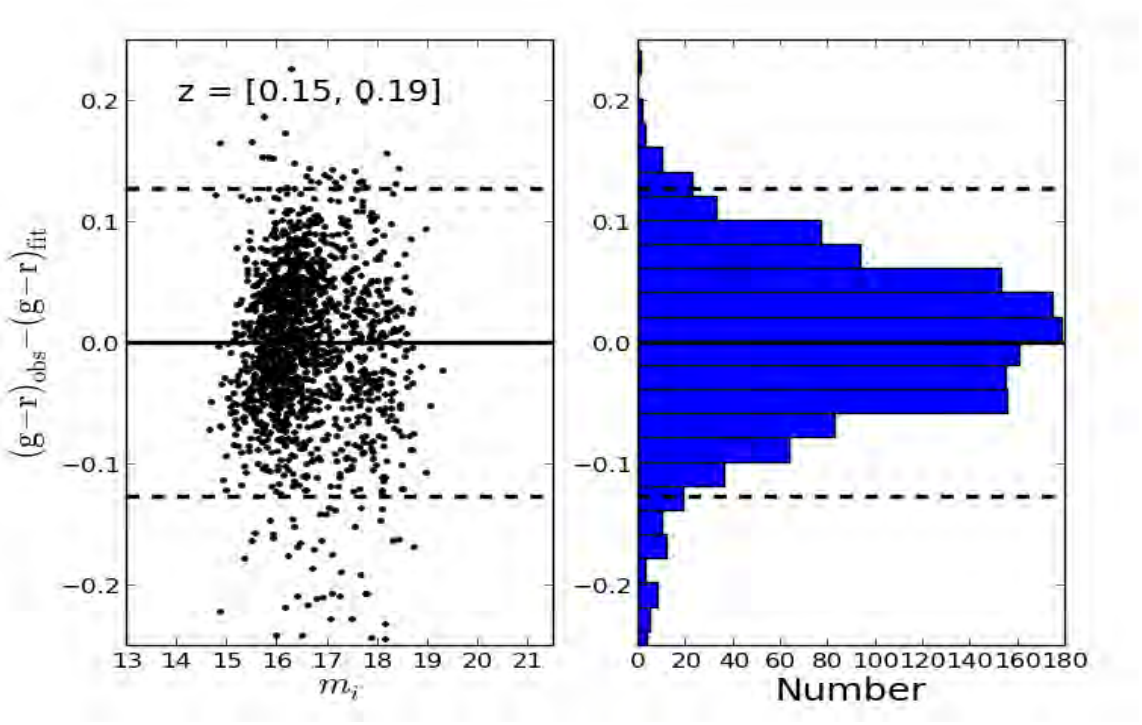

FIGURE C.2: For the galaxies with $0.15 \leq z \leq 0.19$, we investigate the fitted colour-magnitude relation (CMR). Left panel: the fitted and observed CMRs are subtracted and the relative position of each galaxy with respect to the fitted CMR is plotted. Right panel: the distribution of the galaxies relative to the fitted CMR. In both panels the solid line indicate the zero offset while the 2σ limits are indicated by the dashed lines.

In order to determine the width of the best-fitting CMR, we only consider the galaxies redder than the fitted CMR (galaxies above the solid line in Fig C.2) in order to avoid contamination from blue galaxies. The colour-distribution of these galaxies are mirrored and 3σ clipping is then applied to determine the width of the red-sequence.

All galaxies above the lower 2σ limit are considered to be red, while those below this limit are considered to be blue galaxies. The galaxies located above the upper 2σ limit are likely to be included in the catalogue due to projection effects. More specifically, galaxies redder than the red-sequence will be behind the clusters. All galaxies within 2σ of the best-fitting CMR are considered to be located on the red-sequence. A summary of the galaxies in our close pair sample, split according to colour, is given in Table C.1. The pair sample contains approximately 11 000 clusters and 7% of the galaxies within these clusters are blue.

TABLE C.1: Summary of the galaxies in the close pair sample, split according to colour.

	Number
Total	13588
Red galaxies	12756
Blue galaxies	832
Within 2σ of fitted CMR	12337
'Missed' blue galaxies	199

C.2 'Missing' blue galaxies from the redMaPPer catalogue

In the previous section we found that some blue galaxies are also included in the redMaPPer (red sequence member) catalogue. To ensure that we consider all possible merger candidate galaxies that have blue photometric colours, we proceed to determine what number of blue galaxies has not been included in the redMaPPer catalogue and was therefore 'missed' during the catalogue's construction.

From Section C.1 we know where the blue galaxies are located in the CMDs. Using CASJOBS[2] we search SDSS DR8 for blue galaxies that are within (i) $7 < r_{\rm sep} \leq 50$ kpc and (ii) $\Delta m_i = 1.5$ mag[3] of the BCGs in the pair sample. We do not require any of these galaxies to have spectroscopic information and as a result we may include some blue galaxies due to projection effects. We find that a maximum of ~ 200 blue galaxies have been 'missed' during the catalogue's construction.

[2]http://skyserver.sdss.org/casjobs/

[3]For the purpose of this test, we use luminosity ratios (rather than stellar masses) to identify major merger candidates since we found that it makes no difference to the observed pair fraction.

C.3 The effect of colour bimodality on the BCG pair fraction

Using empirical colour cuts, we have shown that the redMaPPer catalogue contains both red and blue galaxies. We proceed to investigate what effect, if any, these two galaxy populations have on the average BCG pair fraction.

Considering only the photometry of the galaxies in the pair sample, we determine the pair fraction from Eq 4.2. We account for projection effects by applying a 50% contamination correction (similar to Edwards & Patton 2012, see Section 4.2.1). The pair fractions are determined for the following cases: (1) no additional colour cuts, apart from the original redMaPPer selection, are applied; (2) red and blue galaxies are separated; (3) only galaxies located on the red-sequence are considered and (4) the 'missing' blue galaxies are included. The resulting pair fractions are shown in Fig C.3. Since the fraction of blue galaxies in the pair sample is small (7%), it is not surprising that the number of mergers between the BCGs and blue companions are small (see blue points).

Compare the BCG pair fraction, derived without any colour cuts (black points) to that derived from mergers between BCGs and (i) red companions (red points) and (ii) red-sequence galaxies (green points). These pair fractions are consistent within the uncertainties, however at $z \sim 0.25$ the pair fractions from the red and red-sequence galaxies are lower than the pair fraction if no colour cuts are applied. This is due to the slight increase in the pair fraction of blue galaxies. If the 200 'missed' blue galaxies are added to the close pair sample, we find that the pair fraction (shown in magenta) is consistent with the overall pair fraction (black points) within the uncertainties.

In summary: By imposing a strict colour selection criteria, we find that not all the galaxies in the redMaPPer catalogue are located on the red-sequence, since a small fraction (7%) of these galaxies are blue. We determined an upper limit to the number of blue galaxies that has been 'missed' during the construction of the redMaPPer catalogue ($\sim$ 200 blue galaxies). We also find that these 'missing' blue galaxies have a negligible influence on the average BCG pair fraction.

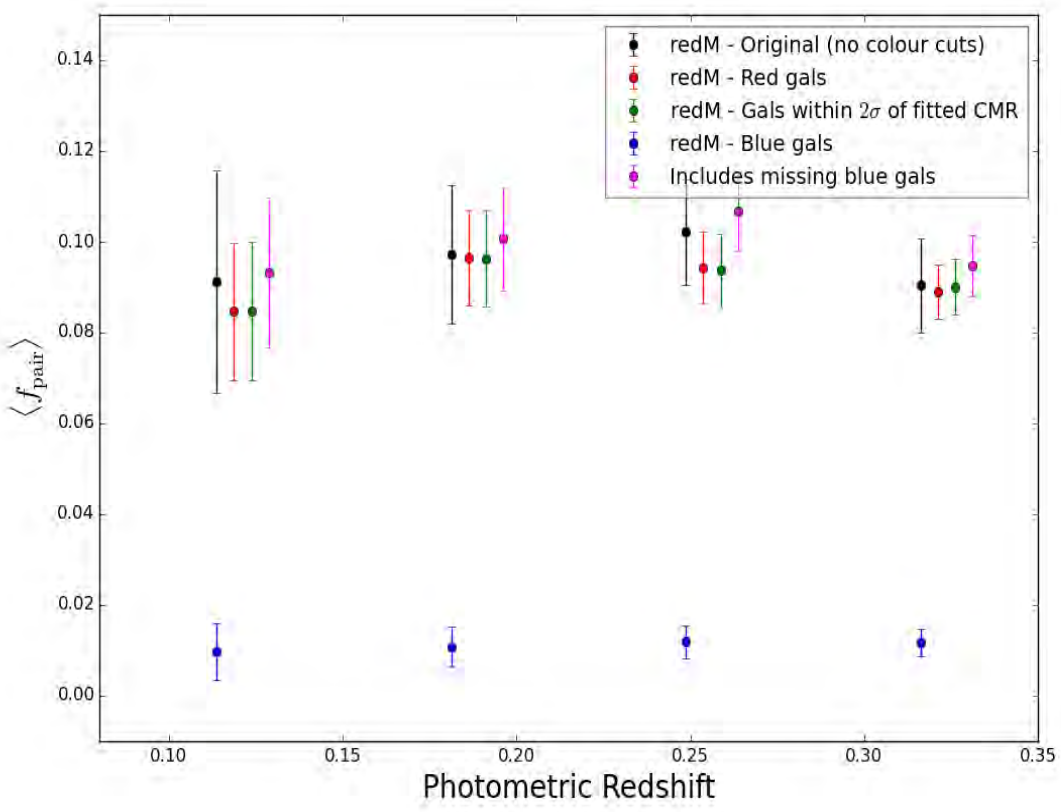

FIGURE C.3: Investigating the influence of red and blue galaxies on the major pair fraction of the BCGs in close pair sample. The pair fraction within $7 < r_{\rm sep} \leq 50$ kpc is derived by only considering the photometry of the galaxies. We account for projection effects by applying a 50% contamination correction. The pair fractions are indicated for the following cases: (1) no colour cuts are applied (black points); (2) separating blue from red galaxies; (3) only considering galaxies on the red-sequence (green points) and (4) including the 'missing' blue galaxies (magenta points). The uncertainties have been derived using the method of Cameron (2011).

Bibliography

Abadi, M. G., Moore, B., & Bower, R. G. 1999, MNRAS, 308, 947

Abazajian, K. N., Adelman-McCarthy, J. K., Agüeros, M. A., et al. 2009, ApJS, 182, 543

Adelman-McCarthy, J. K., Agüeros, M. A., Allam, S. S., et al. 2007, ApJS, 172, 634

Ahn, C. P., Alexandroff, R., Allende Prieto, C., et al. 2012, ApJS, 203, 21

Aihara, H., Allende Prieto, C., An, D., et al. 2011, ApJS, 193, 29

Alam, S., Albareti, F. D., Prieto, C. A., et al. 2015, ApJS, 219, 12

Allen, S. W. 1995, MNRAS, 276, 947

Allen, S. W., Fabian, A. C., Edge, A. C., Bautz, M. W., Furuzawa, A., & Tawara, Y. 1996, MNRAS, 283, 263

Aragon-Salamanca, A., Baugh, C. M., & Kauffmann, G. 1998, MNRAS, 297, 427

Aragon-Salamanca, A., Ellis, R. S., Couch, W. J., & Carter, D. 1993, MNRAS, 262, 764

Arimoto, N. & Yoshii, Y. 1987, A&A, 173, 23

Ascaso, B., Aguerri, J. A. L., Varela, J., Cava, A., Bettoni, D., Moles, M., & D'Onofrio, M. 2011, ApJ, 726, 69

Ascaso, B., Lemaux, B. C., Lubin, L. M., Gal, R. R., Kocevski, D. D., Rumbaugh, N., & Squires, G. 2014, MNRAS, 442, 589

Bai, L., Yee, H. K. C., Yan, R., et al. 2014, ApJ, 789, 134

Baldry, I. K., Balogh, M. L., Bower, R. G., Glazebrook, K., Nichol, R. C., Bamford, S. P., & Budavari, T. 2006, MNRAS, 373, 469

Baldry, I. K., Glazebrook, K., Brinkmann, J., Ivezić, Ž., Lupton, R. H., Nichol, R. C., & Szalay, A. S. 2004, ApJ, 600, 681

Balogh, M., Eke, V., Miller, C., et al. 2004a, MNRAS, 348, 1355

Balogh, M. L., Baldry, I. K., Nichol, R., Miller, C., Bower, R., & Glazebrook, K. 2004b, ApJLett, 615, L101

Balogh, M. L., Navarro, J. F., & Morris, S. L. 2000, ApJ, 540, 113

Beers, T. C. & Geller, M. J. 1983, ApJ, 274, 491

Beers, T. C. & Tonry, J. L. 1986, ApJ, 300, 557

Behroozi, P. S., Marchesini, D., Wechsler, R. H., Muzzin, A., Papovich, C., & Stefanon, M. 2013, ApJLett, 777, L10

Bell, E. F., Naab, T., McIntosh, D. H., et al. 2006a, ApJ, 640, 241

Bell, E. F., Phleps, S., Somerville, R. S., Wolf, C., Borch, A., & Meisenheimer, K. 2006b, ApJ, 652, 270

Bell, E. F., Wolf, C., Meisenheimer, K., et al. 2004, ApJ, 608, 752

Bellstedt, S., Lidman, C., Muzzin, A., et al. 2016, MNRAS, 460, 2862

Benson, A. J., Bower, R. G., Frenk, C. S., Lacey, C. G., Baugh, C. M., & Cole, S. 2003, ApJ, 599, 38

Bernardi, M. 2009, MNRAS, 395, 1491

Bernardi, M., Hyde, J. B., Sheth, R. K., Miller, C. J., & Nichol, R. C. 2007, AJ, 133, 1741

Bernardi, M., Meert, A., Sheth, R. K., Huertas-Company, M., Maraston, C., Shankar, F., & Vikram, V. 2016, MNRAS, 455, 4122

Bertin, E. & Arnouts, S. 1996, A&AS, 117, 393

Bertone, S. & Conselice, C. J. 2009, MNRAS, 396, 2345

Best, P. N., von der Linden, A., Kauffmann, G., Heckman, T. M., & Kaiser, C. R. 2007, MNRAS, 379, 894

Bildfell, C., Hoekstra, H., Babul, A., & Mahdavi, A. 2008, MNRAS, 389, 1637

Bildfell, C., Hoekstra, H., Babul, A., et al. 2012, MNRAS, 425, 204

Binney, J. & Tremaine, S. 1987, Galactic dynamics

Blakeslee, J. P. & Tonry, J. L. 1992, AJ, 103, 1457

Blanton, M. R., Lin, H., Lupton, R. H., Maley, F. M., Young, N., Zehavi, I., & Loveday, J. 2003, AJ, 125, 2276

Blanton, M. R. & Roweis, S. 2007, AJ, 133, 734

Blanton, M. R., Schlegel, D. J., Strauss, M. A., et al. 2005, AJ, 129, 2562

Bower, R. G., Benson, A. J., Malbon, R., Helly, J. C., Frenk, C. S., Baugh, C. M., Cole, S., & Lacey, C. G. 2006, MNRAS, 370, 645

Bower, R. G., Lucey, J. R., & Ellis, R. S. 1992, MNRAS, 254, 601

Boylan-Kolchin, M., Springel, V., White, S. D. M., Jenkins, A., & Lemson, G. 2009, MNRAS, 398, 1150

Bradley, R., Clarke, J., Kinion, D., Rosenberg, L. J., van Bibber, K., Matsuki, S., Mück, M., & Sikivie, P. 2003, Rev. Mod. Phys., 75, 777

Brammer, G. B., Whitaker, K. E., van Dokkum, P. G., et al. 2009, ApJLett, 706, L173

Bressan, A., Chiosi, C., & Fagotto, F. 1994, ApJS, 94, 63

Brinchmann, J., Charlot, S., Heckman, T. M., Kauffmann, G., Tremonti, C., & White, S. D. M. 2004, ArXiv Astrophysics e-prints

Brodwin, M., Stanford, S. A., Gonzalez, A. H., et al. 2013, ApJ, 779, 138

Brough, S., Couch, W. J., Collins, C. A., Jarrett, T., Burke, D. J., & Mann, R. G. 2008, MNRAS, 385, L103

Brough, S., Tran, K.-V., Sharp, R. G., von der Linden, A., & Couch, W. J. 2011, MNRAS, 414, L80

Bruzual, G. & Charlot, S. 2003, MNRAS, 344, 1000

Buckley, D. A. H., Swart, G. P., & Meiring, J. G. 2006, in Society of Photo-Optical Instrumentation Engineers (SPIE) Conference Series, Vol. 6267, Society of Photo-Optical Instrumentation Engineers (SPIE) Conference Series, 0

Bundy, K., Fukugita, M., Ellis, R. S., Targett, T. A., Belli, S., & Kodama, T. 2009, ApJ, 697, 1369

Burbidge, G. 1975, ApJLett, 196, L7

Burgh, E. B., Nordsieck, K. H., Kobulnicky, H. A., Williams, T. B., O'Donoghue, D., Smith, M. P., & Percival, J. W. in , Society of Photo-Optical Instrumentation Engineers (SPIE) Conference Series, Vol. 4841, Instrument Design and Performance for Optical/Infrared Ground-based Telescopes, ed. M. IyeA. F. M. Moorwood, 1463–1471

Burke, C. & Collins, C. A. 2013, MNRAS, 434, 2856

Burke, C., Collins, C. A., Stott, J. P., & Hilton, M. 2012, MNRAS, 425, 2058

Burke, C., Hilton, M., & Collins, C. 2015, MNRAS, 449, 2353

Burke, D. J., Collins, C. A., & Mann, R. G. 2000, ApJLett, 532, L105

Burkey, J. M., Keel, W. C., Windhorst, R. A., & Franklin, B. E. 1994, ApJLett, 429, L13

Butcher, H. & Oemler, Jr., A. 1984, ApJ, 285, 426

Cameron, E. 2011, PASA, 28, 128

Cappellari, M., Bacon, R., Bureau, M., et al. 2006, MNRAS, 366, 1126

Cardiel, N., Gorgas, J., & Aragon-Salamanca, A. 1995, MNRAS, 277, 502

Cardiel, N., Gorgas, J., & Aragón-Salamanca, A. 1998, Ap&SS, 263, 83

Carlberg, R. G., Cohen, J. G., Patton, D. R., et al. 2000, ApJLett, 532, L1

Carlstrom, J. E., Ade, P. A. R., Aird, K. A., et al. 2011, PASP, 123, 568

Catinella, B., Schiminovich, D., Cortese, L., et al. 2013, MNRAS, 436, 34

Chabrier, G. 2003, PASP, 115, 763

Chandrasekhar, S. 1943a, ApJ, 97, 255

—. 1943b, ApJ, 97, 263

—. 1943c, ApJ, 98, 54

Cimatti, A., Cassata, P., Pozzetti, L., et al. 2008, A&A, 482, 21

Ciotti, L. & Ostriker, J. P. 1997, ApJLett, 487, L105

Cole, S., Aragon-Salamanca, A., Frenk, C. S., Navarro, J. F., & Zepf, S. E. 1994, MNRAS, 271, 781

Cole, S., Lacey, C. G., Baugh, C. M., & Frenk, C. S. 2000, MNRAS, 319, 168

Colless, M., Dalton, G., Maddox, S., et al. 2001, MNRAS, 328, 1039

Collins, C. A., Stott, J. P., Hilton, M., et al. 2009, Nature, 458, 603

Conroy, C., Ho, S., & White, M. 2007a, MNRAS, 379, 1491

Conroy, C., Wechsler, R. H., & Kravtsov, A. V. 2007b, ApJ, 668, 826

Conselice, C. J. 2009, MNRAS, 399, L16

Conselice, C. J., Bershady, M. A., Dickinson, M., & Papovich, C. 2003, AJ, 126, 1183

Conselice, C. J., Yang, C., & Bluck, A. F. L. 2009, MNRAS, 394, 1956

Contini, E., De Lucia, G., Villalobos, Á., & Borgani, S. 2014, MNRAS, 437, 3787

Courteau, S., Cappellari, M., de Jong, R. S., et al. 2014, Reviews of Modern Physics, 86, 47

Cowie, L. L. & Binney, J. 1977, ApJ, 215, 723

Crawford, C. S., Allen, S. W., Ebeling, H., Edge, A. C., & Fabian, A. C. 1999, MNRAS, 306, 857

Crawford, S. M., Still, M., Schellart, P., et al. 2010, in Society of Photo-Optical Instrumentation Engineers (SPIE) Conference Series, Vol. 7737, Society of Photo-Optical Instrumentation Engineers (SPIE) Conference Series, 25

Croton, D. J., Springel, V., White, S. D. M., et al. 2006, MNRAS, 365, 11

Cucciati, O., De Lucia, G., Zucca, E., et al. 2012, A&A, 548, A108

Daddi, E., Renzini, A., Pirzkal, N., et al. 2005, ApJ, 626, 680

Davies, L. J. M., Robotham, A. S. G., Driver, S. P., et al. 2016, MNRAS, 455, 4013

Davis, M., Guhathakurta, P., Konidaris, N. P., et al. 2007, ApJLett, 660, L1

de Jong, J. T. A., Verdoes Kleijn, G. A., Boxhoorn, D. R., et al. 2015, A&A, 582, A62

De Lucia, G. & Blaizot, J. 2007, MNRAS, 375, 2

De Lucia, G., Springel, V., White, S. D. M., Croton, D., & Kauffmann, G. 2006, MNRAS, 366, 499

de Ravel, L., Le Fèvre, O., Tresse, L., et al. 2009, A&A, 498, 379

de Vaucouleurs, G. 1974, in IAU Symposium, Vol. 58, The Formation and Dynamics of Galaxies, ed. J. R. Shakeshaft, 1–52

Dekel, A. & Silk, J. 1986, ApJ, 303, 39

DeMaio, T., Gonzalez, A. H., Zabludoff, A., Zaritsky, D., & Bradač, M. 2015, MNRAS, 448, 1162

Demarco, R., Wilson, G., Muzzin, A., et al. 2010, ApJ, 711, 1185

Diaferio, A., Kauffmann, G., Balogh, M. L., White, S. D. M., Schade, D., & Ellingson, E. 2001, MNRAS, 323, 999

Donahue, M., Bruch, S., Wang, E., et al. 2010, ApJ, 715, 881

Drake, N., Merrifield, M. R., Sakelliou, I., & Pinkney, J. C. 2000, MNRAS, 314, 768

Dressler, A. 1980, ApJ, 236, 351

Driver, S. P., Hill, D. T., Kelvin, L. S., et al. 2011, MNRAS, 413, 971

D'Souza, R., Vegetti, S., & Kauffmann, G. 2015, MNRAS, 454, 4027

Dubinski, J. 1998, ApJ, 502, 141

Duncan, M. J., Farouki, R. T., & Shapiro, S. L. 1983, ApJ, 271, 22

Dye, S., Warren, S. J., Hambly, N. C., et al. 2006, MNRAS, 372, 1227

Ebeling, H., Edge, A. C., Allen, S. W., Crawford, C. S., Fabian, A. C., & Huchra, J. P. 2000, MNRAS, 318, 333

Ebeling, H., Edge, A. C., Bohringer, H., Allen, S. W., Crawford, C. S., Fabian, A. C., Voges, W., & Huchra, J. P. 1998, MNRAS, 301, 881

Ebeling, H., Edge, A. C., & Henry, J. P. 2001, ApJ, 553, 668

Ebeling, H., Voges, W., Bohringer, H., Edge, A. C., Huchra, J. P., & Briel, U. G. 1996, MNRAS, 281, 799

Edge, A. C. 1991, MNRAS, 250, 103

—. 2001, MNRAS, 328, 762

Edwards, L. O. V., Hudson, M. J., Balogh, M. L., & Smith, R. J. 2007, MNRAS, 379, 100

Edwards, L. O. V. & Patton, D. R. 2012, MNRAS, 425, 287

Egami, E., Misselt, K. A., Rieke, G. H., et al. 2006, ApJ, 647, 922

Eisenhardt, P. R. M., Brodwin, M., Gonzalez, A. H., et al. 2008, ApJ, 684, 905

Eisenstein, D. J., Annis, J., Gunn, J. E., et al. 2001, AJ, 122, 2267

Ellison, S. L., Mendel, J. T., Scudder, J. M., Patton, D. R., & Palmer, M. J. D. 2013, MNRAS, 430, 3128

Evrard, A. E., Summers, F. J., & Davis, M. 1994, ApJ, 422, 11

Faber, S. M., Willmer, C. N. A., Wolf, C., et al. 2007, ApJ, 665, 265

Fabian, A. C. 1994, ARA&A, 32, 277

Fabian, A. C. & Nulsen, P. E. J. 1977, MNRAS, 180, 479

Fabian, A. C., Nulsen, P. E. J., & Canizares, C. R. 1982, MNRAS, 201, 933

Fakhouri, O., Ma, C.-P., & Boylan-Kolchin, M. 2010, MNRAS, 406, 2267

Farouki, R. & Shapiro, S. L. 1981, ApJ, 243, 32

Finoguenov, A., Guzzo, L., Hasinger, G., et al. 2007, ApJS, 172, 182

Franx, M., van Dokkum, P. G., Schreiber, N. M. F., Wuyts, S., Labbé, I., & Toft, S. 2008, ApJ, 688, 770

Fraser-McKelvie, A., Brown, M. J. I., & Pimbblet, K. A. 2014, MNRAS, 444, L63

Frenk, C. S., White, S. D. M., Davis, M., & Efstathiou, G. 1988, ApJ, 327, 507

Fritz, A., Scodeggio, M., Ilbert, O., et al. 2014, A&A, 563, A92

Fujita, Y. 1998, ApJ, 509, 587

—. 2001, ApJ, 550, 612

Fujita, Y. & Nagashima, M. 1999, ApJ, 516, 619

Gallagher, III, J. S. & Ostriker, J. P. 1972, AJ, 77, 288

Galloway, M. A., Willett, K. W., Fortson, L. F., et al. 2015, MNRAS, 448, 3442

Gao, L., Loeb, A., Peebles, P. J. E., White, S. D. M., & Jenkins, A. 2004a, ApJ, 614, 17

Gao, L., White, S. D. M., Jenkins, A., Stoehr, F., & Springel, V. 2004b, MNRAS, 355, 819

Gebhardt, K. & Beers, T. C. 1991, ApJ, 383, 72

Gehrels, N. 1986, ApJ, 303, 336

Ghigna, S., Moore, B., Governato, F., Lake, G., Quinn, T., & Stadel, J. 1998, MNRAS, 300, 146

Gladders, M. D., López-Cruz, O., Yee, H. K. C., & Kodama, T. 1998, ApJ, 501, 571

Gladders, M. D. & Yee, H. K. C. 2000, AJ, 120, 2148

—. 2005, ApJS, 157, 1

Gómez, P. L., Nichol, R. C., Miller, C. J., et al. 2003, ApJ, 584, 210

Gonzalez, A. H., Zabludoff, A. I., & Zaritsky, D. 2003, Ap&SS, 285, 67

—. 2005, ApJ, 618, 195

Gonzalez, A. H., Zabludoff, A. I., Zaritsky, D., & Dalcanton, J. J. 2000, ApJ, 536, 561

Gordon, K. D., Clayton, G. C., Misselt, K. A., Landolt, A. U., & Wolff, M. J. 2003, ApJ, 594, 279

Gozaliasl, G., Finoguenov, A., Khosroshahi, H. G., Mirkazemi, M., Erfanianfar, G., & Tanaka, M. 2016, MNRAS, 458, 2762

Graham, A. W. & Driver, S. P. 2005, PASA, 22, 118

Groenewald, D. N. & Loubser, S. I. 2014, MNRAS, 444, 808

Gunn, J. E. & Gott, III, J. R. 1972, ApJ, 176, 1

Gunn, J. E., Hoessel, J. G., & Oke, J. B. 1986, ApJ, 306, 30

Gunn, J. E. & Oke, J. B. 1975, ApJ, 195, 255

Guth, A. H. 1981, Phys. Rev. D, 23, 347

Guth, A. H. & Pi, S.-Y. 1982, Physical Review Letters, 49, 1110

Hao, J., McKay, T. A., Koester, B. P., et al. 2010, ApJS, 191, 254

Hashimoto, Y., Henry, J. P., & Boehringer, H. 2014, MNRAS, 440, 588

Hawking, S. W. 1982, Physics Letters B, 115, 295

Hernández-Toledo, H. M., Avila-Reese, V., Conselice, C. J., & Puerari, I. 2005, AJ, 129, 682

Hicks, A. K., Ellingson, E., Hoekstra, H., et al. 2007, ApJ, 671, 1446

Hicks, A. K. & Mushotzky, R. 2005, ApJLett, 635, L9

Hicks, A. K., Mushotzky, R., & Donahue, M. 2010, ApJ, 719, 1844

Hill, D. T., Kelvin, L. S., Driver, S. P., et al. 2011, MNRAS, 412, 765

Hillebrandt, W., Nomoto, K., & Wolff, R. G. 1984, A&A, 133, 175

Hoessel, J. G., Gunn, J. E., & Thuan, T. X. 1980, ApJ, 241, 486

Hoessel, J. G. & Schneider, D. P. 1985, AJ, 90, 1648

Hsieh, B. C., Yee, H. K. C., Lin, H., Gladders, M. D., & Gilbank, D. G. 2008, ApJ, 683, 33

Hubble, E. & Humason, M. L. 1931, ApJ, 74, 43

Inagaki, T., Lin, Y.-T., Huang, H.-J., Hsieh, B.-C., & Sugiyama, N. 2015, MNRAS, 446, 1107

Jogee, S., Miller, S. H., Penner, K., et al. 2009, ApJ, 697, 1971

Jones, C. & Forman, W. 1984, ApJ, 276, 38

—. 1999, ApJ, 511, 65

Kartaltepe, J. S., Sanders, D. B., Scoville, N. Z., et al. 2007, ApJS, 172, 320

Katayama, H., Hayashida, K., Takahara, F., & Fujita, Y. 2003, ApJ, 585, 687

Katz, N., Hernquist, L., & Weinberg, D. H. 1992, ApJLett, 399, L109

Kauffmann, G., Guiderdoni, B., & White, S. D. M. 1994, MNRAS, 267, 981

Kauffmann, G., Heckman, T. M., White, S. D. M., et al. 2003, MNRAS, 341, 54

Kauffmann, G., Li, C., & Heckman, T. M. 2010, MNRAS, 409, 491

Kauffmann, G., Nusser, A., & Steinmetz, M. 1997, MNRAS, 286, 795

Kauffmann, G., White, S. D. M., Heckman, T. M., Ménard, B., Brinchmann, J., Charlot, S., Tremonti, C., & Brinkmann, J. 2004, MNRAS, 353, 713

Kaviraj, S., Khochfar, S., Schawinski, K., et al. 2008, MNRAS, 388, 67

Kaviraj, S., Schawinski, K., Devriendt, J. E. G., et al. 2007, ApJS, 173, 619

Keel, W. C. 2007, The road to galaxy formation

Keenan, R. C., Foucaud, S., De Propris, R., et al. 2014, ApJ, 795, 157

Kelvin, L., Driver, S., Robotham, A., Hill, D., & Cameron, E. in , American Institute of Physics Conference Series, Vol. 1240, American Institute of Physics Conference Series, ed. V. P. DebattistaC. C. Popescu, 247–248

Kelvin, L. S., Driver, S. P., Robotham, A. S. G., et al. 2012, MNRAS, 421, 1007

Kitzbichler, M. G. & White, S. D. M. 2008, MNRAS, 391, 1489

Kochanek, C. S., Eisenstein, D. J., Cool, R. J., et al. 2012, ApJS, 200, 8

Kormendy, J. 1989, ApJLett, 342, L63

Krick, J. E. & Bernstein, R. A. 2007, AJ, 134, 466

Kristian, J., Sandage, A., & Westphal, J. A. 1978, ApJ, 221, 383

Kron, R. G. 1980, ApJS, 43, 305

Kurtz, M. J., Mink, D. J., Wyatt, W. F., Fabricant, D. G., Torres, G., Kriss, G. A., & Tonry, J. L. Astronomical Society of the Pacific Conference Series, Vol. 25, , Astronomical Data Analysis Software and Systems I, ed. D. M. WorrallC. Biemesderfer & J. Barnes, 432

Lake, G., Katz, N., & Moore, B. 1998, ApJ, 495, 152

Laporte, C. F. P., White, S. D. M., Naab, T., & Gao, L. 2013, MNRAS, 435, 901

Larson, R. B. 1974, MNRAS, 166, 585

Larson, R. B., Tinsley, B. M., & Caldwell, C. N. 1980, ApJ, 237, 692

Lauer, T. R. 1988, ApJ, 325, 49

Lauer, T. R., Faber, S. M., Richstone, D., et al. 2007, ApJ, 662, 808

Lauer, T. R. & Postman, M. 1992, ApJLett, 400, L47

Lavery, R. J., Remijan, A., Charmandaris, V., Hayes, R. D., & Ring, A. A. 2004, ApJ, 612, 679

Le Fèvre, O., Abraham, R., Lilly, S. J., et al. 2000, MNRAS, 311, 565

Lee, H. M., Park, M., & Park, W.-I. 2012, Phys. Rev. D, 86, 103502

Leisawitz, D. & Hauser, M. G. 1988, ApJ, 332, 954

Lewis, I., Balogh, M., De Propris, R., et al. 2002, MNRAS, 334, 673

Li, C., Kauffmann, G., Jing, Y. P., White, S. D. M., Börner, G., & Cheng, F. Z. 2006, MNRAS, 368, 21

Lidman, C., Iacobuta, G., Bauer, A. E., et al. 2013, MNRAS, 433, 825

Lidman, C., Suherli, J., Muzzin, A., et al. 2012, MNRAS, 427, 550

Lin, L., Koo, D. C., Willmer, C. N. A., et al. 2004, ApJLett, 617, L9

Lin, L., Patton, D. R., Koo, D. C., et al. 2008, ApJ, 681, 232

Lin, Y.-T., Brodwin, M., Gonzalez, A. H., Bode, P., Eisenhardt, P. R. M., Stanford, S. A., & Vikhlinin, A. 2013, ApJ, 771, 61

Lin, Y.-T. & Mohr, J. J. 2004, ApJ, 617, 879

Lin, Y.-T., Ostriker, J. P., & Miller, C. J. 2010, ApJ, 715, 1486

Liu, F. S., Lei, F. J., Meng, X. M., & Jiang, D. F. 2015, MNRAS, 447, 1491

Liu, F. S., Mao, S., Deng, Z. G., Xia, X. Y., & Wen, Z. L. 2009, MNRAS, 396, 2003

Liu, F. S., Mao, S., & Meng, X. M. 2012, MNRAS, 423, 422

Loh, Y.-S. & Strauss, M. A. 2006, MNRAS, 366, 373

Longair, M. S. 2008, Galaxy Formation

López-Cruz, O., Yee, H. K. C., Brown, J. P., Jones, C., & Forman, W. 1997, ApJLett, 475, L97

López-Sanjuan, C., Cenarro, A. J., Hernández-Monteagudo, C., et al. 2014, A&A, 564, A127

López-Sanjuan, C., Le Fèvre, O., Ilbert, O., et al. 2012, A&A, 548, A7

Lotz, J. M., Davis, M., Faber, S. M., et al. 2008, ApJ, 672, 177

Lotz, J. M., Jonsson, P., Cox, T. J., Croton, D., Primack, J. R., Somerville, R. S., & Stewart, K. 2011, ApJ, 742, 103

Lotz, J. M., Madau, P., Giavalisco, M., Primack, J., & Ferguson, H. C. 2006, ApJ, 636, 592

Loubser, S. I., Babul, A., Hoekstra, H., Mahdavi, A., Donahue, M., Bildfell, C., & Voit, G. M. 2016, MNRAS, 456, 1565

Lu, T., Gilbank, D. G., Balogh, M. L., & Bognat, A. 2009, MNRAS, 399, 1858

Lubin, L. M. 1996, AJ, 112, 23

Lubin, L. M., Brunner, R., Metzger, M. R., Postman, M., & Oke, J. B. 2000, ApJLett, 531, L5

Maier, C., Lilly, S. J., Zamorani, G., et al. 2009, ApJ, 694, 1099

Malmquist, K. G. 1920, Lund Medd. Ser., II

Malumuth, E. M. 1992, ApJ, 386, 420

Mancini, C., Daddi, E., Renzini, A., et al. 2010, MNRAS, 401, 933

Marchesini, D., Muzzin, A., Stefanon, M., et al. 2014, ApJ, 794, 65

Masjedi, M., Hogg, D. W., Cool, R. J., et al. 2006, ApJ, 644, 54

Mathis, J. S., Mezger, P. G., & Panagia, N. 1983, A&A, 128, 212

Matteucci, F. & Tornambe, A. 1987, A&A, 185, 51

Matthews, T. A., Morgan, W. W., & Schmidt, M. 1964, ApJ, 140, 35

McDonald, M., Bayliss, M., Benson, B. A., et al. 2012, Nature, 488, 349

McIntosh, D. H., Guo, Y., Hertzberg, J., Katz, N., Mo, H. J., van den Bosch, F. C., & Yang, X. 2008, MNRAS, 388, 1537

McNamara, B. R. & O'Connell, R. W. 1989, AJ, 98, 2018

McNamara, B. R., Rafferty, D. A., Bîrzan, L., et al. 2006, ApJ, 648, 164

Mendel, J. T., Simard, L., Palmer, M., Ellison, S. L., & Patton, D. R. 2014, ApJS, 210, 3

Merlin, E. & Chiosi, C. 2006, A&A, 457, 437

Merrifield, M. R. & Kent, S. M. 1991, AJ, 101, 783

Merritt, D. 1983, ApJ, 264, 24

—. 1984, ApJ, 276, 26

—. 1985, MNRAS, 214, 25P

Mihos, J. C., Harding, P., Feldmeier, J., & Morrison, H. 2005, ApJLett, 631, L41

Mo, H., van den Bosch, F. C., & White, S. 2010, Galaxy Formation and Evolution

Moffett, A. J., Ingarfield, S. A., Driver, S. P., et al. 2016, MNRAS, 457, 1308

Moore, B., Katz, N., Lake, G., Dressler, A., & Oemler, A. 1996, Nature, 379, 613

Moore, B., Lake, G., & Katz, N. 1998, ApJ, 495, 139

Moore, B., Lake, G., Quinn, T., & Stadel, J. 1999, MNRAS, 304, 465

Morgan, W. W. 1958, PASP, 70, 364

Murante, G., Arnaboldi, M., Gerhard, O., et al. 2004, ApJLett, 607, L83

Murante, G., Giovalli, M., Gerhard, O., Arnaboldi, M., Borgani, S., & Dolag, K. 2007, MNRAS, 377, 2

Muzzin, A., Wilson, G., Yee, H. K. C., et al. 2012, ApJ, 746, 188

—. 2009, ApJ, 698, 1934

Naab, T., Johansson, P. H., & Ostriker, J. P. 2009, ApJLett, 699, L178

Navarro, J. F. & Steinmetz, M. 1997, ApJ, 478, 13

Novikov, I. 1964, Soviet Phys. JETP, 19

O'Dea, C. P., Baum, S. A., Privon, G., et al. 2008, ApJ, 681, 1035

O'Dea, K. P., Quillen, A. C., O'Dea, C. P., et al. 2010, ApJ, 719, 1619

O'Donoghue, D., Buckley, D. A. H., Balona, L. A., et al. 2006, MNRAS, 372, 151

Oegerle, W. R. & Hill, J. M. 2001, AJ, 122, 2858

Oemler, A. 1973, ApJ, 180, 11

Oemler, Jr., A. 1976, ApJ, 209, 693

Oliva-Altamirano, P., Brough, S., Jimmy, Kim-Vy, T., Couch, W. J., McDermid, R. M., Lidman, C., von der Linden, A., & Sharp, R. 2015, MNRAS, 449, 3347

Oliva-Altamirano, P., Brough, S., Lidman, C., et al. 2014, MNRAS, 440, 762

Ostriker, J. P. & Hausman, M. A. 1977, ApJLett, 217, L125

Ostriker, J. P. & Tremaine, S. D. 1975, ApJLett, 202, L113

Ownsworth, J. R., Conselice, C. J., Mortlock, A., Hartley, W. G., Almaini, O., Duncan, K., & Mundy, C. J. 2014, MNRAS, 445, 2198

Pasquali, A., Gallazzi, A., Fontanot, F., van den Bosch, F. C., De Lucia, G., Mo, H. J., & Yang, X. 2010, MNRAS, 407, 937

Patel, P., Maddox, S., Pearce, F. R., Aragón-Salamanca, A., & Conway, E. 2006, MNRAS, 370, 851

Patton, D. R., Carlberg, R. G., Marzke, R. O., Pritchet, C. J., da Costa, L. N., & Pellegrini, P. S. 2000, ApJ, 536, 153

Patton, D. R., Pritchet, C. J., Carlberg, R. G., et al. 2002, ApJ, 565, 208

Peng, C. Y., Ho, L. C., Impey, C. D., & Rix, H. W. 2007, in Bulletin of the American Astronomical Society, Vol. 39, American Astronomical Society Meeting Abstracts, 804

Peng, Y.-j., Lilly, S. J., Kovač, K., et al. 2010, ApJ, 721, 193

Petrosian, V. 1976, ApJLett, 209, L1

Pierre, M., Valtchanov, I., Altieri, B., et al. 2004, JCAP, 9, 011

Pipino, A., Kaviraj, S., Bildfell, C., Babul, A., Hoekstra, H., & Silk, J. 2009, MNRAS, 395, 462

Planck Collaboration, Ade, P. A. R., Aghanim, N., et al. 2014a, A&A, 571, A1

—. 2014b, A&A, 571, A29

Postman, M. & Lauer, T. R. 1995, ApJ, 440, 28

Prestwich, A. H. & Joy, M. 1991, ApJLett, 369, L1

Puchwein, E., Springel, V., Sijacki, D., & Dolag, K. 2010, MNRAS, 406, 936

Quintana, H. & Lawrie, D. G. 1982, AJ, 87, 1

Rafferty, D. A., McNamara, B. R., & Nulsen, P. E. J. 2008, ApJ, 687, 899

Rakos, K. D. & Schombert, J. M. 1995, ApJ, 439, 47

Rasmussen, J., Mulchaey, J. S., Bai, L., Ponman, T. J., Raychaudhury, S., & Dariush, A. 2010, ApJ, 717, 958

Rawle, T. D., Rex, M., Egami, E., et al. 2012, ApJ, 756, 106

Rees, G. A., Norris, R. P., Spitler, L. R., Herrera-Ruiz, N., & Middelberg, E. 2016, MNRAS, 458, L49

Rees, M. J. & Ostriker, J. P. 1977, MNRAS, 179, 541

Rhee, G. F. R. N. & Latour, H. J. 1991, A&A, 243, 38

Richstone, D. O. 1976, ApJ, 204, 642

Rieke, G. H., Lebofsky, M. J., Thompson, R. I., Low, F. J., & Tokunaga, A. T. 1980, ApJ, 238, 24

Robaina, A. R., Bell, E. F., van der Wel, A., Somerville, R. S., Skelton, R. E., McIntosh, D. H., Meisenheimer, K., & Wolf, C. 2010, ApJ, 719, 844

Robotham, A. S. G., Driver, S. P., Davies, L. J. M., et al. 2014, MNRAS, 444, 3986

Robotham, A. S. G., Norberg, P., Driver, S. P., et al. 2011, MNRAS, 416, 2640

Rozo, E. & Rykoff, E. S. 2014, ApJ, 783, 80

Rozo, E., Rykoff, E. S., Bartlett, J. G., & Melin, J.-B. 2015, MNRAS, 450, 592

Rozo, E., Rykoff, E. S., Evrard, A., et al. 2009, ApJ, 699, 768

Rudick, C. S., Mihos, J. C., & McBride, C. K. 2011, ApJ, 732, 48

Rykoff, E. S., Koester, B. P., Rozo, E., et al. 2012, ApJ, 746, 178

Rykoff, E. S., Rozo, E., Busha, M. T., et al. 2014, ApJ, 785, 104

Sánchez, C., Carrasco Kind, M., Lin, H., et al. 2014, MNRAS, 445, 1482

Sandage, A. 1972, ApJ, 178, 1

—. 1976, ApJ, 205, 6

—. 1988, ARA&A, 26, 561

Sandage, A. & Hardy, E. 1973, ApJ, 183, 743

Saracco, P., Longhetti, M., & Gargiulo, A. 2010, MNRAS, 408, L21

Sarazin, C. L. 1986, Reviews of Modern Physics, 58, 1

Sarazin, C. L. & O'Connell, R. W. 1983, ApJ, 268, 552

Schlegel, D. J., Finkbeiner, D. P., & Davis, M. 1998, ApJ, 500, 525

Schneider, D. P. & Gunn, J. E. 1982, ApJ, 263, 14

Schneider, D. P., Gunn, J. E., & Hoessel, J. G. 1983, ApJ, 268, 476

Schombert, J. M. 1986, ApJS, 60, 603

—. 1987, ApJS, 64, 643

—. 1988, ApJ, 328, 475

Scoville, N., Abraham, R. G., Aussel, H., et al. 2007, ApJS, 172, 38

Sharples, R. M., Ellis, R. S., & Gray, P. M. 1988, MNRAS, 231, 479

Silk, J. 1976, ApJ, 208, 646

Silk, J. & Mamon, G. A. 2012, Research in Astronomy and Astrophysics, 12, 917

Silk, J. & Rees, M. J. 1998, A&A, 331, L1

Simard, L., Mendel, J. T., Patton, D. R., Ellison, S. L., & McConnachie, A. W. 2011, ApJS, 196, 11

Skibba, R. A. & Macciò, A. V. 2011, MNRAS, 416, 2388

Smith, G. P., Kneib, J.-P., Smail, I., Mazzotta, P., Ebeling, H., & Czoske, O. 2005, MNRAS, 359, 417

Sommer-Larsen, J., Romeo, A. D., & Portinari, L. 2005, MNRAS, 357, 478

Spergel, D. N., Bean, R., Doré, O., et al. 2007, ApJS, 170, 377

Spergel, D. N., Verde, L., Peiris, H. V., et al. 2003, ApJS, 148, 175

Springel, V., White, S. D. M., Jenkins, A., et al. 2005, Nature, 435, 629

Stott, J. P., Collins, C. A., Burke, C., Hamilton-Morris, V., & Smith, G. P. 2011, MNRAS, 414, 445

Stott, J. P., Collins, C. A., Sahlén, M., et al. 2010, ApJ, 718, 23

Stott, J. P., Edge, A. C., Smith, G. P., Swinbank, A. M., & Ebeling, H. 2008, MNRAS, 384, 1502

Stott, J. P., Hickox, R. C., Edge, A. C., et al. 2012, MNRAS, 422, 2213

Stoughton, C., Lupton, R. H., Bernardi, M., et al. 2002, AJ, 123, 485

Strateva, I., Ivezić, Ž., Knapp, G. R., et al. 2001, AJ, 122, 1861

Strauss, M. A., Weinberg, D. H., Lupton, R. H., et al. 2002, AJ, 124, 1810

Struble, M. F. & Rood, H. J. 1991, ApJS, 77, 363

Sunyaev, R. A. & Zeldovich, Y. B. 1970, Ap&SS, 7, 20

Swetz, D. S., Ade, P. A. R., Amiri, M., et al. 2011, ApJS, 194, 41

Tabor, G. & Binney, J. 1993, MNRAS, 263, 323

Tal, T., van Dokkum, P. G., Nelan, J., & Bezanson, R. 2009, AJ, 138, 1417

Tavasoli, S., Khosroshahi, H. G., Koohpaee, A., Rahmani, H., & Ghanbari, J. 2011, PASP, 123, 1

Taylor, E. N., Franx, M., van Dokkum, P. G., et al. 2009, ApJ, 694, 1171

Taylor, E. N., Hopkins, A. M., Baldry, I. K., et al. 2015, MNRAS, 446, 2144

—. 2011, MNRAS, 418, 1587

Teague, P. F., Carter, D., & Gray, P. M. 1990, ApJS, 72, 715

Toft, S., van Dokkum, P., Franx, M., et al. 2007, ApJ, 671, 285

Toniazzo, T. & Schindler, S. 2001, MNRAS, 325, 509

Tonini, C., Bernyk, M., Croton, D., Maraston, C., & Thomas, D. 2012, ApJ, 759, 43

Tonry, J. L. 1987, in IAU Symposium, Vol. 127, Structure and Dynamics of Elliptical Galaxies, ed. P. T. de Zeeuw, 89–96

Toomre, A. & Toomre, J. 1972, ApJ, 178, 623

Tremaine, S. 1990, The origin of central cluster galaxies., ed. R. Wielen, 394–405

Tremaine, S. D. & Richstone, D. O. 1977, ApJ, 212, 311

Trujillo, I., Conselice, C. J., Bundy, K., Cooper, M. C., Eisenhardt, P., & Ellis, R. S. 2007, MNRAS, 382, 109

Trujillo, I., Förster Schreiber, N. M., Rudnick, G., et al. 2006, ApJ, 650, 18

Valentinuzzi, T., Poggianti, B. M., Saglia, R. P., et al. 2010, ApJLett, 721, L19

van den Bosch, F. C., Aquino, D., Yang, X., Mo, H. J., Pasquali, A., McIntosh, D. H., Weinmann, S. M., & Kang, X. 2008, MNRAS, 387, 79

van der Marel, R. P. 1991, MNRAS, 253, 710

van der Wel, A., Holden, B. P., Zirm, A. W., Franx, M., Rettura, A., Illingworth, G. D., & Ford, H. C. 2008, ApJ, 688, 48

van Dokkum, P. G. 2001, PASP, 113, 1420

—. 2005, AJ, 130, 2647

van Dokkum, P. G. & Franx, M. 1996, MNRAS, 281, 985

—. 2001, ApJ, 553, 90

van Dokkum, P. G., Franx, M., Fabricant, D., Illingworth, G. D., & Kelson, D. D. 2000, ApJ, 541, 95

van Dokkum, P. G., Franx, M., Kriek, M., et al. 2008, ApJLett, 677, L5

van Dokkum, P. G., Kriek, M., & Franx, M. 2009, Nature, 460, 717

van Dokkum, P. G., Whitaker, K. E., Brammer, G., et al. 2010, ApJ, 709, 1018

Vikhlinin, A., Burenin, R. A., Ebeling, H., et al. 2009, ApJ, 692, 1033

von der Linden, A., Best, P. N., Kauffmann, G., & White, S. D. M. 2007, MNRAS, 379, 867

Wang, J., Overzier, R., Kauffmann, G., von der Linden, A., & Kong, X. 2010, MNRAS, 401, 433

Weinmann, S. M., Kauffmann, G., van den Bosch, F. C., Pasquali, A., McIntosh, D. H., Mo, H., Yang, X., & Guo, Y. 2009, MNRAS, 394, 1213

Weinmann, S. M., van den Bosch, F. C., Yang, X., & Mo, H. J. 2006, MNRAS, 366, 2

Whiley, I. M., Aragón-Salamanca, A., De Lucia, G., et al. 2008, MNRAS, 387, 1253

Whitaker, K. E., Labbé, I., van Dokkum, P. G., et al. 2011, ApJ, 735, 86

White, S. D. M. & Frenk, C. S. 1991, ApJ, 379, 52

White, S. D. M. & Rees, M. J. 1978, MNRAS, 183, 341

Williams, R. J., Quadri, R. F., & Franx, M. 2011, ApJLett, 738, L25

Willman, B., Governato, F., Wadsley, J., & Quinn, T. 2004, MNRAS, 355, 159

Wilman, D. J., Zibetti, S., & Budavári, T. 2010, MNRAS, 406, 1701

Wilman, R. J., Edge, A. C., & Swinbank, A. M. 2006, MNRAS, 371, 93

Wilson, G., Muzzin, A., Yee, H. K. C., et al. 2009, ApJ, 698, 1943

Yang, X., Mo, H. J., & van den Bosch, F. C. 2009, ApJ, 695, 900

Yang, X., Mo, H. J., van den Bosch, F. C., Pasquali, A., Li, C., & Barden, M. 2007, ApJ, 671, 153

York, D. G., Adelman, J., Anderson, Jr., J. E., et al. 2000, AJ, 120, 1579

Zabludoff, A. I., Geller, M. J., Huchra, J. P., & Ramella, M. 1993, AJ, 106, 1301

Zabludoff, A. I., Huchra, J. P., & Geller, M. J. 1990, ApJS, 74, 1

Zehavi, I., Blanton, M. R., Frieman, J. A., et al. 2002, ApJ, 571, 172

Zeldovich, Y. B. & Sunyaev, R. A. 1969, Ap&SS, 4, 301

Zepf, S. E. & Koo, D. C. 1989, ApJ, 337, 34

Zhang, Y., Miller, C., McKay, T., et al. 2016, ApJ, 816, 98

Zwicky, F., Herzog, E., Wild, P., Karpowicz, M., & Kowal, C. T. 1961, Catalogue of galaxies and of clusters of galaxies, Vol. I